INVESTIGATIONS OF INORGANIC NANOWIRES, CARBON NANOTUBES AND Co/Mn doped ZnO

A Thesis submitted in partial fulfillment of

the requirements of the degree of

Doctor of Philosophy

BY

Leonard Deepak F

CHEMISTRY AND PHYSICS OF MATERIALS UNIT

JAWAHARLAL NEHRU CENTRE FOR ADVANCED SCIENTIFIC RESEARCH,

(A Deemed University)

BANGALORE – 560064 (INDIA)

November 2005

Dedicated to my family

Declaration

I hereby declare that this thesis entitled **"Investigations of Inorganic Nanowires, Carbon Nanotubes and Co/Mn doped ZnO"** is an authentic record of research work carried out by me under the supervision of Prof. C. N. R. Rao, FRS, at the Chemistry and Physics of Materials Unit, Jawaharlal Nehru Centre for Advanced Scientific Research, Bangalore, India.

In keeping with the general practice of reporting scientific observations, due acknowledgement has been made whenever work described here has been based on the findings of other investigators. Any oversight due to error of judgement is regretted.

Leonard Deepak F

Certificate

Certified that the work described in this thesis entitled **"Investigations of Inorganic Nanowires, Carbon Nanotubes and Co/Mn doped ZnO"** has been carried out by Leonard Deepak F, under my supervision at the Chemistry and Physics of Materials Unit, Jawaharlal Nehru Centre for Advanced Scientific Research, Bangalore, India.

Prof. C. N. R. Rao

Acknowledgements

I would like to express my respect, gratitude and thanks to Prof. C. N. R. Rao, F. R. S, for suggesting the various research problems and for guidance during the course of this entire research work. I am especially thankful for the immense support, constant and continuous encouragement that I have been fortunate enough to have received from him. I am grateful to him for having given me the opportunity to work on different areas of research and for being patient with me when things did not work. I am also grateful to him for financial support that he has been kind enough to extend to me, for various reasons including attending conferences and for my stay in JNCASR. From the days when he picked me up from being a summer student, and through the days when I have worked under him, he has always been there, giving his very best to me.

It is a pleasure to thank Dr. A. Govindaraj for teaching me the art of doing experiments systematically and without giving them up in difficult times. His enthusiasm and positive attitude has made working with him a tremendous learning experience. It has always been enjoyable working with him all along.

I would like to thank Prof. G. U. Kulkarni for introducing me to scanning probe microscopy. He has been patient and understanding whenever I approached him with doubts. I am also grateful for his help that he has been kind enough to extend to me on many an occasion.

I would like to thank Dr. Gautam, Dr. C. P. Vinod, Dr. K. Mukhopadhyay, Dr. Manashi Nath, Dr. P. V. Vanitha, Poovarasan, Nikhil Gunari, Kalyani, Neena, Motin, Vivek, Kripa, Pearl, Ujjal (JNCASR, Bangalore), Dr. Pallavi Teredesai and Prof. A. K. Sood (Physics Department, IISc, Bangalore), Kinson and Prof. A. K. Cheetham (UCSB) for fruitful collaborations.

I am specially grateful to Prof. Manfred Rühle and Dr. Torsten Seeger (Germany) and Drs. Ram Seshadri and K. Ramesha (UCSB) for help with TEM-EELS and magnetic measurements.

I would like to thank the faculty members of CPMU and TSU for coursework - Prof. G. U. Kulkarni, Dr. A. R. Raju, Dr. S. Balasubramaniam, Dr. Chandrabhas, Prof. K. S. Narayan, Dr. S. Natarajan, Dr. Swapan Pati, Dr. S. Narasimhan.

I have been fortunate to have had excellent labmates with whom I have worked with, specially Kalyani, Vivek, Gautam and Manashi (Carbon Lab), Neena, Ved and Ujjal (Nanolab). Thanks are due to John specially for helping me learn STM and XPS. Thanks are also due to Vivek, Kalyani, N. Vinod, Gomathi, S. Lakshmi, Ujjal and Basu for all their help during the course of writing this thesis.

I am indebted to the various technical staff of CPMU specially Usha Madam (TEM), Basavaraj (SEM), Anil (XRD) and Vasu (Measurements), Srinath, Srinivas, Rao (Nanolab). They have helped me with various characterizations during the course of this study.

Special thanks are due to the Administrative, Academic, Library and Complab Staff for providing and maintaining the various facilities that have helped me immensely.

I must specially mention the love, affection and hospitality provided abundantly to me from Mrs. Indumati Rao and Sanjay.

Thanks are due to my friends and batch mates who have stood by me and kept me going all these years. I can never forget the time I spent with N. Vinod, Vivek, Kalyani, Gautam, Pushpa, Lakshmi, Gomathi, Ujjal, Neena, Reji, Sameen, Minaxie, CP, Sudhee, Pattu, Sujay, Sachin, John, Murugs, Arpita, Pearl, Magi, Sebastian, Sandip, Kripa, Jaya, Gargi, Ved, Kapoor, Ram, Rinki, Bhat, Sharmila, Shailesh, Vaidhya, KSiva, Archana, Punit, Arun, Kabra, Dash, Angappane, Bhuvana and pal.

To all my humble achievements till date, I am specially grateful to my parents and to my family for all their love, affection, support and strength. I am grateful to them, for not only having guided me in making my career but also for having helped me all along in very many ways. If not for them I would not have reached this far in my life.

Preface

This thesis deals with the synthesis, characterization and properties of inorganic nanowires, carbon nanotubes especially those of Y-junction nanotubes and the effects of doping ZnO with Co and Mn.

Chapter 1 gives a brief survey of nanowires and nanotubes. Chapter 2 deals with the synthesis of carbon nanotubes, especially those of Y-junction nanotubes. The structure and the electronic properties of the junction nanotubes have been discussed. The synthesis and characterization of nanowires of metal oxides such as MgO, Al_2O_3, SiO_2 and In_2O_3 by the carbon-assisted process form the subject matter of Chapter 3. The nanowires have been characterized by transmission electron microscopy (TEM) and other techniques. The dispersion of oxide nanowires in polar solvents has also been examined.

Chapter 4 presents the results of the synthesis and characterization of the nanostructures of BN, GaN and InN. Studies have also been carried out on Mn-doped GaN nanowires and porous nanostructured GaN. The Mn-doped GaN nanowires are magnetic at room temperature.

The results of a study of the nanostructures of II-VI semiconductor chalcogenides prepared by surfactant-assisted synthesis are discussed in Chapter 5. The nanostructures include both nanowires and nanotubes. These nanostructures have been characterized by TEM, optical absorption and emission spectroscopy and other techniques.

In Chapter 6 investigations of Mn and Co doped ZnO prepared by a low-temperature route are presented. It is shown that Mn and Co doped ZnO samples are not ferromagnetic down to low temperatures.

Contents

Chapter 1

Nanowires and Nanotubes: A Brief Survey

1.1 Introduction to nanostructures

Nanotechnology is the term used to describe the creation and exploitation of materials with structural features in between those of atoms and bulk materials, with at least one-dimension in the nanometer range (1nm = 10^{-9} m). Table 1.1 lists typical nanomaterials of different dimensionalities. The properties of materials with nanometric dimensions are significantly different from those of atoms or bulk materials. Suitable control of the properties of nanometer-scale structures can lead to new science as well as new products, devices and technologies. The underlying theme of nanotechnology is miniaturization, the importance of which was pointed out by Feynman [1], as early as 1959 in his often-cited lecture entitled " There is plenty of *room at the bottom* ". *The challenge is to beat Moore's Law* [2] and accommodate 1000 CDs in a wristwatch [3]. There has been explosive growth of nanoscience and technology in the last decade, primarily because of the availability of new methods of synthesizing nanomaterials, as well as tools for characterization and manipulation [4] (Table 1.2). Several innovative methods for the synthesis of nanoparticles and nanotubes, and their assemblies are now available. There is a better understanding of the size-dependent electrical, optical and magnetic properties of individual nanostructures of metals, semiconductors and other materials. Besides the established techniques of electron microscopy, crystallography and spectroscopy, scanning probe

Table 1.1 Typical nanomaterials

	Size (approx)	Materials
(a) Nanocrystals and clusters (quantum dots)	dia 1-10 nm	Metals, semiconductors, magnetic materials
Other nanoparticles	dia 1-100 nm	Ceramic oxides
(b) Nanowires	dia 1-100 nm	Metals, semiconductors, oxides, sulfides, nitrides
Nanotubes	dia 1-100 nm	Carbon, layered metal chalcogenides
(c) Nanoporous solids	pore dia 0.5-10 nm	Zeolites, phosphates, etc.
(d) 2-D arrays (of nanoparticles)	several nm^2-μm^2	Metals, semiconductors, magnetic materials
Surfaces and thin films	thickness 1-1000 nm	Various materials
(e) 3-D structures (superlattices)	Several nm in all three dimensions	Metals, semiconductors, magnetic materials

Table 1.2 Different methods of synthesis and investigation of nanomaterials

Scale (approx)	Synthetic methods	Structural tools	Theory and simulation
0.1-10 nm	Covalent synthesis	Vibrational spectroscopy NMR Diffraction methods Scanning probe microscopies (SPM)	Electronic structure
< 1-100 nm	Self-assembly techniques	SEM, TEM, SPM	Molecular dynamics and mechanics
100 nm-1 μm	Processing, modifications	SEM, TEM	Coarse-grained models, hopping etc.

microscopies have provided powerful tools for the study of the nanostructures. Novel methods of fabricating patterned nanostructures, as well as new device and fabrication concepts, are constantly being discovered [4]. Size effects constitute a fascinating aspect of nanomaterials. The effects determined by size pertain to the evolution of structural, thermodynamic, electronic, spectroscopic, electromagnetic and chemical features of these finite systems. Size affects the structure of nanoparticles of materials such as CdS and CdSe, and also their properties such as the melting point and electronic absorption spectra. Within the realm of nanoscience and nanotechnology, nanowires and nanotubes play a special role because of their one-dimensionality. When the nanowire or nanotube diameter becomes small, singularities in the electronic density of states is observed (Figure 1.1), resembling more closely the case of molecules and atoms, but appearing to be very different from the case of crystalline solids or even two-dimensional systems [5].

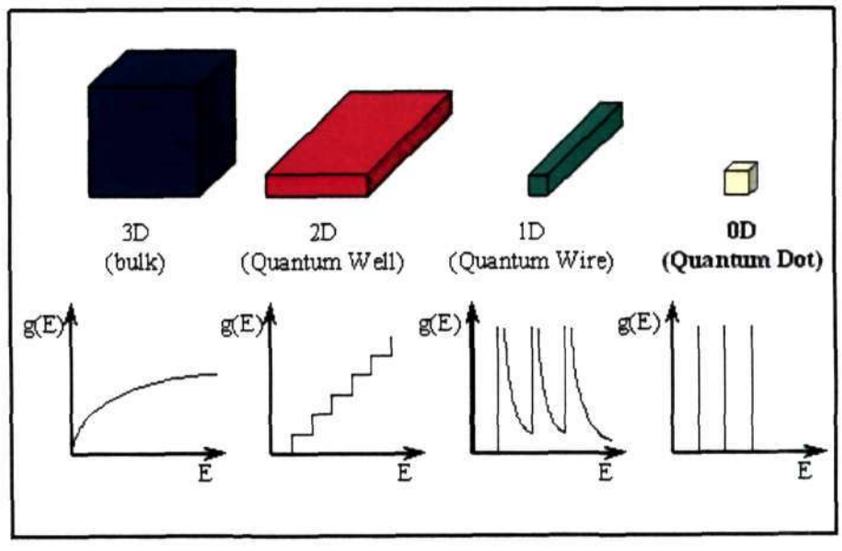

Figure 1.1: Electronic density of states for bulk (3D, blue), quantum well (2D, red), quantum wire (1D, green) and quantum dot (0D, yellow).

1.2 Carbon Nanotubes

1.2.1 Introduction

Iijima [6] in 1991 observed that nanotubules of graphite were deposited on the negative electrode during the direct-current arcing of graphite for the preparation of fullerenes. These nanotubes are concentric graphitic cylinders closed at either end due to the presence of five-membered rings. Nanotubes can be multiwalled with a central tubule of nanometric diameter surrounded by graphitic layers separated by ~ 3.4 Å. Unlike the multi-walled carbon nanotubes (MWNTs), in single-walled carbon nanotubes (SWNTs) there is only the tubule and no graphitic layers. A transmission electron microscope (TEM) image of a MWNT is shown in Figure 1.2 (a). In this nanotube, graphite layers surround the central tubule. Figure 1.2 (b) shows the model of a nanotube formed by two concentric graphitic cylinders. A SWNT can be visualized by cutting C_{60} along the center and spacing apart the hemispherical corannulene end-caps by a cylinder of graphite of the same diameter. In Figure 1.2 (c) we show the TEM image of bundles of SWNTs. Carbon nanotubes and fullerenes are the only form of carbon with extended bonding and yet with no dangling bonds. Since carbon nanotubes are derived from fullerenes, they have been referred to as tubular fullerenes or buckytubes.

Carbon nanotubes are readily prepared by striking an arc between graphite electrodes in 2/3 atm (~ 500 torr) of helium, considerably higher than the pressure of helium used in the production of fullerene soot. A current of 60 - 100 A across a potential drop of about 25 V gives high yields of carbon nanotubes. Besides the conventional arc-evaporation technique, carbon nanotubes are produced by the

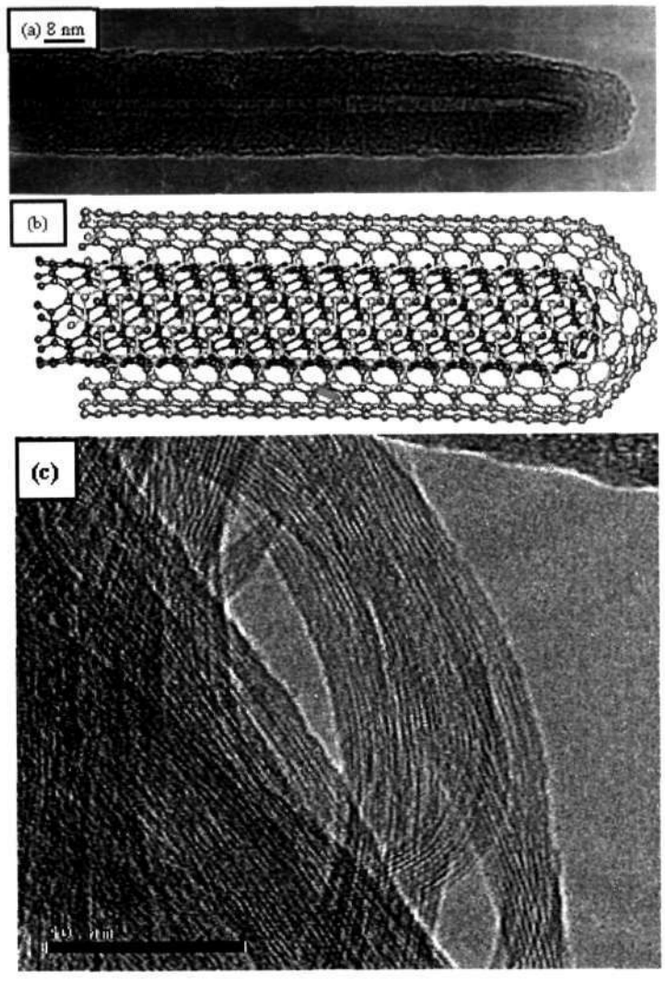

Figure 1.2: (a) A TEM image of a multi-walled carbon nanotube, (b) Minimum energy structure of a double-walled carbon nanotube, (c) TEM image of bundles of SWNTs.

decomposition of hydrocarbons, such as acetylene, under inert conditions around 700 °C over iron/graphite, cobalt/graphite, or iron/silica catalysts. The presence of transition metal particles is essential for the formation of nanotubes by the pyrolysis process and the diameter of the nanotube is determined by the size of the metal particles. The nanotubes generally obtained by the arc method or hydrocarbon

pyrolysis are multi-walled and have several graphitic sheets or layers (Figure 1 (a)). Single-walled nanotubes (SWNTs) (Figure 1 (c)) were first prepared by metal-catalyzed direct-current arcing of graphite rods under a helium atmosphere. The graphite anode was filled with metal powders (Fe, Co, Ni) and the cathode was of pure graphite. SWNTs generally occur in the weblike material deposited behind the cathode. Various metal catalysts have been used to make SWNTs by this route. Considering the importance of the SWNTs, alternate synthesis strategies have been explored. Under controlled conditions of pyrolysis, dilute hydrocarbon-organometallic mixtures yield SWNTs [4].

1.2.2 Structure and Characterization

TEM observations show that the nanotubes prepared by the arcing process generally consist of multilayered, concentric cylinders of single graphitic (graphene) sheets. The diameter of the inner tubes is of the order of a few nanometers. The outermost tubes could be as large as 10 - 30 nm, as shown in Figure 1.2 (a). During the curling of a graphene sheet into a cylinder, helicity is introduced. Electron diffraction studies establish the presence of helicity, to suggest that the growth of nanotubes occurs as in the spiral growth of crystals. The separation between concentric cylinders in MWNTs is about 3.45 Å, which is close to the separation between the (002) planes of graphite. These are the lowest energy surfaces of graphite with no dangling bonds, so that the nanotubes are, in fact, the expected structures. Graphitic cylinders would have dangling bonds at the tips but the carbon nanotubes are capped by dome-shaped hemispherical fullerene-type units. The capping units consist of pentagons to provide the curvature necessary for closure. Ajayan *et al.* [7] studied the distribution of pentagons at the caps of carbon nanotubes, to find that the

caps need not be perfectly conical or hemispherical but can form skewed structures. The simplest possible SWNT can be visualized by cutting the C_{60} structure across the middle and adding a cylinder of graphite of the same diameter.

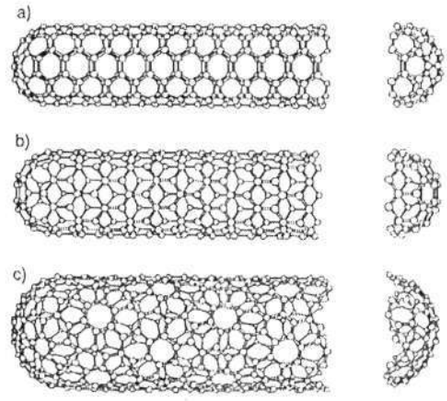

Figure 1.3: Models of a) armchair, b) zigzag, and c) chiral nanotubes.

If C_{60} is bisected normal to a five-fold axis, an armchair tube is formed, and if it is bisected normal to a threefold axis, a zigzag tube is formed. Armchair and zigzag tubes are achiral. In addition to these, a variety of chiral tubes can be formed with the screw axis along the axis of the tube. In Figure 1.3, we show models of the three types of nanotubes formed by bisecting the C_{60} molecule and adding a cylinder of graphite. Nanotubes can be defined by a chiral angle θ and a chiral vector C_h, given by Equation (1), where a_1 and a_2 are unit vectors in a 2D graphene lattice and n and m are integers.

$$C_h = na_1 + ma_2 \qquad (1)$$

The vector C_h connects two crystallographically equivalent sites on a 2D graphene sheet and the chiral angle is the angle it makes with respect to the zigzag direction, Figure 1.4. A tube is formed by rolling up the graphene sheet in such a way that the two points connected by the chiral vector coincide. A number of possible chiral vectors can be specified by Equation (1) in terms of integer pairs (n, m). Many

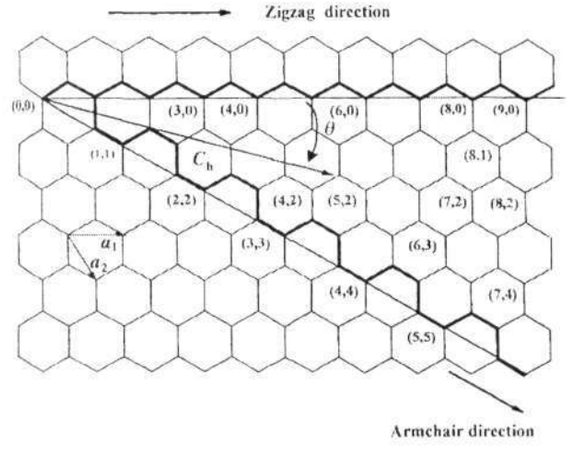

Figure 1.4: A 2D graphene sheet showing chiral vector C_h and chiral angle θ.

such pairs are shown in Figure 1.4 and each pair (n, m) defines a different way of rolling the graphene sheet to form a carbon nanotube of certain chirality. The limiting cases are $n \neq 0$, $m = 0$ (zigzag tube), and $n = m \neq 0$ (armchair tube). For a carbon nanotube defined by the index (n, m), the diameter d and the chiral angle θ are given by Equations (2) and (3), where $a = 1.42\sqrt{3}$ and $0 \leq \theta \leq 30°$,

$$d = \frac{a\sqrt{m^2 + mn + n^2}}{\pi} \qquad (2)$$

$$\theta = \arctan\left(\frac{-\sqrt{3}\,m}{2n + m}\right) \qquad (3)$$

As mentioned earlier, multi-walled carbon nanotubes consist of capped concentric cylinders separated by 3.45 Å, which is slightly larger than interlayer spacing in

graphite. This is because the number of carbon atoms increases as we go from an inner cylinder to an outer cylinder and it is not possible to maintain perfect ABAB... stacking, as in graphite. Thus, an interlayer spacing close to that in turbostratic graphite is observed in MWNTs. In addition to pentagons and hexagons, carbon nanotubes can also have heptagons. Pentagons impart a positive curvature whereas heptagons give rise to a negative curvature, to the otherwise flat graphene sheet made of hexagons. Thus, nanotubes with pentagons and heptagons will have unusual curvatures and shapes. Bent nanotubes arising from the presence of pentagons and heptagons on opposite side of the tube have been observed [8].

1.3 Inorganic Nanotubes

Several layered inorganic compounds possess structures comparable to the structure of graphite, the metal dichalcogenides being important examples. The metal dichalcogenides, MX_2 (M = Mo, W, Nb, Hf; X = S, Se) contain a metal layer sandwiched between two chalcogen layers with the metal in a trigonal pyramidal or octahedral coordination mode [9]. The MX_2 layers are stacked along the *c*-direction in ABAB fashion. The MX_2 layers are analogous to the single graphene sheets in the graphite structure (Figure 1.5). When viewed parallel to the *c*-axis, the layers show the presence of dangling bonds due to the absence of an X or M atom at the edges. Such unsaturated bonds at the edges of the layers also occur in graphite. The dichalcogenide layers are unstable towards bending and have a high propensity to roll into curved structures. Folding in the layered transition metal chalcogenides (LTMCs) was recognized as early as 1979, well before the discovery of the carbon nanotubes. Rag-like and tubular structures of MoS_2 were reported by Chianelli *et al.* [10] who

studied their usefulness in catalysis. The folded sheets appear as crystalline needles in low magnification TEM images, and were described as layers that fold onto themselves. These structures indeed represent those of nanotubes. Tenne *et al.* [11] first demonstrated that Mo and W dichalcogenides are capable of forming nanotubes (Figure 1.6 (a)). Closed fullerene-type structures (inorganic fullerenes) also formed along with the nanotubes (Figure 1.6 (b)). The dichalcogenide structures contain concentrically nested fullerene cylinders, with a less regular structure than in the carbon nanotubes. Accordingly, MX_2 nanotubes have varying wall thickness and contain some amorphous material on the exterior of the tubes. Nearly defect-free MX_2 nanotubes are rigid as a consequence of their structure and do not permit plastic

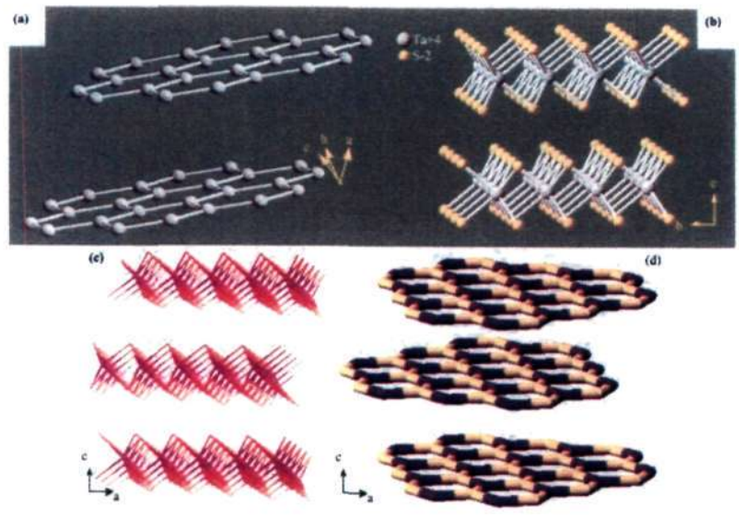

Figure 1.5: Comparison of the structures of (a) graphite and inorganic layered compounds such as (b) NbS_2/TaS_2; (c) MoS_2; (d) BN. In the layered dichalcogenides, the metal is in trigonal prismatic (TaS_2) or octahedral coordination (MoS_2).

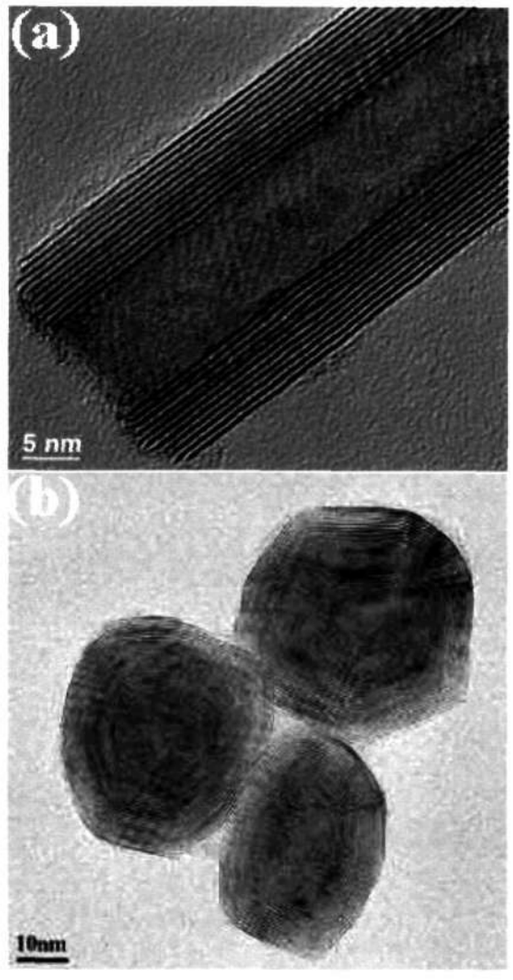

Figure 1.6: TEM images of (a) a multi-walled nanotube of WS_2 and (b) hollow particles (inorganic fullerenes) of MoS_2.

deformation. Considerable progress has been made in the synthesis of the nanotubes of Mo and W dichalcogenides in the last few years. With the synthesis and characterization of the fullerenes and nanotubes of MoS_2 and WS_2, a wide field of research has opened up, enabling the successful synthesis of nanotubes of other metal chalcogenides.

It may be recalled that the dichalcogenides of many of the Group 4 and 5 metals have layered structures suitable for forming nanotubes. Curved structures are not only limited to carbon and the dichalcogenides of Mo and W. Perhaps the most well-known example of a tube-like structure with diameters in the nm range is formed by the asbestos mineral (chrysotil) whose fibrous characteristics are determined by the tubular structure of the fused tetrahedral and octahedral layers. The synthesis of mesoporous silica with well-defined pores in the 2–20 nm range was reported by Beck and Kresge [12]. The synthetic strategy involved the self-assembly of liquid crystalline templates. The pore size in zeolitic and other inorganic porous solids is varied by a suitable choice of the template. However, in contrast to the synthesis of porous compounds, the synthesis of nanotubes is somewhat more difficult. Nanotubes of oxides of several transition metals as well as of other metals have been synthesized employing different methodologies [13-18]. Silica nanotubes were first produced as a spin-off product during the synthesis of spherical silica particles by the hydrolysis of tetraethylorthosilicate (TEOS) in a mixture of water, ammonia, ethanol and D, L-tartaric acid [14]. Since self-assembly reactions are not straightforward with respect to the desired product, particularly its morphology, templated reactions have been employed using carbon nanotubes to obtain nanotubes structures of metal oxides [15,16].

Oxides such as V_2O_5 have good catalytic activity in the bulk phase. Redox catalytic activity is also retained in the nanotubular structure. There have been efforts to prepare V_2O_5 nanotubes by chemical methods as well [17]. Boron nitride (BN) crystallizes in a graphite-like structure and can be simply viewed as replacing a C–C pair in the graphene sheet with the iso-electronic B–N pair. It can, therefore, be

considered as an ideal precursor for the formation of BN nanotubes. Replacement of the C–C pairs partly or entirely by the B–N pairs in the hexagonal network of graphite leads to the formation of a wide array of two-dimensional phases that can form hollow cage structures and nanotubes. The possibility of replacing C–C pairs by B–N pairs in the hollow cage structure of C_{60} was predicted [19] and verified experimentally [20]. BN-doped carbon nanotubes have been prepared [21]. Pure BN nanotubes have been generated by employing several procedures, yielding nanotubes with varying wall thickness and morphology [22]. It is therefore quite possible that nanotube structures of other layered materials can be prepared as well. For example, many metal halides (*e.g.*, $NiCl_2$), oxides (GeO_2) and nitrides (GaN) crystallize in layered structures. There is considerable interest at present to prepare exotic nanotubes and to study their properties.

1.4 Inorganic Nanowires

Eversince the discovery of carbon nanotubes there has been great interest in the synthesis and characterization of other one-dimensional (1D) structures. Nanowires, nanorods and nanobelts constitute an important class of 1D nanostructures, which provide models to study the relationship between electrical transport, optical and other properties with dimensionality and size confinement. The inorganic nanowires can also act as active components in devices as revealed by recent investigations. In the last 3–4 years, nanowires of a variety of inorganic materials has been synthesized and characterized. Thus, nanowires of elements, oxides, nitrides, carbides and chalcogenides, have been generated by employing various strategies. One of the crucial factors in the synthesis of nanowires is the

control of composition, size and crystallinity. Among the methods employed, some are based on vapor phase techniques, while others are solution techniques. Compared to physical methods such as nanolithography and other patterning techniques, chemical methods have been more versatile and effective in the synthesis of these nanowires. Thus, techniques involving chemical vapor deposition (CVD), precursor decomposition, as well as solvothermal, hydrothermal and carbothermal methods have been widely employed. Several physical methods, especially microscopic techniques such as scanning electron microscopy (SEM), transmission electron microscopy (TEM), scanning tunneling microscopy (STM) and atomic force microscopy (AFM) are commonly used to characterize nanowires.

1.4.1 Synthetic strategies

An important aspect of the 1D structures relates to their crystallization [23], wherein the evolution of a solid from a vapor, a liquid, or a solid phase involves nucleation and growth. As the concentration of the building units (atoms, ions, or molecules) of a solid becomes sufficiently high, they aggregate into small nuclei or clusters through homogeneous nucleation. These clusters serve as seeds for further growth to form larger clusters. Several synthetic strategies have been developed for 1D nanowires with different levels of control over the growth parameters (Figure 1.7). These include: (i) the use of the anisotropic crystallographic structure of the solid to facilitate 1D nanowire growth (Figure 1.7 (a)); (ii) the introduction of a solid–liquid interface (Figure 1.7 (b)); (iii) use of templates (with 1D morphologies) to direct the formation of nanowires (Figure 1.7 (c)); (iv) supersaturation control to modify the growth habit of a seed; (v) use of capping agents to kinetically control the growth rates of the various facets of a seed (Figure 1.7 (d)); and (vi) self-assembly of zero-

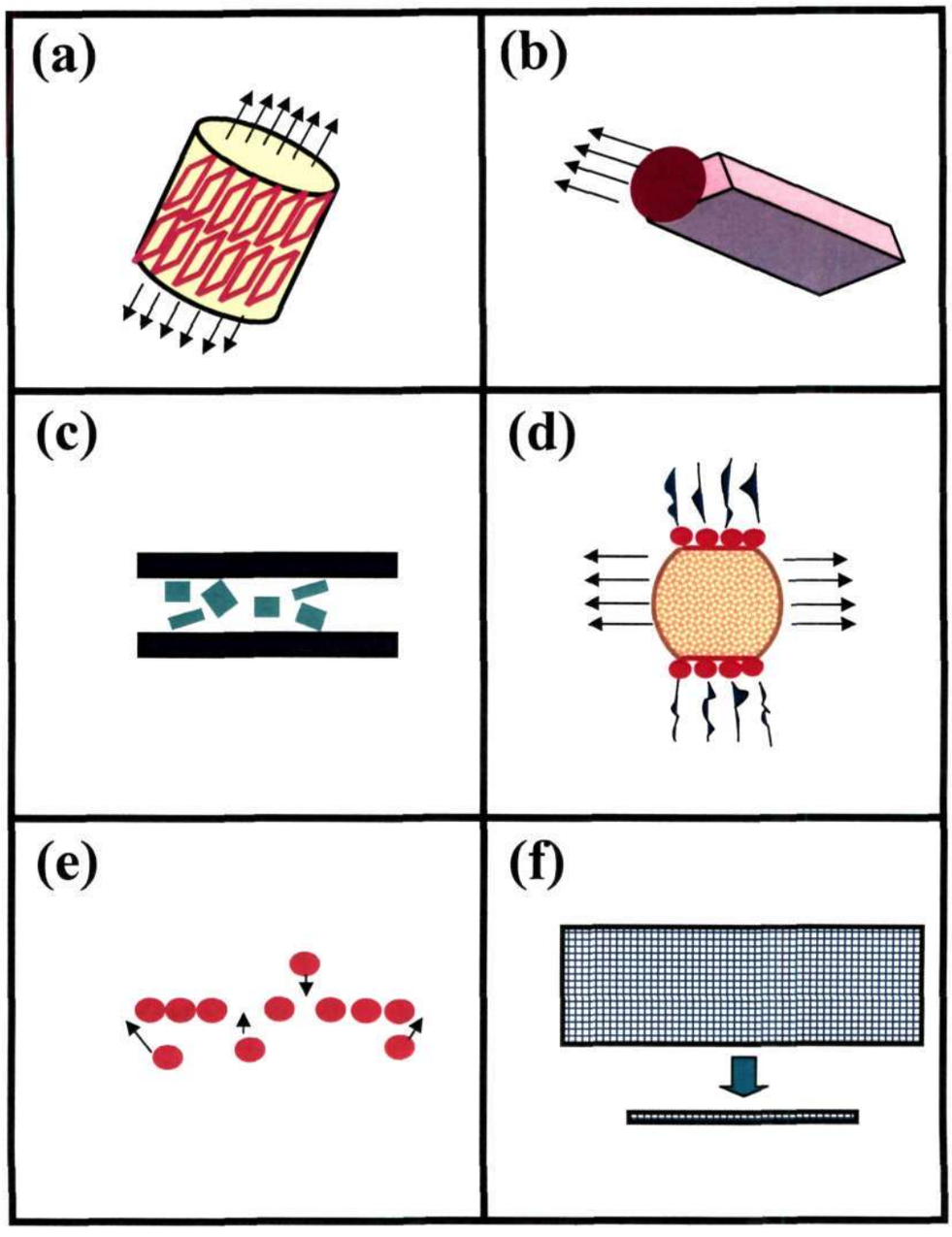

Figure 1.7: Schematic illustration showing the six different strategies that have been demonstrated for achieving 1D growth.

dimensional (0D) nanostructures (Figure 1.7 (e)) and (vii) size reduction of 1D microstructures (Figure 1.7 (f)). They are conveniently categorized into (a) growth in the vapor phase; and (b) solution-based growth.

Vapor phase growth of nanowires

Vapor phase growth is extensively used for producing nanowires. Starting with the simple evaporation technique in an appropriate atmosphere to produce elemental or oxide nanowires, vapor–liquid–solid (VLS), vapor–solid (VS) and other processes are also made use of.

Vapor–liquid–solid growth

The growth of nanowires via a gas phase reaction involving the vapor–liquid–solid (VLS) process has been widely studied. Wagner [23], during his studies of growth of large single-crystalline whiskers, proposed in 1960s, a mechanism for the growth via gas phase reaction involving the so-called vapor–liquid–solid process (Figure 1.8). He studied the growth of mm-sized Si whiskers in the presence of Au particles. According to this mechanism, the anisotropic crystal growth is promoted by the presence of the liquid alloy/solid interface. This mechanism has been widely accepted and applied for understanding the growth of various nanowires including those of Si and Ge among others. The growth of Ge nanowires using Au clusters as a solvent at high temperature is explained based on the Ge-Au phase diagram shown in Figure 1.9. Ge and Au form a liquid alloy when the temperature is higher than the eutectic point (363 °C) as shown in Figure 1.9 (a-I). The liquid surface has a large accommodation coefficient and is therefore a preferred deposition site for the incoming Ge vapor. After the liquid alloy becomes supersaturated with Ge,

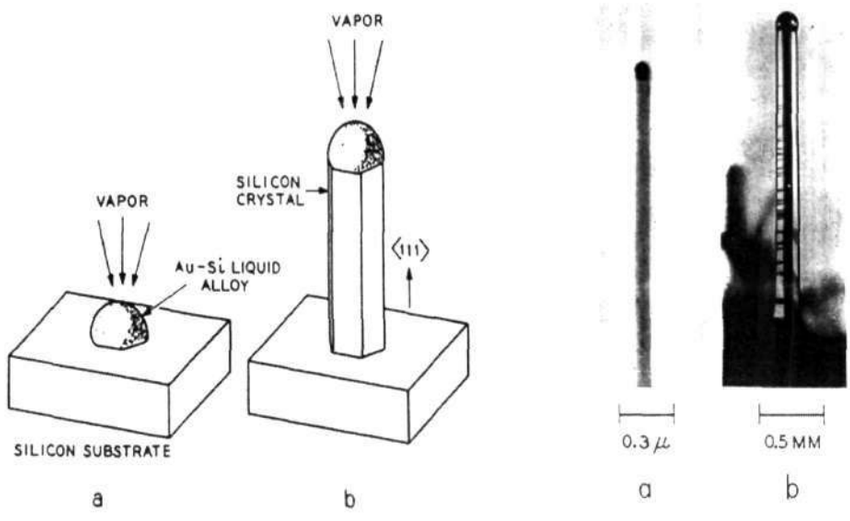

Figure 1.8: VLS mechanism as demonstrated in the case of Si whiskers by Wagner.

precipitation of the Ge nanowire occurs at the solid- liquid interface (Figure 1.9 (a-II–III). Until recently, the only evidence that nanowires grew by this mechanism was the presence of alloy droplets at the tips of the nanowires. Wu *et al.* [24] have reported real-time observations of Ge nanowire growth in an in situ high-temperature TEM, which demonstrate the validity of the VLS growth mechanism. Their experimental observations suggest that there are three growth stages: metal alloying, crystal nucleation and axial growth (Figure 1.10). Figure 1.10 (a)–(f) shows a sequence of TEM images during the in situ growth of a Ge nanowire. Three stages, I–III, are clearly identified. (I), Alloying process, (Figure 10 (a)–(c)): The maximum temperature that could be attained in the system was 900 °C, up to which the Au clusters remain in the solid state in the absence of Ge vapor. With increasing amount of Ge vapor condensation and dissolution, Ge and Au form an alloy and liquefy. The volume of the alloy droplet increases and the elemental contrast decreases, while the

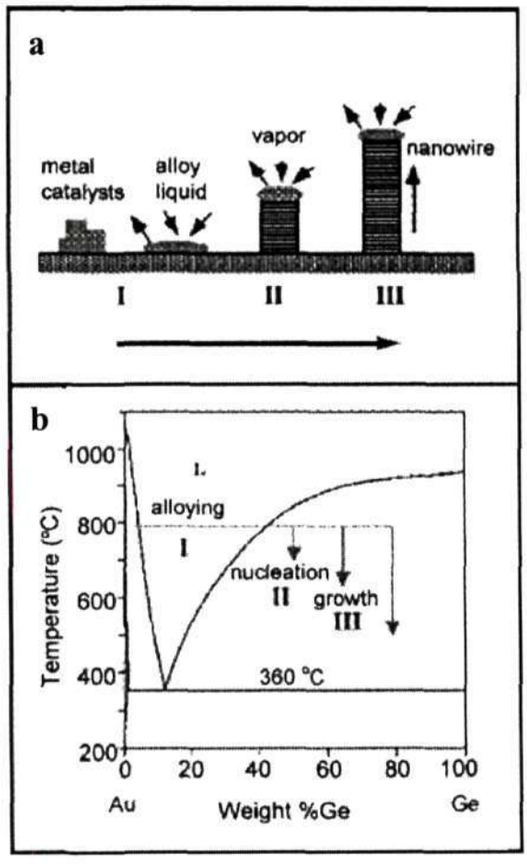

Figure 1.9: (a) Schematic illustration of vapor-solid growth mechanism including three stages (I) alloying, (II) nucleation and (III) axial growth. Three stages are projected onto the conventional Au-Ge phase diagram; (b) shows the compositional and phase evolution during the nanowire growth process.

alloy composition crosses sequentially, from left to right, a biphasic region (solid Au and Au/Ge liquid alloy) and a single phase region (liquid). An isothermal line in the Au-Ge phase diagram (Figure 1.9 (b)) shows the alloying process. (II), Nucleation,

(Figure 1.10 (d)–(e)): As the concentration of Ge increases in the Au-Ge alloy droplet, the process of nucleation of the nanowire begins. Knowing the alloy volume change, it is estimated that the nucleation generally occurs at a Ge weight percentage of 50–60%. (III), Axial growth, (Figure 1.10 (d)–(f)): Once the Ge nanocrystal nucleates at the liquid/solid interface, further condensation/dissolution of the Ge vapor into the system increases the amount of Ge precipitation from the alloy. The incoming Ge vapors diffuse and condense at the solid/liquid interface, thus suppressing secondary nucleation events. The interface is then pushed forward (or backward) to form nanowires (Figure 1.10 (f)).

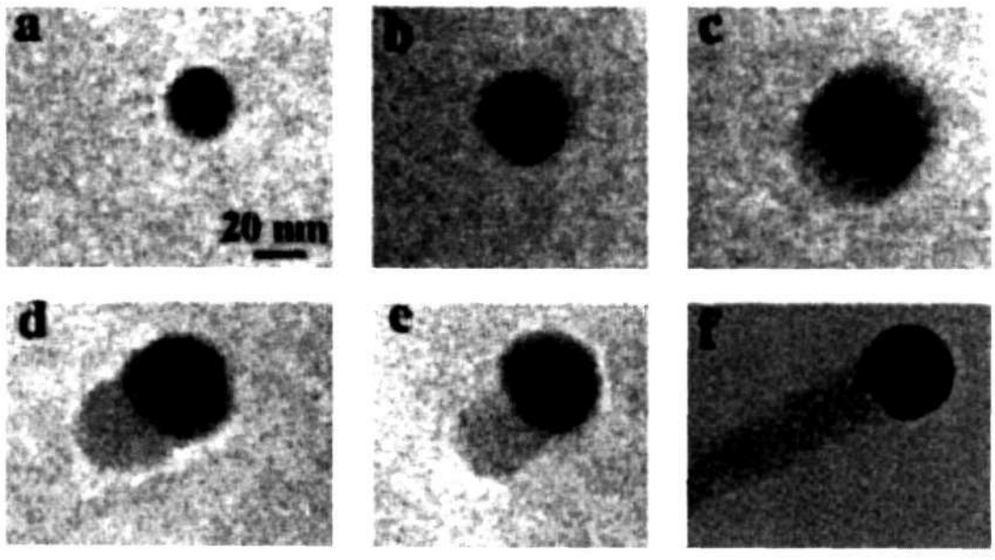

Figure 1.10: In situ TEM images recorded during the process of nanowire growth. (a) Au nanoclusters in solid state at 500 °C; (b) alloying initiated at 800 °C, at this stage Au exists mostly in solid state; (c) liquid Au/Ge alloy; (d) the nucleation of Ge nanocrystal on the alloy surface; (e) Ge nanocrystal elongates with further Ge condensation and eventually forms a wire (f).

This study confirms the validity of the VLS growth mechanism at the nanometer scale. Since the diameter of the nanowires is determined by the diameter of the catalyst particles, this method provides an efficient means to obtain uniform-sized nanowires. Also, with the knowledge of the phase diagram of the reacting species, the growth temperature can be set in between the eutectic point and the melting point of the material. Physical methods, such as laser ablation or thermal evaporation, as well as chemical methods such as chemical vapor deposition can be used to generate the reactant species in vapor form, required for the nanowire growth. Catalyst particles can be sputtered onto the substrates or metal nanoparticles prepared by solution-based routes used as the catalysts. An advantage of this route is that patterned deposition of catalyst particles yields patterned nanowires. Using this growth mechanism, nanowires of various materials including elements, oxides, carbides, phosphides, etc., have been successfully obtained.

Vapor–solid growth

The vapor–solid (VS) method for whisker growth also holds for the growth of 1D nanomaterials [23]. In this process, evaporation, chemical reduction or gaseous reaction first generates the vapor. The vapor is subsequently transported and condensed onto a substrate. The VS method has been used to prepare whiskers of oxide, as well as metals with micrometer diameters. It is, therefore, possible to synthesize the 1D nanostructures using the VS process if one can control the nucleation and the subsequent growth process. Using the VS method, nanowires of the oxides of Zn, Sn, In, Cd, Mg, Ga and Al have been obtained.

Carbothermal reactions

Nanowires of a variety of oxides, nitrides and carbides can be synthesized by carbothermal reactions. For example, carbon (activated carbon or carbon nanotubes) in mixture with an oxide produces sub-oxidic vapor species, which reacts with C, O_2, N_2 or NH_3 to produce the desired nanowires. Carbothermal reactions generally involve the following steps:

metal oxide + C $\rightarrow$ metal suboxide + CO

metal suboxide + O_2 $\rightarrow$ metal oxide nanowires

metal suboxide + NH_3 $\rightarrow$ metal nitride nanowires + CO + H_2

metal suboxide + N_2 $\rightarrow$ metal nitride nanowires + CO

metal suboxide + C $\rightarrow$ metal carbide nanowires + CO

The first step normally involves the formation of a metal suboxide by the reaction of the metal oxide with carbon. Depending on the desired product, the suboxide heated in the presence of O_2, NH_3, N_2 or C yields oxide, nitride or carbide nanowires. The versatility of the carbon-assisted synthesis is illustrated with a typical example in Scheme 1.1.

Solution-based growth of nanowires

This synthetic strategy for nanowires makes use of anisotropic growth dictated by the crystallographic structure of the solid material, or confined and directed by templates, or kinetically controlled by supersaturation, or by the use of appropriate capping agent.

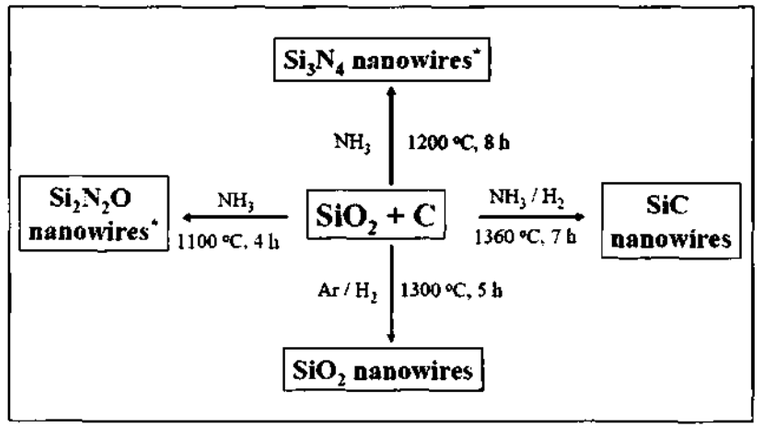

* 0.5 % of Fe catalyst used

Scheme 1.1

Highly anisotropic crystal structures

Solid materials such as polysulphurnitride, $(SN)_x$, grow into 1D nanostructures, the habit being determined by the anisotropic bonding in the structure [25,26]. Other materials, such as selenium [27,28], tellurium [29] and molybdenum chalcogenides [30] are easily obtained as nanowires due to anisotropic bonding, which dictates the crystallization to occur along the *c*-axis, favoring the stronger covalent bonds over the relatively weak van der Waals forces between the chains.

Template-based synthesis

Template-directed synthesis represents a convenient and versatile method for generating 1D nanostructures. In this technique, the template serves as a scaffold against which other materials with similar morphologies are synthesized. That is, the in situ generated material is shaped into a nanostructure with a morphology

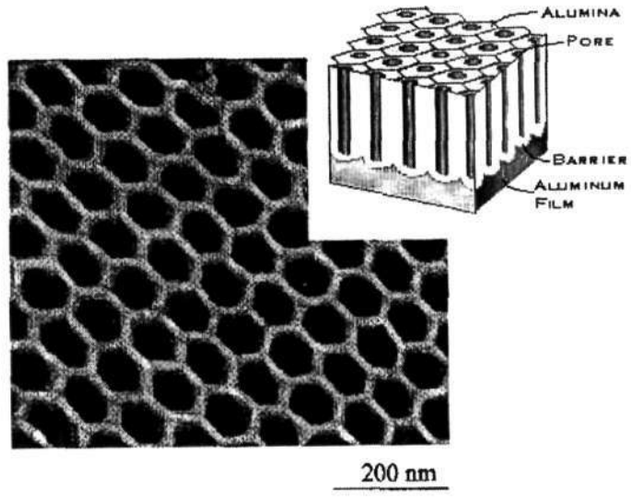

Figure 1.11: TEM micrograph of an anodic alumina membrane (AAM).

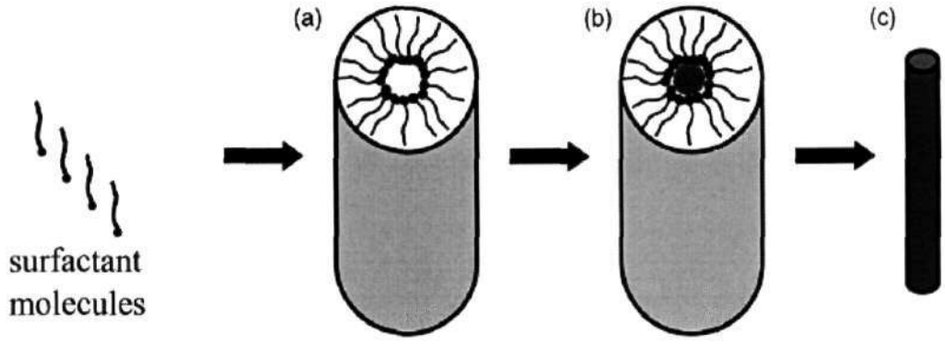

Figure 1.12: Schematic illustration showing the formation of nanowires by templating against mesostructures, which are self-assembled from surfactant molecules. (a) Formation of cylindrical micelle; (b) formation of the desired material in the aqueous phase encapsulated by the cylindrical micelle; (c) removal of the surfactant molecule with an appropriate solvent (or by calcination) to obtain an individual nanowire.

complementary to that of the template. The templates could be nanoscale channels within mesoporous materials, porous alumina and polycarbonate membranes. The nanoscale channels are filled using, the solution, the sol-gel or the electrochemical method. The nanowires so produced are released from the templates by removal of the host matrix [31]. Unlike the polymer membranes fabricated by track etching, anodic alumina membranes (AAMs) containing a hexagonally packed 2D array of cylindrical pores with a uniform size are prepared using anodization of aluminium foils in an acidic medium (Figure 1.11). Nanowires of several materials have been fabricated using AAMs as templates. The various inorganic materials include Au, Ag, Pt, TiO_2, MnO_2, ZnO, SnO_2, In_2O_3, CdS, CdSe, CdTe, electronically conducting polymers such as polypyrole, poly(3-methylthiophene) and polyaniline, as well as carbon nanotubules. The only drawback of this method is that it is difficult to obtain materials that are single-crystalline. Besides alumina and polymer membranes with high surface areas and uniform pore sizes, mesoporous silica has been successfully used as a template for the synthesis of polymer and inorganic nanowires. Mesophase structures self-assembled from surfactants (Figure 1.12) provide another class of useful and versatile templates for generating 1D nanostructures in relatively large quantities. It is well known that at critical micellar concentration (CMC) surfactant molecules spontaneously organize into rod-shaped micelles [32]. These anisotropic structures can be used immediately as soft templates to promote the formation of nanorods when coupled with appropriate chemical or electrochemical reaction. The surfactant needs to be selectively removed to collect the nanorods/nanowires. Nanowires themselves can be used as templates to generate the nanowires of other materials. The template may be coated to the nanowire (physical) forming coaxial nanocables [33], or it might react with the nanowires forming a new material [34]. In

the physical methods (solution or sol-gel coating), surfaces of the nanowires are directly coated with conformal sheaths made of a different material to form coaxial nanocables. Subsequent dissolution of the original nanowires leads to nanotubes of the coated materials. The sol-gel coating method is a generic route to synthesize co-axial nanocables that may contain electrically conductive metal cores and insulating sheaths. Govindaraj *et al.* [35] have demonstrated that a variety of metal nanowires of 1–1.4 nm diameter can be readily prepared by filling SWNTs, opened by acid treatment. Nanowires of Au, Pt, Pd and Ag have been synthesized by employing sealed-tube reactions, as well as solution methods. In addition, incorporation of thin layers of metals in the intertubular space of the SWNT bundles has been observed.

Solution–liquid–solid process

Buhro and coworkers [36] have developed a low temperature solution–liquid–solid (SLS) method for the synthesis of crystalline nanowires of III–V semiconductors [37]. In a typical procedure, a metal (e.g. In, Sn, Bi) with a low melting point is used as a catalyst, and the desired material generated through the decomposition of organometallic precursors. Nanowhiskers of InP, InAs and GaAs have been prepared by low temperature (≤ 203 °C) solution phase reactions. The schematic illustration in Figure 1.13 clearly shows the growth of nanowires or whiskers through the SLS method. The products obtained are generally single-crystalline. Korgel *et al.* [38] have used the supercritical fluid–liquid–solid (SFLS) method to synthesize bulk quantities of defect-free silicon and germanium nanowires. In addition to these solution routes to elemental III–V semiconductor nanowires, it has been reported recently that by exploiting the selective capping capacities of mixed surfactants, it is possible to

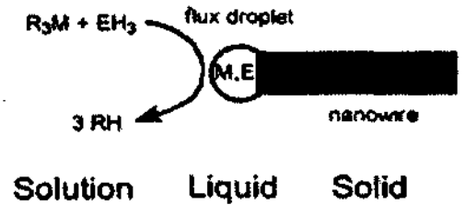

Figure 1.13: Schematic illustration showing the growth of nanowire through the solution–liquid–solid (SLS) mechanism which is similar to the vapor–liquid–solid (VLS) process.

extend the synthesis of the II–VI semiconductor nanocrystals to that of semiconductor nanorods [39], a version of nanowires with relatively shorter aspect ratios.

Solvothermal synthesis

Solvothermal methodology is extensively employed as a solution route to produce semiconductor nanowires and nanorods. In this process, a solvent is mixed with metal precursors and crystal growth regulating or templating agents, such as amines. This solution mixture is placed in an autoclave maintained at relatively high temperatures and pressures to carry out the crystal growth and the assembly process. The methodology is quite versatile and has enabled the synthesis of crystalline nanowires of semiconductors and other materials.

1.4.2 Growth control and integration

A significant challenge in the chemical synthesis of nanowires is how to rationally control the nanostructure assemblies so that their size, dimensionality,

interfaces and their 2D and 3D superstructures can be tailor-made towards desired functionality. Many physical and thermodynamic properties are diameter-dependent. Several groups of workers have synthesized uniform-sized nanowires by the VLS process using clusters with narrow size distributions. Controlling the growth orientation is important for the applications of nanowires. By applying the conventional epitaxial crystal growth technique to the VLS process, a vapor–liquid–solid epitaxy technique has been developed for the controlled synthesis of nanowire arrays. Nanowires generally have preferred growth directions. For example, zinc oxide nanowires prefer to grow along their c-axis, that is along the <001> direction. Also, Si nanowires grow along the <111> direction when grown by the VLS growth

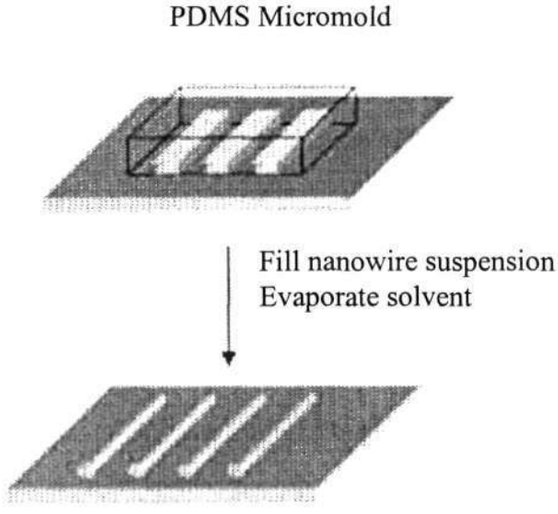

Figure 1.14: Schematic illustration of the microfluidic-assisted nanowire integration process for nanowire surface patterning.

process, but can be made to grow along the <112> or the <110> direction by the oxide-assisted growth mechanism. It is clear from the VLS nanowire growth mechanism that the initial positions of Au clusters or Au thin films controls the

positions of the nanowires. By creating desired patterns of Au using a lithographic technique, it is possible to grow ZnO nanowires of the same designed pattern since they grow vertically only from the region coated with Au and form the designed patterns of ZnO nanowire arrays [40,41]. Similarly, networks of nanowires with the precise placement of individual nanowires on substrates with the desired configuration are achieved by the surface patterning strategy [40,41]. Integration of nanowire building blocks into complex functional networks in a controlled fashion is a major challenge. The direct one-step growth process has been used [40,41]. In this process, the nanowires, grown by the VLS method, are patterned on substrates by selectively depositing in catalyst particles. Another way is to place the nanowire building blocks together into the functional structure to develop a hierarchical assembly. By using a simple dubbed microfluidic-assisted nanowire integration process, wherein the nanowire solution/suspension is filled in the microchannels formed between poly(dimethylsiloxane) (PDMS) micromould and a flat Si substrate, followed by the evaporation of the solvent, nanowire surface patterning and alignment has been achieved [42,43]. A schematic illustration of the microfluidic-assisted nanowire integration process is shown in Figure 1.14. The Langmuir Blodgett technique has also been used to obtain aligned, high-density nanowire assemblies [44].

1.5 Some properties and applications of nanostructures

Nanostructures have a variety of interesting properties because of their reduced dimensions and consequently find a wide variety of applications. Some of these may be superior to their bulk analogues. Such exciting and novel applications

have prompted wide research to fully understand and exploit these nanostructures. Listed below are some of the important areas where they find a wide range of applications, some fully explored whereas some others where more understanding may be required.

Hydrogen Storage

Carbon nanotubes have been investigated for H_2 storage properties [45]. It would be worthwhile to look into the H_2 storage ability of some of the inorganic nanotubes. The chalcogenide nanotubes with ~ 6 Å van der Waals gap between the layers, are potential candidates for showing storage capacity. It has been shown recently that BN nanotubes can store a reasonable quantity of H_2 [46]. Multi-walled BN nanotubes have been shown to possess a capacity of 1.8–2.6 wt % of H_2 uptake under ~ 10 MPa at room temperature. This value, though smaller than that reported for CNTs, nevertheless suggests the possible use of BN nanotubes as a hydrogen storage system. MoS_2 nanotubes could be electrochemically charged and discharged with a capacity of 260 mA h g^{-1} at 20 °C, corresponding to a formula of $H_{1.24}MoS_2$ [47]. The high storage capacity is believed to be due to the enhanced electrochemical-catalytic activity of the highly nanoporous structure. This may find wide applications in high energy batteries.

Mechanical Properties

Single-walled carbon nanotubes are known to possess extraordinary strength [48]. Mechanical properties of BN nanotubes would be worthy of exploration. Unlike carbon nanotubes, BN nanotubes are predicted to have stable insulating properties independent of their structure and morphology. Thus, BN tubes can be used as nano-

insulating devices for encapsulating conducting materials like metallic wires. Filled BN nanotubes are expected to be useful for the preparation of nano-structured ceramics.

Sensor applications

Chemical sensitivity of SiNW bundles has been studied [49a]. Upon exposure to NH_3 gas and water vapor, the electrical resistance of the HF-etched SiNWs relative to the non-etched SiNWs decreases at room temperature. This phenomenon serves as the basis for a new sensor. A novel Si-nanowire based field effect sensor device [Figure 1.15] has been developed [49b].

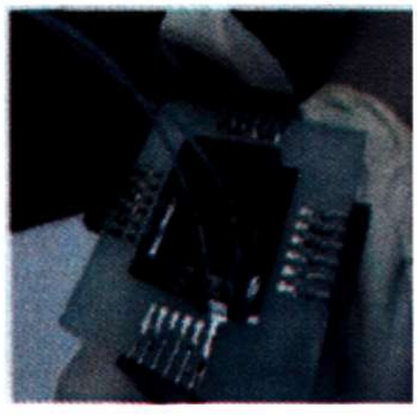

Figure 1.15: A photograph of a prototype nanowire FET sensor biochip.

Field-emission properties

Field emission studies on GaN nanowires have shown significant emission currents at low electric field with current densities of 20 $\mu A/cm^2$ at a field of 14 $V/\mu m$ [50].

Optical Properties

Ultraviolet-blue laser action has been reported in monocrystalline GaN nanowires, using both near-field and far-field optical microscopy to characterize the waveguide mode structure and the spectral properties of the radiation at room temperature [51].

Semiconductor nanowire building blocks have been used to assemble functional device elements and element arrays [52]. Nanowire junction arrays have been configured as OR, AND and NOR logic-gate structures with substantial gain and have been used to implement basic computation. Functional 1D resonant tunneling diodes have been obtained via bottom-up assembly of designed segments of different semiconducting materials in III/V nanowires [53].

1.6 Conclusions and future directions

One-dimensional nanostructures clearly constitute a fascinating class of materials with a variety of novel properties, some known and some yet to be discovered. Today, it can be claimed that these materials of the desired form can be produced in relatively large quantities. The various possible applications such as in the case of field-emission displays, nanosensors and in hydrogen storage have prompted intensive and rigorous research in the synthesis of these materials. The electronic properties of nanowires and nanotubes hold promise in nanoelectronics. Our ability to manipulate such nanostructures by atomic probe microscopies reinforces this conviction, while nanotubes themselves can be used to advantage as AFM and STM tips. There is still much need for the careful and systematic investigations of several of the properties and phenomena associated with one-

dimensional materials. It is necessary to be able to obtain highly reproducible preparations of nanowires and nanotubes possessing the desired characteristics and to dope them in a controlled manner. This also applies to the other chemical manipulations with these materials. In the case of nanotubes of layered metal chalcogenides, besides obtaining good reproducible samples, their tribological and other properties are yet to be fully explored. There is little doubt that nanowires and nanotubes of many more inorganic materials will be prepared in the future. New strategies will also be developed for the synthesis and manufacture of these materials. To be able to synthesize nanomaterials, organize them and manipulate them for various specific applications is one of the goals of modern materials and nanoscience. Surely we can look forward to several exciting and interesting phenomena that will be unraveled in the coming years.

1.7 References

[1] R. P. Feynman, *Miniaturization*, Reinhold, New York, 1961.

[2] P. L. Packman, *Science*, 1999, **285**, 2079.

[3] G. M. Whitesides, *Nanotechnology: Art of the Possible, Technology Review*, Technology Review Inc., Cambridge, MA, Nov/Dec 1998.

[4] (a) C. N. R. Rao, A. K. Cheetham, *J. Mater. Chem.*, 2001, **11**, 2887, (b) C. N. R. Rao, A. Müller, A. K. Cheetham (Eds), *The Chemistry of Nanomaterials*, Vol 1 and 2, Wiley-VCH, Weinheim, 2004, (c) C. N. R. Rao, A. Govindaraj, *Nanotubes and Nanowires*, RSC, 2005.

[5] (a) A. P. Alivisatos, *Science*, 1996, **271**, 933, (b) M. S. Dresselhaus, Y. M. Lin, O. Rabin, A. Jorio, A. G. Sonza Filho, M. A. Pimenta, R. Saito, Ge. G. Samsonidze, G. Dresselhaus, *Mater. Sci. Eng. C.*, 2003, **23**, 129.

[6] S. Iijima, *Nature*, 1991, **354**, 56.

[7] P. M. Ajayan, T. Ichihashi, S. Iijima, *Chem. Phys. Lett.*, 1993, **202**, 384.

[8] S. Iijima, *MRS Bull.*, 1994, **19**, 43.

[9] (*a*) P. Ratnasamy, L. Rodrigues, A. J. Leonard, *J. Phys. Chem.*, 1973, 77, 2242, (*b*) J. Wilson, A. D. Yoffe, *Adv. Phys.*, 1969, **269**, 193.

[10] R. R. Chianelli, E. Prestridge, T. Pecorano, J. P. DeNeufville, *Science*, 1979, **203**, 1105.

[11] (*a*) R. Tenne, L. Margulis, M. Genut, G. Hodes, *Nature*, 1992, **360**, 444, (*b*) L. Margulis, G. Salitra, R. Tenne, *Nature*, 1993, **365**, 113, (*c*) Y. Feldman, E. Wasserman, D. J. Srolovitch, R. Tenne, *Science*, 1995, **267**, 222.

[12] (*a*) C. T. Kresge, M. E. Leonowicz, W. J. Roth, J. C. Vartulli, J. S. Beck, *Nature*, 1992, **259**, 710, (*b*) J. S. Beck, J. C. Vartulli, W. J. Roth, M. E.

Leonowicz, C. T. Kressge, K. D. Schmitt, C. T. W. Chu, D. H. Olson, E. W. Sheppard, S. B. McCullen, J. B. Higgins, J. C. Scwenker, *J. Am. Chem. Soc.*, 1992, **114**, 10834.

[13] G. R. Pratzke, F. Krumeich, R. Nesper, *Angew. Chem., Int. Ed.*, 2002, **41**, 2446.

[14] (*a*) W. Stöber, A. Fink, E. Bohn, *J. Colloid Interface Sci.*, 1968, **26**, 62, (*b*) M. Nakamura, Y. Matsui, *J. Am. Chem. Soc.*, 1995, **117**, 2651.

[15] P. M. Ajayan, O. Stephane, Ph. Redlich, C. Colliex, *Nature*, 1995, **375**, 564.

[16] (*a*) B. C. Satishkumar, A. G. Govindaraj, E. M. Vogl, L. Basumallick, C. N. R. Rao, *J. Mater. Res.*, 1997, **12**, 604, (*b*) B. C. Satishkumar, A. Govindaraj, M. Nath, C. N. R. Rao, *J. Mater. Chem.*, 2000, **10**, 2115.

[17] M. E. Spahr, P. Bitterli, R. Nesper, M. Müller, F. Krumeich, H. U. Nissen, *Angew. Chem., Int. Ed.*, 1998, **37**, 1263.

[18] L. Pu, X. Bao, J. Zou, D. Feng, *Angew. Chem., Int. Ed.*, 2001, **40**, 1490.

[19] (*a*) M. L. Cohen, *Solid State Commun.*, 1994, **92**, 45, (*b*) J. L. Corkill, M. L. Cohen, *Phys. Rev. B*, 1994, **49**, 5081, (*c*) Y. Miyamoto, A. Rubio, S. G. Louie, M. L. Cohen, *Phys. Rev. B*, 1994, **50**, 18360.

[20] (*a*) K. Kobayashi, N. Kurita, *Phys. Rev. Lett.*, 1993, **70**, 3542, (*b*) Z. W. -Sieh, K. Cherrey, N. G. Chopra, X. Blasé, Y. Miyamoto, A. Rubio, M. L. Cohen, S. G. Louie, A. Zettl, P. Gronsky, *Phys. Rev. B*, 1994, **51**, 11229.

[21] (*a*) R. Sen, B. C. Satishkumar, A. Govindaraj, K. R. Harikumar, G. Raina, J. P. Zhang, A. K. Cheetham, C. N. R. Rao, *Chem. Phys. Lett.*, 1998, **287**, 671, (*b*) O. Stephan, P. M. Ajayan, C. Colliex, Ph. Redlich, J. M. Lambert, P. Bernier, P. Lefing, *Science*, 1994, **266**, 1683.

[22] (*a*) P. Gleize, M. C. Schouler, P. Gadelle, M. Caillet, *J. Mater. Sci.*, 1994, **29**, 1575, (*b*) O. R. Lourie, C. R. Jones, B. M. Bertlett, P. C. Gibbons, R. S. Ruoff, W. E. Buhro, *Chem. Mater.*, 2000, **12**, 1808, (*c*) R. Ma, Y. Bando, T. Sato, *Chem. Phys. Lett.*, 2001, **337**, 61.

[23] (a) R. S. Wagner, *Whisker Technology* (Ed: A. P. Levitt) 1970, Wiley-Interscience, New York, (b) R. S. Wagner, W. C. Ellis, *Appl. Phys. Lett.*, 1964, **4**, 89.

[24] Y. Wu, P. Yang, *J. Am. Chem. Soc.*, 2001, **123**, 5.

[25] J. J. Stejny, R. W. Trinder, J. J. Dlugosz, *Mater. Sci.*, 1981, **16**, 3161.

[26] J. J. Stejny, R. W. Dlugosz, A. J. Keller, *Mater. Sci.*, 1979, **14**, 1291.

[27] H. R. Kruyt, A. E. V. Arkel, *Kolloid-Z*, 1928, **32**, 29.

[28] B. Gates, B. Mayers, B. Cattle, Y. Xia, *Adv. Funct. Mater.*, 2002, **12**, 219.

[29] B. Mayers, Y. Xia, *J. Mater. Chem.*, 2002, **12**, 1875.

[30] (a) B. Messer, J. H. Song, M. Huang, Y. Wu, F. Kim, P. Yang, *Adv. Mater.*, 2000, **12**, 1526, (b) J. Song, B. Messer, Y. Wu, H. Kind, P. Yang, *J. Am. Chem. Soc.*, 2001, **123**, 9714.

[31] (a) C. R. Martin, *Science*, 1994, **266**, 1961, (b) D. Almawlawi, C. Z. Liu, M. Moskovits, *J. Mater. Res.*, 1994, **9**, 1014, (c) M. Zheng, L. Zhang, X. Zhang, J. Zhang, G. Li, *Chem. Phys. Lett.*, 2001, **334**, 298.

[32] (a) Y. Xia, P. Yang, Y. Sun, Y. Wu, B. Mayers, B. Gates, Y. Yin, F. Kim, H. Yan, *Adv. Mater.*, 2003, **15**, 353, (b) H. Ringsdorf, B. Schlarb, J. Verzmer, *Angew. Chem. Int. Ed.*, 1988, **27**, 113.

[33] Y. Yin, Y. Lu, Y. Sun, Y. Xia, *Nano Lett.*, 2002, **2**, 427.

[34] B. Gates, Y. Wu, Y. Yin, P. Yang, Y. Xia, *J. Am. Chem. Soc.*, 2001, **123**, 11500.

[35] A. Govindaraj, B. C. Satishkumar, M. Nath, C. N. R. Rao, *Chem. Mater.*, 2000, **12**, 202.

[36] T. J. Trentler, K. M. Hickman, S. C. Geol, A. M. Viano, P. C. Gibbons, W. E. Buhro, *Science*, 1995, **270**, 1791.

[37] (a) T. J. Trentler, S. C. Goel, K. M. Hickman, A. M. Viano, M. Y. Chiang, A. M. Beatty, P. C. Gibbons, W. E. Buhro, *J. Am. Chem. Soc.*, 1997, **119**, 2172, (b) P. D. Markowitz, M. P. Zach, P. C. Gibbons, R. M. Penner, W. E. Buhro, *J. Am. Chem. Soc.*, 2001, **123**, 4502, (c) O. R. Lourie, C. R. Jones, B. M. Bartlett, P. C. Gibbons, R. S. Ruoff, W. E. Buhro, *Chem. Mater.*, 2000, **12**, 1808.

[38] J. D. Holmes, K. P. Johnston, R. C. Doty, B. A. Korgel, *Science*, 2000, **287**, 1471.

[39] (a) L. Manna, E. C. Scher, A. P. Alivisatos, *J. Am. Chem. Soc.*, 2000, **122**, 12700, (b) C.-C. Chen, C.-Y. Lang, Z.- H. Lang, *Chem. Mater.*, 2000, **12**, 1516.

[40] M. H. Huang, Y. Wu, H. Feick, N. Tran, E. Weber, P. Yang, *Adv. Mater.*, 2001, **13**, 113.

[41] M. H. Huang, S. Mao, H. Feick, Y. Yun, Y. Wu, H. Kind, E. Weber, R. Russo, P. Yang, *Science*, 2001, **292**, 1897.

[42] B. Messer, J. H. Song, P. Yang, *J. Am. Chem. Soc.*, 2000, **122**, 10232.

[43] (a) Y. Huang, X. Duan, Q. Q. Wei, C. M. Lieber, *Science*, 2001, **291**, 630, (b) Y. Wu, H. Yan, M. Huang, B. Messer, J. H. Song, P. Yang, *Chem. Eur. J.*, 2002, **8**, 1260.

[44] F. Kim, S. Kwan, J. Arkana, P. Yang, J. Am. Chem. Soc., 2001, **123**, 4360.

[45] (*a*) H. M. Cheng, Q. H. Yang, C. Liu, *Carbon*, 2001, **39**, 1447, (*b*) P. Hou, Q. Yang, S. Bai, S. Xu, M. Liu, H. Cheng, *J. Phys. Chem. B*, 2002, **106**, 963 and references therein.

[46] R. Ma, Y. Bando, H. Zhu, T. Sato, C. Xu, D. Wu, *J. Am. Chem. Soc.*, 2002, **124**, 7672.

[47] J. Chen, N. Kuriyama, H. Yuan, H. T. Takeshita, T. Sakai, *J. Am. Chem. Soc.*, 2001, **123**, 11813.

[48] (*a*) M. Treacy, T. Ebbesen, *Nature*, 1996, **381**, 678, (*b*) C. F. Cornwell, L. T. Wille, *Solid State Commun.*, 1997, **101**, 505.

[49] (a) X. T. Zhou, J. Q. Hu, C. P. Li, D. D. D. Ma, C. S. Lee, S. T. Lee, *Chem. Phys. Lett.*, 2003, **369**, 220, (b) F. Patolsky, C. M. Lieber, Mater. Today., 2005, 20.

[50] C –C. Chen, C –C. Yeh, C –H. Chen, M –Y. Yu, H –L. Liu, J -J. Wu, K -H. Chen, L -C. Chen, J -Y. Peng, Y -F. Chen, *J. Am. Chem. Soc.*, 2001, **123**, 2791.

[51] J. C. Johnson, H -J. Choi, K. P. Knutsen, R. D. Schaller, P. Yang, R. J. Saykally, *Nature Mater.*, 2001, **1**, 106.

[52] Y. Huang, X. Duan, Y. Cui, L. J. Lauhon, K. H. Kim, C. M. Lieber, *Science*, 2001, **294**, 1313.

[53] M. T. Björk, B. J. Ohlsson, C. Thelander, A. I. Persson, K. Deppert, L. R. Wallenberg, L. Samuelson, *Appl. Phys. Lett.*, 2002, **81**, 4458.

Chapter 2

Multi-walled and Single-walled Carbon Nanotubes and Carbon Nanotubes with Y-junctions

Summary*

This chapter deals with the synthesis of carbon nanotubes by the pyrolysis of organometallic precursors. Y-junction carbon nanotubes can be produced in relatively large quantities by the vapor phase pyrolysis of a mixture of nickelocene, cobaltocene ferrocene or iron pentacarbonyl with thiophene in a hydrogen atmosphere. The carbon nanotubes with junction have been examined extensively by TEM and EELS. The junctions are free from sulfur and contain only carbon or carbon and nitrogen. Pyrolysis of Ni- and Fe-phthalocyanines with thiophene yields N-doped Y-junction nanotubes. Good yields of Y-junction carbon nanotubes were obtained by pyrolysing thiophene over an Ni(Fe)/SiO_2 catalyst as well. Many of the nanotubes show multiple Y-junctions. Of the various methods employed by us, the pyrolysis of thiophene with metallocenes or over the Ni (Fe)/SiO_2 catalyst yields the best results and is also a less expensive route.

We have also carried out the pyrolysis of ferrocene in combination with ethylene/acetylene along with water vapour. By this procedure we have been able to

* Papers based on these studies have appeared in Chem. Phys. Lett., (2001) and (2005).

obtain junction nanotubes at the inlet and large yields of SWNTs at the outlet regions. By carrying out the same reaction in the absence of water vapour we have been able to obtain multi-walled nanotubes containing junctions with reduced number of graphitic layers.

The electronic properties of the junction nanotubes have been investigated by scanning tunneling microscopy. Tunneling conductance measurements reveal rectifying behavior with regions of coulomb blockade, the effect being much larger in the N-doped junction nanotubes.

2.1 Introduction

Carbon nanotubes (CNTs) are conveniently obtained by carrying out the pyrolysis of hydrocarbons such as ethylene and acetylene over nanoparticles of iron, cobalt, and other metals dispersed over a solid substrate [1-3] The presence of nanoparticles is essential not only to form nanotubes but also to control the diameter of the nanotube to some extent [4]. Since a carbon source as well as metal nanoparticles is necessary for producing carbon nanotubes by the pyrolysis of hydrocarbons, the strategy of employing an appropriate organometallic precursor which can serve as a dual source of both the carbon and the metal nanoparticles was explored by us. The first experiments carried out on the pyrolysis of organometallic precursors such as metallocenes and iron pentacarbonyl were successful in producing multiwalled nanotubes (MWNTs) [5,6]. This method is used not only to synthesize multiwalled and single-walled nanotubes (SWNTs) but also Y-junction nanotubes.

Y-and T-shaped carbon nanotube junctions are considered likely to be the basic building units for nanoelectronic devices. The Y- and T-junctions appear to defy the conventional models in favor of an equal number of five- and seven-membered rings to create nanotube junctions. Instead, the Y-and T-junctions can also be created with an equal number of five- and eight-membered rings (Figure 2.1-2.3) [7]. An ordinary carbon nanotube involving a bend or a kink arising from the presence of a diametrically opposite pentagonal-heptagonal pair connects two nanotubes of different chirality and hence of different electronic structure, thereby leading to an intramolecular device (Figure 2.4). Such a device with a single-walled carbon nanotube can behave as a diode rectifier [8]. For device applications, it is important to

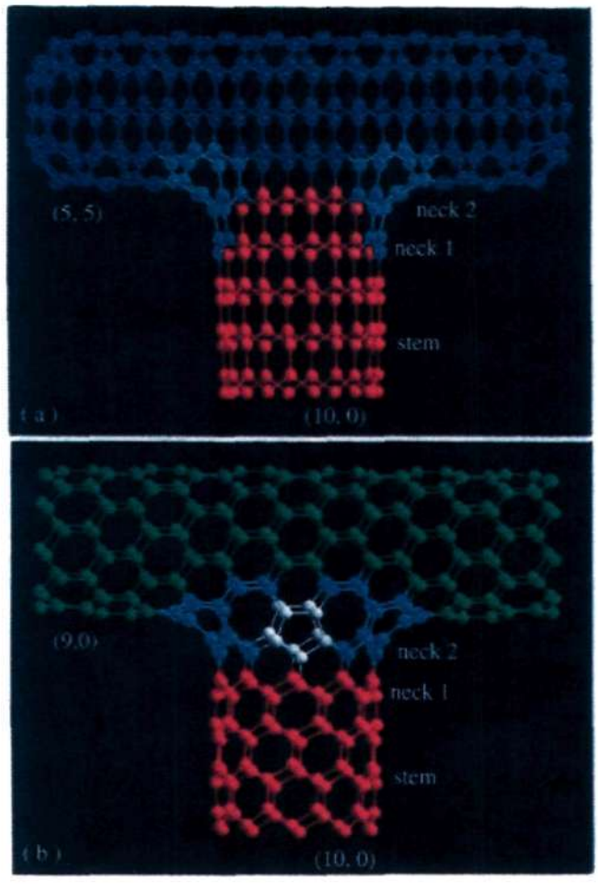

Figure 2.1: Model of T-junction carbon nanotubes (a) (5,5)-(10,0)-(5,5) tube (**T1**), the turquoise colored balls denote the atoms forming the heptagons. The structure contains six heptagons and no pentagons and (b) (9,0)-(10,0)-(9,0) tube (**T2**). The turquoise colored balls denote the atoms forming the heptagons. Pentagons are denoted by white balls. The structure contains eight heptagons and two pentagons.

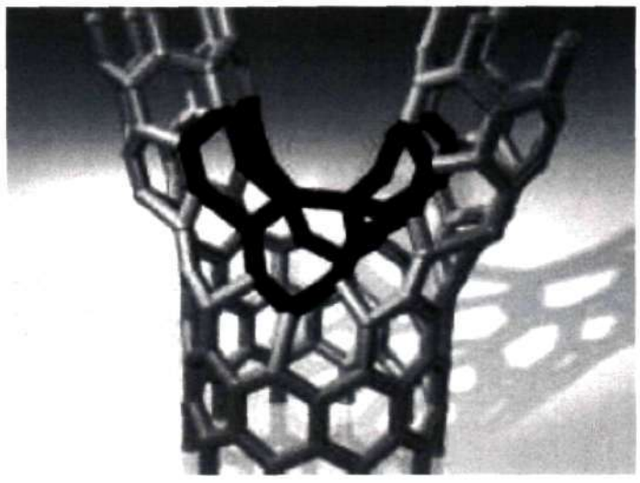

Figure 2.2: Structural models of carbon nanotube Y-junctions (the six heptagons are highlighted in black).

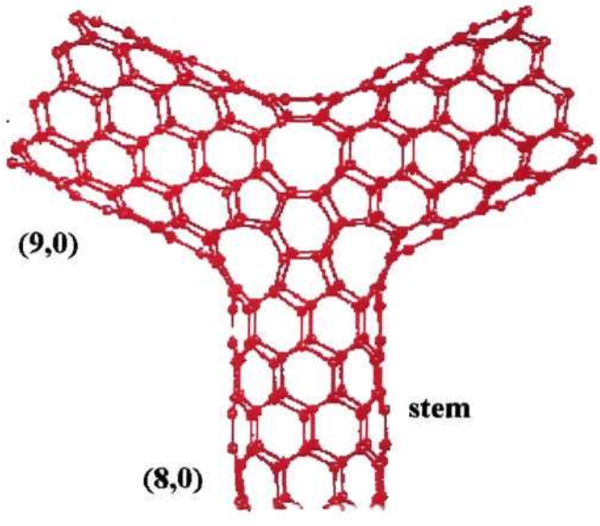

Figure 2.3: Model of a Y-junction nanotube with two (9,0) and one (8,0) arms. The presence of 6 octagons and 6 pentagons are clearly seen.

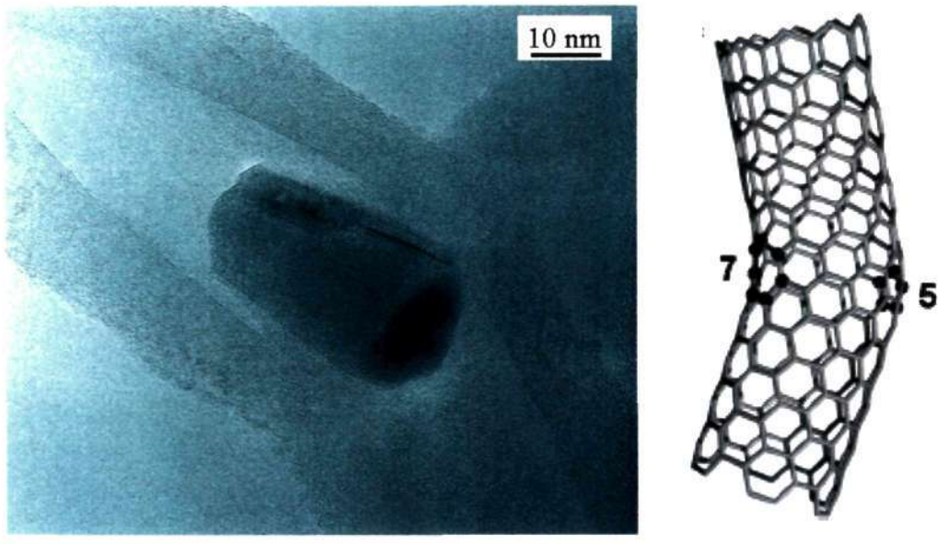

Figure 2.4: TEM image and the corresponding model of a bend or kink in a carbon nanotube created by the presence of five-membered (pentagon) and seven-membered (heptagon) rings.

be able to connect nanotubes of different diameters and chirality [9-11]. To date, there have been no practical devices made of real three-point nanotube junctions. However, junctions consisting of crossed nanotubes have been fabricated to study their transport characteristics [12]. In this context it is important to be able to devise methods that can deliver junction nanotubes of high purity and in good yields. The ability to obtain such methods will aid largely in investigating the electronic properties of junction nanotubes in detail. In this chapter, the salient features of the various types of nanotubes obtained by employing the organometallic route is presented and also some of the properties of the nanotubes so produced is examined. Y-junction nanotubes thus prepared could be useful as building blocks in nanoelectronics. The nanotubes

produced from organometallics are also usefully employed as starting materials to prepare other types of nanostructures. In what follows, the scope of the present investigations has been outlined.

2.2 Scope of the present investigations

Y-junction MWNTs

Y-junction nanotubes have been prepared by using Y-shaped nanochannel alumina templates in the presence of cobalt particles [13]. More significantly, it has been possible to prepare Y-junction nanotubes by chemical means through the pyrolysis of nickelocene in the presence of thiophene at 1000 °C [14]. Such a direct and simple chemical synthesis of Y-junction nanotubes on a large scale would be of value for applications in nanodevices. Y-junction nanotubes have also been formed by hot tantalum-filament chemical vapor deposition using evaporated copper catalyst and acetone as the carbon source [15]. The junctions were later prepared by the pyrolysis of CH_4 over Co supported on MgO by Li *et al.* [16]. The yield of junctions seems to be superior by the pyrolysis procedure [14]. Apart from producing Y-junction nanotubes by the pyrolysis of nickelocene-thiophene mixtures, we have studied the pyrolysis of other metallocenes such as ferrocene and cobaltocene along with thiophene. In addition, we have examined the pyrolysis of thiophene in the presence of iron and nickel phthalocyanines as well as iron pentacarbonyl. The pyrolysis involving Fe- and Ni-phthalocyanines was carried out to obtain N-doped Y-junction carbon nanotubes. Since thiophene plays an important role in the formation of Y-junctions, we have investigated the pyrolysis of thiophene over Ni or Fe nanoparticles dispersed on silica surfaces. Interestingly, this method yields high quantities of Y-

junction nanotubes, comparable to that obtained by the pyrolysis of nickelocene-thiophene mixtures. Pyrolysis of $Fe(CO)_5$ with thiophene has also been carried out to produce Y-junction nanotubes. Pyrolysis of metallocenes in mixture with CS_2 and alkane thiols has also been carried out to find out whether other sulphur-containing compounds favor the formation of junction nanotubes.

An important aspect of the junction nanotubes relates to the structure and chemical composition of the junction itself, these factors having a bearing on the electronic properties. In the case of the junction nanotubes prepared by the pyrolysis of organometallics in the presence of organosulphur compounds, it becomes necessary to establish whether sulfur atoms are incorporated at the junctions, considering the high propensity of sulfur to form rings. If sulfur is absent in the junction region, it would imply the presence of five-, seven- or eight- membered rings required to bring about necessary curvature to form a junction [7]. In this context, the disposition of the graphene layers around the junction is a relevant aspect. Since metal nanoparticles are neccessary for the formation of the nanotubes, it is of interest to understand their role as well. In this context we have investigated the Y-junction carbon nanotubes extensively by transmission electron microscopy (TEM) and electron energy loss spectroscopy (EELS) to throw light on the nature of the Y-junctions.

Y-junction nanotubes and single-walled nanotubes by precursor pyrolysis in the presence of water vapour

In addition to the synthesis of Y-junction MWNTs we were interested in examining the role of water vapour in preparing junction nanotubes as well as

SWNTs. For this purpose, we have examined the nanotubes obtained by the pyrolysis of ferrocene in mixture with ethylene or acetylene bubbled through thiophene in a stream of moist H_2. For purpose of comparison, we have also carried out the pyrolysis of the ferrocene-hydrocarbon mixtures in the absence of water vapour. In the presence of water vapour, we have obtained MWNTs with junctions at the inlet of the furnace and SWNTs in the outlet region. In the absence of water vapour, we obtain MWNTs with T- and Y- junctions.

Electronic Properties of the junction CNTs

There have been a few reports on the electronic properties of junction nanotubes [14, 17-21]. Rao and coworkers carried out scanning tunneling spectroscopy (STS) measurements on Y-junction nanotubes and reported that the junction acts as a diode [14]. A theoretical study of the electron transport properties of doped nanotubes has shown that a doped nanotube with donor atoms on one side and acceptor atoms on the other, can function as a nanodiode [19]. Negative differential resistance behavior predicted for intramolecularly doped carbon nanotube junctions [20] was subsequently observed experimentally in the case of K-doped SWNTs [21]. We have carried out a detailed study of the Y-junctions both in CNTs and in N-doped CNTs by scanning tunneling microscopy (STM). The results show that the Y-junctions, particularly in the N-doped carbon nanotubes, possess rectification behavior. This is the first study of its kind on doped carbon nanotube junctions.

2.3 Experimental

2.3.1 Synthesis

Y-junction MWNTs

The experimental setup employed by us for the synthesis of the Y-junction carbon nanotubes consists of stainless steel gas flow lines and a two-stage furnace system fitted with a quartz tube (10 mm inner diameter) as shown in Figure 2.5. The flow rates of the gases were controlled using UNIT mass flow controllers. The pyrolysis of the metallocenes with thiophene was carried out as follows. A known quantity of metallocene was sublimed in the first furnace and carried along with a flow of argon (Ar) gas to the pyrolysis zone in the second furnace. Simultaneously

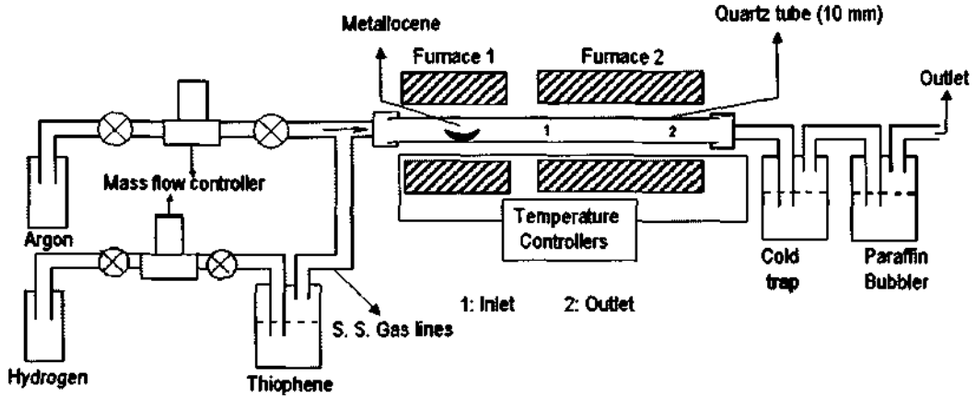

Figure 2.5: Pyrolysis setup for the synthesis of carbon nanotube Y-junctions employing metallocene and thiophene.

hydrogen (H_2) was bubbled through thiophene and was mixed with the argon-metallocene vapors at the inlet of the furnace and carried to the pyrolysis zone. Pyrolysing these mixed vapors at 1000 °C yielded Y-junction nanotubes. Several experiments were carried out by varying the flow rate of Ar and H_2 between 100-200 sccm and 150-50 sccm respectively. The pyrolysis of Ni/Fe phthalocyanines in

mixture with thiophene was carried out in a similar manner taking the phthalocyanines in the place of metallocenes. Carbon deposits were found to accumulate at the inlet and the outlet ends of the second furnace.

Pyrolysis of thiophene was carried out over a nickel catalyst prepared by the following procedure. About 2.4 g of nickel acetate (corresponding to 0.01 mol) was dissolved in 5ml of acidified ethanol followed by the addition of 2 ml of tetraethyl orthosilicate (TEOS) and stirred for 5 minutes. To this homogeneous solution, 1.5 ml of HF (38%) was added drop-wise and the resultant mixture stirred at 50 °C till it resulted in the formation of a gel. The gel was dried in an oven at 75 °C for 24 h, calcined at 400 °C for 2 hrs and reduced in H_2 atmosphere for 2 h. The temperature was subsequently raised to 1000 °C and thiophene vapors were passed over the catalyst for 20 min, by bubbling H_2 (50 sccm) through thiophene. The sample collected from the boat was observed under the microscope. Similar experiments were also carried out with a Fe/SiO_2 catalyst.

Y-junction nanotubes and single-walled nanotubes by precursor pyrolysis in the presence of water vapour

In order to study the effect of water vapour on the nanotubes obtained by the pyrolysis of thiophene and organometallic mixtures we have employed two procedures. In both the procedures, a known quantity of ferrocene was sublimed in the first furnace and was carried by the flow of Ar gas (2000 sccm) to the second furnace. In procedure (i), three streams of gases were carried to the second furnace where the pyrolysis occurred. Ethylene or acetylene (10 sccm) bubbled through thiophene, was carried to pyrolysis zone in the second furnace in the second stream,

while the third stream involved H_2 (20 sccm) which bubbled through water. Pyrolysing these mixtures in the second furnace at 1000 °C yielded nanotubes in the inlet and outlet regions. We have compared the results of procedure (i) with the results from the pyrolysis carried out by procedure (ii) in the absence of water vapour.

2.3.2 Characterization

The nanotubes were examined with a JEOL JEM-3010 transmission electron microscope (TEM) operating at 300 kV and also with a JEM 4000 EX microscope (Fa. JEOL, Japan) with an accelerating voltage of 400 kV and a LaB_6 cathode. EELS chemical mapping was performed with an energy-filtering microscope (Zeiss 912 Omega, acceleration Voltage, 125 keV and LaB_6 cathode). Electron energy loss spectra were recorded with a Gatan imaging filter system attached to the JEOL microscope and fitted with a CCD camera. X-ray diffraction (XRD) patterns were recorded using a Seifert instrument with Cu Kα radiation.

2.3.2 STM and STS measurements

The carbon nanotube junctions were investigated by tunneling conductance measurements. Highly oriented pyrolytic graphite (HOPG) was used as the substrate. Freshly cleaved HOPG substrates were prepared by peeling the upper layers with an adhesive tape. The nanotubes were then taken as a suspension in an organic solvent (typically CCl_4 and ethanol was used) sonicated for 30 min, after which a drop was deposited onto the substrate. The substrate was left in air but covered, for a period of 12 h for drying. Imaging and spectroscopy were carried out using Au tips prepared by electrochemical etching. The STM and STS studies were carried out at room temperature (using a Omicron Vakumphysik STS) operated in air. Atomically

resolved images of HOPG were used for internal calibration. Current-voltage (I-V) data were collected in the spectroscopy mode with the feedback loop turned off (maximum current, 50 nA). Tunneling conductance measurements were carried out by positioning the tip atop a Y-junction (the point of contact between the three arms) as well as on the individual arms. The I-V data from the clean areas of the HOPG substrate were collected repeatedly as reference to ensure the reliability of the measurements.

2.4 Results and discussion

2.4.1 Y-junctions in carbon nanotubes and N-doped carbon nanotubes

Y-junction carbon nanotubes by pyrolysis: Carbon deposits obtained from the pyrolysis of cobaltocene-thiophene mixtures showed Y-junction nanotubes both at the inlet and outlet ends of the second furnace. In Figure 2.6 (a), we show the Y-junction nanotubes obtained when the flow rates of H_2 and Ar were 100 sccm and 150 sccm respectively. The diameter of the inner core of the nanotubes is 9 nm and the outer diameter is 24 nm. In Figure 2.6 (b), we show the Y-junction nanotubes obtained by using a H_2 flow rate of 50 sccm and Ar flow rate of 200 sccm. The diameter of the inner core of the nanotubes is 15 nm whereas the outer diameter is 65 nm. Multiple junctions are found in the nanotubes at these flow rates. The formation of multiple junctions suggests the possibility of multiple tunnel devices in a single carbon nanotube. When the H_2 flow rate was increased to more than 200 sccm, there was no significant change in the features of the nanotubes.

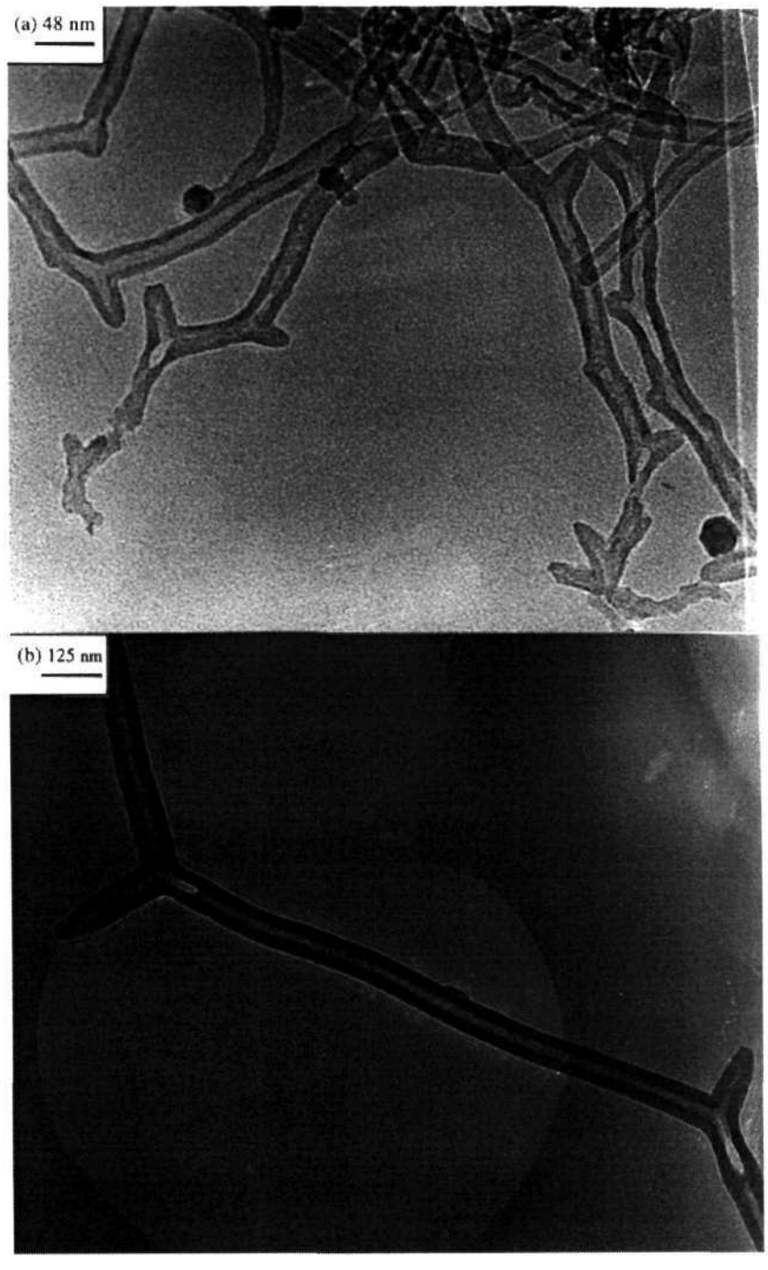

Figure 2.6: TEM images of Y-junction nanotubes obtained by the pyrolysis of cobaltocene-thiophene mixtures: (a) image with Y-junction nanotubes, (b) image showing a single multiple junction nanotube.

Figure 2.7: High resolution electron microscope image of the Y-junction nanotube obtained by the pyrolysis of cobaltocene-thiophene mixture.

At low flow rates of H_2 (less than 25 sccm), no junction nanotubes were found. When Ar was bubbled through thiophene instead of H_2, there was a greater proportion of amorphous carbon and the junctions obtained were not of good quality.

A typical high resolution transmission electron microscope (HREM) image of the Y-junction nanotubes obtained by the pyrolysis of cobaltocene-thiophene mixtures is shown in Figure 2.7. The interlayer separation of the graphitic layer is ~ 3.4 Å as expected. The graphitic layers are seen parallel to the corners of the junctions although fishbone-type stacking is also present.

The TEM images of the Y-junction nanotubes obtained by the pyrolysis of ferrocene-thiophene mixtures are shown in Figure 2.8. The H_2 flow rate used was 25 sccm, that of Ar being 225 sccm. Deposits collected predominantly from the outlet ends showed the presence of junctions. The presence of junctions in the inlet region was rare. The flow rate of H_2 was crucial in the formation of junctions. The junction in Figure 2.8 (a) has an outer diameter of 30 nm and an inner core diameter of 10-15 nm. The junction in Figure 2.8 (b) has an outer diameter of 70 nm and an inner core diameter of 25 nm.

Pyrolysis of CS_2 with nickelocene (flow rate: H_2 = 50 sccm, Ar = 200 sccm) gave good yields of junction nanotubes as can be seen from the TEM image in Figure 2.9 (a). Pyrolysis of thiophene with $Fe(CO)_5$ carried out by bubbling H_2 (50-100 sccm) through the pentacarbonyl along with Ar (150-200 sccm) bubbled through thiophene showed the presence of interesting junction structures as revealed in Figure 2.9 (b). Gan *et al.* [15] have carried out the growth of Y-junction nanotubes by using an in situ evaporated copper catalyst and acetone bubbled by H_2 as the carbon source.

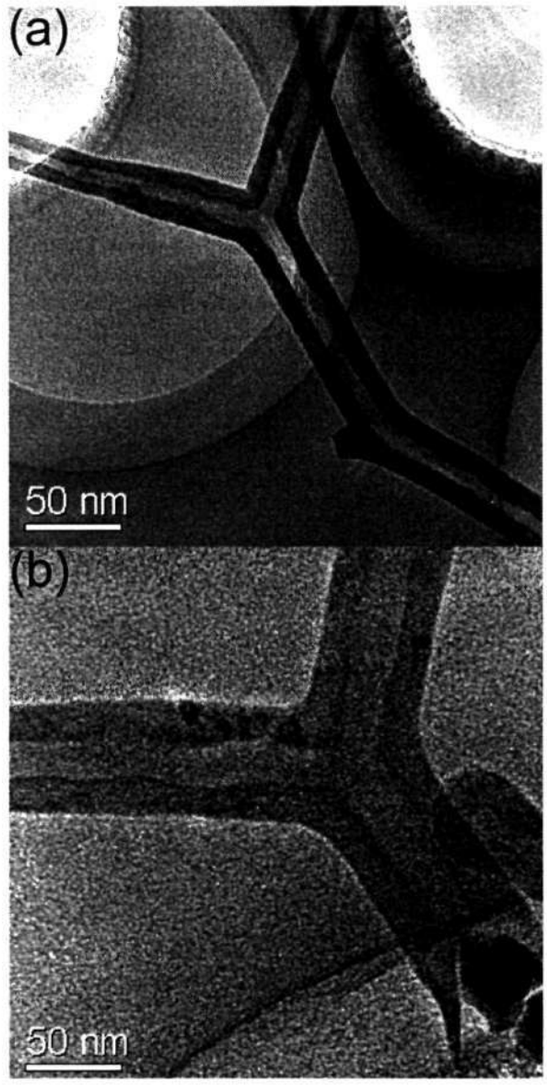

Figure 2.8: TEM images of the Y-junction nanotubes obtained by the pyrolysis of ferrocene-thiophene mixtures: (a) image showing a multiple Y-junction nanotube, (b) image showing a single junction nanotube.

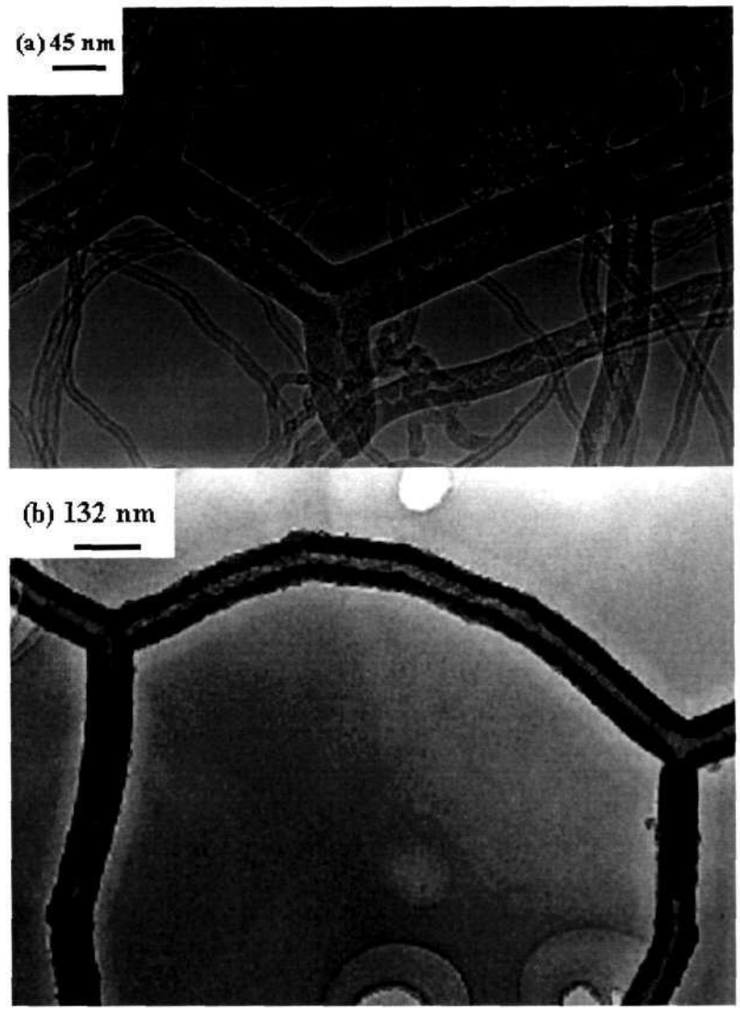

Figure 2.9: TEM images of (a) image of a multiple junction nanotube obtained by the pyrolysis of nickelocene-CS_2 mixture, (b) image of a nanotube obtained by the pyrolysis of a $Fe(CO)_5$-thiophene

We have carried out a similar reaction by carrying out the pyrolysis of vapors of acetone and copper (II) acetyl acetonate ($Cu(acac)_2$) to produce Y-junctions. To achieve this, $Cu(acac)_2$ vapors carried by Ar (flow rate = 200 sccm) was mixed with acetone carried by H_2 (flow rate = 50 sccm) and the mixture pyrolysed at 1000 °C. Although this method yielded Y-junctions, they were not as good as those obtained by using metallocenes or the Ni/SiO_2 catalyst (see next section). Furthermore, large quantities of amorphous carbon were present in the product.

N-doped Y-junction carbon nanotubes: The use of Ni- and Fe-phthalocyanines instead of metallocenes yields N-doped Y-junctions. Figure 2.10 (a) shows a TEM image of the multiple junctions formed continuously with Ni-phthalocyanine-thiophene mixture at a H_2 flow rate of 150 sccm and Ar flow rate of 100 sccm, respectively. Figure 2.10 (b) shows an image of the junctions obtained by using Fe-phthalocyanine-thiophene mixture under similar conditions as in Figure 2.10 (a).

Y-Junction carbon nanotubes using Ni/SiO_2 catalyst: In Figure 2.11 (a) and (b), we show the SEM and TEM images of the silica supported nickel catalyst. We see that the metal is present as nanoparticles on the silica substrate. TEM images of the Y-junctions obtained by the pyrolysis of thiophene over the Ni/SiO_2 catalyst are as shown in Figure 2.12 (a). The walls of the junctions are however significantly thicker than those observed previously. The outer and core diameters of the nanotubes were as high as 136 nm and 55 nm respectively. The nanotube junctions obtained by this method are as good as those obtained by the pyrolysis of metallocene-thiophene mixtures. The amorphous carbon material associated with the nanotubes was, however, negligible by this procedure. We have also lowered the proportion of nickel catalyst. Shown in Figures 2.12 (b-d) are the TEM images obtained by using a lower

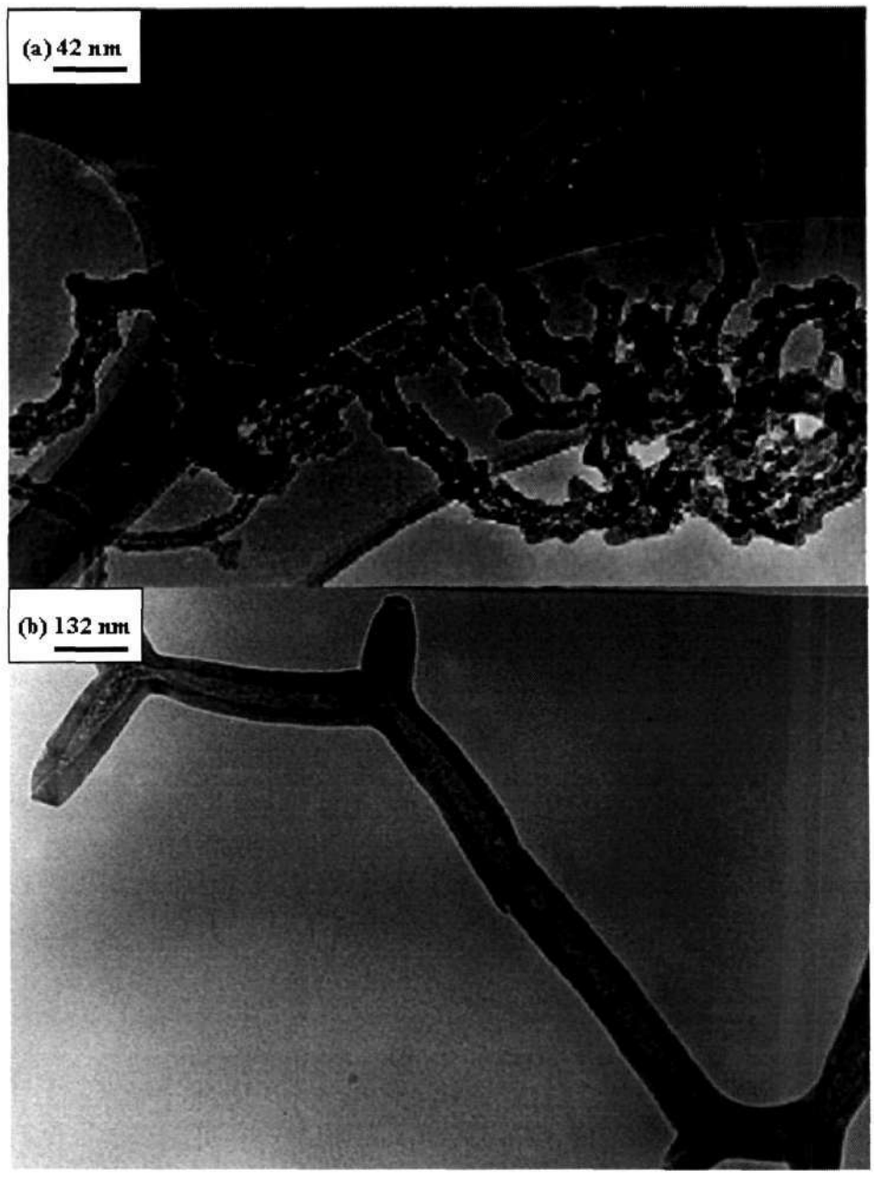

Figure 2.10: TEM images of the Y-junctions obtained by the pyrolysis of thiophene along with (a) Ni-phthalocyanine and (b) Fe-phthalocyanine.

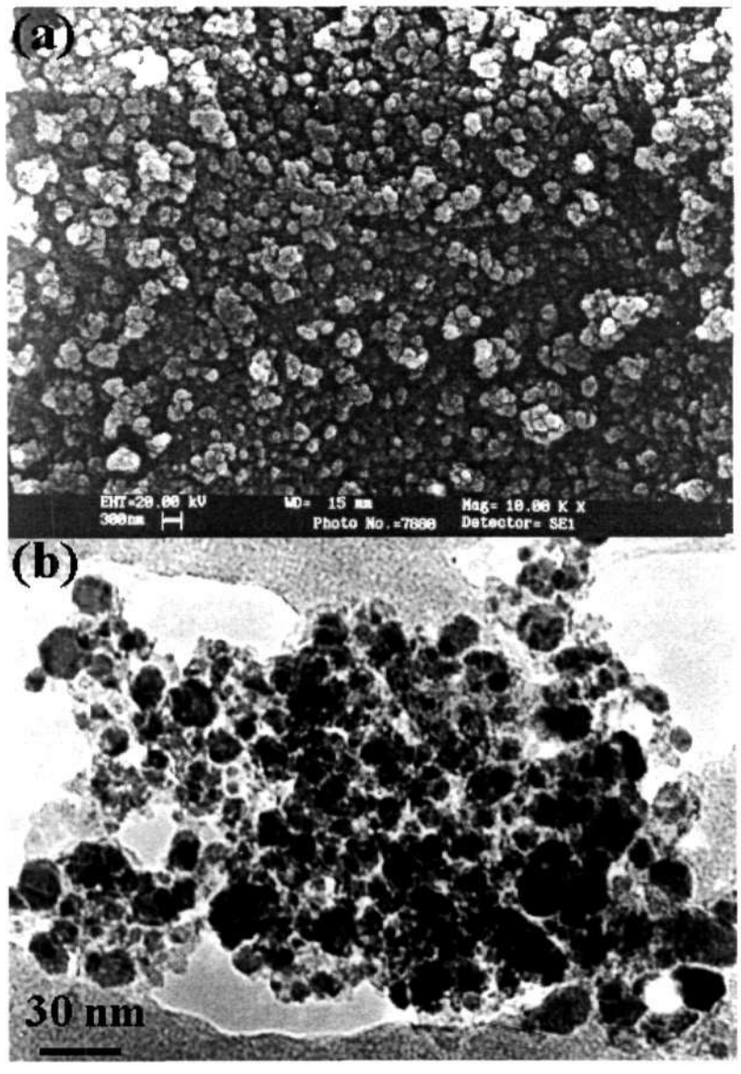

Figure 2.11: (a) SEM and (b) TEM images of the Ni/silica catlyst.

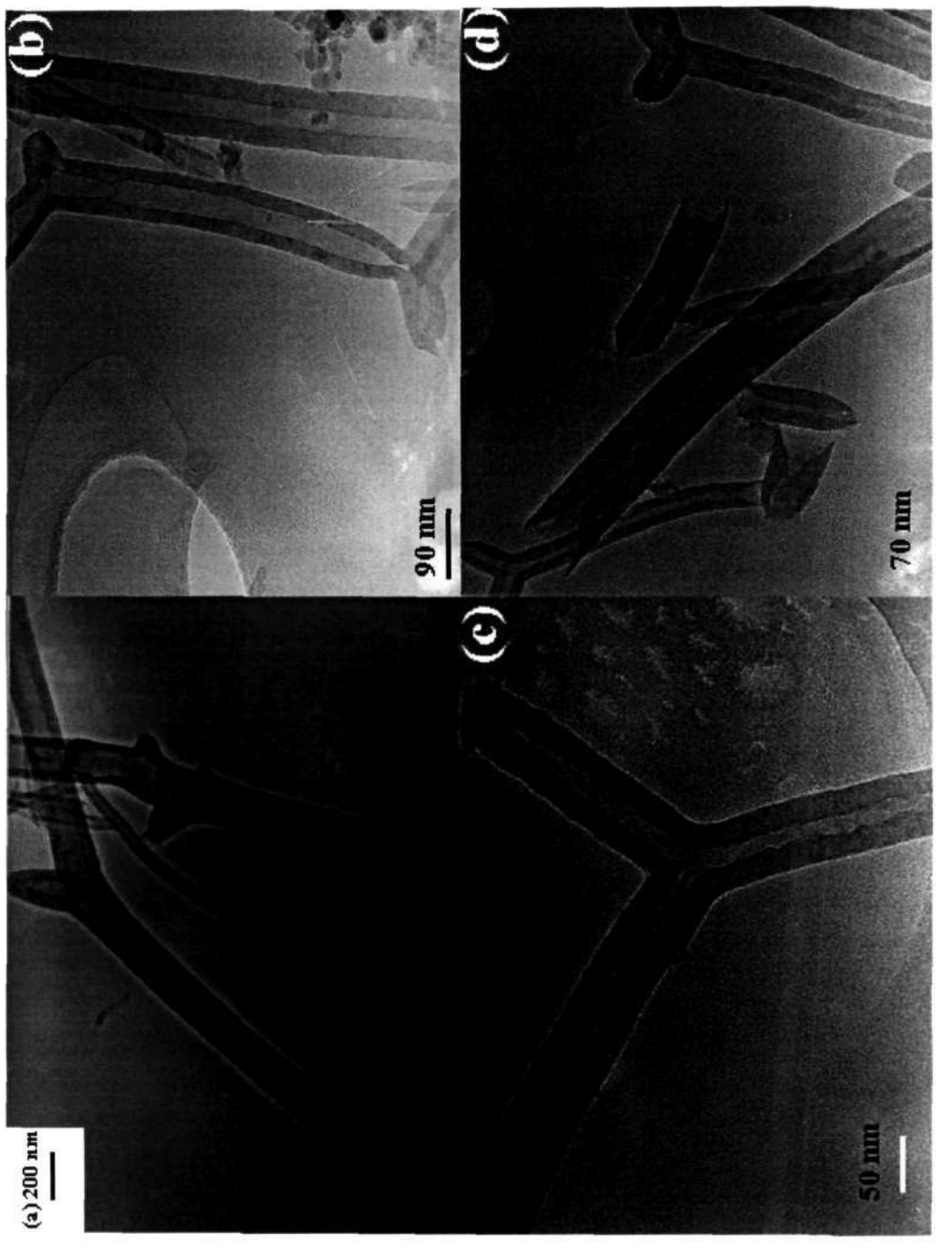

Figure 2.12: TEM images of Y-junction nanotubes obtained by the pyrolysis of thiophene over a Ni/SiO_2 catalyst: (a) image shows the presence of several junctions on a single nanotube, (b) – (d) junction nanotubes obtained by using a lower loading of the catalyst on the SiO_2 support.

loading of the nickel catalyst on the silica support. By lowering the proportion of the nickel catalyst on the silica support it is seen that the Y-junction CNTs had a smaller diameter. Thus the outer diameters of the nanotubes shown in Figure 2.12 (b-d), are 60, 50 and 40 nm respectively, the inner diameters being 30, 16 and 12 nm respectively. The number of graphitic layers are rather large going upto 50 layers. Multiple junction features occur commonly by this method as can be seen in Figure 2.11 (a) and 2.12 (b). Long and straight junctions, several nm in length, were also observed. In effect this method may be useful to tune the diameter of the junction nanotubes suitably by varying the proportion of the nickel catalyst supported over silica.

Structure and mechanism of formation of Y-junction carbon nanotubes

(a) Structure

Investigations of the TEM images of the products of pyrolysis of nickelocene-thiophene mixtures show the presence of highly crystalline Y-junction carbon nanotubes with well-formed arms (Figure 2.13 (a)). The images also reveal certain unusual nanotube structures such as asparagus-like branches and bamboo structures (see the inset of the Figure 2.13 (a)). We show the EELS chemical mapping for carbon in Figure 2.13 (b) to demonstrate how the nanotube is made entirely of carbon. We failed to observe any sulfur in the junction region. We have examined the nickel nanoparticles produced in-situ by the pyrolysis of the nickelocene-thiophene mixtures. The TEM image of a Ni-nanoparticle is shown in the inset of Figure 2.13 (b). EELS mapping showed the presence of a considerable amount of sulfur, close to 25%, in the nanoparticle. The XRD pattern of the Ni nanoparticles after the reaction with

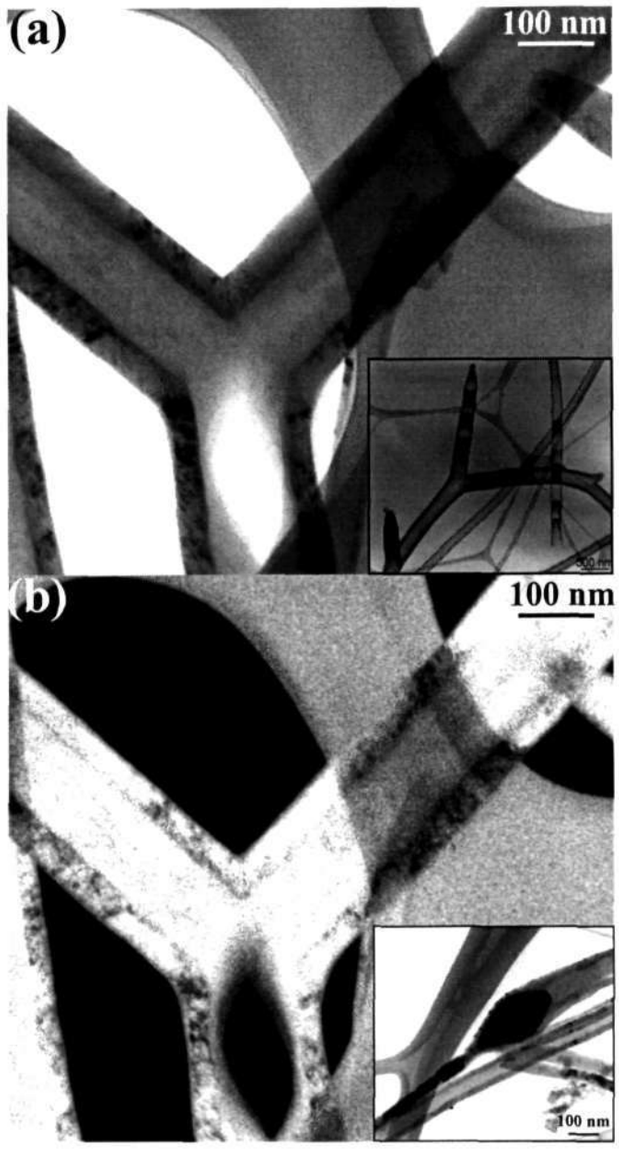

Figure 2.13: (a) TEM image of a Y-junction carbon nanotube obtained by the pyrolysis of nickelocene-thiophene mixture. The inset in (a) shows asparagus tips in the Y-junction nanotube. (b) EELS mapping of carbon in the Y-junction carbon nanotube. The inset in (b) shows the TEM image of a Ni nanoparticle inside a carbon nanotube.

thiophene showed characteristic reflections of rhombohedral Ni_3S_2 with unit cell dimensions of a = 5.75 Å and c = 7.13 Å (JCPDS file : 44-1418). The sulfur from the thiophene is entirely removed by the nickel particles leaving the thiophene-carbon fragment, which could form, 5-, or 7-membered carbon rings by adding on to different carbon centers in the nascent graphene sheets. Traces of S, in the nanotubes, if at all present, could not be detected at all by EELS or EDX.

The nanotube shown in Figure 2.13 (a) was examined by normal-incidence selected area electron diffraction (SAED) with the electron beam perpendicular to the junction. The diffraction pattern of one of the arms close to the junction (Figure 2.14 (a)), shows a set of arcs corresponding to four (002) maxima. Similar diffraction patterns were obtained from the other two arms next to the junction, suggesting that the graphene layers close to the junction are well-graphitized and are possibly slanted with some curvature. The electron diffraction pattern of the center shown in Figure 2.14 (b) reveals streaks of arcs corresponding to the (002) maxima arising from the three sets of graphitic planes in the three arms close to the junction [22-25]. The intensity distribution is not uniform in the arcs due to the complex nature of the orientation of the graphitic planes at the junction. In Figures 2.14 (c) and (d) we show schematic representations of the likely disposition of the graphene sheets around a Y-junction. The structure in Figure 2.14 (c) has gradual bends around the junction the which can arise due the presence of 5-, and 7- membered carbon rings in the graphene sheets. It is also possible to have a junction with different fishbone-like orientations of the graphene sheets. From the observations depicted in Figures 2.14 (a) and (b), it seems likely that the bends at the junctions may not be entirely continuous but instead

consist of short straight segments arising from a fishbone-type stacking as in Figure 2.14 (d).

N-doped Y-junction carbon nanotubes obtained by the pyrolysis of nickel-phthalocyanine mixture have rounded tips and uneven arms (Figure 2.15 (a)). Chemical mapping of the tubes revealed a small amount of nitrogen but there was no

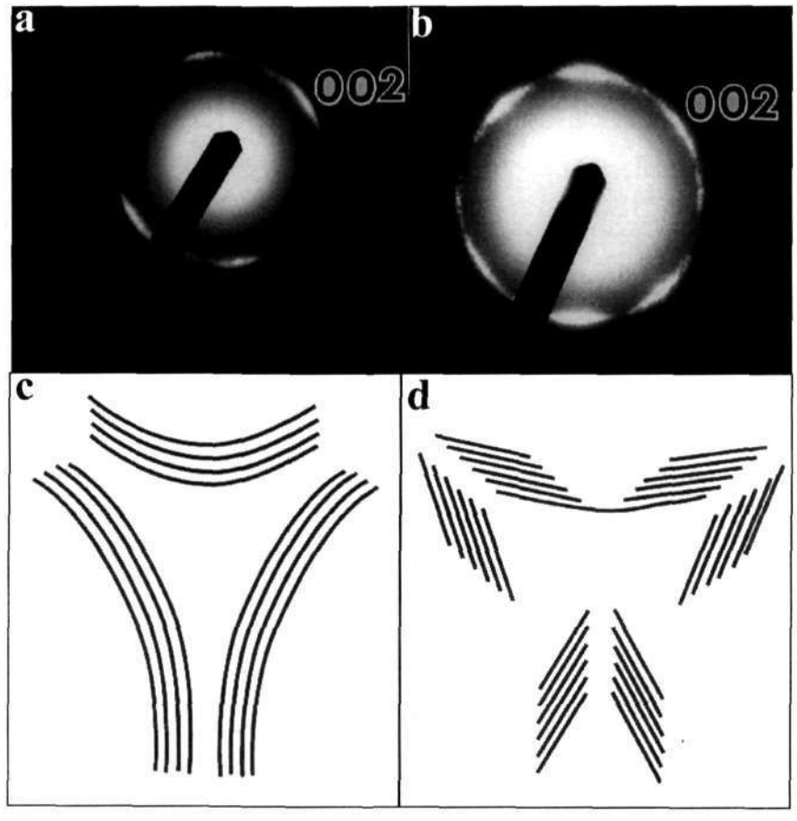

Figure 2.14: Selected area electron diffraction (SAED) patterns of the Y-junction carbon nanotubes: (a) of the arms and (b) of the junction region, (c) and (d) Schematic drawings showing different ways of stacking of the graphene sheets in the Y-junction carbon nanotubes.

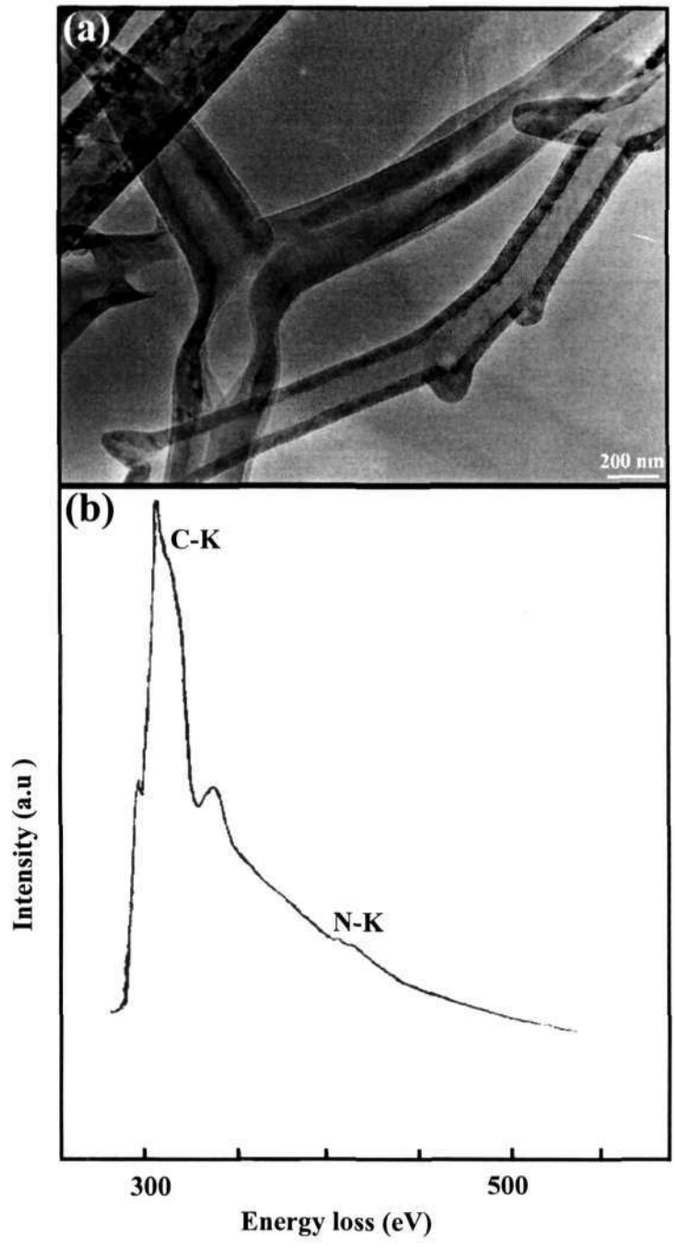

Figure 2.15 (a) TEM image of N-doped Y-junction carbon nanotubes prepared by the pyrolysis of a Ni-phthalocyanine - thiophene mixture. (b) EEL spectrum showing the presence of doped nitrogen.

sulfur in the junction region. Thus, the EEL spectrum (Figure 2.15 (b)) shows characteristic edges at 284 eV and 400 eV corresponding to the K-shell ionization of carbon and nitrogen respectively. The nitrogen signal is a doublet due to π^* and σ^* levels, thereby indicating that the nitrogen is present substitutionally in the graphene sheet. Based on the EEL spectrum, the average composition of the nanotubes is estimated to be $C_{45\pm5}N$ [26,27].

(b) Mechanism

Based on the above observations, the mechanism of growth of Y-junction CNTs is discussed. In our case involving the pyrolysis of organometallic precursors the growth of carbon nanotubes follows the well known tip-growth model. When CNTs grow, normally the growth is either randomly oriented or aligned in the direction of the flow of the gas which carries with it the supply of hydrocarbons necessary for its growth. The alignment is due to Van der waals forces [28], electrical forces [29,30], or interfacial forces [31]. Without these forces the growth is random, unless a template is used. It is therefore conceivable that as a CNT starts to grow from a catalyst there is a force guiding each CNT growth. During the growth, branching of CNTs occurs. As a result, it is believed that the growth of multi-walled Y-junction CNTs follows the following steps (Figure 2.16):

Step 1: Formation of catalyst particles.

The first step involved is the formation and nucleation of fine metal clusters. In this study the metallocenes or the corresponding phthalocyanines were used as the catalyst precursors giving rise to fine cluters of Fe, Co or Ni. These catalyst precursors are either evaporated and/or decomposed before they condense. The

melting point of bulk Fe is 1538 °C, although in this case the presence of fine clusters of Fe for example needs to be considered. At the growth temperature (~ 1000 °C), these precursors would evaporate and then nucleate or condense onto the substrate as in a physical vapor deposition (PVD) process. Thermodynamic calculations have shown that the partial vapor pressures are very low and in the range of 10^{-7} to 10^{-9} Torr. On the other hand, thermal decomposition of ferrocene ($C_{10}H_{10}Fe$) occurs at ~ 450 °C. Ferrocene decomposes to release Fe atoms at this temperature. In other words the formation of Fe catalyst is similar to a CVD process. In addition, the partial pressure of Fe is in the order of 10^{-3} Torr. The Fe adatoms from ferrocene therefore give rise to more catalyst particles for the growth of CNTs. Adatoms in a CVD process are much more energetic than that in a PVD process [32]. As a result, the energetic Fe adatoms from ferrocene could diffuse on the quartz tube surface to favorable high energy sites, i.e., the rough edges, to form catalyst particles. The catalyst particles therefore distributed randomly on the surface and the growth of CNT is random. The pyrolysis of the other metallocenes and phthalocyanines can be rationalized in a similar way.

Step 2: Tip-growth of individual CNTs starts.

In this step the carbon atoms nucleate and diffuse through the catalyst particle to allow the lengthening of a CNT. As a CNT lengthens, the direction is directed by the flow of the gas. With increase in the supply of the hydrocarbons a constant and continuous growth takes place. The supply of carbon fragments can be both from the metallocenes as well as those from thiophene. It is not clear as to which of the two dominates or whether they are in equal amounts depending certainly on the relative concentrations employed.

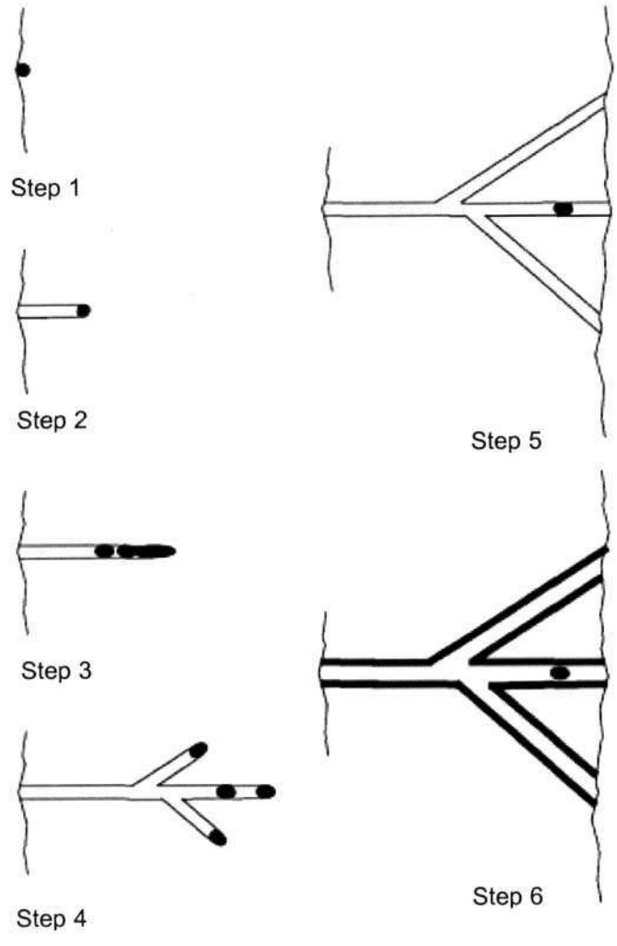

Figure 2.16: A schematic showing the growth of Y-junction carbon nanotubes. That the catalyst is present in the arms or within the junction nanotube (Step 6) has been observed in TEM images (Figure 2.17).

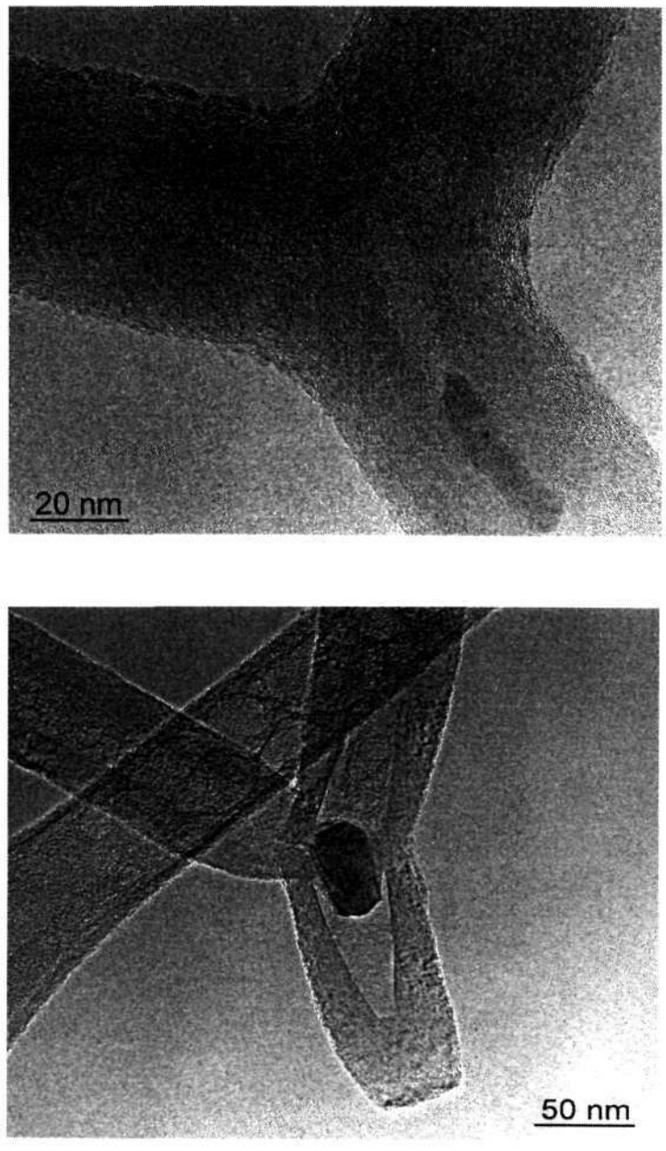

Figure 2.17: Presence of the catalyst seen within the junction nanotubes.

Step 3: Elongation and breaking of catalyst particles.

As a CNT lengthens, the catalyst particle located at the tip elongates and then breaks into smaller fragments. The elongation and separation of a catalyst particle inside a CNT is commonly due to the melting of the catalyst. Breaking of an elongated, rod-like particle into two short rod-like ones is mostly possible. The melting point of catalyst particles (Fe for instance from ferrocene) is 1538 °C. The growth temperature (1000 °C) is therefore about 60-70 % of the melting point in the absolute scale. The melting point of fine clusters of Fe is however expected to be lower. Under these circumstances, it is thought that the catalyst particle not only elongates but also breaks due to the existence of compressive stress [35]. It is noted that the elongation is necessary, as it would then give the rod-like particles, before and after the separation of the same diameter. If the initial particle mass is high enough, multiple separations would occur.

Step 4: CNT branching after the catalyst separation.

As a catalyst particle separates into two or more, branching of CNT occurs. In other words, one more CNT grows from the additional catalyst due to the particle's separation into two. It is noted that although the initial growth of CNT follows the tip-growth model, a catalyst may be trapped inside a CNT during or after the branching as shown in Figure 2.17.

Step 5: Lengthening of individual CNT stems ceases.

As a stem collides with the surface of another catalyst or alternatively if there is lack of supply of the hydrocarbons its growth terminates. The growth could also be terminated by the presence of defect sites in the quartz tube.

Step 6: Thickening of CNT.

After a CNT stem ceases to grow thickening may take place, depending on the hydrocarbon concentration. Therefore the higher the hydrocarbon concentration is, the larger the diameter is, as mentioned above. We have varied the hydrocarbon concentration and we have found that this is indeed true. We could get a variety of uniform diameters starting from a particular concentration of the hydrocarbon source.

The above mechanism is not without flaws. However, all the arguments are supported by the experimental observations and reasonable assumptions.

2.4.2 Y-junction nanotubes and single-walled nanotubes by precursor pyrolysis in the presence of water vapour

The products collected from the pyrolysis of ferrocene-water-ethylene-thiophene mixtures by procedure (i) showed distinct differences in the inlet and outlet regions. Thus, the inlet regions showed the presence of Y-junction MWNTs, whereas the outlet regions contained considerable quantities of SWNTs. Shown in Figure 2.18 (a) is a TEM image of the Y-junction MWNT obtained by using ethylene-thiophene mixture. The corresponding high resolution electron microscope image is shown in Figure 2.18 (b). The diameter of the nanotube was ~ 25 nm with the number of graphitic layers being 10-15 in number. The HREM image reveals the presence of the metal catalyst at and near the junction regions. In contrast to the inlet region, the

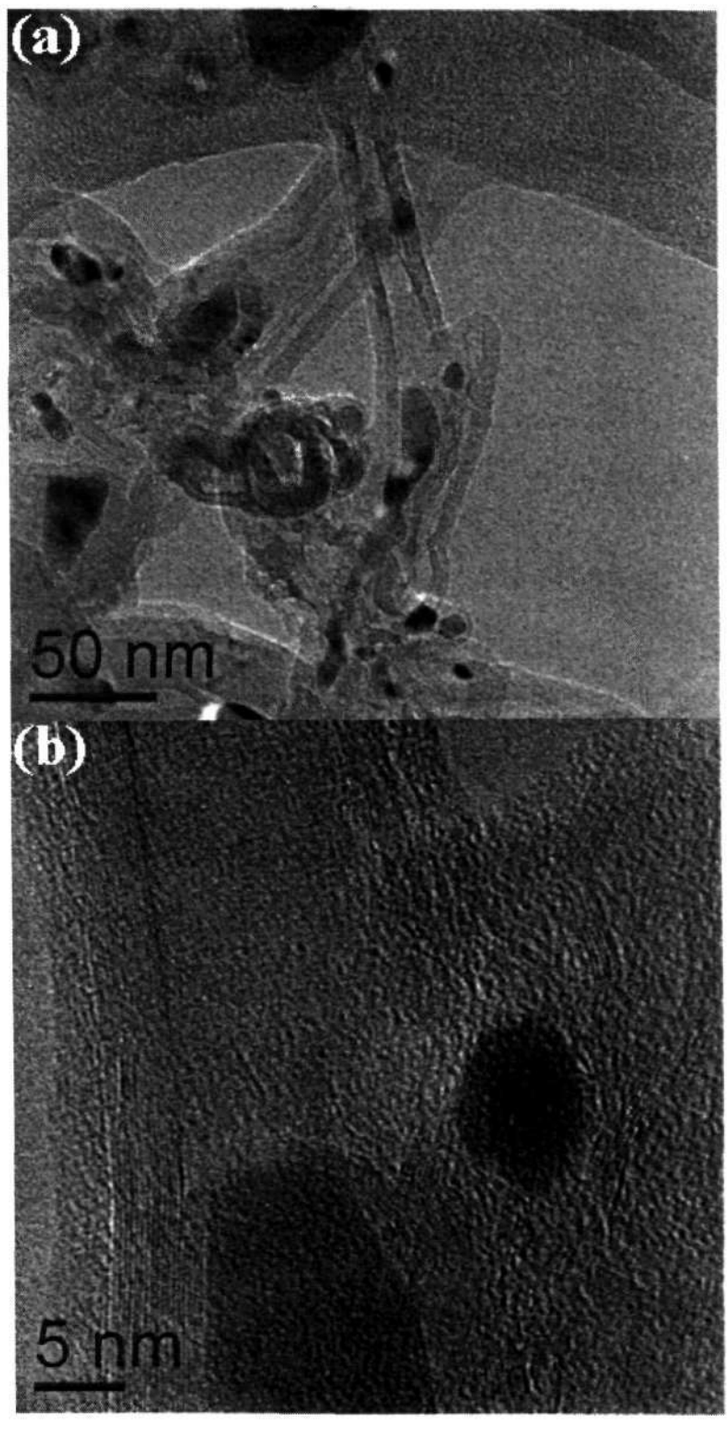

Figure 2.18: (a) and (b) TEM and HREM image of Y-junction nanotube found in the inlet regions obtained by the pyrolysis of ferrocene-water-ethylene-thiophene mixtures (procedure i).

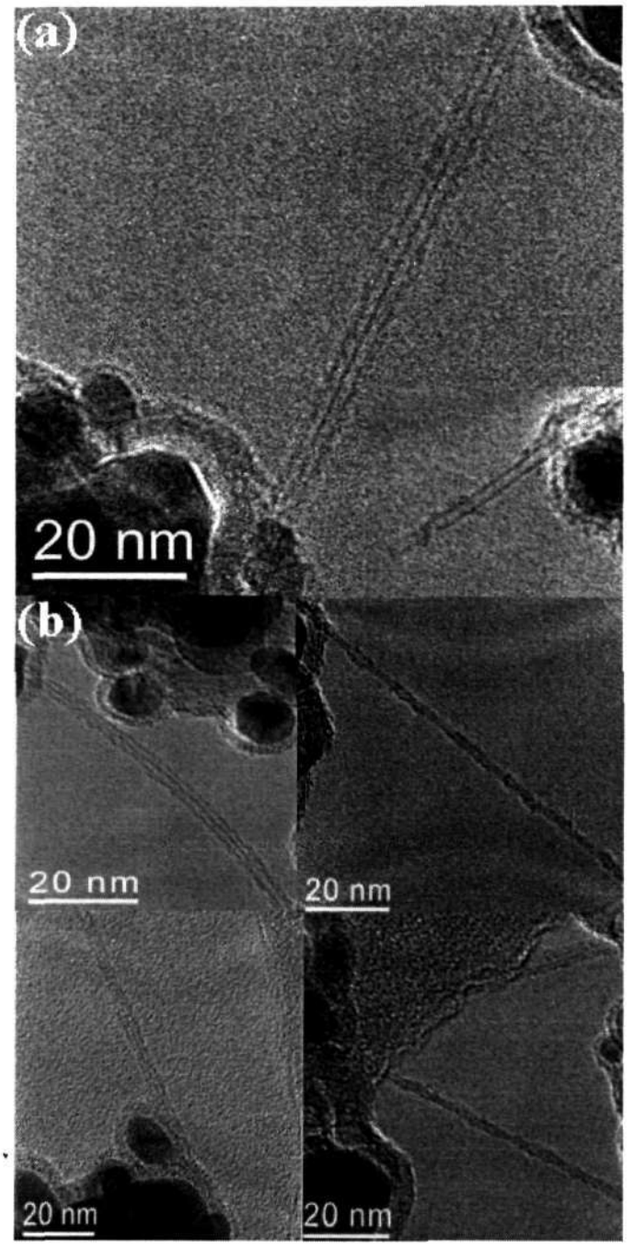

Figure 2.19: (a) TEM images of SWNTs found in the outlet regions obtained by the pyrolysis of ferrocene-water-ethylene-thiophene mixtures (procedure i) and (b) TEM images of SWNTs found in the outlet regions (procedure i, using acetylene instead of ethylene.

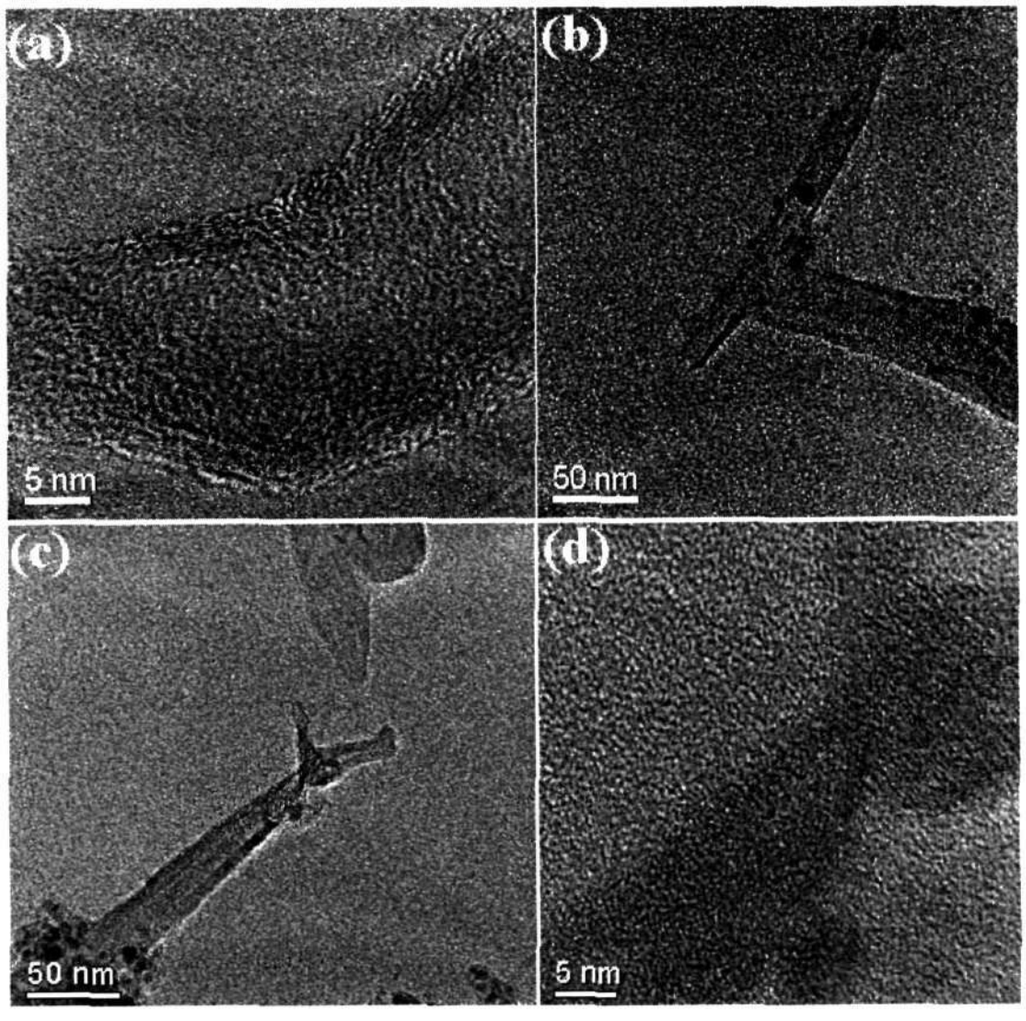

Figure 2.20: HREM images of MWNTs obtained by the pyrolysis of ferrocene - thiophene mixtures: (a) image of MWNT with a bend or a kink, (b) and (c) TEM images of T-junction and Y- junction nanotubes, (d) HREM image of the Y-junction CNT shown in (c). (procedure ii).

outlet region contained copious quantities of SWNTs. Isolated SWNTs were present besides smaller bundles. We show the TEM images of isolated SWNTs in Figure 2.19 (a). In Figure 2.19 (b), we show TEM images of SWNTs obtained at the outlet regions when acetylene-thiophene mixture was used.

In contrast to procedure (i), the pyrolysis of the ferrocene-thiophene mixtures in the absence of water vapor, by procedure (ii), showed the presence of MWNTs with kinks and junctions. In Figure 2.20 (a) we show a HREM image of a MWNT possessing around 6-10 graphitic layers obtained at the inlet. The diameter of the nanotubes were about 15-25 nm. In the outlet region MWNTs with T- and Y-junctions were found as revealed in the TEM images of Figures 2.20 (b) and (c). An examination of the HREM image (Figure 2.20 (d)) reveals that the nanotube has only 6 - 10 graphitic layers, unlike in earlier preparations where the number of graphitic layers of the junction nanotubes was rather large.

2.4.3 STM studies of Y-junction nanotubes

Undoped Y-junction CNTs:

Typical results from the STM measurements on the Y-junction carbon nanotubes are shown in Figure 2.21. The image in Figure 2.21 (a) shows nanotubes with multiple junctions named J_A, J_B, J_C and J_D, where J_A and J_C are terminal junctions and J_B and J_D are junctions in the middle segments of the nanotubes. A high resolution image of junction J_A, given in the inset, suggests the possible presence of five and eight membered rings near the junction region along with the six membered rings. This is in accordance with the understanding of the structure of junctions in carbon nanotubes, wherein the introduction of 5-membered, 7-membered or 8-membered

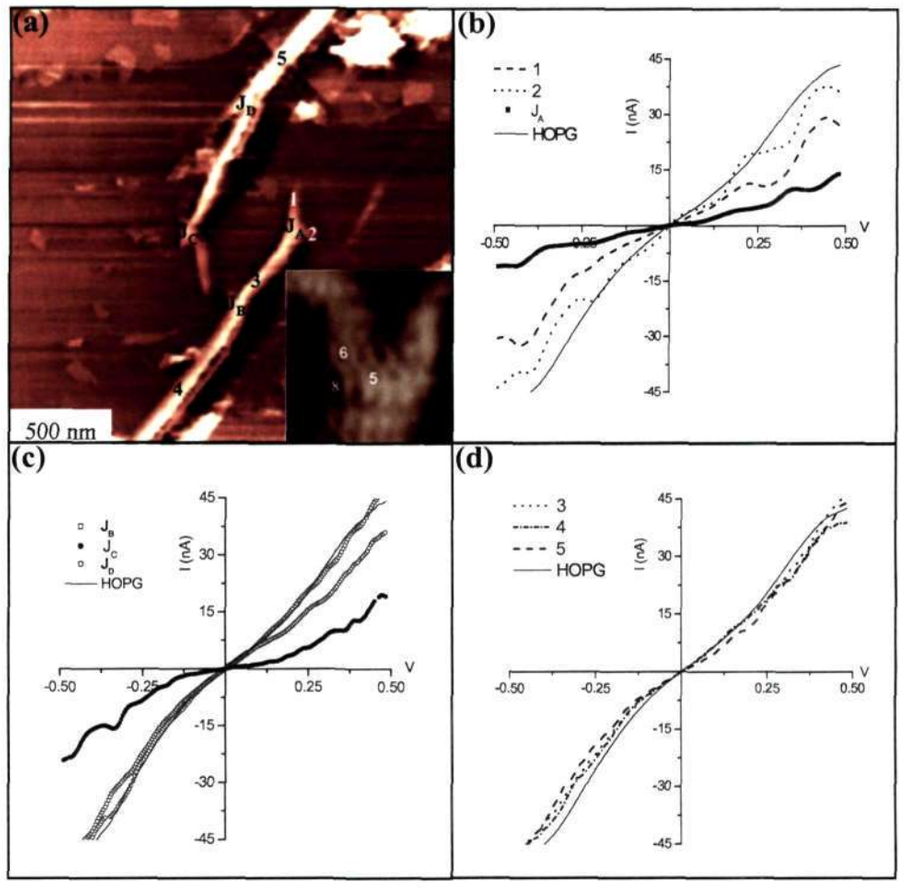

Figure 2.21: (a) STM image of undoped carbon nanotubes with multiple junctions. Inset gives a close-up image revealing a five-membered ring (pentagon), and an eight-membered ring (octagon) at the junction region along with many six-membered rings (hexagons) as marked in the figure. (b)-(d) I-V data from the regions marked in (a).

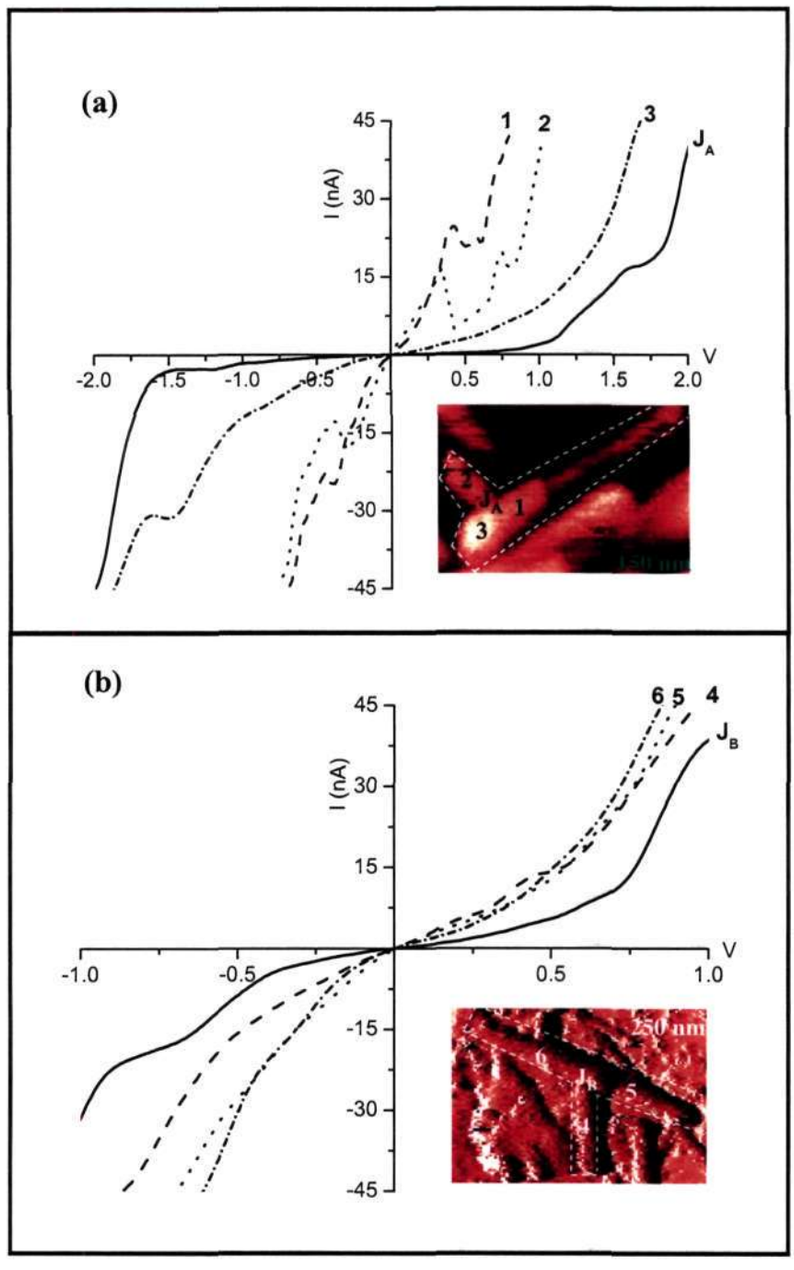

Figure 2.22: I-V data of N-doped Y-junction carbon nanotubes shown along with the STM images. The regions where the I-V data were collected are marked with numbers.

rings in an otherwise hexagonal framework is responsible for formation of the junctions. The I-V data collected by positioning the tip over junction J_A exhibits an overall reduction in the current as compared to the HOPG substrate, with steps in the current at ± 0.2 and ± 0.4 V (Figure 2.21 (b)), perhaps due to incremental charging. The low current flat region enclosed by the first step (± 0.2 V) corresponds to coulomb blockade at the junction. The curve is also somewhat asymmetric with a rectification ratio (which is the ratio of the forward and reverse currents at a given bias) of 1.3 at ± 0.5 V. The data collected from the side arms 1 and 2 showed an overall increase in the current with prominent jumps at similar bias values. The terminal junction J_C exhibits a rectifying behavior similar to J_A (see Figure 2.21 (c)) while the interior junctions J_B and J_D show I-V characteristics comparable to those of the graphite substrate. This is also true of the regions-3, 4, 5 (Figure 2.21 (d)) along the length of the tubes, a behavior characteristic of metallic nanotubes. What is noteworthy is the rectification behavior of the terminal junctions J_A and J_C.

N-doped Y-junction CNTs:

We have carried out tunneling conductance measurements on a large number of N-doped Y-junction carbon nanotubes. The junction (J_A) in Figure 2.22 (a) exhibits a rectification behavior with distinct change of slope in the I-V data at -1.5 V and + 1 V. A high value of rectification ratio of 4.75 is obtained for bias voltages of ± 1.5 V. Coulomb blockade is easily identifiable in the bias range, - 0.4 V to + 0.6 V. The arms of the tube, however, are devoid of blockade but exhibit varied behavior. The arm-1 shows distinct features at ± 0.4 V. In the case of arm-2, similar features are seen at a slightly lower bias of ± 0.3 V. It also exhibits an additional feature in the positive bias region at 0.75 V. The I-V data for arm-3 shows a feature around – 1.5 V. While the

distinct spectroscopic features corresponding to regions with negative differential resistance would arise from charging or other effects, the occurrence of a wide blockade region at the tube junction is noteworthy. Figure 2.22 (b) shows a nanotube with junction J_B, bearing a low-current flat region in the I-V data, from -0.4 to + 0.75 V, indicative of a rectification behavior, similar to J_A shown in Figure 2.22 (a). The rectification ratio in this case is 1.21 at ± 1.0 V. The I-V curves from the arms (regions 4,5 and 6) are somewhat asymmetric across zero bias, but do not exhibit any blockade.

2.5 Conclusions

Although arc evaporation of graphite has traditionally been found to yield both single-walled and multiwalled carbon nanotubes, the pyrolysis of organometallic precursors with or with out the presence of additional carbon sources seems to provide a direct and effective method of producing nanotubes of various kinds. A particularly important finding is the synthesis of Y-junction nanotubes which cannot be made by arc evaporation or other methods easily. It is also noteworthy that nanotubes produced by organometallic precursors may also find applications in field emission and hydrogen storage. In the case of the Y-junction CNTs a detailed study of the pyrolysis of various organometallics with sulfur containing compounds has shown that pyrolysis of thiophene with metallocenes yields excellent Y-junction nanotubes. Pyrolysis of thiophene with Fe- or Ni-phthalocyanines yields N-doped Y-junction nanotubes. While the pyrolysis of nickelocene with CS_2 yields similar junctions, the yield and quality of the nanotubes is not satisfactory. Similarly, pyrolysis of thiophene and iron pentacarbonyl does not yield sufficient quantities of Y-junction nanotubes.

Y-junction carbon nanotubes prepared by the pyrolysis of metallocene-thiophene and Ni- or Fe-phthalocyanine-thiophene mixtures do not contain sulfur at the junction but consist entirely of carbon or carbon and nitrogen, suggesting the presence of five-, seven-, or eight- membered rings at the junction.

Pyrolysis of thiophene over a Ni/SiO_2 catalyst provides a good alternative procedure to the metallocene route. This method may be useful to tune the diameter of the junction nanotubes suitably by varying the proportion of the nickel catalyst supported over silica. A narrow diameter distribution of the junction nanotubes has been obtained by this method, unlike the case of the pyrolysis of thiophene with organometallic precursors. The use of a catalyst is also less expensive and is probably preferable.

Pyrolysis of hydrocarbon-organometallic mixtures in the presence of water vapor seems to favor the formation of SWNTs. MWNTS with junctions are obtained as additional products in the synthesis. The junction nanotubes so obtained have reduced number of graphitic layers. The observation of T-junction nanotubes by this method is significant, since they have not been observed by this method earlier.

STM investigations show that rectification behavior at the junction is a fairly general feature, although it is more prominent in the N-doped CNTs. In addition, some of the junction nanotubes show coulomb blockade and features of NDR (negative differential resistance) as well.

2.6 References

[1] M. Jose-Yacaman, M. Miki-Yoshida, L. Rendon, T. G. Santiesteban, *Appl. Phys. Lett.*, 1993, **62**, 202.

[2] V. Ivanov, J. B. Nagy, Ph. Lambin, A. Lucas, X. B. Zhang, X. F. Zhang, D. Bernaerts, G. Van Tendeloo, S. Amelinckx, J. Van Landuyt, *Chem. Phys. Lett.*, 1994, **223**, 329.

[3] K. Hernadi, A. Fonseca, J. B. Nagy, D. Bernaerts, J. Riga, A. Lucas, *Synth. Met.*, 1996, **77**, 31.

[4] N. M. Rodriguez, *J. Mater. Res.*, 1993, **8**, 3233.

[5] R. Sen, A. Govindaraj, C. N. R. Rao, *Chem. Phys. Lett.*, 1997, **267**, 276.

[6] R. Sen, A. Govindaraj, C. N. R. Rao, *Chem. Mater.*, 1997, **9**, 2078.

[7] (a) M. Menon, D. Srivatsava, *Phys. Rev. Lett.*, 1997, **79**, 4453, (b) M. Menon, D. Srivatsava, *J. Mater. Res.*, 1998, **13**, 2357.

[8] P. G. Collins, A. Zettl, H. Bando, A. Thess, R. E. Smalley, *Science*, 1997, **278**, 100.

[9] L. Chico, V. H. Crespi, L. X. Benedict, S. G. Louie, M. L. Cohen, *Phys. Rev. Lett.*, 1996, **76**, 971.

[10] L. Kouwenhoven, *Science*, 1997, **275**, 1896.

[11] P. L. McEuen, Nature, 1998, **393**, 494.

[12] M. S. Fuhrer, J. Nygard, L. Shih, M. Forero, Y. G. Yoon, M. S. C. Mazzoni, H. J. Choi, J. Ihm, S. G. Louie, A. Zettl, P. L. McEuen, *Science*, 1998, **288**, 494.

[13] J. Li, C. Papadopoulos, J. Xu, *Nature*, 1999, **402**, 254.

[14] B. C. Satishkumar, P. J. Thomas, A. Govindaraj, C. N. R. Rao, *Appl. Phys.*

Lett., 2000, **77**, 2530.

[15] (a) B. Gan, J. Ahn, Q. Zhang, Rusli, S. F.Yoon, J. Yu, Q. -F. Huang, K. Chew, V. A. Ligatchev, X. -B. Zhang, W. -Z. Li, *Chem. Phys. Lett.*, 2001, **333**, 23, (b) B. Gan, J. Ahn, Q. Zhang, Q. F. -Huang, C. Kerlit, S. F. Yoon, Rusli, V. A. Ligachev, X. -B. Zhang, W. Z. Li, *Mater. Lett.*, 2000, **45**, 315.

[16] W. Z. Li, J. G. Wen, Z. F. Ren, *Appl. Phys. Lett.*, 2001, **79**, 1879.

[17] C. Papadopoulos, A. Raitkin, J. Li, A. S. Vedeneev, J. M. Xu, *Phys. Rev. Lett.*, 2000, **85**, 3476.

[18] C. Papadopoulos, A. J. Jin, J. M. Xu, *Appl. Phys. Lett.*, 2004, **85**, 1769.

[19] K. Esfarjani, A. A. Farajian, Y. Hashi, Y. Kawazoe, *Appl. Phys. Lett.*, 1999, **74**, 79.

[20] A. A. Farajian, K. Esfarjani, Y. Kawazoe, *Phys. Rev. Lett.*, 1999, **82**, 5084.

[21] C. Zhou, J. Kong, E. Yenilmez, H. Dai, *Science*, 2002, **290**, 1552.

[22] S. Amelinckx, A. Lucas, P. Lambin, *Rep. Prog. Phys.*, 1999, **62**, 1471.

[23] B. Gan, J. Ahn, Q. Zhang, S. F. Yoon, Rusli, Q.-F. Huang, H. Yang, M.-B. Yu, W.- Z. Li, *Diamond and Related Mat.*, 2000, **9**, 897.

[24] J. Liu, M. Shao, X. Chen, W. Yu, X. Liu, Y. Qian, *J. Am. Chem. Soc.*, 2003, **125**, 8088.

[25] J. Liu, L. Xu, W. Zhang, W. J. Lin, X. Chen, Z. Wang, Y. Qian, *J. Phys. Chem. B.*, 2004, **108**, 20090.

[26] R. Sen, B. C. Satishkumar, A. Govindaraj, K. R. Harikumar, G. Raina, J -P. Zhang, A. K. Cheetham, C. N. R. Rao, *Chem. Phys. Lett.*, 1998, **287**, 671.

[27] M. Yudasaka, R. Kikuchi, Y. Ohki, S. Yoshimura, *Carbon*, 1997, **35**, 195.

[28] D. C. Li, L. Dai, S. Huang, A. W. H. Mac, Z. L. Wang, *Chem. Phys. Lett.*, 2000, **316**, 349.

[29] Y. Zhang, A. Chang, J. Cao, Q. Wang, W. Kim, Y. Li, N. Morris, E. Yenilmez, J. Kong, H. Dai, *Appl. Phys. Lett.*, 2001, **79**, 3155.

[30] M. Tanemura, K. Iwata, K. Takahashi, Y. Fujimoto, F. Okuyama, H. Sugie, V. Filip, *J. Appl. Phys.*, 2001, **90**, 1529.

[31] V. I. Merkulov, A. V. Melechko, M. A. Guillorm, D. H. Lowndes, M. L. Simpson, *Appl. Phys. Lett.*, 2001, **79**, 2970.

[32] D. L. Smith, *Thin-film deposition.*, New York, NY: Mc Graw Hill; 1995, **370**, 307-370.

Chapter 3

Synthesis and characterization of MgO, Al_2O_3, SiO_2 and In_2O_3 nanowires

Summary*

In this chapter, the synthesis of nanostructures of MgO, Al_2O_3, SiO_2 and In_2O_3 by the carbothermal method (carbon-assisted synthesis) and their characterization are presented. MgO nanowires and related nanostructures have been prepared starting from polycrystalline MgO or Mg without the use of metal catalysts. The study has been carried out with different sources of carbon. It has been possible to obtain nanotrees and other interesting nanostructures of MgO, besides aligned nanowires by carrying out the reaction over Au-coated Si substrates. A vapor–solid mechanism of one-dimensional growth seems to be operative in the reactions carried out in bulk, but a vapor–liquid–solid mechanism applies when Au-coated Si substrates were used.

Nanostructures of Al_2O_3 including nanowires and nanotubes have been synthesized by the reaction of Al metal with carbon (active carbon or graphite). The Al_2O_3 nanostructures thus obtained have been characterized by X-ray diffraction, electron microscopy and photoluminescence spectroscopy. These nanostructures are likely to be of use as catalyst supports and in other technological applications.

* Papers based on these studies have appeared in Mater. Res. Bull. (2005), Topics in Cat. (2003), J. Mater. Res. (2004), and Chem. Phys. Lett. (2004), (2005).

SiO_2 (α-cristobalite) nanowires of 50–100 nm diameter with lengths of several microns have been synthesized for the first time by the solid-state reaction of fumed silica and activated charcoal. The nanowires have been characterized by X-ray diffraction, electron microscopy, photoluminescence, and Raman scattering. The nanowires are single-crystalline as revealed by high-resolution electron microscope images. The crystalline nanowires are clad by an amorphous silica sheath when the carbon to fumed silica ratio in the starting mixture is small. Use of hydrogen along with Ar helps to eliminate the amorphous sheath.

In_2O_3 nanowires have been prepared starting from In_2O_3 or In metal along with carbon. The nanowires have been characterized by X-ray diffraction, electron microscopy and photoluminescence spectroscopy. The nanowires are single crystalline and grow in the (100) direction, as established by high resolution electron microscopy. When a mixture of In_2O_3 and carbon was used as the starting material, nanowires were obtained along with nanotrees and nanobouquets. The observation of these nanostructures indicates that the growth of the nanowires occurs by the vapor–liquid–solid mechanism. Starting with In metal, only the oxide nanowires were obtained.

Dispersions of the nanowires of Al_2O_3, MgO and ZnO in dimethylformamide (DMF), dimethylsulfoxide (DMSO) and acetonitrile have been studied by electron microscopy and PL spectroscopy, and by examining their sedimentation behavior. Stable nanowire dispersions were best obtained in DMF. The best PL spectra of the nanowires were also generally obtained with DMF dispersions.

3.1 Introduction

Inorganic nanowires and nanorods have been synthesized by a variety of methods, including physical evaporation, laser ablation, chemical vapor deposition and solvothermal reactions [1]. The mechanism of formation of many of these nanostructures involves a vapor-solid (VS) or vapor-liquid-solid (VLS) growth process. Compared to the methods mentioned above, one of the simplest methods of synthesis of inorganic nanowires that has emerged in the last two to three years employs the carbothermal route [2]. The presence of carbon during the synthesis has been reported to favor the formation of nanowires (NWs) of metal oxides and other materials. Accordingly, crystalline nanowires of metal oxides such Ga_2O_3 and ZnO [3], nitrides such as Si_3N_4 and carbides such as SiC [4], as well as of elemental Si, have been prepared successfully under carbothermal conditions. The method essentially involves heating a metal oxide with an adequate quantity of carbon in an appropriate atmosphere (Scheme 1). For example, ammonia provides the atmosphere for the formation of nitrides. An inert atmosphere and a slight excess of carbon yield carbides. In these reactions, carbon helps to form an oxidic species, usually a sub-oxide, in the vapor phase, which then transforms to the final crystalline product. In view of the simplicity of the process we have been interested in the synthesis of nanowires of MgO, Al_2O_3, SiO_2 and In_2O_3 by this route. Dispersion of oxide nanowires of Al_2O_3, MgO and ZnO in various polar solvents have been investigated. This has been done to identify the solvent best suited for obtaining stable nanowire dispersions, suitable for a variety of applications that may not be otherwise accessible, if the nanowires are in the solid state.

Scheme 1: VS mechanism involved in the growth of metal oxide NWs

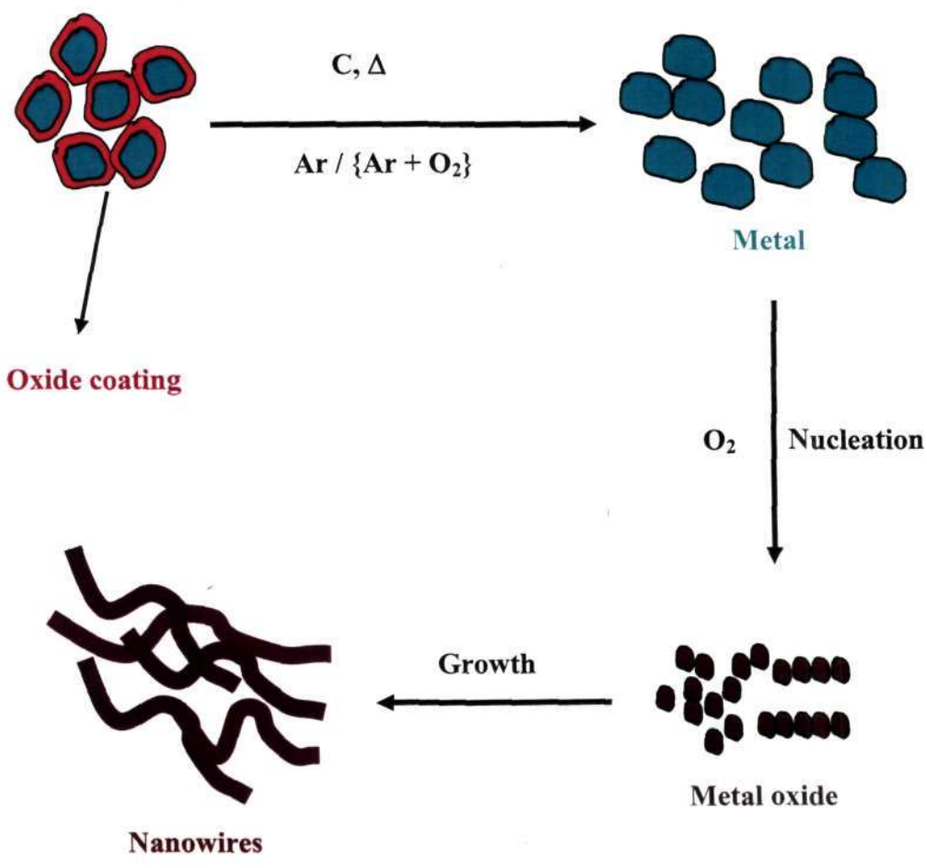

3.2 Scope of the present investigations

MgO

MgO is a wide band gap insulator, showing high secondary electron emission yield [5]. MgO has the well known cubic rock salt structure [6] (Figure 3.1).

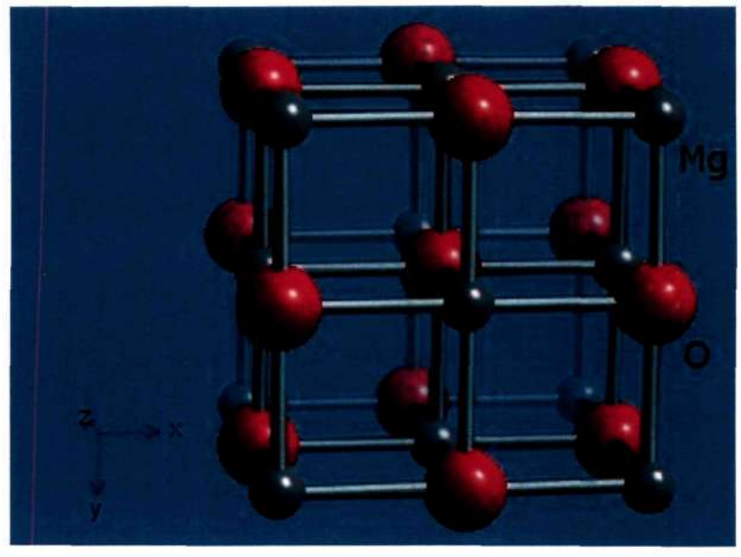

Figure 3.1: Structure of MgO.

One-dimensional nanostructures of MgO have attracted some attention because of their unique ability to pin the magnetic flux lines within a high temperature superconductor [7]. The MgO nanorods in this case were obtained starting with a mixture of MgO powder and graphite; but their investigation was neither focused on the growth of these nanorods under different experimental conditions, nor using different sources of carbon. Due to their appreciable strength, high melting point and low density, MgO whiskers find suitable applications in spaceflight and other

composite materials [8]. Several methods of synthesis of MgO nanostructures have been reported in literature. Thus, Zhu *et al.* [9] have prepared MgO fishbone fractal nanostructures by selective Co-catalyzed growth. Starting with a halide source, MgO nanorods [10] and nanobelts have been prepared [11]. Li *et al.* [12] have reported the preparation of network-like MgO nanostructures on a Si substrate by the CVD process using IR radiation to heat a Mg/Al target under vacuum. MgO nanowires have been prepared by the direct heating of Mg in oxygen [13] as well as by oxide-assisted growth using B_2O_3 powder [14]. Yin *et al.* [15] have achieved this through a vapor-phase precursor method, starting with MgB_2 powder. Nanobelts of MgO have been prepared by thermal evaporation of Mg powder [16] as well as by starting with Mg_3N_2 [17]. The synthesis of two- and three-dimensional MgO nanostructures as well as networked rectangular MgO nanostructures has been reported [18]. Multi-dimensional MgO nanostructures with cone-shaped branching have been reported recently [19]. The synthesis of MgO and Ga-filled MgO nanotubes has also been reported, where carbon was used to reduce Ga_2O_3 to obtain metallic Ga which then catalyzed the formation of MgO nanotubes [20,21]. In the above synthetic procedures, carbon has not been effectively looked into, specially in the absence of additional catalysts like B/Si powder [22], nor has carbon been employed as a reactant as in carbon-assisted syntheses of metal oxide nanowires. We have, therefore, investigated the carbon-assisted synthesis of MgO nanowires and related nanostructures, by varying the source of carbon and other reaction conditions. We have employed polycrystalline MgO as well as Mg as the starting material, and not used any catalyst other than carbon in the synthesis. In addition to the use of carbon we have also used gold-coated Si substrates to obtain aligned nanowires.

Al_2O_3

Aluminium oxide (Al_2O_3), also known as corundum [6], has a rhombohedral structure (Figure 3.2). It has mechanical and physical properties particularly suitable for electrical and thermal insulation, for cutting tools and abrasives. It also has very good anti-corrosion properties. Aluminium oxide is commonly used as an adsorbent or as a catalyst support in many chemical processes, including cracking, hydrocracking and hydrodesulfurization of petroleum feedstocks. Porous alumina has been used as a template for the synthesis of carbon nanotubes [23].

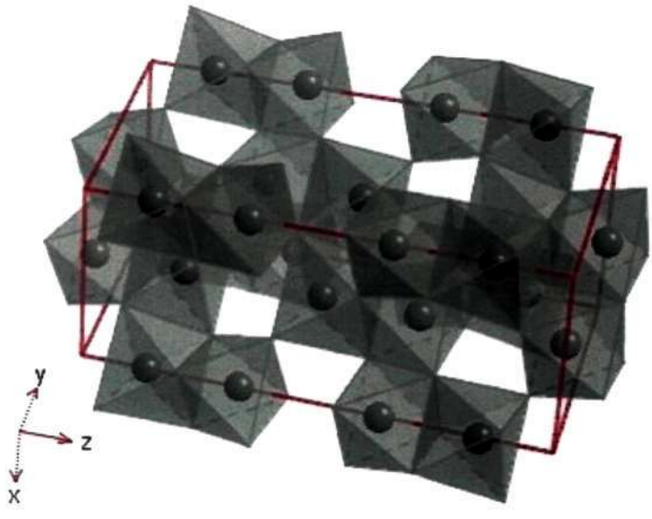

Figure 3.2: Structure of Al_2O_3.

Nanotubes and nanowires of Al_2O_3 are of interest for their one-dimensional behavior and related applications. In the last few years, there has been considerable effort to synthesize nanostructures of alumina by employing various strategies. Mesostructured forms of γ-Al_2O_3 have been prepared by the use of a

suitable precursor or a surfactant such as aluminium hydrate with poly(ethylene oxide) [24,25]. Hollow alumina macrotubes were obtained by heating partially hydrolyzed $AlCl_3$ powder [26]. Alumina whiskers with aspect ratios and the mean diameters in the ranges of 10-40 and 2-4 nm respectively are formed during the preparation of ultrafine spherical alumina powders [27]. Nanotubes and nanowires of Al_2O_3 have been prepared using carbon nanotubes (CNTs) as templates or by heating a mixture of Al and Al_2O_3 powders covered with CNTs [28,29]. Electrochemical anodic processes are employed for the synthesis of linear and branched alumina nanotubes [30-32] while ordered arrays of alumina nanotubes and nanowires or nanopillars are obtained by etching porous alumina membranes [33,34]. Single-crystal Al_2O_3 fibers and nanowires are obtained by placing an aluminium piece over a shallow bed of SiO_2 containing catalysts like Fe_2O_3 [35,36]. Synthesis of novel 1-D forms of Al_2O_3 such as nanotrees and nanobelts starting from Al powders have been reported [37,38]. Hydrothermal synthesis of unidirectional alumina nanostructures involving the use of a surfactant has been reported by Lee *et al.* [39]. We have been exploring simple ways to prepare Al_2O_3 nanowires and nanotubes by employing carbothermal procedures wherein graphite or active carbon is one of the reactants. We have indeed succeeded in obtaining nanowires and nanotubes of Al_2O_3, starting with Al powder and graphite or active carbon.

SiO_2

Among the various one-dimensional inorganic nanostructures, much attention has been devoted to the synthesis of nanotubes and nanowires of silica [40-42]. Using molten Ga as the catalyst, the vapor–liquid–solid process has been used to obtain

aligned silica nanowires [43,44]. Use of other catalysts such as Sn also yields densely aligned silica nanowires by a similar process [45]. Other methods for the synthesis include the laser ablation of a mixture of Si, SiO_2, and Fe [46], thermal oxidation of Si wafers [47], and the oxidation of Si vapor catalyzed by Au [48]. Thermal treatment of Si powder with graphite is also found to yield silica nanowires [49]. A recent report employs the solid-state transformation of silica films to obtain silica nanowires [50]. The transformation of silica nanowires to nanotubes has also been examined [51]. In all the preparations reported previously, the silica nanowires obtained are amorphous, showing intense blue luminescence. We were interested in exploring the possibility of producing crystalline silica nanowires, which might find useful applications in optical data transmission, in areas related to low thermal expansion, as a refractory and in composites. Besides, it would be interesting to establish the exact conditions under which they form. For this purpose, we have used the carbon-assisted process. By this method we have been able to synthesize single crystalline α-cristobalite nanowires for the first time. Shown in Figure 3.3 is the structure of α-cristobalite which is one of the polymorphs of SiO_2 [6].

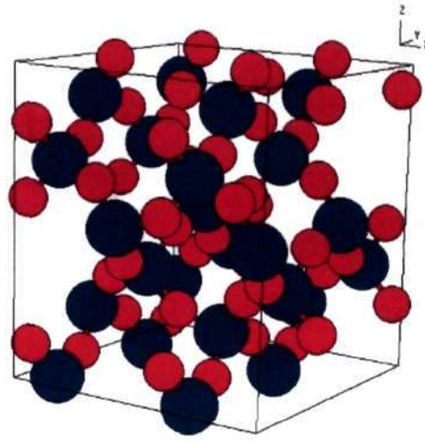

Figure 3.3: Structure of silica (α-cristobalite).

In_2O_3

In_2O_3 is an important oxide, being a wide band-gap semiconductor material (~ 3.6 eV). In_2O_3 has a cubic *c*-type rare earth oxide (Ia3, bixbyite) structure [6] (Figure 3.4). It is widely used in microelectronic applications including window heaters, solar cells and displays. Nanowires of In_2O_3 have potential applications as field effect transistors and as chemical sensors for the detection of NO_2 and NH_3 [52,53]. In_2O_3 fibers have been prepared by thermal evaporation-oxidation of an InP substrate [54]. Porous alumina membranes have been used to deposit In metal nanowires, which are subsequently oxidized to obtain In_2O_3 nanowires [55]. In_2O_3 nanowires can be obtained by the direct oxidation of In metal granules by the vapor-solid process [56]. Laser ablation of an In target in the presence of Au films or clusters also yields In_2O_3 nanowires [57]. Vapor transport-condensation processing of In_2O_3 on Au-coated SiO_2/Si substrates has been used to generate In_2O_3 nanowires [58].

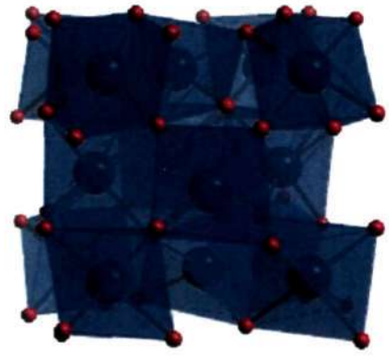

Figure 3.4: Structure of In_2O_3.

We have employed the carbon-assisted synthesis to prepare In_2O_3 nanowires starting from the oxide as well as In metal. More importantly, we have obtained interesting TEM images, which reveal two distinct mechanisms of formation of the In_2O_3 nanowires, depending on the starting material.

Dispersion of oxide nanowires in polar solvents

Smalley *et al.* [59] reported a successful method to prepare stable aqueous suspensions of single-walled carbon nanotubes (SWNTs) by employing sodium dodecylsulfate as the surfactant. The separation of metallic from semiconducting SWNTs via ac dielectrophoresis has been achieved starting from a suspension of SWNTs in D_2O containing 1 weight % of the surfactant SDS [60]. Spectrofluorimetric measurements on SWNTs isolated in aqueous surfactant suspensions have revealed distinct electronic absorption and emission transitions [61]. Solubilization of carbon nanotubes in non-aqueous solvents by functionalization has also been reported [62]. Efforts on the functionalization and solubilization of carbon nanotubes have enabled the exploitation of some of the properties and applications, not accessible otherwise in the solid state. In addition to this, dispersions of carbon nanotubes in polymeric nanocomposites have also been achieved [63]. Apart from the carbon nanotubes, the functionalization and solubilization of boron nitride nanotubes has been accomplished [64]. Interest in such studies has expanded to other 1-D systems as well. For example, the solubility of the $Mo_6S_{4.5}I_{4.5}$ nanowires in common solvents has been investigated recently [65,66]. Apart from this work the solubility and dispersion of inorganic nanowires is relatively unexplored. In this context, it is to be noted that oxide nanostructures are generally dispersed in polar solvents such as dimethylformamide (DMF) and dimethylsulfoxide (DMSO) in optical tweezing and

other experiments [67]. We have examined the dispersions of Al_2O_3, ZnO and MgO nanowires in DMF, DMSO and acetonitrile. For this purpose, we have examined the sedimentation behavior of the oxide nanowires in the polar solvents, and studied the photoluminescence spectra of the dispersions.

3.3 Experimental

3.3.1 Synthesis

The setup employed for the synthesis of oxide nanowires is shown in Figure 3.5. It consists of stainless steel gas flow lines and a furnace fitted with quartz or alumina tube (25 mm i.d.). The flow rate of the gas is crucial for the formation of the nanowires and is controlled by means of mass flow controllers. The reaction is carried out by placing the starting material (metal/metal oxide) taken in a suitable boat and placing it at the center of the furnace and heating it to a pre-set temperature by means of a temperature controller in a flowing gas. The exact details of the various reactions are described subsequently.

Synthesis of MgO nanowires and related nanostructures

Five different procedures were employed for the synthesis of MgO nanostructures. In procedure 1(a), activated carbon, prepared by the thermal decomposition of polyethylene glycol (600 units) at 800 °C in an Ar atmosphere, for 5 h [68], was mixed with MgO powder in a molar ratio (carbon:MgO) of 1:1 and ground well to get a fine powder. This mixture was placed in an alumina boat and heated in an alumina tube at 1300 °C (3 °C/min) for 5 h in an Ar atmosphere (50 standard cubic centimeter per minute, sccm). The above reaction was carried out in a

quartz boat, starting with Mg powder at 850 °C, procedure l(b). In procedure 2(a) charcoal (Sarabhai Chemicals, India), which was activated by heating in a mixture of H_2 / He at 700 °C for 5 h, was mixed with MgO powder in the molar ratio 1:1. The rest of the procedure was the same as in procedure l(a). In procedure 2(b), Mg powder was used instead of MgO. Graphite powder was used as yet another source of carbon in procedure 3. The reaction conditions were the same as in procedures 1 and 2. In procedure 3(a), graphite was mixed with MgO powder in the molar ratio 1:0.6 and placed in an alumina boat. In procedure 3(b), Mg powder was taken instead of MgO, ground with graphite powder in the ratio 1:1 and the reaction carried out in a quartz boat. In procedure 4(a) the reaction was carried out with multiwalled carbon nanotubes (MWNTs) as the carbon source, mixing them with MgO powder in the molar ratio (MWNTs:MgO) 1:0.6. In procedure 4(b) Mg powder was taken with MWNTs in a quartz boat. The MWNTs that were used in the reaction were prepared by the arc-discharge method [69]. In procedure 5, a gold-coated Si substrate was placed on top of the reaction mixture and the reaction carried out at 800 °C for 5 h in an Ar atmosphere (50 sccm). In procedure 5(a), the reaction mixture contained MgO and activated carbon (molar ratio of activated carbon:MgO being 0.5:1), while in procedures 5(b) and 5(c), graphite powder was used with MgO and Mg powders, respectively, in the molar ratio (graphite:MgO/Mg) 0.5:1. The products obtained in all the above reactions were white in colour.

Synthesis of Al_2O_3 nanowires and nanotubes

Al_2O_3 nanowires and nanotubes were synthesized by the carbothermal procedure involving the use of a mixture of Al and graphite or active carbon powders. In procedure (i), a finely ground intimate mixture of Al and graphite

powders (molar ratio 1:1) was placed in an alumina boat kept and heated under the flow of Ar (50 sccm) and oxygen (10 sccm). The temperature was maintained at 1300 °C for 6 h. In procedure (ii), the above reaction mixture was heated under Ar (50 sccm) using a zirconia boat. The oxygen flow was not mandatory as it is expected that the formation of Al_2O_3 can result from Al and graphite powders.

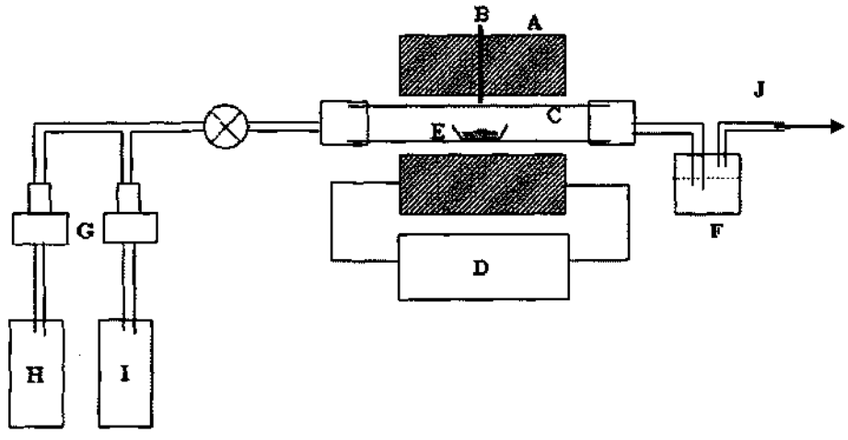

A – Programmable furnace, B – Thermocouple,
C – Alumina/quartz tube, D – Temperature controller
E – Boat containing sample, F – Paraffin bubbler
G – Mass flow controllers, H – Oxygen cylinder
I – Argon cylinder, J - Outlet

Figure 3.5: Experimental setup for the synthesis of oxide nanowires.

There was a difference in the morphologies of the products obtained by the two procedures not only due to the absence of oxygen atmosphere in (ii), but also as a result of different boats for the reaction. Procedure (iii) involved heating a mixture of Al powder and activated carbon (molar ratio 1:1) in Ar. The activated carbon was prepared by decomposing polyethylene glycol (600 units) in Ar atmosphere at

700 °C for 3h [68]. A finely ground intimate mixture of Al powder with activated carbon was taken in a zirconia boat placed in an alumina tube and heated in Ar (50 sccm) at a temperature of 1200 °C (heating and cooling rates 3 °C/min) for 3 h. The product from each of the procedures was white wool-like, formed on top of the boat or fine grey powders found at the bottom of the boat.

Synthesis of crystalline SiO_2 nanowires

The procedure used for the synthesis of the SiO_2 nanowires was as follows. Fumed silica (Sarabhai Chemicals, India) was thoroughly mixed and ground with activated charcoal (Sarabhai Chemicals, India) heated to 700 °C in flowing H_2/He mixture or with activated carbon prepared by the decomposition of polyethylene glycol-600 units in an Ar atmosphere at 700 °C [68]. The mixture was placed in an alumina boat and heated to 1300 °C (heating and cooling rates, 3 °C/min) for 5 h in flowing Ar (50 sccm) or a mixture of Ar (50 sccm) and H_2 (20 sccm). The relative molar ratio of the carbon source with respect to fumed silica was varied between 0.5 and 2. The final product that was obtained in the alumina boat at the end of the reaction was a white or grey powder.

Synthesis of In_2O_3 nanowires and related nanostructures

In_2O_3 nanowires were prepared by different procedures. In procedure (i), In_2O_3 powder (Aldrich) was mixed with charcoal [(Sarabhai Chemicals, India) activated by heating to 700 °C in flowing H_2 / He mixture] in stoichiometric quantities, taken in an alumina boat and heated in an Ar atmosphere at 1000°C for 5 h (heating and cooling rates 3 °C/min). The molar ratio of activated charcoal with respect to In_2O_3 was varied between 1-3, and the flow rate of Ar was varied between 50-150 sccm.

Graphite powder was also used instead of activated charcoal in this procedure. Accordingly, a mixture of In_2O_3 and graphite powder with a molar ratio of 1:3 was heated in Ar at 1000 °C for 5 h. In procedure (ii), a mixture of In metal powder and activated charcoal with two different molar ratios (1:1 and 1:2) was heated in Ar at 1000 °C for 5 h (heating and cooling rates 3 °C/min, Ar flow rate: 50 sccm). In all the above procedures, reactions were carried out in a mixture of oxygen (10-25 sccm) with Ar. The product, obtained as a spongy yellow powder, was collected in the boat as well as near the cooler end (outlet) of the furnace tube.

Dispersion of oxide nanowires in polar solvents

The Al_2O_3 and MgO nanowires used for this study were prepared by the carbon-assisted synthesis as mentioned above. The synthesis of the ZnO nanowires on the other hand was carried out starting from a mixture of zinc oxide / zinc oxalate and MWNTs or active carbon in Ar atmosphere along with O_2 at 900 °C.

The dispersions of the various oxide nanowires were obtained as follows. A known quantity of the nanowires (32 mg of Al_2O_3 or ZnO nanowires) was dispersed in DMF, DMSO or acetonitrile (30 ml of the solvent individually) and sonicated for 1 h. The dispersion was allowed to stand for about 12 h after which the sediment (sediment-1) that settled down was weighed and collected for scanning electron microscopy (SEM). The remaining dispersion was resonicated and allowed to sediment for 60 h. Thereafter the remaining sediment (sediment-2) was again weighed and collected for SEM. Similarly a drop of the dispersion was taken and deposited on a glass slide and observed under the microscope. SEM observations of the dispersions

were carried out at regular intervals of time to monitor the presence of nanowires in each case (for example 12, 24, 36, 48 and 60 h) (Scheme 2).

Scheme 2: SEM study of Al_2O_3/ZnO nanowires in DMF, DMSO and acetonitrile

Dispersion = 32mg/30 ml

↓

Sonicated for 1 h

↓

allowed to stand for 12 h

↓

Sediment after 12 h (sediment-1)

↓

Remaining dispersion resonicated

and allowed to sediment for 60 h

↓

Decantation to separate sediment (sediment-2)

[SEM was carried out on the starting sample, sediment-1, sediment-2, dispersions at various intervals of time (12, 24, 36, 48, 60 h respectively]

The dispersions of the MgO nanowires were obtained as follows. A known quantity of the nanowire (7 mg) was dispersed in DMF (15 ml) and sonicated for 1 h. This dispersion was allowed to stand during the course of which a drop of the dispersion taken at various intervals of time was deposited onto a copper grid for transmission electron microscopy (TEM). The TEM observations of the dispersions were carried out at regular intervals of time (3, 6, 12, 24, 96 h). Apart from this the

sediment that was obtained at the end of 96 h was also observed by TEM (Scheme 3). The dispersions of the various oxide nanowires in DMF, DMSO and acetonitrile were characterized by PL spectroscopy.

Scheme 3: TEM study of MgO nanowires in DMF

Dispersion = 7mg/15 ml

↓

Sonicated for 1 h

↓

allowed to stand

↓

A drop of the dispersion was added onto the TEM grid for microscopic analysis at various intervals of time (T = 0, 3, 6, 12, 24, 96 h). The sediment collected after 96 h was also observed by TEM.

3.3.2 Characterization

The MgO, Al_2O_3, SiO_2 and In_2O_3 nanostructures obtained by the different procedures were characterized as follows.

X-ray diffraction

Powder X-ray diffraction (XRD) patterns were recorded using CuKα radiation with a Rich-Siefert, XRD–3000-TT diffractometer. Samples were prepared by finely grinding the product and depositing on a glass slide.

Scanning electron microscopy

Scanning Electron Microscopy (SEM) images were obtained with a LEICA S440i scanning electron microscope. Energy dispersive analysis of X-rays (EDAX) was performed with a Oxford microanalysis group 5526 system attached to the SEM employing Links (ISIS) software and a Si(Li) detector. Samples for SEM and EDAX were prepared by spreading 10–20 mg of product onto a conducting carbon tape pasted on an aluminum stub, followed by sputter-coating with a gold film. EDAX analysis was carried out in the spot profile mode with a beam diameter of 1 μm at several places on the sample.

Transmission electron microscopy

Transmission Electron Microscopy (TEM) images were obtained with a JEOL JEM 3010 operating with an accelerating voltage of 300 kV. Samples for TEM studies were prepared by dispersing the nanostructures by sonication in CCl_4. A drop of the suspension was put on a holey carbon coated Cu grid and allowed to evaporate slowly.

Photoluminescence

Photoluminescence measurements were carried out at room temperature with a Perkin Elmer model LS50B luminescence spectrometer. The excitation wavelength used depended on the sample that was being studied.

Raman Spectroscopy

Raman spectra were recorded at room temperature with a Nd-YAG laser (532 nm) and an Ar-ion laser (488 nm and 514.5 nm).

Differential scanning calorimetry (DSC)

Differential Scanning calorimetry (DSC) measurements was carried out with a Perkin-Elmer instrument employing a heating rate of 20 K min^{-1}.

3.4 Results and discussion

3.4.1 MgO nanowires and related nanostructures

The various procedures mentioned in the experimental section under synthesis all gave MgO nanostructures as verified by the XRD patterns. The patterns were characteristic of the cubic structure of MgO (a = 4.211 Å ; JCPDS Card No: 45-0946). It must be noted that when MgO or Mg powder alone was heated in an alumina boat at 1300 or 850 °C for 5 h in an Ar atmosphere, we failed to obtain nanostructures of MgO. The product obtained from the reaction of activated carbon with MgO powder by procedure 1(a) contained different types of nanostructures. The SEM image of the sample in Figure 3.6 (a) illustrates this result. The image reveals the various nanostructures formed, including nanosheets and nanobelts. The diameter of these nanostructures varies from 20 to 200 nm. The nanosheets have a width of about 8 μm and length in the range of 10 μm. The nanobelts on the other hand are of widths ranging from 50 to 200 nm and lengths going to several micrometers. The TEM image of a nanostructure given in Figure 3.6 (b) shows an interesting feature with jagged-edges. The inset in Figure 3.6 (b) shows the selected area electron diffraction (SAED) pattern of this jagged-edged nanostructure, revealing its single crystalline nature. The reflections correspond to the (222) and (420) planes of cubic MgO. The jagged-edged or saw-like structure is an interesting observation in the case of MgO. When the reaction was carried out using commercial activated charcoal, by procedure

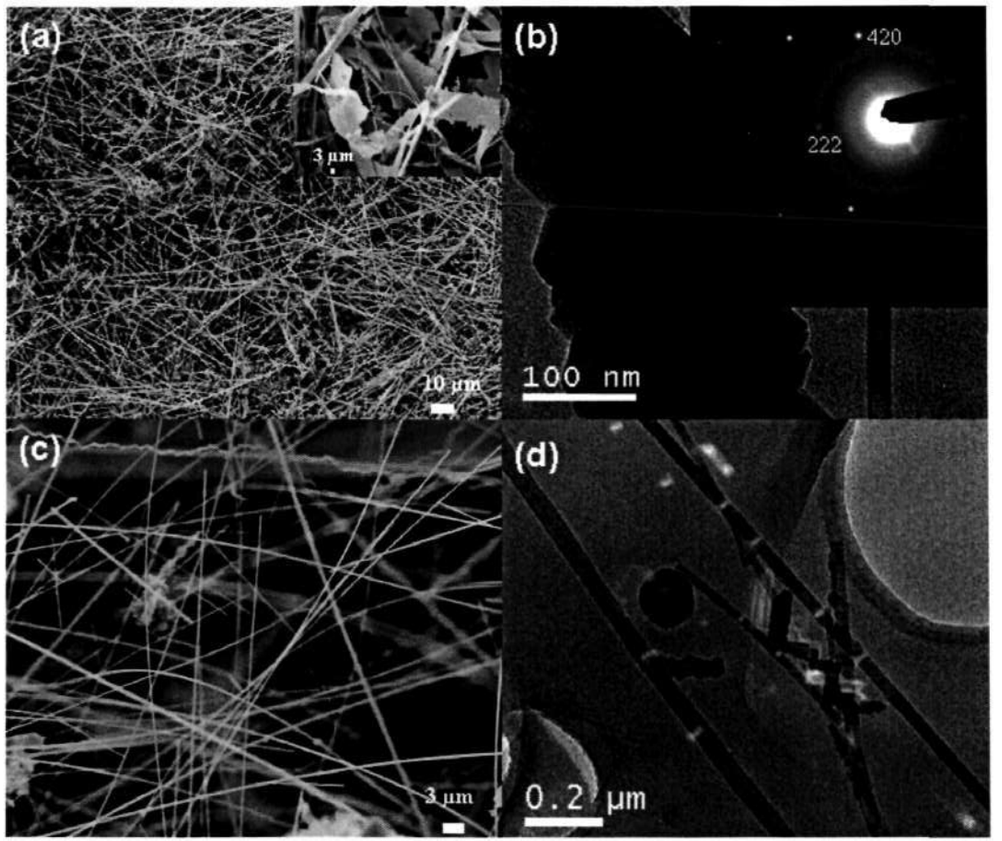

Figure 3.6: (a) SEM images of MgO nanostructures prepared by procedure l(a).The inset is the SEM image of the nanosheets and nanobelts. (b) A high magnification TEM image of a jagged-edged nanostructure obtained by procedure l(a). The inset is the SAED pattern of the jagged-edged nanostructure. (c) SEM and (d) TEM images of the nanostructures prepared by procedure 2(a).

2(a), we obtained a good yield of different nanostructures comprising nanowires and nanobelts with high aspect ratios. The SEM image in Figure 3.6 (c) shows the morphology of the different nanostructures formed. The transmission electron micrograph in Figure 3.6 (d) shows the nanostructures, comprising nanobelts along with different shapes and edge structures. The diameter of the nanostructures varies from 20 to 50 nm, with length extending to several tens of micrometers.

The reaction of MgO powder with graphite, by procedure 3(a) also yielded a mixture of different nanostructures including belts, wires, etc., as seen in the SEM image (Figure 3.7 (a)). The diameter of the nanowires varies in the range 50–200 nm and their length extends to several tens of microns. The use of MWNTs as the carbon source, by procedure 4(a), gave the best yield of uniform nanowires (see the SEM image in Figure 3.7 (b)). The diameter of the nanowires varies from 50 to 150 nm and their length extends to tens of microns. In Figure 3.7 (c) we show a finger-shaped nanowire with decreasing diameter towards the apex. The inset in Figure 3.7 (c) is the SAED pattern of the nanowire taken from its apex. The reflections correspond to the (200) and (220) planes of cubic MgO. The TEM image of yet another nanowire is shown as an inset in Figure 3.7 (c). The HREM image of a nanowire given in Figure 3.7 (d) shows a lattice spacing of 0.21 nm corresponding to the (200) planes of cubic MgO. The growth direction of the nanowire (shown by an arrow in Figure 3.7 (d)) is perpendicular to the (200) planes and is along the <100> axis. The SAED pattern and HREM image confirm the single-crystalline nature of the nanowires. Thus by employing MWNTs, we could obtain nanowires of uniform distribution. The reaction of Mg powder with activated carbon by procedure l(b) gave nanowire-networks in good yield. The SEM image in Figure 3.8 (a) reveals the

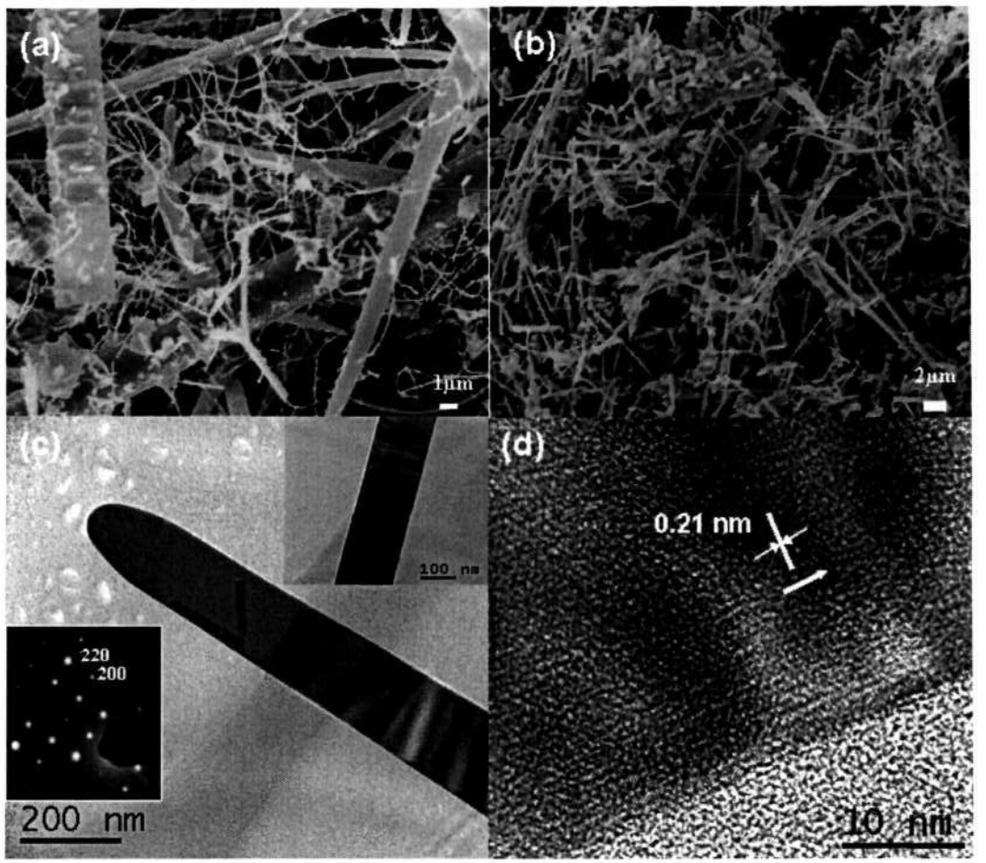

Figure 3.7: (a) SEM of the MgO nanostructures obtained by procedure 3(a). (b) SEM image of the nanostructures obtained by procedure 4(a). (c) TEM image of a finger-shaped nanowire obtained by procedure 4(a). The SAED pattern of the nanowire and the TEM image of another nanowire are shown as insets. (d) HREM image of a nanowire showing the (200) planes. The arrow indicates the growth direction of <100>.

overall morphology of the ID nanostructures. The image shows single nanowires as well as those that form complex junctions along with star-shaped nanostructures. TEM images reveal the formation of MgO nanotubes as well, as can be seen from Figure 3.8 (b). The diameter of the nanotube is ~ 50 nm and the length extends up to a micron. The reaction of Mg powder with activated charcoal by procedure 2(b) gave nanostructures with complex networks, as revealed by the SEM image in Figure 3.8 (c). The TEM image in Figure 3.8 (d) shows nanostructures with T-junction, having rectangular cross-section morphology and a peculiar dot-pattern. The slight shrinkage in cross-section along the direction of branch length may be due to the gradual decrease in the vapor supply during the growth. The diameter of the nanostructures varies from 100 to 300 nm and their length extends to tens of micrometers. The presence of dot-patterns in this case is significant and can be understood similar to that of the dot-patterned GeO_2 nanowires [70].

The reaction of Mg with graphite powder, by procedure 3(b) yields interesting nanostructures. In Figure 3.9 (a) we show one such nanostructure, a nanotree like morphology with nanotube branches. The diameter of these nanotubes is about 100 nm and their length extends to a few microns. When the reaction was carried out with MWNTs by procedure 4(b), structures such as cubes with nanorod-fingers originating from them were obtained (see SEM image in Figure 3.9 (b)). In Figure 3.9 (c) we show the TEM image of one such structure with nanorods originating from it. Such nanocubes with nanorods originating from them have been observed for the first time in the case of MgO. In Figure 3.9 (d), we show the TEM image of a single nanotube obtained by this preparation. The diameter of the nanotube is ~ 60 nm and its length goes up to a micron. The inset in Figure 3.9 (d) shows the SAED pattern of the

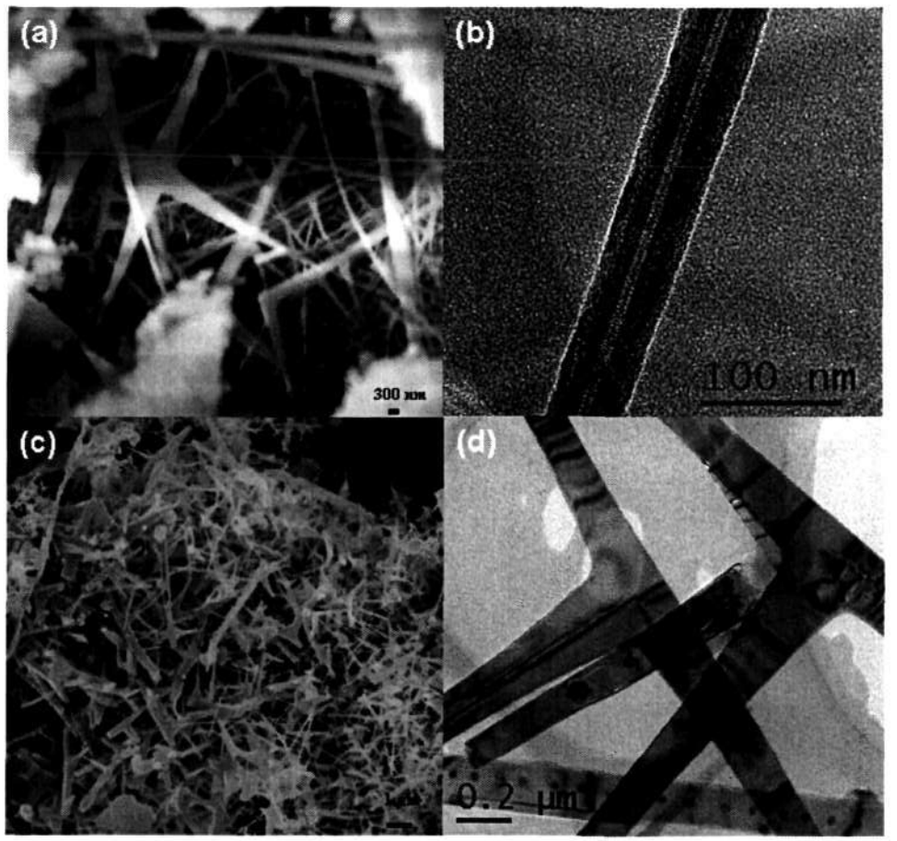

Figure 3.8: (a) SEM image of the MgO nanostructures including star-shaped nanowires prepared by procedure l(b). (b) TEM image of a MgO nanotube prepared by procedure l(b). (c) SEM image of the nanostructures obtained by procedure 2(b). (d) TEM image of T-junctions.

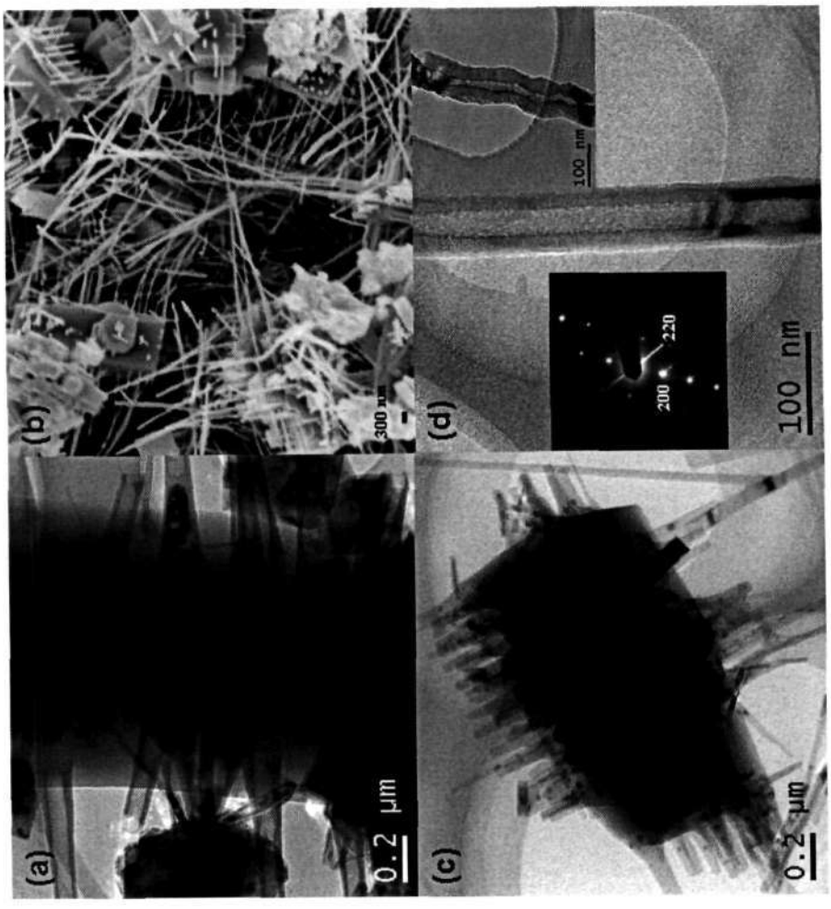

Figure 3.9: (a) TEM image of a MgO nanotree with protruding nanotube fingers, obtained by procedure 3(b). (b) SEM image of MgO nanostructures (mainly cubes with nanorod like structures originating from them) prepared by procedure 4(b). (c) TEM image of a cube, with nanorods originating from it. (d) TEM image of a well-formed, straight nanotube obtained by procedure 4(b). Insets show the SAED pattern of a nanotube and the TEM image of a helical-shaped nanotube obtained by procedure 3(b).

nanotube with Bragg reflections corresponding to the (200) and (220) planes of cubic MgO. Also shown as an inset in Figure 3.9 (d) is a helical-shaped nanotube obtained from the reaction of Mg powder and graphite by procedure 3(b).

The reactions of Mg and MgO with carbon on gold-coated Si substrates yielded uniform nanowires of MgO. In Figure 3.10 (a) we show the SEM image of aligned MgO nanowires with gold catalyst particles at their tips, obtained by procedure 5(a). The diameter of the nanowires is about 100 nm and their length extends to several tens of microns. The reaction with graphite by procedure 5(b) gave high yields of uniform MgO nanowires with high aspect ratios as revealed by the SEM image in Figure 3.10 (b). The diameter of the nanowires ranges from 100 to 200 nm, their length extending to tens of micrometers. Figure 3.10 (c) gives a SEM image of well-formed nanowires obtained from the reaction of Mg powder and graphite by procedure 5(c), grown on a gold-coated silicon substrate at 800 °C. Figure 3.10 (d) shows the TEM image and the SAED pattern (inset) of the nanowires with tapered tips. The spots in the pattern correspond to the (220) Bragg planes of cubic MgO, revealing their single-crystalline nature. The diameter of the nanowires is around 30 nm and their length goes up to a micron.

The MgO 1D nanostructures showed characteristic photoluminescence properties. With an excitation wavelength of 315 nm, we obtained a peak at around 440 nm. Rosenblatt *et al.* [71] have obtained a similar band by time-resolved spectra of bulk MgO with different defect densities. They have attributed these bands to F+ and F centres. Zhang and Zhang [16] have reported an intensive green light emission from MgO nanobelts. The 440 nm emission peaks in our case may also be attributed to the existence of oxygen vacancies or surface states of the 1D MgO nanostructures.

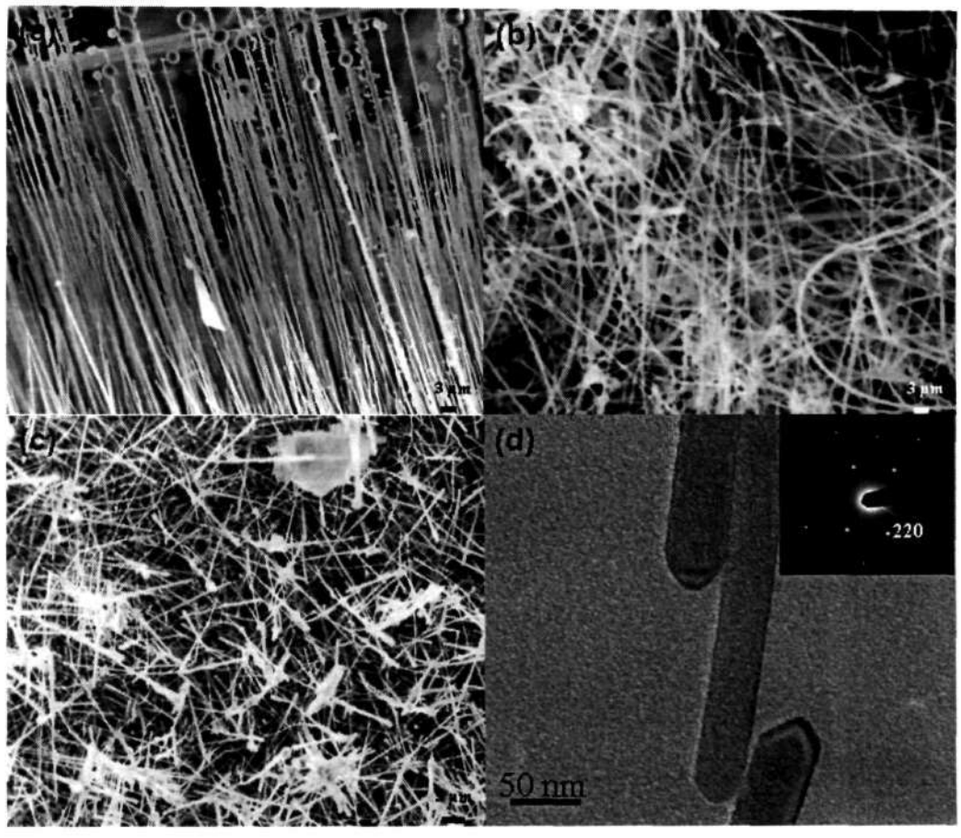

Figure 3.10: (a) SEM image of aligned MgO nanowires with gold nanoparticles at their ends, prepared by procedure 5(a). (b) SEM image of the nanowires prepared by procedure 5(b) on a silicon substrate with gold coating. (c) SEM image of the nanowires prepared by procedure 5(c), on a gold-coated silicon substrate at 800 °C. (d) TEM image of the nanowires with the SAED pattern, shown as an inset.

The growth of the different 1D nanostructures of MgO can be explained in terms of the following two mechanisms. The first is the vapor–solid (VS) mechanism, which occurs predominantly in the present study.

$$MgO\ (s) + C \rightarrow MgO_x\ (v) + CO \qquad (1)$$

$$2MgO_x\ (v) + O_2 \rightarrow 2MgO\ (s) \qquad (2)$$

MgO first gets reduced to a "suboxide" as shown in reaction (1). The suboxide combines with the oxygen present in the reaction system, to give MgO particles as in Eq. (2). The oxide particles get transported by the Ar gas and are deposited in the boat. The nanowires are formed from the nuclei of MgO particles. The morphology of the nanostructures is determined by the level of supersaturation of MgO vapor, resulting in nanowires as well as complex networks. The nanowires and nanotubes may require a lower supersaturation than the complex networks or the cubes, the complex structures being favored by the presence of defects. After a nanowire grows to a certain length, the defects present in it may switch the growth direction, resulting in the formation of branches perpendicular to it. The vapor–liquid–solid (VLS) mechanism [72] would apply when we employ the gold-coated Si substrates. Here, the MgO vapor is transported by the Ar gas and deposited on the Au-coated Si substrate for further nucleation and crystallization. The SEM image in Figure 3.10 (a) clearly reveals the presence of Au particles at the tips of nanowires, establishing the validity of the VLS mechanism.

The present study on the synthesis of one-dimensional MgO nanostructures by employing different sources of carbon has shown that MgO nanowires and related nanostructures can be obtained in copious quantities by carbon-assisted synthesis (Table 1). The variety of nanostructures obtained includes nanosheets, nanobelts and nanotrees (Scheme 4). Using the Au covered Si substrates carbon-assisted synthesis

permits the formation of aligned nanowires. A variety of novel nanostructures have been obtained for the first time.

Table 1: MgO nanostructures obtained under different experimental conditions

Procedure	Source	Nanostructures
1(a)	Activated carbon: MgO (1:1)	Sheets, belts, wires, jagged-edge structures.
1(b)	Activated carbon: Mg (1:1)	Star shaped wires, complex networks, tubes.
2(a)	Activated charcoal: MgO (1:1)	Wires, belts, zigzag shaped structures.
2(b)	Activated charcoal: Mg (1:1)	Wires, T-junctions, complex networks.
3(a)	Graphite: MgO (1:0.6)	Wires, belts.
3(b)	Graphite: Mg (1:1)	Tree-like structures, tubes.
4(a)	MWNTs: MgO (1:0.6)	Wires.
4(b)	MWNTs: Mg (1:1)	Tubes, cubes with finger outgrowths.
5(a) (Au / Si)	Activated Carbon: MgO (1:0.5)	Wires.
5(b) (Au / Si)	Graphite: MgO (1:0.5)	Wires.
5(c) (Au / Si)	Graphite: Mg (1:0.5)	Wires.

Scheme 4: MgO nanostructures obtained under different experimental conditions

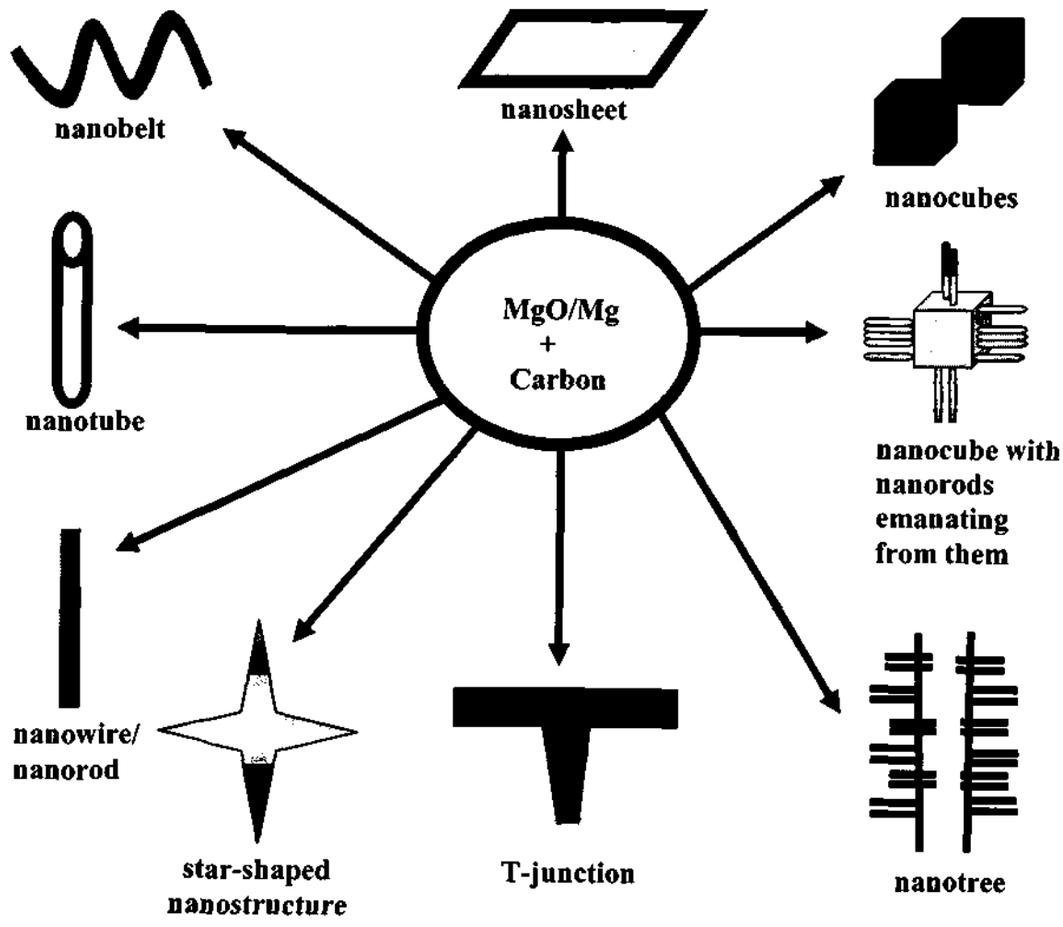

3.4.2 Al_2O_3 nanowires and nanotubes

The XRD patterns of the nanostructures of alumina prepared by the various procedures showed them to possess the rhombohedral structure of α - Al_2O_3 with lattice parameters, a = 4.759 Å and c = 12.991 Å (JCPDS Card No: 11-0661). In Figure 3.11, we show the SEM image of the hollow alumina structures obtained by using procedure (i) which involves the heating of Al and graphite powders in an Ar + O_2 mixture. The hollow alumina structures, consisting of smooth inner cores with a diameter of around 1-2 μm, were found to be abundant.

Figure 3.11: SEM image of hollow alumina nanostructures obtained by using procedure (i).

In Figure 3.12 (a) and (b), we show the SEM images of the alumina nanostructures obtained by procedure (ii), that involves the heating of Al and graphite powders in Ar. The nanostructures comprise of nanowires of high aspect ratios. Certain other network-like structures, with a radial outgrowth originating from a single stem-like structure, are also seen. Such novel nanostructures have been observed earlier in the case of the oxides of Sn and Zn [73-75].

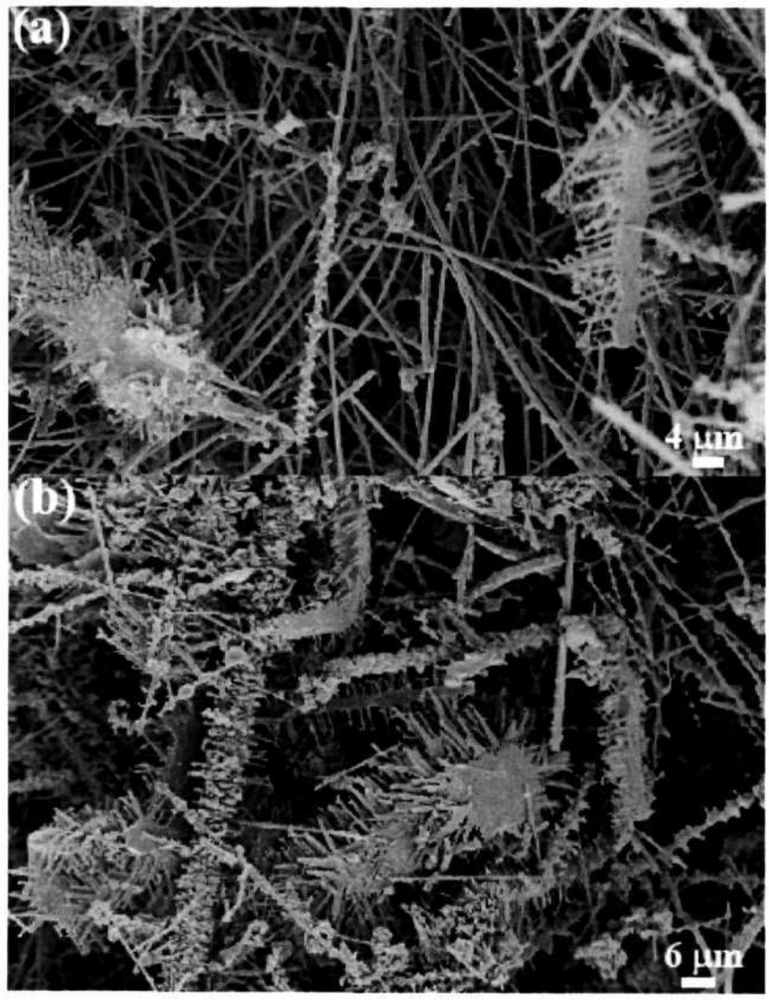

Figure 3.12: (a) and (b) SEM images of nanowires and other nanostructures of Al_2O_3 obtained by procedure (ii).

TEM images of the alumina nanotubes, prepared by the use of active carbon as in procedure (iii), are shown in Figure 3.13. The nanotubes generally have an outer diameter of 40-50 nm and an inner diameter of 20-25 nm. Certain collapsed nanotube-like structures also occur as shown in Figure 3.13 (c). Similar nanotube structures of alumina have been obtained earlier by the use of MWNTs as templates and by electrochemical processes [28-33].

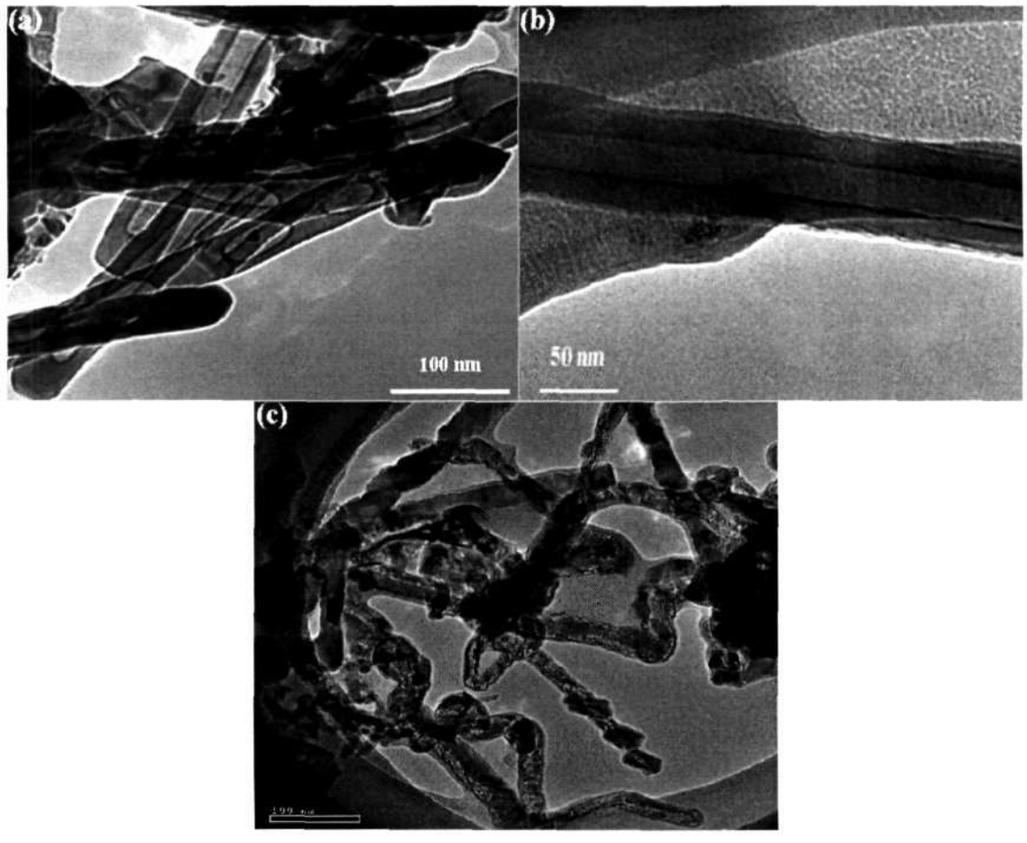

Figure 3.13: (a), (b) and (c) TEM images of nanotubes of Al_2O_3 obtained by procedure (iii).

The nanowires obtained are single-crystalline with a spacing of 0.253 nm corresponding to the (104) lattice planes. We show a typical high-resolution electron microscope (HREM) image of a nanowire prepared by procedure (ii) in Figure 3.14. The nanowire appears to grow in a direction, which makes an acute angle of ~ 35° with the (104) planes.

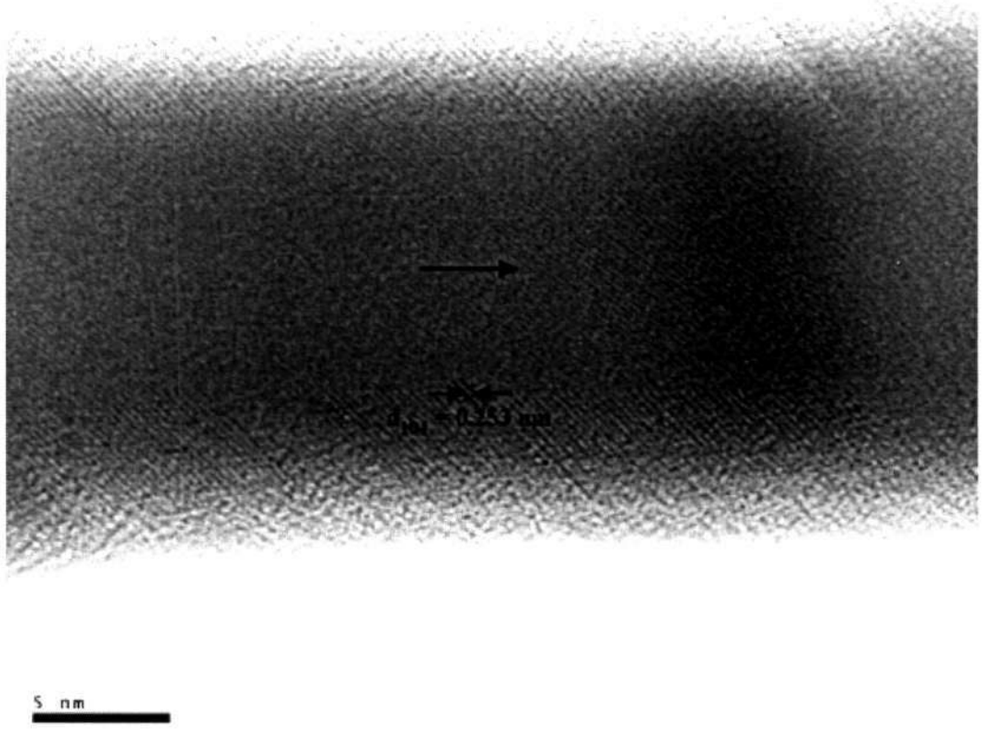

Figure 3.14: HREM image of an Al_2O_3 nanowire prepared by procedure (ii) showing lattice spacing of 0.253 nm corresponding to (104) lattice planes. The arrow denotes the growth direction of the nanowire, making an angle of ~ 35° with the normal to the (104) plane.

The PL spectrum of the nanowires and nanotubes of Al_2O_3, obtained by excitation at 255 nm, is shown in Figure 3.15. There is a strong PL band at 380 nm in the case of the nanowires and at 386 nm in the case of the nanotubes.

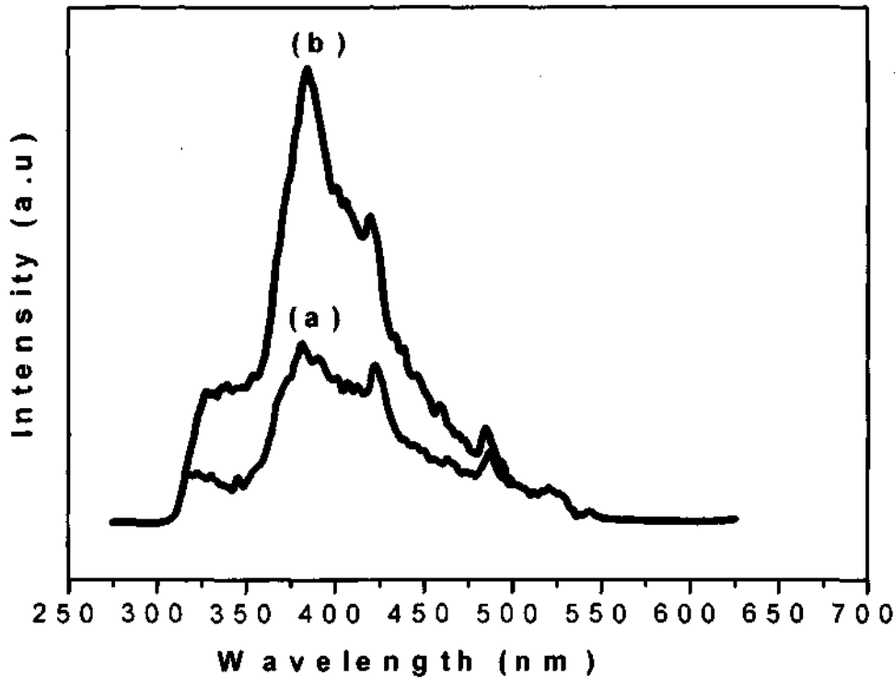

Figure 3.15: PL spectrum of (a) nanowires and (b) nanotubes of Al_2O_3.

In the literature, Al_2O_3 nanowires and nanobelts are reported to show bands around 393 nm and 392 nm at the same excitation wavelength [38]. The PL intensities of the nanotubes are stronger than those of nanowires. In the alumina nanostructures obtained by us, it is likely that there are oxygen vacancies. The origin of the PL emission is likely to be related to oxygen-related defects and F^+ centers (oxygen vacancies with one-electron centers) [54].

The growth mechanism of the nanowires can be understood on the basis of a vapor-solid mechanism since extensive microscopic investigations reveal no catalyst/liquid droplets at the ends of the nanowires. The relevant reactions can be written as follows:

$$Al\ (s) + C\ (s) + O_2\ (g) \rightarrow AlO_x\ (v) + CO\ (g)$$

$$AlO_x\ (v) + O_2\ (g) \rightarrow Al_2O_3\ (s)$$

The first step involves the formation of the suboxide in vapor form, which gets oxidized to Al_2O_3 in the presence of oxygen. Similar reactions have been proposed for the growth of Ga_2O_3 nanowires [3]. Under the vapor-solid reaction conditions, Al_2O_3 nanowires tend to form on the (104) lattice planes, since the reaction is far away from thermodynamic equilibrium conditions [76,77].

Thus, by varying the source of carbon and starting with Al powder, various nanowires, nanotubes and other interesting network-like structures of Al_2O_3, with satisfactory PL characteristics, have been prepared. The nanostructures of Al_2O_3 may be useful as catalyst supports. It would not be difficult to prepare such nanostructures with various metal nanoparticles embedded in them.

3.4.3 Crystalline SiO_2 nanowires

In Figure 3.16, we show SEM images of the SiO_2 nanowires obtained under different conditions. Shown in Figure 3.16 (a) are crystalline silica nanowires obtained on heating a mixture of fumed silica and activated charcoal (molar ratio of 1:2) in 50 sccm Ar. The nanowires have a diameter between 50 and 100 nm, with lengths extending up to tens of microns. We notice the presence of a small quantity ($\leq$ 5 %) of unreacted carbon as identified by energy dispersive x-ray analysis (EDAX). The carbon content is, however, reduced or eliminated by starting with a low carbon:silica ratio. The XRD pattern of the nanowires shown in Figure 3.17 (a) corresponds to that of α-cristobalite with the tetragonal structure (lattice parameters: a = 4.97 Å, c = 6.92 Å, JCPDS (NBS, USA) Card No. 39-1425). We observe no peaks due to silicon or other impurities. A low-magnification TEM image of the sample is shown in Figure 3.18 (a). Selected area electron diffraction (SAED) patterns of several nanowires were recorded at different points along the length of the wires. The inset in the Figure 3.18 (a) shows a representative SAED pattern with the Bragg spots corresponding to (101), revealing the single crystalline nature of the nanowires. By carrying out the reaction of fumed silica with reduced amounts of carbon (molar ratio of 1:0.5) in 50 sccm Ar, we obtained a high yield of nanowires with no or negligible carbon content. We show a typical SEM micrograph of these nanowires in Figure 3.16 (b). The nanowires have a uniform diameter of approximately 70 nm with lengths of tens of microns. The nanowires contain a crystalline core (~ 30 nm) sheathed by an amorphous layer as can be seen from the TEM image in Figure 3.18 (b). Reducing the ratio of carbon to fumed silica appears to increase the amorphous

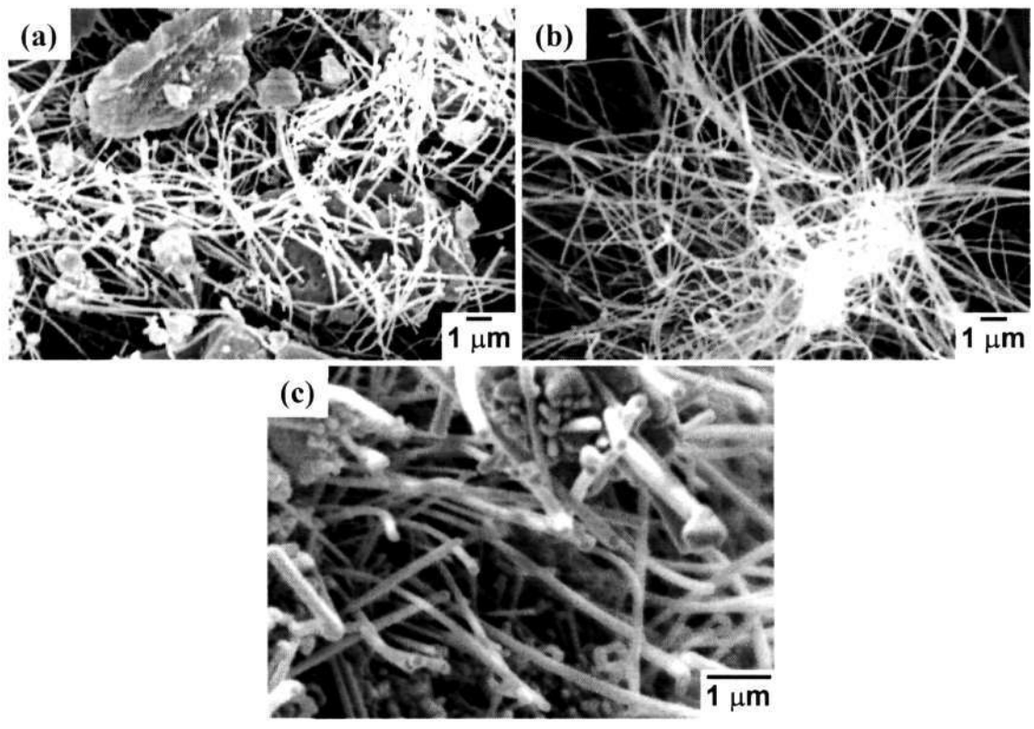

Figure 3.16: SEM images of the silica nanowires found in the alumina boat by the reaction of fumed silica with activated charcoal at 1300 °C for 5 h: (a) with silica to carbon molar ratio 1:2 in 50 sccm Ar, (b) with a molar ratio 1:0.5 in 50 sccm Ar, and (c) with a molar ratio 1:2 in 50 sccm Ar and 20 sccm H_2.

coating on the crystalline core, while eliminating or minimizing the carbon content. The amorphous sheath is SiO_2 and not carbon. There is, however, some competition between the magnitude of the amorphous sheath and carbon content in the preparation. Based on independent experiments with nanowires and nanotubes, we have found that any amorphous carbon in the sample is eliminated entirely on heating in hydrogen around 1000 °C. We therefore conclude that no amorphous carbon is present in the silica nanowires subjected to hydrogen treatment at 1000 °C. The sheath is not due to SiC which requires a high C:SiO_2 ratio for formation.

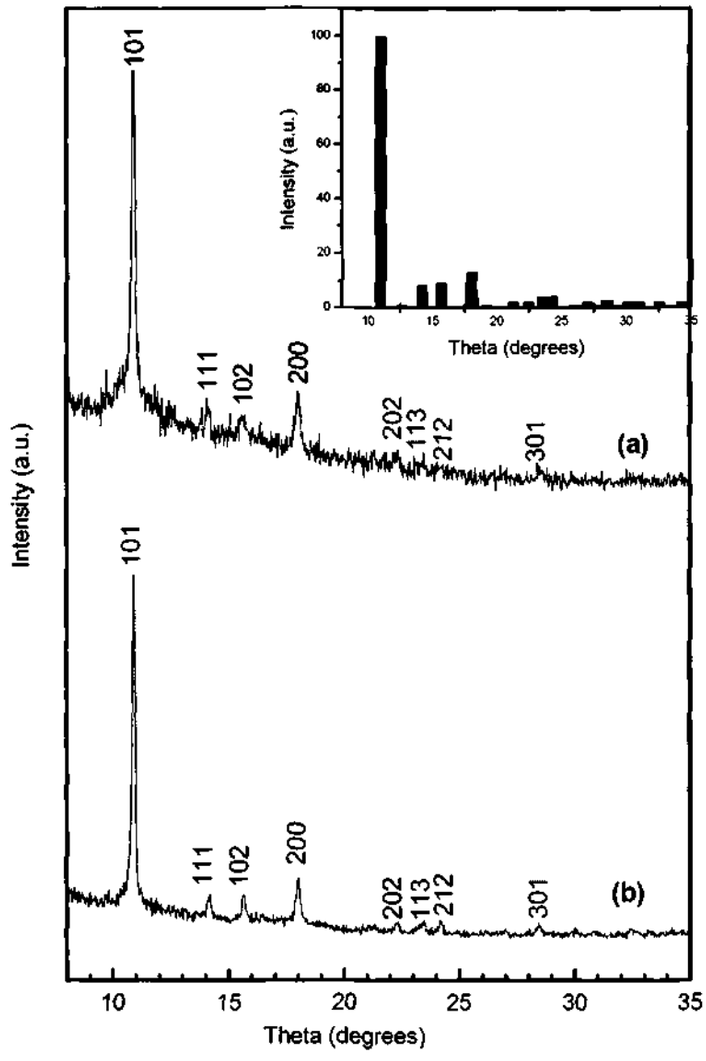

Figure 3.17: XRD patterns of the silica nanowires obtained by (a) the reaction of fumed silica and activated charcoal (molar ratio 1:2) at 1300 °C for 5 h in 50 sccm Ar and (b) the reaction of fumed silica and activated charcoal (molar ratio 1:1) at 1300 °C for 5 h in 50 sccm Ar + 20 sccm H_2. Inset shows the standard JCPDS pattern (Card No. 39-1425).

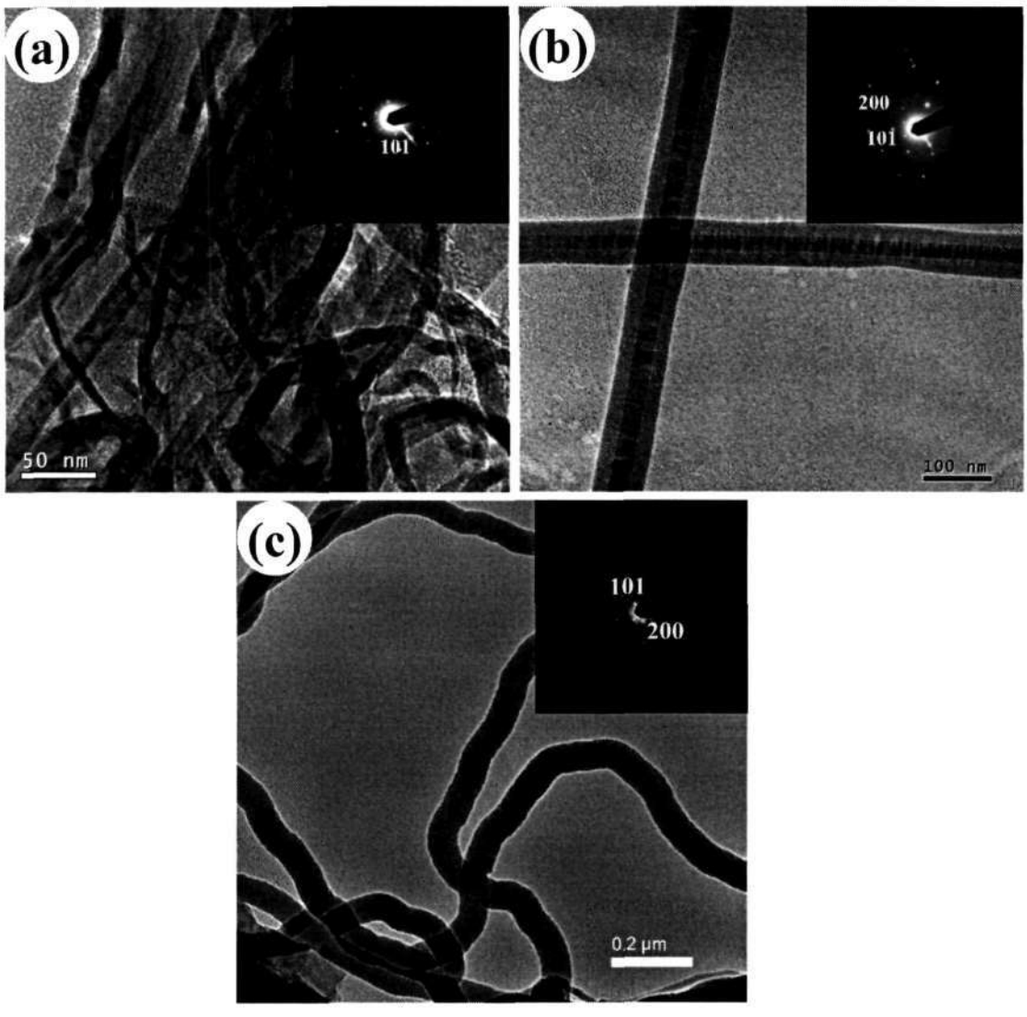

Figure 3.18: Low-magnification TEM images of silica nanowires obtained by the reaction of (a) fumed silica with activated charcoal (molar ratio 1:2) in 50 sccm Ar, (b) fumed silica with activated charcoal (molar ratio 1:0.5) in 50 sccm Ar, and (c) fumed silica with activated carbon (molar ratio 1:1) in 50 sccm Ar and 20 sccm H_2 at 1300 °C for 5 h. The insets show the corresponding SAED patterns.

The SAED pattern, shown as an inset in Figure 3.18 (b), reveals the nanowires to be single-crystalline α-cristobalite. The Bragg spots in this case arise due to (101) and (200) reflections of the tetragonal structure of α-cristobalite. With a 1:1 molar ratio of fumed silica and activated charcoal, however, we obtained a good crystalline α-cristobalite nanowires of diameters in the 70–100 nm range [Figure 3.18 (c)]. The diffraction pattern in the inset of Figure 3.18 (c) reveals the crystalline nature of the nanowires.

The high-resolution TEM image of a single silica nanowire presented in Figure 3.19, shows (102) planes with the expected spacing of 0.28 nm between the planes. The normal to the (102) planes makes an angle of approximately 12° with the growth direction of the nanowire.

A good yield of α-cristobalite nanowires was also obtained when 20 sccm of H_2 gas was passed along with 50 sccm Ar while heating a 1:2 mixture of fumed silica to activated charcoal as evident from the SEM image shown in Figure 3.16 (c). The use of H_2 helps to remove the unreacted carbon, as found by us in repeated experiments. We find a similar situation in the case of carbon nanotubes where again amorphous carbon is best removed by hydrogen treatment at 1000 °C. This can be seen by a comparison of Figures 3.16 (a) and 3.16 (c). We show a representative XRD pattern of the sample obtained by the reaction of a mixture of fumed silica and activated charcoal (molar ratio of 1:1) heated in a mixture of Ar (50 sccm) and H_2 (20 sccm) in Figure 3.17 (b). The line-widths of the reflections in this XRD pattern are somewhat narrower suggesting greater crystallinity.

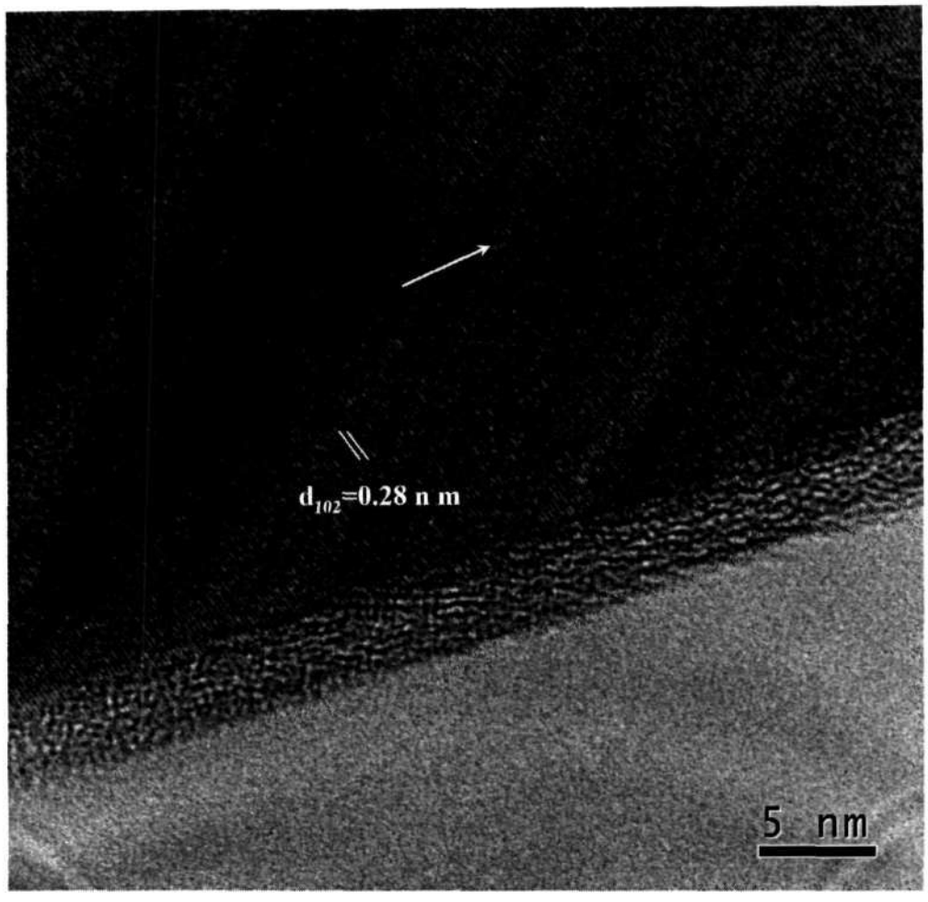

Figure 3.19: High-resolution electron microscopy image of a crystalline silica nanowire prepared by the reaction of fumed silica with activated charcoal (molar ratio 1:0.5) at 1300 °C for 5 h in 50 sccm Ar. The arrow denotes the direction of growth of the nanowire.

The photoluminescence spectrum of the α-cristobalite nanowires was recorded along with that of fumed silica. As shown in Figure 3.20 (a), fumed silica exhibits a shoulder in the UV region at 375 nm and a broad band in the blue region centered at 440 nm. These features are nearly absent in the spectrum of the nanowires. The

presence of intense blue emission in fumed silica arises from the high density of defects and oxygen related vacancies. We have recorded the Raman spectrum of the sample and observed two bands at 200 cm^{-1} (A_1) and 424 cm^{-1} (A_1 or B_2) in addition to a weak band around 790 cm^{-1} (E) [Figure 3.20 (b)]. There is a lot of controversy regarding the band assignment in the literature of the α- and β- phases of cristobalite [78,79]. The spectrum resembles that of the α-phase reported in the literature.

DSC of the crystalline nanowires revealed a reversible transformation from the α-form to the β-form at 510 K [Figure 3.21]. This α–β transition is known to occur in cristobalite around this temperature [80]. Under the preparation conditions used by us, the nanowires are first formed in the β-form, and are then converted to the α-form on cooling to room temperature.

We could obtain α-cristobalite nanowires only with fumed silica but not with other sources of silica. This may be because fumed silica is amorphous, containing very tiny particles with a high surface area. Carbon plays a crucial role in the reaction in reducing silica to its reactive suboxide SiO_x. The presence of a high proportion of carbon relative to silica and use of hydrogen give rise to good crystalline nanowires. A lower proportion of carbon or the absence of hydrogen results in crystalline SiO_2 nanowires coated with an amorphous silica layer. The exothermic nature of the reduction of silica by carbon may give rise to considerable local heating, which may help the crystallization of fumed silica into the cristobalite form. The reaction involved in the formation of crystalline silica can be written as follows:

$SiO_2 + C \rightarrow SiO + CO$ (1)

$2SiO + O_2 \rightarrow 2SiO_2$ (2)

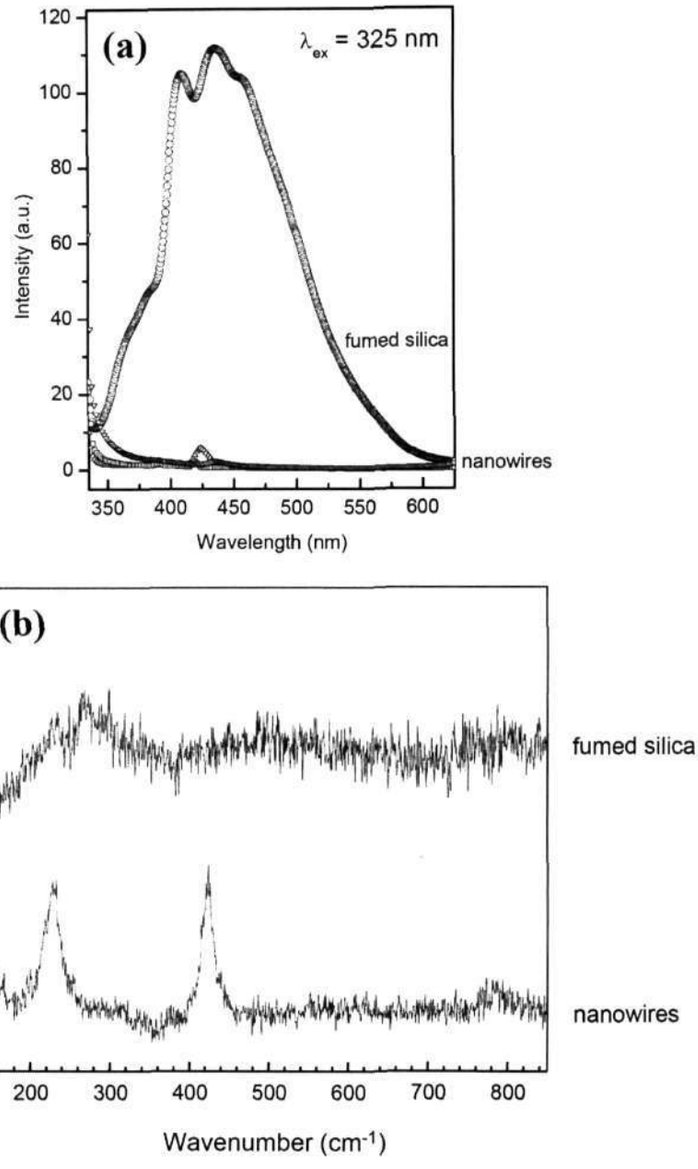

Figure 3.20: (a) Photoluminescence spectra of fumed silica and crystalline nanowires obtained by the different routes using 325 nm as the excitation wavelength and (b) Raman spectra of fumed silica and the nanowires prepared by the reaction of fumed silica with activated carbon (molar ratio 1:1) at 1300 °C for 5 h in a mixture of Ar (50 sccm) and H_2 (20 sccm).

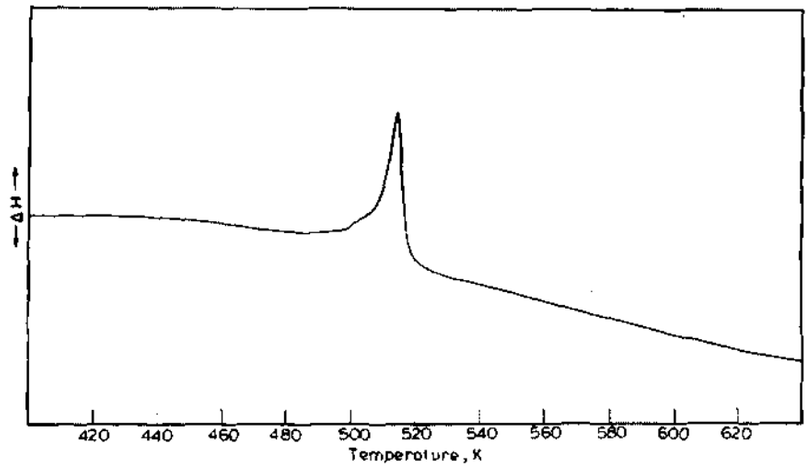

Figure 3.21: DSC curve of crystalline silica nanowires

We do not feel that disproportionation of SiO occurs since elemental Si is not formed in the product. The SiO vapors deposited on the walls of the alumina boat react with the oxygen contained in the reaction system to form crystalline nanowires. Such oxidation reactions are well documented [81,82]. The growth of the nanowires is likely to occur by the vapor–solid mechanism since no metal catalyst has been used in the synthesis. Accordingly, microscopic investigations do not reveal the presence of catalyst/liquid droplets at the ends of the nanowires. In conclusion, we have, for the first time, synthesized good single-crystalline nanowires of silica in the α-cristobalite form by a simple carbothermal procedure. The nanowires might find useful applications.

3.4.4 In_2O_3 nanowires and related nanostructures

In Figure 3.22 (a) and (b), we show the SEM images of the In_2O_3 nanowires obtained by procedures (i) and (ii) respectively. In procedure (i), the ratio of the In_2O_3 and activated charcoal was 1:1 and the Ar flow rate was 150 sccm, while in procedure (ii), the ratio of In and activated charcoal was 1:2 and the Ar flow rate was 50 sccm. The diameter of the nanowires obtained by us varies in the 50-100 nm range, with the length extending upto several microns. The images also indicate yields of the nanowires to be high.

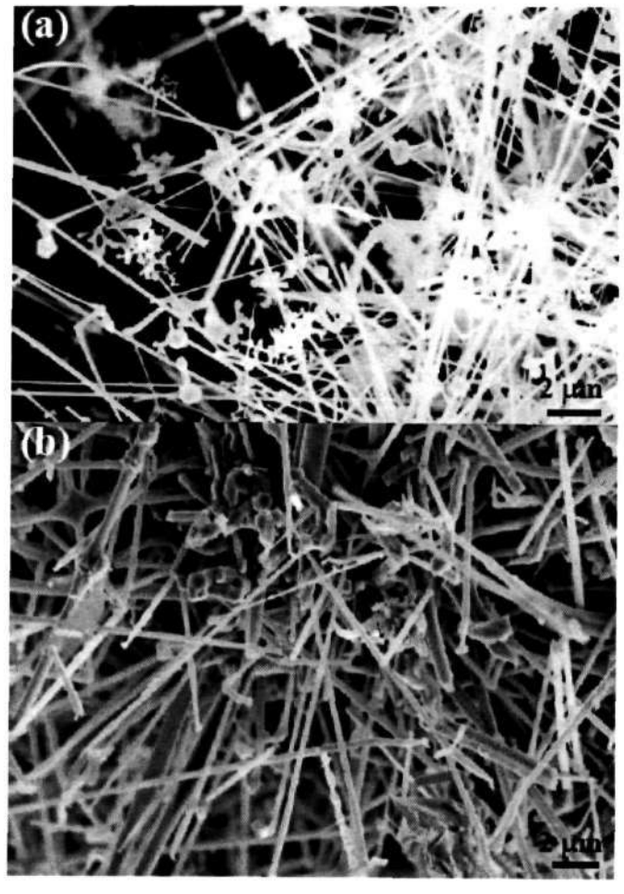

Figure 3.22: (a) and (b) SEM images of In_2O_3 nanowires prepared by procedure (i) and (ii).

The x-ray diffraction patterns of the nanowires obtained by procedures (i) and (ii) are shown in Figure 3.23 (a) and (b) respectively. The patterns correspond to In_2O_3 with the cubic *c*-type rare earth oxide (Ia3, bixbyite) structure [10] with a = 10.11 Å [JCPDS Card No: 06-0416]. The XRD pattern in Figure 3.23 (a), also shows additional peaks corresponding to metallic In. We do not see the XRD peaks due to In metal in Figure 3.23 (b), suggesting possible differences in the mechanism of formation by procedures (i) and (ii).

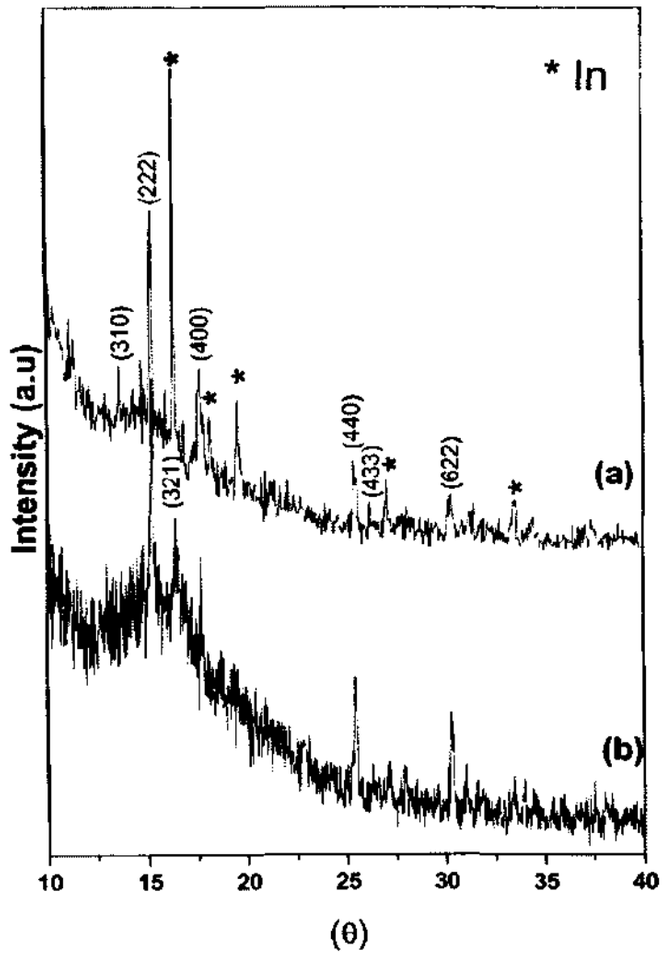

Figure 3.23: (a) and (b) XRD patterns of In_2O_3 nanowires prepared by procedure (i) and (ii).

TEM images of individual nanowires obtained by procedure (i), starting with In_2O_3 and activated charcoal are shown in Figure 3.24 (a) and (b). The diameter of the nanowire is around 70 nm. The inset in Figure 3.24 (b) shows the selected area diffraction (SAED) pattern of the nanowire with Bragg spots corresponding to (200) and (222) planes, revealing the single-crystalline nature of the nanowire. A high resolution electron microscope (HREM) image of a nanowire is shown in Figure 3.24 (c). The HREM image shows (200) planes with the expected spacing of 0.502 nm between the planes. The presence of (200) planes perpendicular to the nanowire axis suggests that the growth of the nanowire is along the [100] direction. There is also support from other workers that [100] is the growth direction of the In_2O_3 nanowires [54,83,84]. We show the TEM images of In_2O_3 nanostructures obtained by procedure (ii) starting with a 1:1 molar ratio of the In metal and activated charcoal. The nanowire in Figure 3.24 (d) has a diameter of ~ 100 nm and the inset in this figure shows the SAED pattern of the nanowire with Bragg spots corresponding to (400) and (440), revealing that they are single-crystalline. The TEM image in the inset of Figure 3.24 (d) shows a nanostructure with a diameter of ~ 200 nm possessing ragged edges. The presence of teeth on both sides of the nanostructure is unusual. By using ordinary crystalline graphite powder in place of activated charcoal, we were able to obtain a good yield of single crystalline nanowires by procedure (i), although the diameter of the nanowires was somewhat larger.

We have characterized the In_2O_3 nanowires by photoluminescence spectra using 330 nm as the excitation wavelength. The spectra show a blue emission peak at 426 nm, with a shoulder at 406 nm and a smaller feature at 450 nm. It is known that

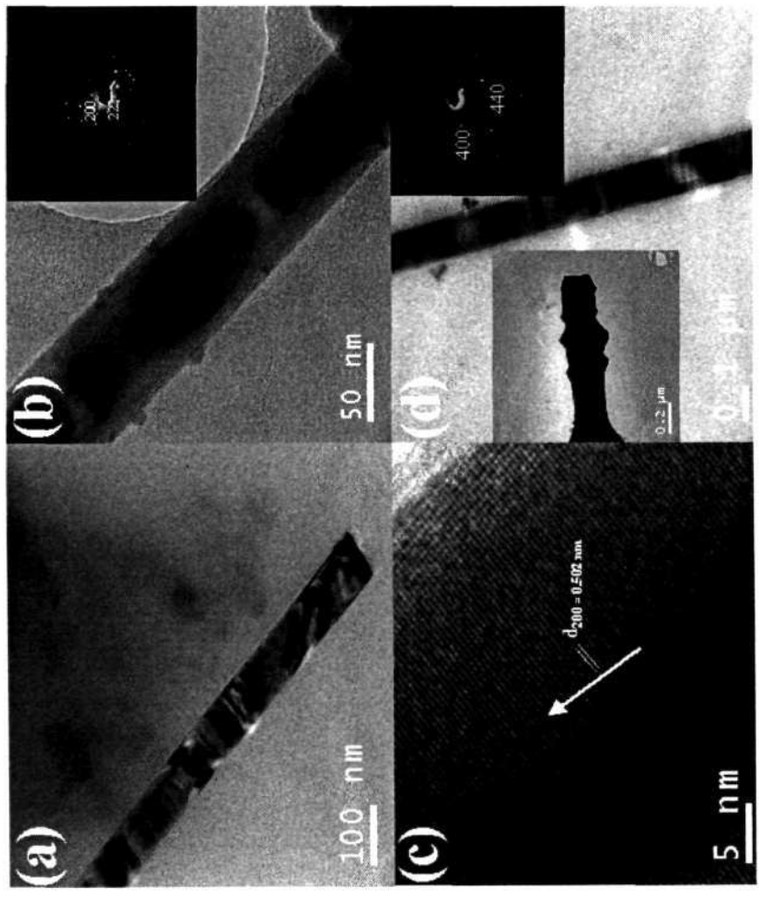

Figure 3.24: (a) and (b) TEM images of In_2O_3 nanowires prepared by procedure (i). Inset in (b) shows the SAED pattern, (c) HREM image of the nanowire shown in (b), (d) shows the TEM images of In_2O_3 nanostructures prepared by procedure (ii). The inset in the same figure shows a nanostructure with teeth on either side along with the corresponding SAED pattern.

bulk In_2O_3 does not emit light at room temperature [85]. It is, therefore, significant that the nanowires exhibit the blue emission. Other workers have reported emission bands at 480 nm and 520 nm in In_2O_3 nanoparticles [86], at 617 nm in nanotubes [87], at 470 nm in nanofibers [54] and at 570 nm in nanobelts [84]. Quantum confinement can be ruled out since the exciton Bohr diameter for indium oxide is in the range between 2.6 and 5 nm and the diameter of the nanowires that we have obtained are much larger. The origin of the emission is likely to be oxygen-related vacancies, which are created under the conditions of preparation. The oxygen vacancies would induce the formation of new energy levels in the bandgap. The emission occurs due to the radiative recombination of a photo-excited hole with an electron occupying the oxygen vacancies [54-56,83,84]. We have previously observed such oxygen-related emission in the case of Ga_2O_3 [3]. Annealing in oxygen does not eliminate the blue emission but instead enhances it [55]. A similar observation has been made in the case of In_2O_3 nanoparticles [86].

While we obtain In_2O_3 nanowires from both procedures (i) and (ii), starting from either In_2O_3 or In metal, the mechanism of formation appears to be different in the two procedures. One would be tempted to suggest that the formation of the In_2O_3 nanowires by procedure (i), wherein we start with In_2O_3 and carbon, is by the vapor-solid (oxide-assisted) process as in the case of Ga_2O_3 [3]. The reaction of carbon with Ga_2O_3 yields a suboxide in the vapor phase. The suboxide gets oxidized subsequently to produce the nanowires. Although indium suboxides are known, it is significant that we observe the presence of metallic In (see Figure 3.23 (a)). The mechanism therefore is likely to be different. Carbothermal reduction of In_2O_3 leads to the formation of the metallic In possibly via the suboxides, as given by,

In_2O_3 (s) + 3 C (s) → 2 In (v) + 3 CO (g) (1)

The metal vapor gets oxidized to give In_2O_3 as given by,

4 In (v) + 3 O_2 (g) → 2 In_2O_3 (s) (2)

In order to better understand what really happens in the formation of the nanowires, we have examined the TEM images in detail. The TEM images in Figure 3.25, show interesting nanostructure morphologies, a common one being the tree-like structure (Figure 3.25(a)), wherein periodic ladder-like steps are formed on a central column by nanowire segments containing metal droplets at the tips. These were obtained with a 1:1 molar ratio of the oxide and activated charcoal at an Ar flow rate of 100 sccm. The inset in the same figure shows nanotrees (small tree-like structures) formed at a higher Ar flow rate of 150 sccm. These images show nanowires with In metal droplets at the tips. In some of the TEM images, we have found spherical metal clusters as well as metal droplets with short nanowires attached to them as in a peg or a nail (see inset of Figure 3.25 (d)). We also commonly observe nano-paintbrush or nanobouquet structures obtained under similar conditions (Figure 3.25 (b-d)), somewhat comparable but distinctly different to those described in the literature in the case of Ga_2O_3 nanowires generated from Ga metal [88]. What is, however, different is that in the case of Ga_2O_3, no metal droplets were observed at the nanowire tips. The formation of the nanobouquet structure would require the formation of the metal nuclei initially by the deposition of the metal vapor. The initially formed nuclei are trapped and the subsequent growth from the nuclei results in the nanowire, albeit the oxidation step wherein the oxide is formed along the nanowire except the tip. This is reminiscent of the vapor-liquid-solid (VLS) growth mechanism, except that in the

present case, it is a self-catalytic VLS mechanism [89,90], the reduction of the metal oxide causing the formation of metallic clusters which themselves serve as nuclei for growth and oxidation. Agglomeration of neighboring nanoscale nuclei is likely to be responsible for the bouquet morphology. The relatively low decomposition temperature of In_2O_3 (b.pt = 850 ° C) and the low melting point of In metal (156 °C) favor this mechanism. The requirement of equimolar or greater proportion of carbon can be understood in terms of the VLS mechanism and reaction (1).

In Figure 3.26, we provide a schematic description of the various features found in the TEM images of Figure 3.25. The first stage would involve the formation of fine In metal droplets. The initially formed droplets form smaller clusters under Ar flow. The metal clusters act as nuclei to give rise to nanowires (**I**) by the VLS mechanism. The nanowires are tapered due to the crowded environment present when they grow from individual metal clusters. While the nanobouquet structures (**III,** Figure 3.25 (b) and (c)), arise from metal nuclei coming closer, the tree-like structures (**IV**, Figure 3.25 (a)) arises from the decomposition of the oxide along the length of the nanowires giving rise to new metal nuclei. When the Ar flow rate is high, we observe multiple growth occurring from a single-nucleation center as well as the high-way type branching (**II**) shown in Figure 3.25 (d). In procedure (ii), where we start with the In metal, the oxide coating on the surface gets reduced by the carbon. The metal nanowires initially formed then get oxidized in-situ rapidly and completely into the In_2O_3 oxide nanowires [55], under ambient conditions. It is noteworthy that we do not observe metal droplets at the nanowire tips or bouquet structures when we start with In metal thereby providing evidence for the vapor-solid mechanism. The metal

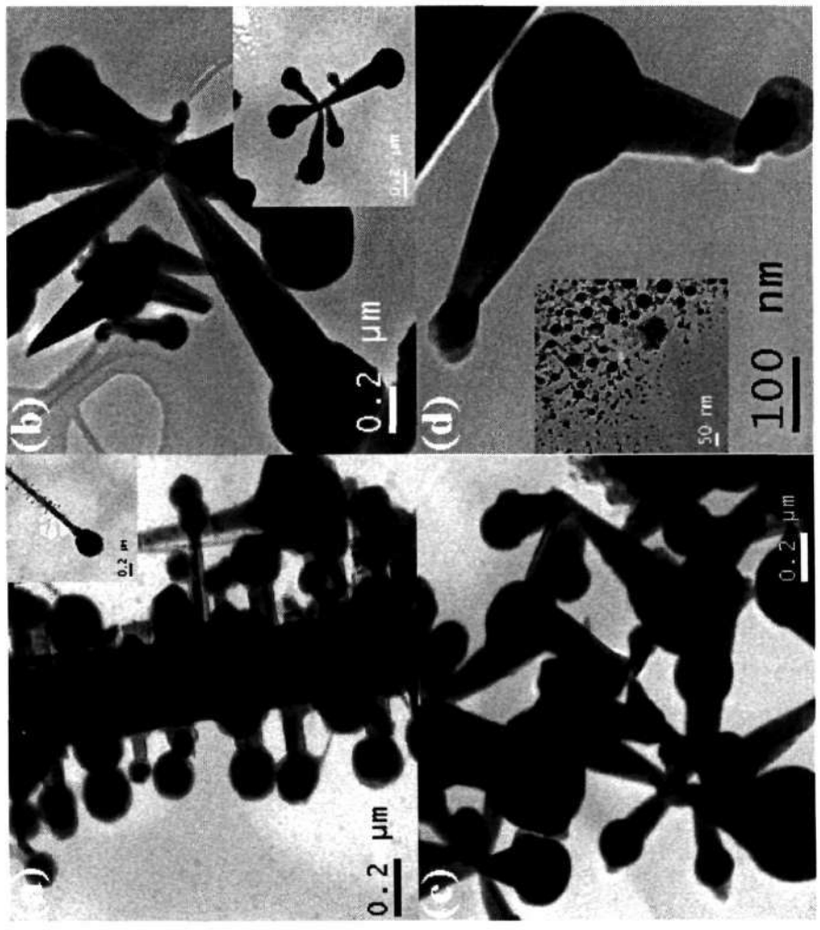

Figure 3.25: TEM images of In_2O_3 nanostructures: (a) nanotrees, (b) and (c) nanobouquets, (d) a highway-type branch structure. Inset in (d) shows short nanowires as pegs or nails.

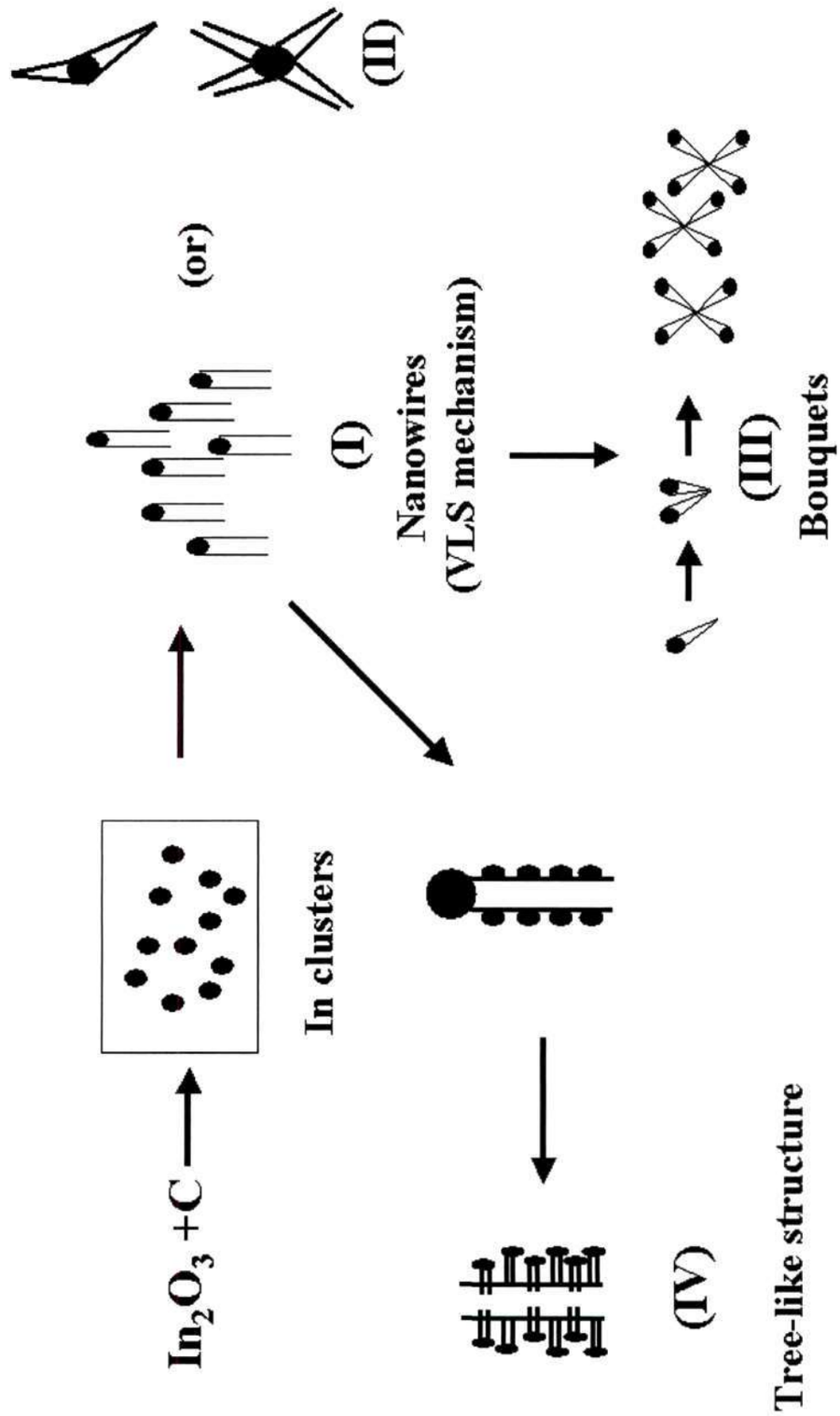

Figure 3.26: Schematic showing the formation of various In_2O_3 nanostructures.

vapor form droplets which form nanowires just as in the case of Si. The nanowire gets oxidized under ambient conditions.

Thus, in the synthesis of the In_2O_3 nanostructures we have varied parameters such as the source of In and the flow rates of the gas. Interestingly, at high flow rates we observe various nanostructures such as the nanotrees and nanobouquets. At very high flow rates, we encounter nanostrutures with multiple arms. In all of this, the self-assisted VLS mechanism seems to be operative aided by the carbothermal reduction, which is the first step in the formation of these nanostructures. The formation of In_2O_3 nanowires starting from In, on the other hand, can be understood in terms of the VS mechanism.

3.4.5 Dispersion of oxide nanowires in polar solvents

The dispersions of the various oxide nanowires in the polar solvents showed interesting features as found from electron microscopy and PL spectroscopy. Dispersions of Al_2O_3 nanowires in DMF were stable upto 24 h in contrast to those in DMSO and acetonitrile which were not stable, with the sedimentation starting much earlier. In the case of acetonitrile, the sedimentation started just after it is allowed to stand. MgO nanowires dispersed in DMF are more stable upto 12 h in comparison to DMSO and acetonitrile. Starting with a known amount of Al_2O_3 nanowires dispersed in the various solvents, we measured the proportion of solute in the solvent at the end of 60 h and found that DMF and DMSO have about 6 % of the solute remaining in solution, whereas in the case of acetonitrile it was 3 % or less. Visual observations indicated that DMF forms the best dispersions in comparison to DMSO and acetonitrile. In the case of ZnO nanowires dispersed in DMF, the proportion of solute

remaining in the solvent was about ~ 9 %. Such a high percentage of solute stably dispersed in the solvent is useful for several measurements and applications, which cannot otherwise be achieved in the solid state.

In Figure 3.27 (a), we show the SEM image of the starting Al_2O_3 nanowires. The nanowires occur individually and in large bundles. In Figure 3.27 (b), we show the SEM image of the nanowire dispersion in DMF obtained after 60 h. The presence of large bundles of the nanowires can be seen, indicating the stability of the bundles of nanowires in the dispersion. The SEM image in Figure 3.27 (c) shows the Al_2O_3 nanowires dispersed in DMSO after a period of 36 h. The image reveals smaller bundles and isolated nanowires, in contrast to that in DMF. The SEM image of the dispersion of the Al_2O_3 nanowires in acetonitrile obtained after 60 h is shown in Figure 3.27 (d), revealing isolated individual nanowires in large numbers. The SEM image of the sediment obtained from acetonitrile after 12 h is shown in Figure 3.27 (e). Large bundles of nanowires are seen in the sediment in contrast to the dispersion. The SEM image in Figure 3.28 (a) shows the raw MgO nanowires used for the study. The nanowires extend to several microns in length. The TEM image of the MgO nanowires in DMF shown in Figure 3.28 (b) reveals nanowires of uniform diameter of 150-200 nm obtained in the dispersion at a time period of 24 h. The dispersion of the ZnO nanowires obtained in DMF after a time period of 24 h and the sediment after 12 h are shown in SEM image of Figure 3.28 (c) and (d) respectively. The SEM image in Figure 3.28 (c) reveals the presence of bundles of nanowires, whereas the image of the sediment in Figure 3.28 (d) reveals the presence of a few isolated nanowires (along with other types of particles) that seem to have been excluded from the dispersion during the course of time. Thus, sedimentation studies have shown that in

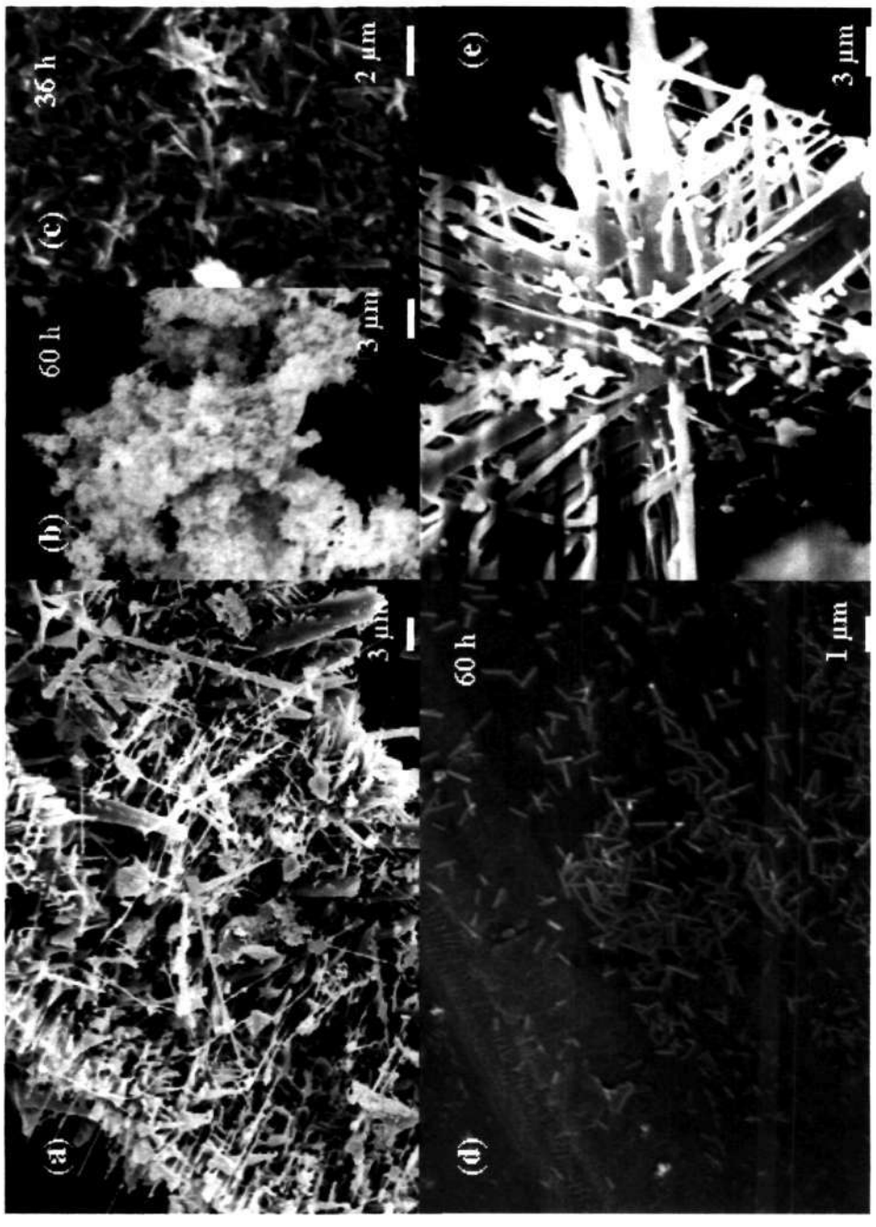

Figure 3.27: SEM images of (a) starting Al_2O_3 nanowires. (b), (c) and (d) dispersions of Al_2O_3 nanowires in DMF, DMSO and acetonitrile respectively. (e) Sediment obtained from acetonitrile.

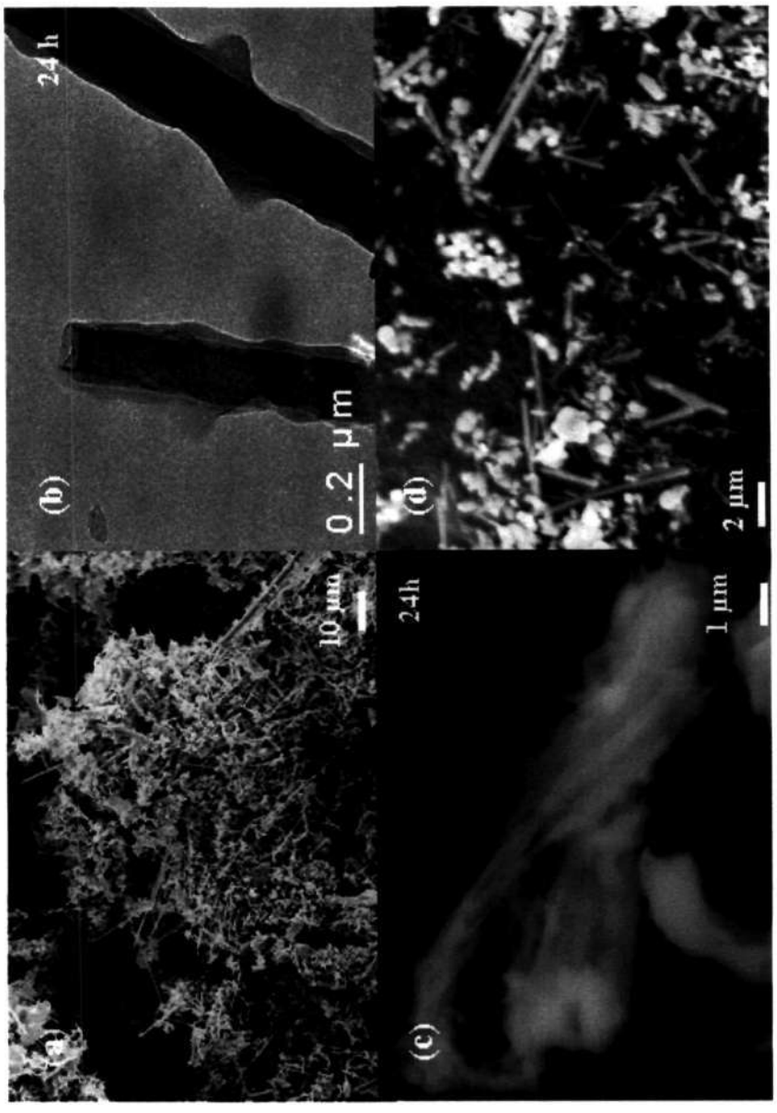

Figure 3.28: SEM images of (a) raw MgO nanowires, (b) TEM image of MgO nanowire dispersion in DMF, (c) ZnO nanowire dispersion in DMF, (d) SEM image of the sediment of ZnO nanowires.

general DMF is a good solvent for obtaining stable dispersions of the nanowires. In comparison, DMSO and acetonitrile may not be as suitable, acetonitrile being the poorest solvent of the three.

The PL spectra of the dispersions of Al_2O_3 nanowires excited at 300 nm are shown in Figure 3.29. Shown in the inset is the spectrum of the Al_2O_3 nanowires in the solid state. The spectrum in the solid state reveals two bands at 380 nm and 420 nm which are generally known to arise from oxygen-related defects [1,2,38]. The nanowire dispersion in DMF shows two sharp and clear bands at 408 nm and 430 nm, slightly red-shifted from the spectrum of solid Al_2O_3. The spectrum of the dispersion in DMSO shows weak features which are slightly red-shifted relative to the bands in DMF. Thus, the peak positions in DMSO are 410 nm and 435 nm. The spectrum of the dispersion in acetonitrile shows several bands between 400-450 nm in the region extending upto 475 nm which may arise from isolated nanowires.

The PL spectra of the ZnO nanowire dispersions (Figure 3.30) show interesting features (excitation wavelength, 280 nm). The solid spectrum shows a peak at 395 nm and a shoulder around 420 nm the emission corresponding to near-band edge emission in the case of ZnO [1,2] (inset of Figure 3.30). The PL spectrum of the nanowires in DMF shows slight red-shifts with the peak positions at 406 nm and 429 nm. The presence of clear and intense bands in this case is noteworthy. In the case of the nanowire dispersions in DMSO, there is a band centered at 420 nm and a shoulder at 435 nm. The acetonitrile dispersion shows only a small feature centered at 420 nm.

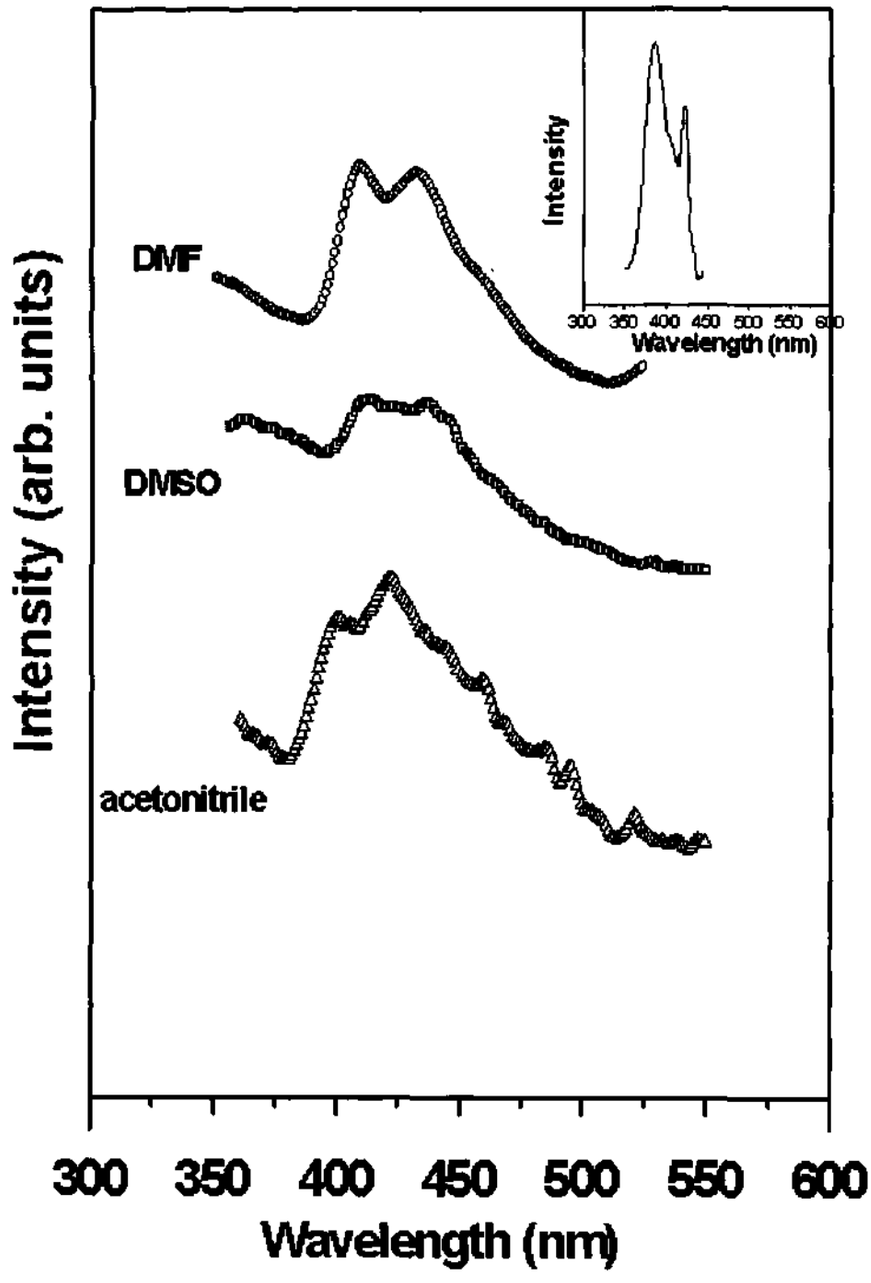

Figure 3.29: PL spectra of Al_2O_3 nanowire dispersions in the various polar solvents. Inset shows the PL spectrum in the solid state.

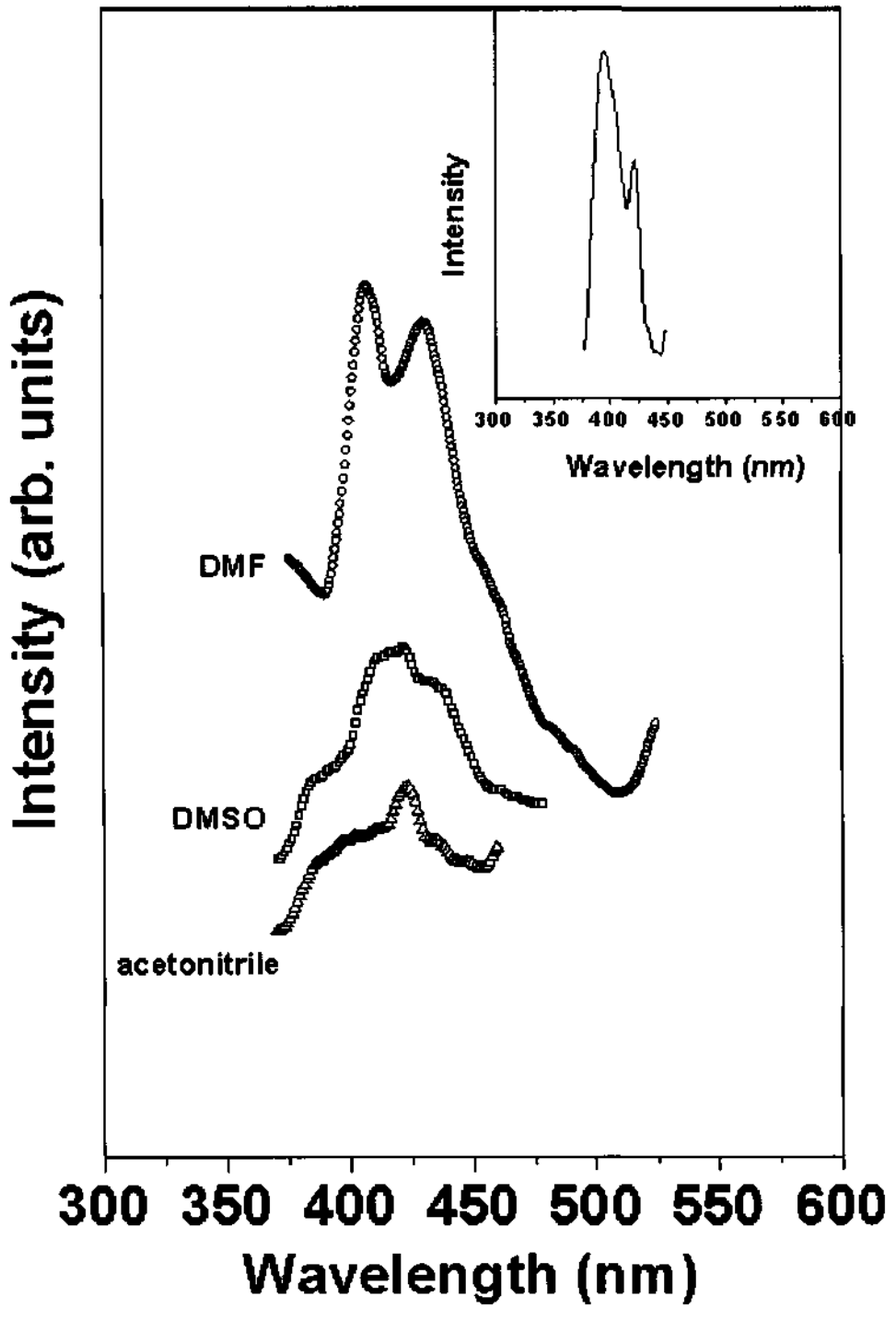

Figure 3.30: PL spectra of ZnO nanowire dispersions in the various polar solvents. Inset shows the PL spectrum in the solid state.

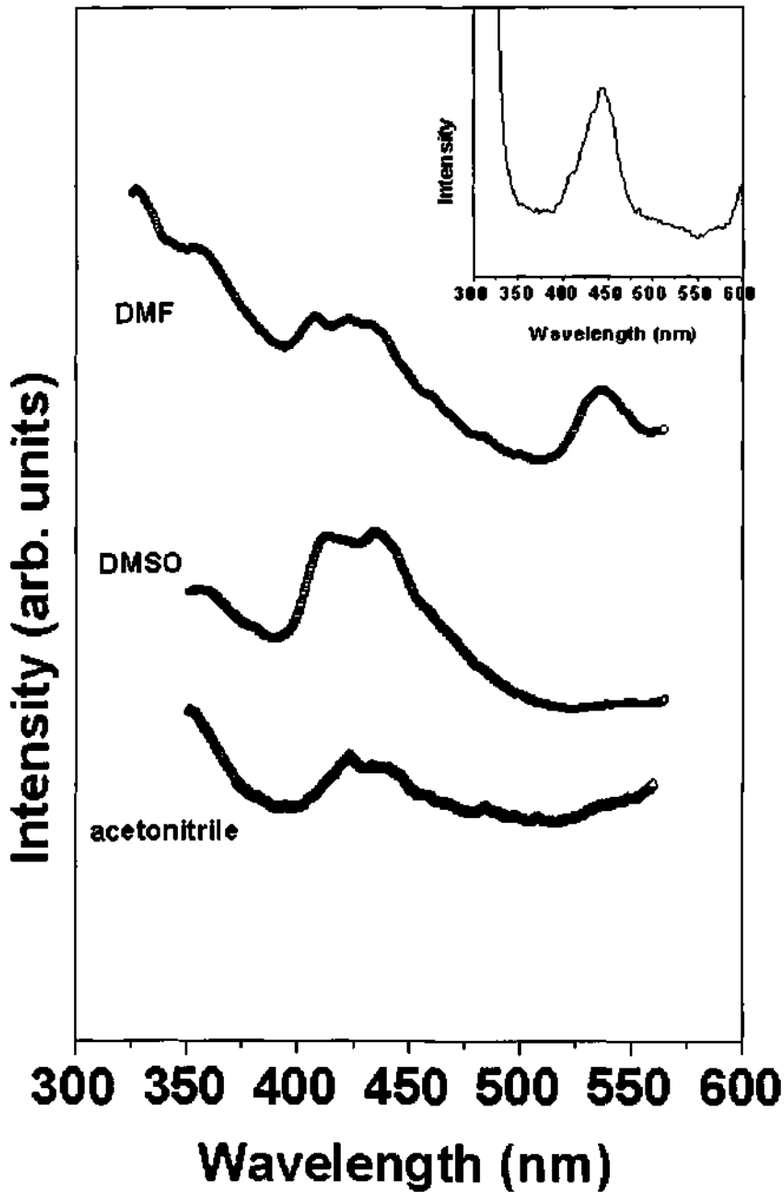

Figure 3.31: PL spectra of MgO nanowire dispersions in the various polar solvents. Inset shows the PL spectrum in the solid state.

The PL spectrum of solid MgO (see inset of Figure 3.31) shows a peak at 443 nm, (excitation wavelength, 300 nm), the emission corresponding to oxygen vacancies. The PL spectrum of the nanowires in DMF shows two peaks around 406 nm and 430 nm. In addition, there is a band around 535 nm. These emission bands have been reported previously in the case of bulk MgO by Rosenblatt and coworkers [71]. In the case of DMSO dispersions, there is a slight red shift with peaks appearing at 411 nm and at 435 nm. The dispersion of the nanowires in acetonitrile shows several features centered around 430 nm (Figure 3.31).

3.5 Conclusions

We have been able to synthesize one-dimensional nanostructures of MgO, Al_2O_3, SiO_2 and In_2O_3 by a simple carbothermal procedure involving the use of carbon as one of the reactants. The method that we have used is simple and avoids contamination due to external catalysts. It also provides some insight into the mechanism of formation of the nanowires. Crystalline silica nanowires (α-cristobalite) have been synthesized for the first time by this method. Apart from this a variety of novel and interesting nanostructures have been obtained in large quantities for the first time. These nanostructures could be of use in sensors and other devices. Thus this method offers a wide scope for the preparation of many other oxide nanowires in significant amounts for a variety of applications. Investigations of the dispersions of Al_2O_3, MgO and ZnO nanowires in polar solvents by electron microscopy and PL spectroscopy have revealed that of the solvents that have been examined, DMF seems to be the best for obtaining stable nanowire dispersions, although acetonitrile dispersions in the case of Al_2O_3 nanowires may represent

features of isolated nanowires. Stable oxide nanowire dispersions in DMF should be useful not only to investigate the properties but also in some applications.

3.6 References

[1] See, for example, Special issue on nanowires, *Adv. Mater.*, 2003, **15**.

[2] C. N. R. Rao, F. L. Deepak, G. Gundiah, A. Govindaraj, *Prog. Solid. State. Chem.*, 2003, **31**, 5.

[3] G. Gundiah, A. Govindaraj, C. N. R. Rao, *Chem. Phys. Lett.*, 2002, **351**, 189.

[4] G. Gundiah, G. V. Madhav, A. Govindaraj, Md. Motin Seikh, C. N. R. Rao, *J. Mater. Chem.*, 2002, **12**, 1606.

[5] W. Yi, S. Yu, W. Lee, I. T. Han, T. Jeong, Y. Woo, J. Lee, S. Jin, W. Choi, J. Heo, D. Jeon, J. M. Kim, *J. Appl. Phys.*, 2001, **89**, 4091.

[6] F. S. Galasso, *Structure and Properties of Inorganic Solid*, Pergamon, New York, 1970.

[7] (a) P. Yang, C. Lieber, *Science*, 1996, **273**, 1836, (b) P. Yang, C. Lieber, *J. Mater. Res.*, 1997, **12**, 2981.

[8] (a) C. O. House, *J. Am. Ceram. Soc.*, 1961, **44**, 572, (b) Z. Wei, H. Qi, P. Ma, J. Bao, *Inorg. Chem. Commun.*, 2002, **5**, 147.

[9] Y. Q. Zhu, W. K. Hsu, W. Z. Zhou, M. Terrones, H. W. Kroto, D. R. M. Walton, *Chem. Phys. Lett.*, 2001, **347**, 337.

[10] Z. Cui, G. W. Meng, W. D. Huang, G. Z. Wang, L. D. Wang, *Mater. Res. Bull.*, 2000, **35**, 1653.

[11] J. Zhang, L. Zhang, X. Peng, X. Wang, *Appl. Phys. A*, 2001, **73**, 773.

[12] Y. Li, Y. Bando, T. Sato, *Chem. Phys. Lett.*, 2002, **359**, 141.

[13] H. Y. Dang, J. Wang, S. S. Fang, *Nanotechnology*, 2003, **14**, 738.

[14] C. Tang, Y. Bando, T. Sato, *J. Phys. Chem. B*, 2002, **106**, 7449.

[15] Y. Yin, G. Zhang, Y. Xia, *Adv. Funct. Mater.*, 2002, **12**, 293.

[16] J. Zhang, L. Zhang, *Chem. Phys. Lett.*, 2002, **363**, 293.

[17] R. Ma, Y. Bando, *Chem. Phys. Lett.*, 2003, **370**, 770.

[18] (a) K. L. Klug, V. P. Dravid, *Appl. Phys. Lett.*, 2002, **81**, 1687, (b) M. Zhao, X. L. Chen, X. N. Zhang, H. Li, H. Q. Li, L. Wu, *Chem. Phys. Lett.*, 2004, **388**, 7.

[19] Z. Zhou, S. Xie, D. Wan, D. Liu, Y. Gao, X. Yan, H. Yuan, J. Wang, L. Song, W. Zhou, Y. Wang, H. Chen, J. Li, *Solid State Commun.*, 2004, **131**, 485.

[20] J. Zhan, Y. Bando, J. Hu, D. Goldberg, *Inorg. Chem.*, 2004, **43**, 2462.

[21] Y. B. Li, Y. Bando, D. Golberg, Z. W. Liu, *Appl. Phys. Lett.*, 2003, **83**, 999.

[22] Y. Chen, J. Li, Y. Han, X. Yang, J. Dai, *J. Cryst. Growth*, 2002, **245**, 163.

[23] H. Liu, Y. Li, L. Jiang, H. Luo, S. Xiao, H. Fang, H. Li, D. Zhu, J. Xu, B. Xiang, *J. Am. Chem. Soc.*, 2002, **124**, 13370.

[24] Z. Zhang, R. W. Hicks, T. R. Pauly, T. J. Pinnavaia, *J. Am. Chem. Soc.*, 2002, **124**, 1592.

[25] H. Y. Zhu, J. D. Riches, J.C. Barry, *Chem. Mater.*, 2002, **14**, 2086.

[26] S. S. Berdonosov, S. B. Baronov, Yu. V. Kuzmicheva, D. G. Berdonosova, I. V. Melikhov, *Inorg. Mater.*, 2001, **37**, 1037.

[27] Z. Q. Yu, Y. W. Du, *J. Mater. Res.*, 1998, **13**, 3017.

[28] B. C. Satishkumar, A. Govindaraj, E. M. Vogl, L. Basumallick, C. N. R. Rao, *J. Mat. Res.*, 1997, **12**, 604.

[29] Y. Zhang, J. Liu, R. He, Q. Zhang, X. Zhang, J. Zhu, *Chem. Phys. Lett.*, 2002, **360**, 579.

[30] G. Hornyak, M. Kroll, R. Pugin, T. Sawitowski, G. Schmid, J-O. Bovin, G. Karsson, H. Hofmeister, S. Hopfe, *Chem. Eur. J.*, 1997, **12**, 1951.

[31] L. Pu, X. Bao, J. Zou, D. Feng, *Angew. Chem. Intl. Ed.*, 2001, **40**,

1490.

[32] J. Zou, L. Pu, X. Bao, D. Feng, *Appl. Phys. Lett.*, 2002, **80**, 1079.

[33] Z. L. Xiao, C. Y. Han, U. Welp, H. H. Wang, W. K. Kwok, G. A. Willing, J. M. Hiller, R. E. Cook, D. J. Miller, G. W. Crabtree, *Nano. Lett.*, 2002, **2**, 1293.

[34] Z. Yuan, H. Huang, S. Fan, *Adv. Mater.*, 2002, **14**, 303.

[35] V. Valcarcel, A. Souto, F. Guitian, *Adv. Mater.*, 1998, **10**, 138.

[36] C. C. Tang, S. S. Fan, P. Li, M. Lamy de la Chapelle, H. Y. Dang, *J. Cryst. Growth*, 2001, **224**, 117.

[37] J. Zhou, S. Z. Deng, J. Chen, J. C. She, N.S. Xu, *Chem. Phys. Lett.*, 2002, **365**, 505.

[38] X. S. Peng, L. D. Zhang, G. W. Meng, X. F. Wang, Y. W. Wang, C. Z. Wang, G. S. Wu, *J. Phys. Chem. B*, 2002, **106**, 11163.

[39] H. C. Lee, H. J. Kim, S. H. Chung, K. H. Lee, H. C. Lee, J. S. Lee, *J. Am. Chem. Soc.*, 2002, **125**, 2882.

[40] J. Zygmunt, F. Krumeich, and R. Nesper, *Adv. Mater.*, 2003, **15,** 1538.

[41] C. N. R. Rao and M. Nath, *Dalton Trans.*, 2003, **1,** 1.

[42] Z. L. Wang, *Adv. Mater.*, 2003, **15,** 432.

[43] B. Zheng, Y. Wu, P. Yang, and J. Liu, *Adv.Mater.*, 2002, **14,** 122.

[44] Z. W. Pan, Z. R. Dai, C. Ma, and Z. L. Wang, *J. Am. Chem. Soc.*, 2002, **124,** 1817.

[45] S. Sun, G. Meng, M. Zhang, Y. Hao, X. Zhang, and L. Zhang, *J. Phys. Chem. B*, 2003, **107,** 13029.

[46] D. P. Yu, Q. L. Hang, Y. Ding, H. Z. Zhang, Z. G. Bai, J. J. Wang, Y. H. Zou, W. Qian, G. C. Xiong, and S. Q. Feng, *Appl. Phys. Lett.*, 1998, **73,** 3076.

[47] J. Q. Hu, Y. Ziang, X. M. Meng, C. S. Lee, and S. T. Lee, *Chem.Phys. Lett.*, 2003, **367**, 339.

[48] Y. W. Wang, C. H. Liang, G. W. Meng, X. S. Peng, and L. D. Zhang, *J. Mater. Chem.*, 2002, **12**, 651.

[49] K. S. Wenger, D. Cornu, F. Chassagneux, T. Epicier, and P. Miele, *J. Mater. Chem.*, 2003, **13**, 3058.

[50] K. H. Lee, H. S. Yang, K. H. Baik, J. Bang, R. R. Vanfleet, and W. Sigmund, *Chem. Phys. Lett.*, 2004, **383**, 380.

[51] R. Fan, Y. Wu, D. Li, M. Yue, A. Majumdar, and P. Yang, *J. Am. Chem. Soc.*, 2003, **125**, 5254.

[52] D. Zhang, C. Li, S. Han, X. Liu, T. Tang, W. Jin, C. Zhou, *Appl. Phys. Lett.*, 2003, **82**, 112.

[53] C. Li, D. Zhang, X. Liu, S. Han, T. Tang, J. Han, W. Jin, C. Zhou, *Appl. Phys. Lett.*, 2003, **82**, 112.

[54] C. Liang, G. Meng, Y. Lei, F. Phillipp, L. Zhang, *Adv. Mater.*, 2001, **13**, 1330.

[55] M. J. Zheng, L. D. Zhang, G. H. Li, X. Y. Zhang, X. F. Wang, *Appl. Phys. Lett.*, 2001, **79**, 839.

[56] X. S. Peng, G. W. Meng, J. Zhang, X. F. Wang, Y. W. Wang, C. Z. Wang, L. D. Zhang, *J. Mater. Chem.*, 2002, **12**, 602.

[57] C. Li, D. Zhang, S. Han, X. Liu, X. Liu, T. Tang, C. Zhou, *Adv. Mater.*, 2003, **15**, 143.

[58] J. Lao, J. Huang, D. Wang, Z. Ren, *Adv. Mater.*, 2004, **16**, 65.

[59] M. J. O'Connell, S. M. Bachilo, C. B. Huffman, V. C. Moore, M. S. Strano, E. H. Haroz, K. L. Rialon, P. J. Boul, W. H. Noon, C. Kittrell, J. Ma, R. H. Hauge, R. B. Weisman, R. E. Smalley, *Science*, 2002, **297**, 593.

[60] R. Krupke, F. Hennrich, H. v. Löhneysen, M. M. Kappes, *Science*, 2003, **301**, 344.

[61] S. M. Bachilo, M. S. Strano, C. Kittrell, R. H. Hauge, R. E. Smalley, R. B. Weisman, *Science*, 2002, **298**, 2361.

[62] Y. Lin, S. Taylor, W. Huang, Y -P. Sun, *J. Phys. Chem. B*, 2003, **107**, 914.

[63] S. M. O'Flaherty, R. Murphy, S. V. Hold, M. Cadek, J. N. Coleman, W. J. Blau, *J. Phys. Chem. B*, 2003, **107**, 958.

[64] S –Y. Xie, W. Wang, K. A. S. Fernando, X. Wang, Y. Lin and Y –P. Sun, *Chem. Commun.*, 2005, 3670.

[65] V. Nicolosi, D. Vrbanic, A. Mrzel, J. McCauley, S. O'Flaherty, C. McGuinness, G. Compagnini, D. Mihailovic, W. J. Blau, J. N. Coleman, *J. Phys. Chem. B*, 2005, **109**, 7124.

[66] V. Nicolosi, D. Vrbanic, A. Mrzel, J. McCauley, S. O'Flaherty, D. Mihailovic, W. J. Blau, J. N. Coleman, *Chem. Phys. Lett.*, 2005, **401**, 13.

[67] A. van der Horst, D. L. J. Vossen, K. Visscher, M. Dogterom and A. von Blaaderen, *Microscopy and analysis*, 2005, **44**, 15.

[68] X. C. Wu, W. H. Song, W. D. Huang, M. H. Pu, B. Zhao, Y. P. Sun and J. J. Du, *Mater. Res. Bull*, 2001, **36**, 847.

[69] R. Seshadri, A. Govindaraj, H. N. Aiyer, R. Sen, G. N. Subbanna, A. R. Raju, C. N. R. Rao, *Current Sci.*, 1994, **66**, 839.

[70] J. Q. Hu, Q. Li, X. M. Meng, C. S. Lee, S. T. Lee, *Adv. Mater.*, 2002, **14**, 1396.

[71] G. H. Rosenblatt, M. W. Rowe, G. P. Williams Jr., R. T. Williams, Y. Chen, *Phys. Rev. B*, 1989, **39**, 10309.

[72] R. S. Wagner, W. C. Ellis, *Appl. Phys. Lett.*, 1964, **4**, 89.

[73] Z. L. Wang, Z. Pan, *Adv. Mater.*, 2002, **14**, 1029.

[74] P. Gao, Z. L. Wang, *J. Phys. Chem. B*, 2002, **106**, 12653.

[75] J. Y. Lao, J. Y. Huang, D. Z. Wang, Z. F. Ren, *Nano. Lett.*, 2002, **3**, 235.

[76] H. Y. Peng, N. Wang, X. T. Zhou, Y. F. Zheng, C. S. Lee, S. T. Lee, *Chem. Phys. Lett.*, 2004, **359**, 241.

[77] S. M. Zhou, Y. S. Feng, L. D. Zhang, *Chem. Phys. Lett.*, 2003, **369**, 610.

[78] I. P. Swainson, M. T. Dove, and D. C. Palmer, *Phys. Chem. Miner.*, 2003, **30,** 353.

[79] V. N. Sigaev, E. N. Smelyanskaya, V. G. Plotnichenko, V. V. Koltashev, A. A. Volkov, P. Pernice, *J. Non-Cryst. Solids,* 1999, **248,** 141.

[80] N. N. Greenwood and A. Earnshaw, Chemistry of the Elements, 2nd ed. (Butterworth Heinemann, U.K.), pp. 343.

[81] Y. Yin and Y. Xia, *Adv. Funct. Mater.*, 2002, **12,** 293.

[82] Z. W. Pan, Z. R. Dai, C. Ma, and Z. L. Wang, *J. Am. Chem. Soc.*, 2002, **124,** 1817.

[83] J. Zhang, X. Qing, F. Jiang, Z. Dai, *Chem. Phys. Lett.*, 2003, **371**, 311.

[84] J. S. Jeong, J. Y. Lee, C. J. Lee, S. J. An, G. –C. Yi, *Chem. Phys. Lett.*, 2004, **384**, 246.

[85] Y. Ohhata, F. Shinoki, S. Yoshida, *Thin Solid Films*, 1979, **59**, 255.

[86] H. Zhou, W. Cai, L. Zhang, *Appl. Phys. Lett.*, 1999, **75**, 495.

[87] Y. Li, Y. Bando, D. Goldberg, *Adv. Mater.*, 2003, **15**, 581.

[88] S. Sharma, M. K. Sunkara, *J. Am. Chem. Soc.*, 2002, **124**, 12288.

[89] Y. Chen, X. Cui, K. Zhang, D. Pan, S. Zhang, B. Wang, J.G. Hou, *Chem. Phys. Lett.*, 2003, **369**, 16.

[90] H. Y. Dang, J. Wang, S. S. Fan, *Nanotechnology*, 2003, **14**, 738.

Chapter 4

BN, GaN, InN nanowires and related nanostructures

Summary*

In this chapter, the synthesis and properties of nanostructures of III-V nitrides such as BN, GaN, InN and related materials are presented. In the case of BN, simple methods of preparing nanotubes and nanowires have been investigated. The methods involve heating boric acid with activated carbon, multi-walled carbon nanotubes, catalytic iron particles or a mixture of activated carbon and iron particles, in the presence of NH_3. While with activated carbon, BN nanowires constitute the primary product, high yields of clean BN nanotubes are obtained with multi-walled carbon nanotubes. Aligned BN nanotubes are produced when aligned multi-walled carbon nanotubes are employed as the starting material suggesting the templating role of the carbon nanotubes. BN nanotubes with different structures have been obtained by reacting boric acid with NH_3 in the presence of a mixture of activated carbon and Fe particles.

Single crystal GaN nanowires have been obtained by heating gallium acetylacetonate [$Ga(acac)_3$] with NH_3 in the presence of carbon nanotubes or activated carbon at 910 °C. GaN nanowires were also obtained when the reaction of $Ga(acac)_3$

* Papers based on these studies have appeared in J. Nanosci. Nanotech. (2001), Chem. Phys. Lett. (2002), (2003), Solid. State. Sci. (2004) and Small (2005).

with NH_3 was carried out over catalytic Fe/Ni particles dispersed over silica. In order to tune the diameter of the nanowires, we have carried out the synthesis by employing single-walled carbon nanotubes or by varying the proportion of the metal catalyst. The former procedure with carbon nanotubes is preferable because it avoids the presence of metal particles in the nanowire bundles.

Mn-doped GaN nanowires have been prepared by reacting a mixture of acetylacetonates with NH_3 at 950 °C in the presence of multi-walled (MWNTs) and single-walled (SWNTs) carbon nanotubes, the nanowires prepared with SWNTs being considerably smaller in diameter. GaMnN nanowires with 1%, 3% and 5% Mn so obtained have been characterized by X-ray diffraction, EDAX analysis and photoluminescence (PL) spectra. The GaMnN nanowires are all ferromagnetic even at 300 K, exhibiting magnetic hysteresis. The PL spectra of the GaMnN nanowires prepared with SWNTs show a large blue-shift of the Mn^{2+} emission.

Various methods have been employed to prepare nanostructured GaN exhibiting reasonable surface areas. The methods include ammonolysis of γ-Ga_2O_3 or Ga_2O_3 prepared in the presence of a surfactant, and the reaction of a mixture of Ga_2O_3 and $Ga(acac)_3$ with NH_3. The latter reaction was also carried out in the presence of H_3BO_3. All the methods yield good GaN samples as characterized by X-ray diffraction, electron microscopy and photoluminescence measurements. Relatively high surface areas were obtained with the GaN samples prepared by the ammonolysis of γ-Ga_2O_3 (53 $m^2\ g^{-1}$), and of Ga_2O_3 prepared in the presence of a surfactant (66 $m^2\ g^{-1}$). GaN obtained by the reaction of NH_3 with a mixture of Ga_2O_3, $Ga(acac)_3$ and boric acid gave a surface area of 59 $m^2\ g^{-1}$. GaN nanoparticles prepared by the nitridation of mesoporous Ga_2O_3 samples generally retain some porosity.

Owing to the importance of InN as an electronic material, we considered it important to carry out a systematic investigation of the nanostructures produced at relatively low temperatures, with specific interest in the optical properties. We report a study of nanowires and nanotubes of InN synthesized at low temperatures by a new chemical route involving the use of indium acetate and 1,1,1,3,3,3-hexamethyl disilazane (HMDS). The nanostructures have been characterized by X-ray diffraction, electron microscopy, and various spectroscopic methods. It has been shown that the near-infrared band around 0.7 eV is characteristic of these materials.

4.1 Introduction

III-V semiconductors are compounds comprising elements of groups III (e.g. gallium or indium) and V (e.g. arsenic or phosphorous) of the periodic table (Figure 4.1). Many of these compounds, for example gallium arsenide (GaAs) or indium phosphide (InP) are materials used for high-frequency (e.g. high-bandwidth connectivity) or optoelectronic (e.g. integrated optics or LEDs) applications. III-V nitride semiconductor materials are unique in their ability to reliably and efficiently emit light with wavelengths from green through ultraviolet. III- V nitride-based optoelectronics are emerging as an important enabling technology with a wide range

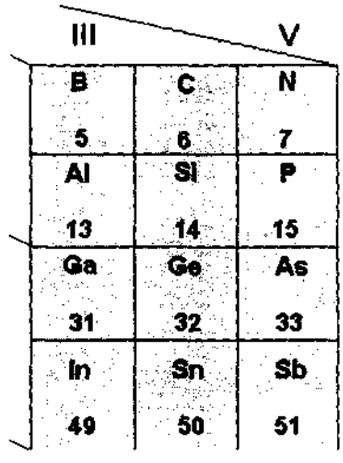

Figure 4.1: Periodic table of III-V semiconductors.

of applications, from traffic lights and large outdoor full-color displays to high-density digital video disk (HD DVD) players and laser printers. Although nitride-based light-emitting diodes (LEDs) have been commercially available since 1993, many problems remain that have prevented the full realization of optoelectronic devices from this material system. The III-V nitrides have not only become

technologically important for optoelectronics and high power electronics, but also a fast growing and exciting area of research [1,2].

III-V semiconductor nanowires have unique electrical and optical properties, which are used as building blocks in nanoscale devices. Nanowires especially those of III-V semiconductors are increasingly used in electronic devices including field-effect transistors, sensors, detectors and light-emitting diodes. More complicated devices are expected soon, requiring new and improved ways of growing such wires. Researchers have examined various ways of growing III-V semiconductor nanowires, including laser ablation, chemical vapor deposition (CVD) and template-assisted growth. We have been interested in preparing III-V semiconductor nitride nanowires and nanotubes of BN, GaN and InN by simple chemical routes at low temperatures. We have been successful in synthesizing large quantities of these nitride nanostructures by a variety of methods. Moreover we have studied their optical properties and understood their mechanism of growth. More importantly we have also been able to dope nanowires of GaN for instance with Mn and have studied their magnetic properties. We have been able to synthesize porous nanostructured GaN and have studied their adsorption properties also. In what follows we describe the scope of the investigations on these systems.

4.2 Scope of the present investigations

(a) Boron Nitride

Boron Nitride is isoelectronic with carbon, and like carbon, its properties are highly dependent on the crystalline modification under study. The structure of h-BN is analogous to the graphitic form of carbon, with strong bonding within the atomic

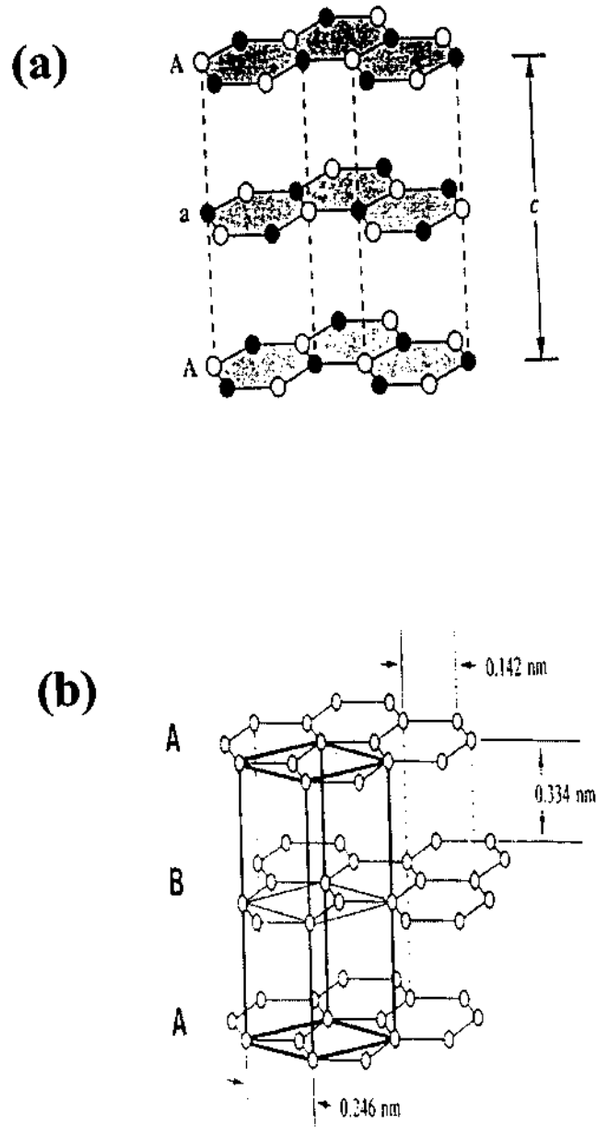

Figure 4.2: (a) Structure of hexagonal BN, closed circles: B, open circles: N (b) Structure of graphite.

layers and weak bonding between layers, the h-BN differs by having the planar, fused, six-membered rings directly stacked on top of each other, with the boron atoms in one layer serving as the nearest neighbour to the N atoms in adjacent layers (Figure 4.2 (a)). In the graphitic carbon structure, the carbon atoms in adjacent layers are slightly offset (Figure 4.2 (b)). The layered structures of BN and graphite, with very strong in-plane covalent bonding and weak interplanar attractions, are unique in ceramic materials, and this feature results in a number of quite anisotropic mechanical, thermal and electrical properties.

Boron Nitride nanotubes have a band gap of 5.5 eV (versus 5.8 eV for bulk hexagonal BN) and the gap is nearly independent of tube diameter, chirality and the number of tube walls. The measured Young's modulus (1.22 Tpa) of BN nanotube exceeds those of all known insulating fibers. Thus a BN nanotube may serve as a perfect insulating tubular shield for any conducting material encapsulated within. The calculated uniform electronic properties of BN tubes contrast sharply with the heterogeneity of carbon tubes and other carbon-containing tubes such as those formed from BC_2N and BC_3, suggesting that BN tubes may have significant advantages for applications. Nanotubes and nanorods of boron nitride (BN) have attracted considerable attention in the last two years. Nanotubes of boron nitride were first prepared by Chopra *et al.* [3] by a carbon-free plasma discharge between a BN packed tungsten rod and a cooled copper electrode. Arc discharge between ZrB_2 electrodes in a nitrogen atmosphere also yields BN nanotubes [4]. BN nanotubes have been prepared by the carbothermal reduction of ultradisperse amorphous boron oxide and B_4C in the presence of nitrogen between 1100 and 1450 °C [5], and by thermal annealing of ball-milled boron powder in an ammonia atmosphere [6]. Most of the

recent efforts, however, employ chemical methods involving suitable catalysts. Thus, Lourie *et al.* [7] have synthesized BN nanotubes by the CVD deposition of borazine over nickel boride catalyst particles at a temperature of about 1100 °C. A chemical vapor deposition route employing melaminediborate at 1700 °C yields BN nanotubes, although the material occurs along with amorphous B-N-O clusters [8]. Carbon nanotubes have been used to prepare BN nanotubes by the reaction with B_2O_3 in a nitrogenous atmosphere. Thus, Golberg *et al.* [9] have synthesized multi-walled BN nanotube ropes by carrying out the reaction of a mixture of B_2O_3 and MWNTs at 1500 °C in a nitrogen atmosphere in the presence of a MoO_3 catalyst. Tang *et al.* [10] have obtained nanotube and nanobamboo structures of boron nitride by the reaction of boron and iron oxide in flowing ammonia gas in the 1200 –1500 °C range. It was our interest to develop simple chemical methods for preparing BN nanotubes and nanowires and hence we have explored various strategies for this purpose. We find that a variety of BN nanotubes and nanowires can be readily produced by the reaction of boric acid with ammonia in the presence of activated carbon or carbon nanotubes, with or without catalytic iron particles. By using aligned carbon nanotube bundles, we have obtained aligned BN nanotubes. Furthermore, the temperature of the reaction can be as low as 1000 °C. In these preparations, NH_3 acts as a nitriding agent and also provides the reducing atmosphere, required for the reaction.

(b) Gallium Nitride

GaN is a wide band gap semiconductor (~ 3.4 eV), generally having the wurtzite structure (Figure 4.3). Gallium nitride is one of the important materials today

because of its applications in light emitting diodes, laser diodes, field–effect transistors and a variety of other electronic and opto-electronic devices [11,12].

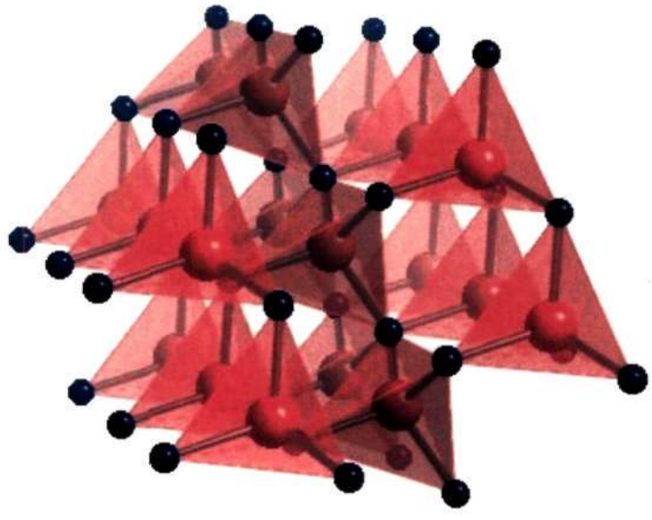

Figure 4.3: Structure of GaN.

There has been much activity in the preparation of quantum-dot and quantum-well structures of GaN in recent years, and the preparation of nanowires is also attracting interest. GaN nanowires of 4-50 nm diameter were prepared by Han *et al.* [13] by the reaction of gallium sub-oxide (Ga_2O) vapor with NH_3 gas in the presence of carbon nanotubes. GaN nanowires of 14 nm diameter were prepared by Cheng *et al.* by gas phase reaction of Ga_2O vapor with NH_3 in an anodic alumina membrane [14]. The growth direction was ascertained by neither Han *et al.* [13] nor Cheng *et al.* [14]. GaN nanowires (10–40 nm dia.) are formed by the reaction of Ga and NH_3 over catalytic nickel nanoparticles deposited on solid substrates [15], where the direction of the growth of the fiber is along [120], whereas nanowires of 20–50 nm diameter are

obtained by the reaction of molten gallium with ammonia in the presence of polycrystalline indium powder [16]. Single crystal GaN nanowires (10 nm dia.) with a growth direction along [100] have been prepared by laser-assisted catalytic growth, wherein a pulsed laser is used to vaporize a solid target containing GaN and a Fe catalyst [17]. Hot filament chemical vapor deposition in ammonia atmosphere, employing a mixture of Ga_2O_3 and carbon as the solid source, has yielded GaN nanowires (5–12 nm dia.) in the absence of a catalyst [18]. We have been able to obtain good single crystal GaN nanowires by employing a GaO_x precursor. The methods employed involve (i) the reaction of gallium acetylacetonate [$Ga(acac)_3$] with NH_3 in the presence of carbon nanotubes or activated carbon, (ii) the reaction of NH_3 with $Ga(acac)_3$ in the presence of a small proportion of iron (III) acetylacetonate [$Fe(acac)_3$] or nickel (II) acetylacetonate (in silica gel). In order to tune the diameter of the nanowires, we have carried out the synthesis by employing single-walled carbon nanotubes or by varying the proportion of the metal catalyst.

(c) Mn-doped GaN

Dilute magnetic semiconductors are being investigated extensively over the last several years, typical of these materials being Mn doped GaAs, which is ferromagnetic with a T_c of 110 K. There is great current interest in the study of Mn doped GaN, with the main objective of examining whether ferromagnetism can be induced in this material. Zajac *et al.* [19] reported Mn doped GaN to be paramagnetic, but Theodoropoulou *et al.* [20] find that p-type GaN films, on implantation with high doses of Mn (3-5 %), exhibit ferromagnetic behavior upto ~ 250 K. Reed *et al.* [21] have recently reported ferromagnetism in $Ga_{1-x}Mn_xN$ films in the temperature range 228-370 K. We were interested in exploring whether single-crystalline Mn doped

GaN nanowires could be produced and also in examining their magnetic and optical properties. Pure single crystalline GaN nanowires themselves have been synthesized by a variety of techniques as mentioned above in the section of GaN [13-18]. We have modified the procedure based on using carbon nanotubes (used for synthesizing undoped GaN nanowires as described earlier) to prepare Mn doped GaN nanowires and investigated their photoluminescence and magnetic properties. We have employed both MWNTs and SWNTs to prepare GaMnN nanowires in order to vary the diameter of the nanowires.

(d) Porous GaN

There has been some interest recently in preparing porous GaN, but the efforts have only been partially successful [22-24]. Relatively large surface areas or pore sizes are obtained only when long-chain amines are used as templates with a gallium precursor, where a small amount of carbon is always present in the final product. We have attempted to prepare GaN nanoparticles by several procedures and characterized the samples by various methods including surface area measurements. The various procedures employed include ammonolysis of mesoporous γ-Ga_2O_3, of a mixture of $Ga(acac)_3$ with Ga_2O_3 and also of Ga_2O_3 in the presence of a surfactant.

(e) Indium Nitride

Indium nitride has attracted increasing attention in the last few years because of its useful properties of potential value in opto-electronic devices and other technologies [25]. InN generally has the well known wurtzite structure (Figure 4.4).

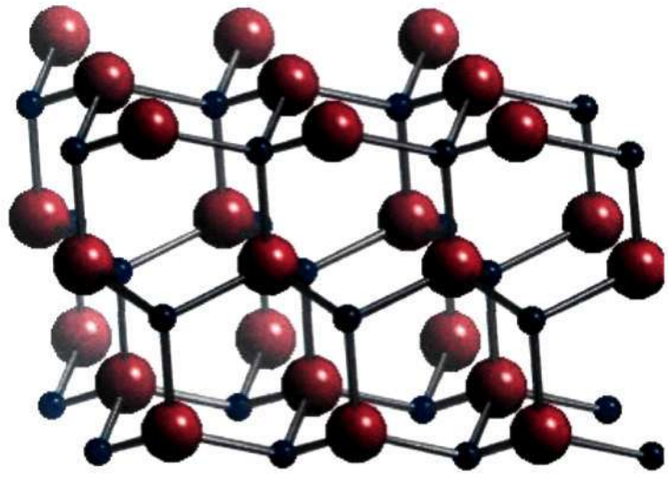

Figure 4.4: Structure of InN.

There have been several efforts to prepare InN nanostructures, but the results reported are not altogether complete and satisfactory. Nanocrystals of InN have been produced by the reaction of $InCl_3$ and Li_3N at 250 °C but the material obtained contained a mixture of both the cubic and hexagonal phases [26]. The reaction of In_2S_3 and $NaNH_2$ gave rise to hexagonal nanocrystals with diameters in the range of 10-30 nm, with an absorption band centered around 1.9 eV [27]. Indium halide CVD on a Si(100) substrate in the presence the of NH_3 has been used to produce flower-like hexagonal crystals, but the size of the crystals is in the micrometer regime [28]. In the decomposition of azido precursors, a solution-liquid-solution (SLS) process gives rise to ~ 20 nm diameter InN fibers which are polycrystalline [29]. Decomposition of another azido precursor yielded InN whiskers of 10-200 nm diameter by the vapor-liquid-solid (VLS) process, but the optical properties of the whiskers have not been

reported [30]. InN nanowires have been grown on a gold-coated silicon substrate by the thermal evaporation of pure In metal in the presence of NH_3. The nanowires had a diameter in the 40-80 nm range, with a strong broad emission peak at 1.85 eV [31]. By employing a VLS route, in which a mixture of In_2O_3 and In metal was reacted with NH_3 at ~ 700 °C, nanowires with diameters in the 10-100 nm range were obtained, but the optical spectra were not reported [32]. CVD with a mixture of In_2O_3 and In along with NH_3 on a Si/SiO_2 substrate coated with 20 nm thick gold, gave nanowires of 15-30 nm diameter with an absorption band at ~ 1.85 eV [33]. We notice that some of the procedures used to produce the InN nanostructures employ relatively high temperatures, which can give rise to defects or cause decomposition. Where low-temperature reactions have been employed, optical properties reported are not in tune with the present understanding of the material. While most of the studies on InN nanostructures report the 1.9 eV absorption band as characteristic of the material, it is now believed that the characteristic band of InN is in the near IR region [34-36]. Because of the importance of InN as an electronic material, we considered it important to carry out a systematic investigation of the nanostructures produced at relatively low temperatures, with specific interest in the optical properties. We report a study of nanowires and nanotubes of InN synthesized at low temperatures by a new chemical route.

4.3 Experimental

4.3.1 Synthesis

(a) BN nanotubes and nanowires

In order to prepare BN nanotubes and nanowires, the following methods of synthesis were employed. Procedure (i) involved the carbothermal reduction of a mixture of activated carbon and boric acid in the presence of ammonia at 1300 °C. The activated carbon was prepared by decomposing polyethylene glycol (600 units) in argon atmosphere at 700 °C for 3h [37]. An intimate mixture of finely ground activated carbon and H_3BO_3 (mole ratio 3:1) was taken in an 8 mm quartz tube closed at one end, and held vertically inside a larger quartz tube placed in a furnace (experimental set-up: see Figure 4.5). NH_3 gas was passed through the quartz tube (flow rate 10 sccm) and the temperature of the furnace, maintained initially at 200 °C for 2 h, was slowly raised to 1300 °C and maintained at that temperature for 3 h. Procedure (ii) was similar to procedure (i), except that a mixture of 0.36 g of multiwalled carbon nanotubes and 0.62 g boric acid was taken in the inner quartz tube. Reactions with the carbon nanotubes were also performed at a lower temperature of 1000 °C. MWNTs were prepared by the arc evaporation of graphite while aligned carbon nanotube bundles were prepared by the pyrolysis of ferrocene in the presence of acetylene at 1100 °C [38]. Procedure (iii) employed a homogeneous solution of an iron catalyst and H_3BO_3 in silica gel as the starting material. About 0.6183 g of H_3BO_3 (0.1 mol) and 0.404 g of $Fe(NO_3)_3.9H_2O$ (0.001 mol) were dissolved in 20 ml methanol. To this solution, 2 ml of tetraethylorthosilicate (TEOS) was added and stirred for 20 min. About 1.5 ml of 48% HF was added dropwise and the solution stirred till it formed a gel. This gel was dried at 60 °C for 12 h and was powdered. This homogeneous mixture containing finely divided Fe particles was calcined at 200 °C and subsequently heated in NH_3 (flow rate, 10 sccm) at 1200 °C for 4 h (experimental set-up: see Figure 4.6). In Procedure (iv), an intimate mixture of

0.36 g of activated carbon with 0.618 g of H_3BO_3 and 0.404 g of ferric nitrate (mole ratio of 3:1:0.1) was dried in the oven at 60 °C for 6 hrs, and then heated in a flow of NH_3 (flow rate, 10 sccm) at 1300 °C for 4 hrs.

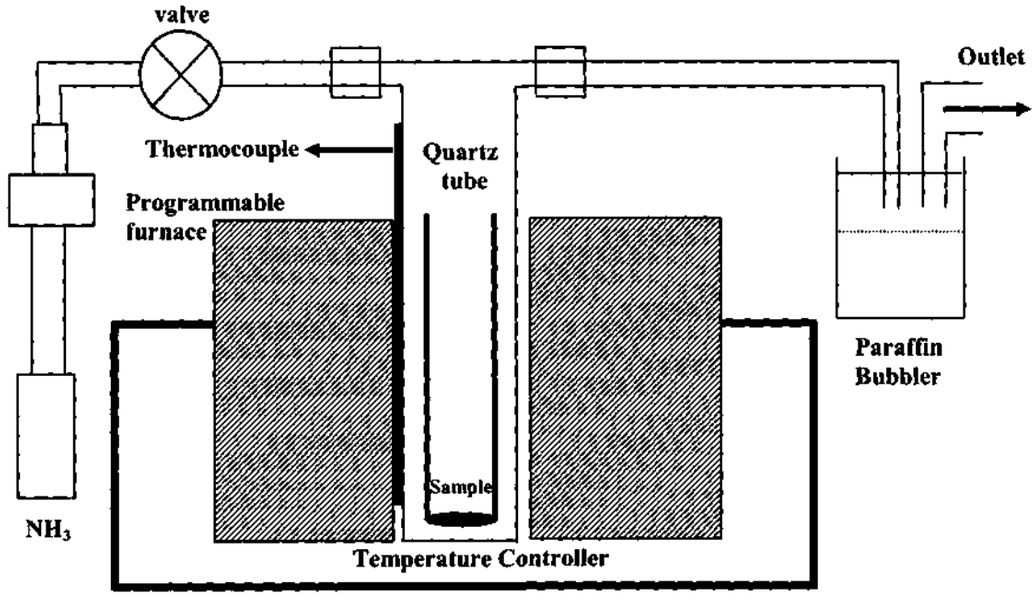

Figure 4.5: Vertical furnace configuration employed for the synthesis of the nitride nanostructures.

The products in the above procedures were generally obtained as light grey powders formed at the bottom of the inner quartz tube. White deposits formed at the mouth of the inner quartz tube and also at the outlet of the outer quartz tube. The white product was identified as pure BN. The grey product had some carbon depending on the carbon content in the starting composition.

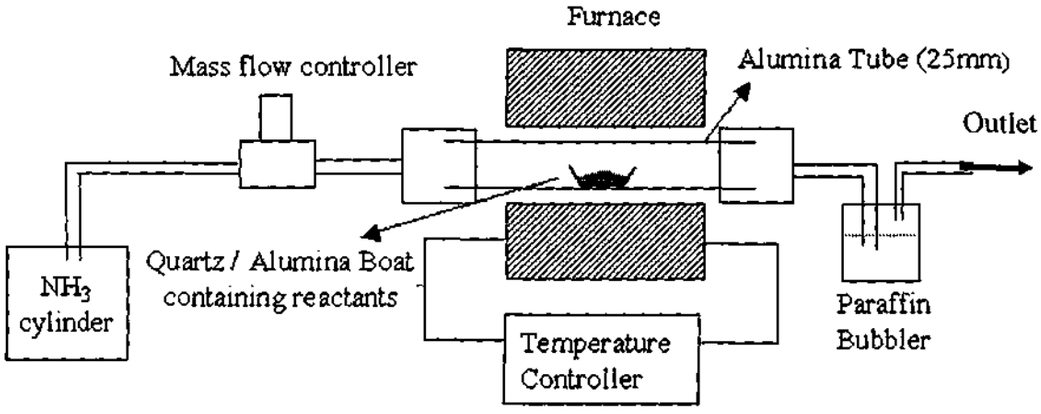

Figure 4.6: Horizontal furnace configuration employed for the synthesis of the nitride nanostructures.

(b) GaN nanowires

The procedures employed by us for the preparation of GaN nanowires are as follows. In procedure (i), GaN nanowires were prepared by using MWNTs or activated carbon. In a quartz tube (12 cm length, 6 mm dia.) closed at one end, 100 mg of $Ga(acac)_3$ were taken, above which 25 mg of MWNTs or activated carbon were placed. The quartz tube was placed in another quartz tube of a larger diameter and connected to a dynamic NH_3 atmosphere (flow rate: 150 ml min^{-1}) with a suitable T joint arrangement (experimental set-up: Figure 4.5). This quartz tube set-up was held vertically in a tubular furnace, heated to 910 °C, and held at that temperature for 3 h. MWNTs prepared by arc discharge as well as by hydrocarbon pyrolysis were used for the preparation. Aligned MWNTs prepared by pyrolysis of organometallic precursors were also used as templates [38]. Procedure (ii) involves two steps. In the first step, a homogeneous mixture of $Fe(acac)_3$ and $Ga(acac)_3$ was prepared in silica gel, followed

by calcination and reduction to yield a dispersion of Fe and GaO_x particles in the gel. The second step involved the reaction with ammonia. The dispersion of GaO_x and the Fe catalyst in the silica gel was obtained as follows: 0.991 gm of $Ga(acac)_3$ and 0.353 g of $Fe(acac)_3$ (corresponding to 0.3 at % of Ga and 0.1 at % of Fe) were dissolved in 25 ml of methanol. To this solution, 2 ml of tetraethylorthosilicate (TEOS) were added slowly under stirring. To the resulting solution, 1.5 ml of 30% HF were added drop-wise and stirred for another 30 min to achieve slow gelation. The gel was transferred to a petri dish and dried in an oven at 70 °C for 12 h. The dried gel was fragmented into small sections (5-15 mm^2 area), calcined under argon at 400 °C for 2 h, and then reduced in hydrogen at the same temperature for further 2 h. This material was heated in NH_3 (flow rate: 150 ml min^{-1}) at 910 °C for 4 h (experimental set-up: Figure 4.6). The synthesis of GaN nanowires was also carried out by using Ni particles in place of Fe particles in procedure (ii), that is, by using $Ni(acac)_2$ in place of $Fe(acac)_3$. Some experiments were conducted with a mixture of H_2 and NH_3 for nitridation, but it was found that H_2 did not affect the nitridation in any way. Similarly, the reduction step with H_2 was not found to be essential. Direct reaction of NH_3 with the metal oxides in procedure (ii) also gave GaN nanowires.

(c) Mn-doped GaN nanowires

Mn-doped GaN nanowires were prepared starting with a mixture of the acetylacetonates of gallium and manganese taken in the required mole ratios corresponding to 1%, 3% and 5% doping. MWNTs were prepared by arc discharge [38] and were of high purity. Since no catalyst was employed there was no contamination from the metal particles. Accordingly, thermogravimetry showed 100 % weight loss. The nanotubes were used as removable templates, which burn off

during the course of the reaction. The diameter of the nanotubes was in the 40-50 nm range. A thoroughly ground mixture of the acetylacetonates was mixed with MWNTs and the mixture was taken in a quartz tube (12 cm length, 6 mm dia.) closed at one end. The quartz tube was placed inside another quartz tube of a larger diameter and connected to a dynamic NH_3 atmosphere (flow rate: 150 ml min^{-1}). This set-up (see Figure 4.5) was placed vertically in a furnace, heated slowly (1 °C/ min) to reach the melting point of $Ga(acac)_3$ (195 °C), and maintained at that temperature for 1 h. It was then heated to the melting point of $Mn(acac)_2$ (260 °C) and maintained at that temperature for 1 h. The temperature was then raised to 950 °C (3 °C/ min) and held at that temperature for 4 h. This procedure was crucial in obtaining high yields of GaMnN nanowires of good quality. The same procedure was employed to prepare Mn-doped GaN nanowires with SWNTs as templates, having prepared the SWNTs themselves by the literature procedure [39]. The SWNTs individually had diameters of ~ 1.2 nm and occurred in bundles.

(d) Porous GaN

The methods employed for the preparation of porous nanostructured GaN are as follows. Procedure (i) made use of γ-Ga_2O_3 prepared by slightly modifying the procedure reported in the literature [40,41]. $Ga(acac)_3$ was dissolved in ethanol (approximately 0.5 g in 40 ml ethanol), concentrated ammonia (25 vol %) solution added slowly to the solution under continuous stirring at room temperature until no further precipitate formed. The resulting gel was filtered, washed with ethanol, and vacuum-dried in a desiccator. The xerogel thus obtained was found to be amorphous by x-ray diffraction. Calcination at 500 °C for 1 h yielded the γ-polymorph of Ga_2O_3,

which was characterized by a variety of techniques. In procedure (i), γ-Ga_2O_3 was converted to GaN by passing NH_3 at 700 °C for 2 h (flow rate of NH_3: 120 bubbles/min). In procedure (ii), γ-Ga_2O_3 was converted to GaN by passing NH_3 at 750 °C for 2 h (flow rate of NH_3: 120 bubbles/min). In procedure (iii) γ-Ga_2O_3 was prepared initially by dissolving $Ga(NO_3)_3$ in ethanol. (approximately 2 g of the salt was dissolved in 35 ml ethanol) and adding concentrated aqueous ammonia (25 vol %) slowly under continuous stirring at room temperature until no further precipitate formed. The resulting gel was filtered, washed with ethanol, and vacuum-dried in a desiccator. Without calcining the xerogel, direct treatment in NH_3 was carried out at 700 °C for 2 h (flow rate of NH_3 : 120 bubbles/min). In procedure (iv), the reaction of a mixture of $Ga(acac)_3$, Ga_2O_3 and activated charcoal taken in the ratio 1:1:1 was carried out with NH_3 at 800 °C for 2 h. The flow rate of NH_3 was maintained at 120 bubbles/min. In procedure (v), the above reaction was carried out along with H_3BO_3. The ratio of $Ga(acac)_3$, Ga_2O_3, H_3BO_3 and activated charcoal was 1:1:1:1. In procedure (vi), a $LaGaO_3$ pellet was heated with ammonia flow at 1000 °C for 12 h at 50 sccm. The extraction of GaN was performed by acid leaching with 2M HNO_3 for 12 h and dried in an oven at 60 °C overnight to obtain GaN. Procedure (vii) involved a strategy to synthesize meso-ordered GaN, starting from mesostructured gallium oxide prepared by the procedure of Yada *et al.* [42], using a templating agent. $Ga(NO_3)_3$, sodium dodecyl sulfate (SDS), urea and water were mixed at a molar ratio of 1:2:30:60. The mixture formed a precipitate, which was washed and dried at 60 °C in air. The template was removed by anion exchanging with 0.05 M sodium acetate in ethanol solution at 40 °C for 1 h. The powder diffraction pattern of the template-assisted Ga_2O_3 and Ga_2O_3 obtained after template removal shows a major peak

located at $2\theta \approx$ ca. 2.8° and peak broadening between 2θ = 3-12° due to the decrease in crystallinity. After the anion-exchange process, we observed a reduction in the d-spacing from 31 Å to 13 Å. This corresponds to the partial collapse of the hexagonal structure as reported in the literature [42]. The mesostructured gallium oxide was converted to GaN by passing NH_3 at 600 °C for 2 h at 50 sccm.

(e) InN nanowires and nanotubes

One-dimensional nanostructures of InN were obtained by the reaction of $In(acetate)_3$ (99.99 %, Aldrich, (0.0005 mole)) and 1,1,1,3,3,3-hexamethyldisilazane (HMDS - 5ml) in a 25 ml stainless steel autoclave (Swagelok, home made), kept in a furnace at a temperature of 300 °C for a time period of 48 h. No external solvent or surfactant was added and HMDS itself acted as the solvent. After the reaction was complete, the contents were cooled down slowly to room temperature. The product was carefully removed by filtration, washed with absolute ethanol and dried. The aspect ratio of these 1D nanostructures could be controlled by varying the relative reactant concentrations and temperature.

4.3.2 Characterization

The different nitride nanostructures obtained by the various procedures described above were characterized by a variety of techniques.

Thermogravimetric analysis

Thermogravimetric analysis (TGA) was carried out on a Mettler-Toledo-TG-850 instrument.

X-ray diffraction

Powder X-ray diffraction (XRD) patterns of the products were recorded using CuKα radiation with a Rich-Seifert, XRD-3000-TT diffractometer. Samples were prepared by finely grinding the product and depositing on a glass slide.

Scanning electron microscopy

Scanning electron microscope (SEM) images were obtained with a Leica S440 i scanning electron microscope. Energy dispersive analysis of X-rays (EDAX) was performed with a Oxford microanalysis group 5526 system attached to the SEM employing Links (ISIS) software and a Si(Li) detector. Samples for SEM and EDAX were prepared by spreading 10–20 mg of product onto a conducting carbon tape pasted on a aluminum stub, followed by sputter-coating with a gold film. EDAX analysis was carried out in the spot profile mode with a beam diameter of 1 μm at several places on the sample.

Transmission electron microscopy

Transmission Electron Microscopy (TEM) images were obtained with a JEOL (JEM 3010) operating with an accelerating voltage of 300 kV. Powder samples for TEM studies were prepared by dispersing the samples in CCl_4 and sonicating them using an ultrasonic bath, A drop of the suspension was put on a copper support grid covered with holey carbon film and allowed to evaporate slowly.

X-ray Photoelectron spectroscopy

X-ray photoelectron spectra of the nanostructures were recorded with an ESCALAB MKIV spectrometer employing AlKα radiation (1486.6 eV) to establish the composition.

Magnetization measurements

Magnetization measurements were carried out with a vibrating sample magnetometer (VSM 7300).

Adsorption Studies

Nitrogen adsorption measurements were made on the samples at liquid nitrogen temperature using a Cahn-2000 electrobalance.

Electronic absorption spectra

Electronic absorption spectra were recorded using a Perkin-Elmer Lambda 900 UV/VIS/NIR spectrophotometer. The samples were dispersed in absolute ethanol or toluene and recorded in the 2000-200 nm range.

Photoluminescence

Photoluminescence measurements were carried out at room temperature with a Perkin Elmer model LS50B luminescence spectrometer. The excitation wavelength used depended on the sample that was being studied.

Infrared Spectroscopy

Infrared spectra were recorded with a Bruker FT-IR spectrometer. The samples were prepared by grinding with KBr and pressing into a disk.

4.4 Results and discussion

4.4.1 BN nanotubes and nanowires

All the four procedures employed by us gave BN nanotubes although their yields varied from one method to another. By procedure (i), involving the reaction of H_3BO_3 with activated carbon and NH_3, we obtained a high proportion of nanowires. The reaction of H_3BO_3 with carbon nanotubes and NH_3, however, gave a high yield of BN nanotubes at a relatively low temperature of 1000 °C. While the reaction of H_3BO_3 with NH_3 in the presence of a Fe catalyst gave a mixture of nanotubes and nanowires at 1200 °C, the reaction of H_3BO_3 with NH_3 in presence of the Fe catalyst and activated carbon at 1300 °C yielded nanotubes with varied structures. The nanostructures obtained by the various methods generally showed the hexagonal structure (a = 2.54 Å, c = 6.70 Å; JCPDS Card No: 34-0421), but were in mixture with a small proportion of the rhombohedral structure, of the type reported by Tang *et al.* [10], Han *et al.* [43] and Golberg *et al.* [44], in some of the preparations.

In Figure 4.7 (a), we show a SEM image of the nanostructures obtained by reacting a mixture of H_3BO_3 and activated carbon with NH_3 at 1300 °C by procedure (i). These nanostructures comprise both nanowires and nanotubes as revealed by the TEM investigations. We show typical TEM images of single crystal nanowires in Figure 4.7 (b) and of a nanotube in Figure 4.7 (c). While the nanowires have a diameter in the range of 75 nm, the nanotube has an outer diameter of 20 nm. The inset in Figure 4.7 (c) shows a BN nanotube, inside a bigger one. This procedure gave nanowires as the majority product rather than nanotubes. The basic chemical reaction involved here can be written as,

$$2\,H_3BO_3 + 3\,C + 2\,NH_3 \rightarrow 2\,BN + 3\,CO + 3\,H_2 + 3\,H_2O \qquad (1)$$

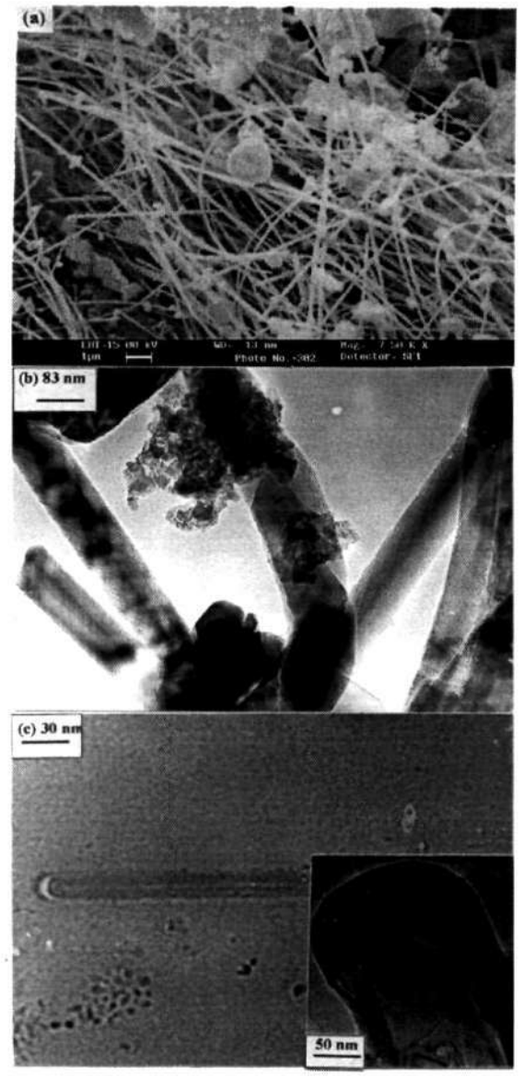

Figure 4.7: Nanostructures obtained by the reaction of H_3BO_3 and activated carbon with NH_3 by procedure (i): (a) SEM image, (b) TEM image of nanowires, (c) TEM image of a nanotube. Inset shows an interesting nanotube in a nanotube.

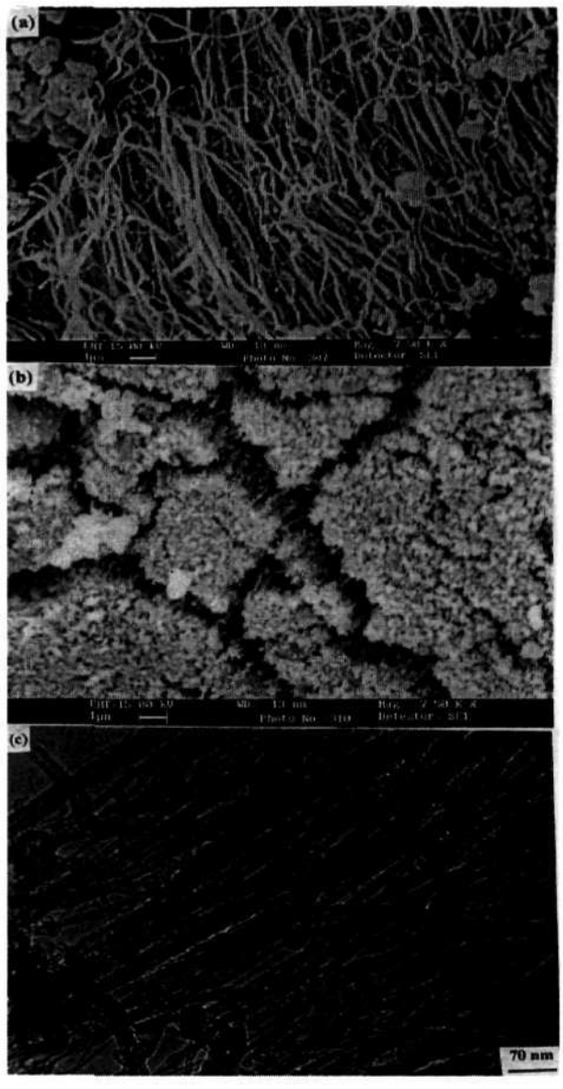

Figure 4.8: SEM and TEM images of aligned BN nanotube bundles obtained by the reaction of H_3BO_3 and aligned multi-walled carbon nanotubes with NH_3 by procedure (ii): (a) and (b) give side and top view SEM images respectively, (c) TEM image of pure BN nanotubes obtained at the mouth of the inner quartz tube.

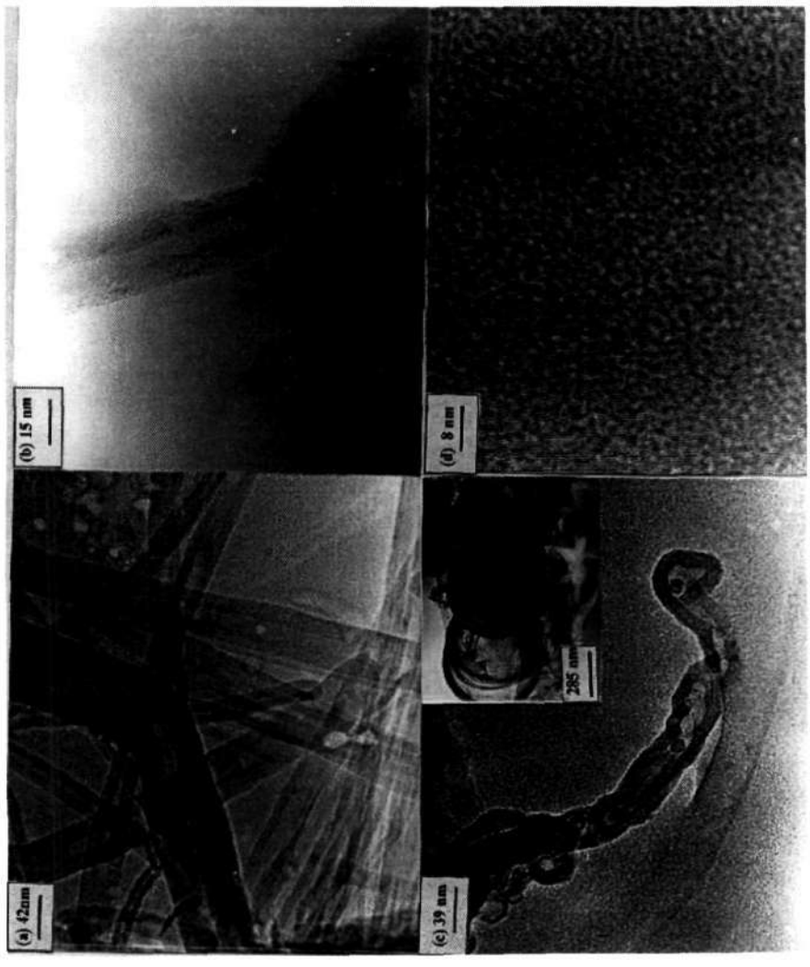

Figure 4.9: TEM images of BN nanotubes obtained by procedure (ii): (a) a collection nanotubes, (b) a nanotube with an interesting bend or kink, (c) nanotube showing an unusual cap, (d) a high-resolution image indicating the discontinuous lattice planes, Inset in (c) show bulbous structures found occasionally with the nanotubes.

Unlike the reaction of activated carbon with H_3BO_3, the reaction with carbon MWNTs by procedure (ii) gave good yields of BN nanotubes, although the basic chemical reaction remains the same as (1). While BN nanotubes were obtained with MWNTs prepared by arc-discharge as well as precursor pyrolysis methods, by using aligned MWNT bundles, we could obtain aligned BN nanotube bundles at the bottom of the inner quartz tube as shown in the SEM images in Figure 4.8 (a) and (b). In Figure 4.8 (c) we show the TEM image of pure BN nanotubes obtained at the mouth of the inner quartz tube. The images clearly reveal BN nanotubes aligned in two different orientations and establish that the carbon MWNTs not only take part in the reaction, but also serve as templates. Shelimov and Moskovits [45], have reported that aligned BN nanotubes can be prepared by the decomposition of trichloroborazine on porous alumina templates. The present method appears to be considerably simpler. We show typical TEM images of the individual BN nanotubes in Figure 4.9 (a). The average outer diameter of the nanotubes varies from 15 to 40 nm. Figure 4.9 (b) reveals an interesting bend or kink of the type generally encountered in multi-walled carbon nanotubes. Figure 4.9 (c) shows an interesting BN nanotube tip with a triangular flag-like shape, similar to the one reported by Saito and Maida [4]. Such capped structures in BN nanotubes arise from the presence of odd numbered rings, for example by introducing four B_2N_2 squares and two B_3N_4 heptagons into the hexagonal network. In the inset of Figure 4.9 (c), we show hairy bulb-like structures with a diameter of 550 nm. The high-resolution TEM image in Figure 4.9 (d) shows discontinuous lattice planes with a spacing of 0.33 nm corresponding to the interplanar distance between (002) planes (0.333 nm in bulk hexagonal BN). The irregularity of the layers may be because of the high beam sensitivity of these nanotubes. An important aspect of the reaction of H_3BO_3 with carbon nanotubes by

procedure (ii) is that the reaction temperature can be as low as 1000 °C. BN nanotubes are not obtained at such a low temperatures by the other methods of synthesis. Furthermore, there is no need for an additional catalyst in the present procedure.

We have recorded the X-ray photoelectron spectra of the BN nanotubes and nanowires obtained by the different procedures (Figure 4.10). Core level spectra of these samples gave distinct B(1s) and N(1s) signals at 190 eV and 398.5 eV respectively. These binding energy values correspond well with those reported for BN thin films in the literature [46]. After normalizing with respect to the photoionization cross sections, the intensities of the signals gave B:N ratios close to 1:1. To ensure reproducibility, the samples were subjected to two cycles of Ar etching (4 keV for 15 min). The proportion of boron and nitrogen remained the same after etching. The composition of the white product at the mouth of the reaction tube in procedure (ii) was found to be BN with no carbon. The C/B ratio was however high (0.5-3) in the grey samples collected from the bottom of the reaction tube in procedure (ii). Han *et al.* [47] have obtained such high C/B ratios in $B_xC_yN_z$ nanotubes. This is surprising since the reaction of B_2O_3 with carbon alone gives lower C/B ratios in the range 0.1-0.2 [48]. Furthermore, pure BN nanotubes have been obtained from the reaction of MWNT and B_2O_3 in an atmosphere of N_2 [43]. In order to ensure the composition of the products obtained by procedure (ii), we have varied the C/B ratios in the starting compositions and found that the white powder collected at the mouth of the quartz tube by sublimation always contained pure BN nanotubes without any carbon. We consider the variable C/B ratios in the grey product at the bottom of the reaction tube to be due to the unreacted carbon nanotubes left over after the reaction with boric acid. The oxygen content in the BN nanotubes was negligible. Considering that pure

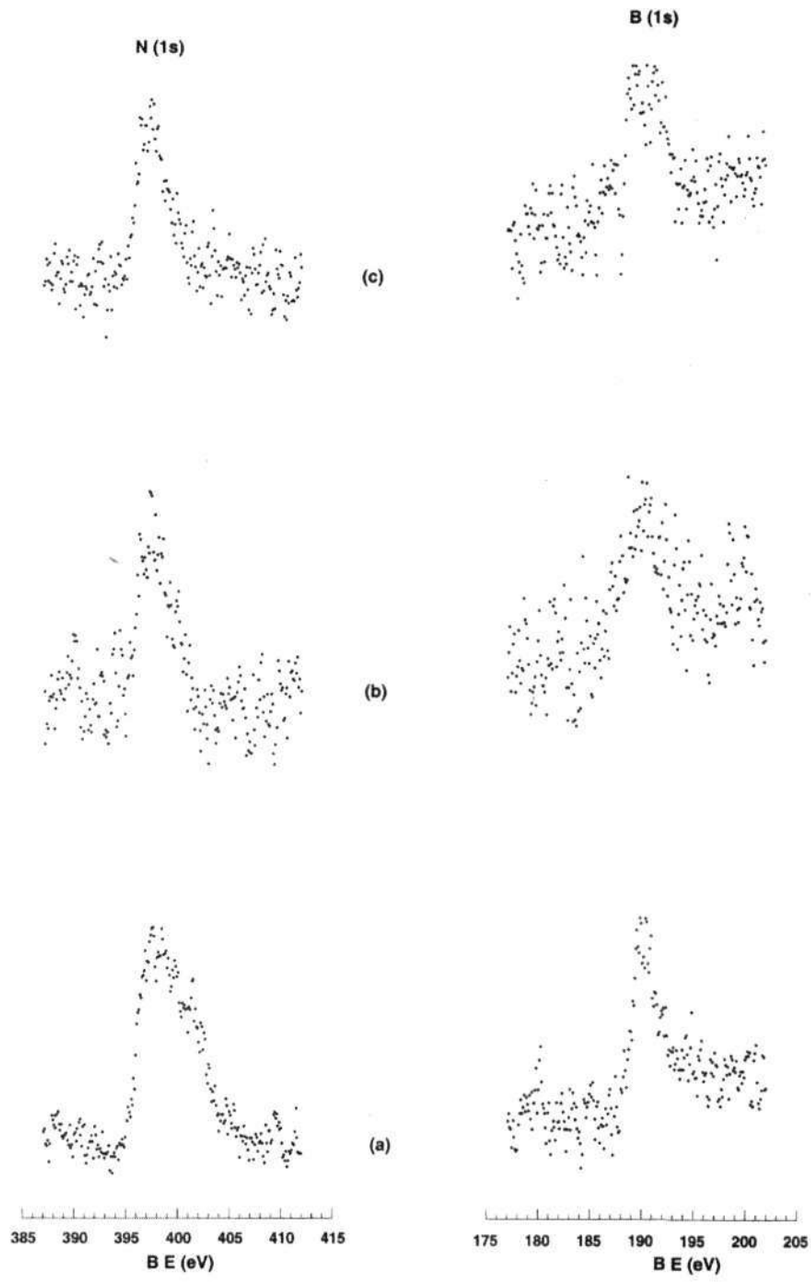

Figure 4.10: XPS of BN nanotubes showing B(1s) and N(1s) signals, (a) initially and (b) after etching (4 keV Ar) for 15 min and (c) after a second etching for 15 min.

BN nanotubes constitute almost the entire product by procedure (ii), we estimate the conversion of boric acid to BN to be 100%.

We have carried out the reaction of H_3BO_3 and catalytic Fe particles in an ammonia atmosphere at 1300 °C by procedure (iii). We obtain plates and whiskers of BN as shown in the SEM image in Figure 4.11 (a). In addition, nanowires are obtained in small quantities. We show TEM images of the nanowires in Figure 4.11 (b). The nanowires have a diameter of 60 nm, with the lengths going upto 1 μm. The occasional presence of BN nanotubes is revealed by the TEM image in Figure 4.11 (c). The nanotube has an inner diameter of 30 nm and an outer diameter of 140 nm. Iron particles coated with an amorphous layer of BN are also formed in this procedure, along with nanowires and other structures. We show a typical TEM image of a BN-coated iron particle in Figure. 4.11 (d). It appears that the growth of BN nanotubes originally starts by the deposition of amorphous BN onto a metal particle. The BN coating may pull away from the innermost layer and grow outward to form a tube. The tube growth is likely to terminate when a metal particle collides with the growing end of a tube and attaches itself to the dangling bond, forming a stable nitride or boride [3]. The chemical reaction involved in the formation of BN by procedure (iii) is given by,

$$2\ H_3BO_3 + 2\ Fe + 2\ NH_3 \rightarrow 2\ BN + Fe_2O_3 + 3\ H_2 + 3\ H_2O \qquad (2)$$

The catalytic Fe particles are regenerated by reduction of Fe_2O_3 by H_2. The composition of the nanotubes obtained by procedure (iii) had a B:N ratio of 1:1. Procedure (iii) using catalytic Fe particles alone is not satisfactory to produce BN nanotubes. We have, therefore carried out the reaction of H_3BO_3 and activated carbon

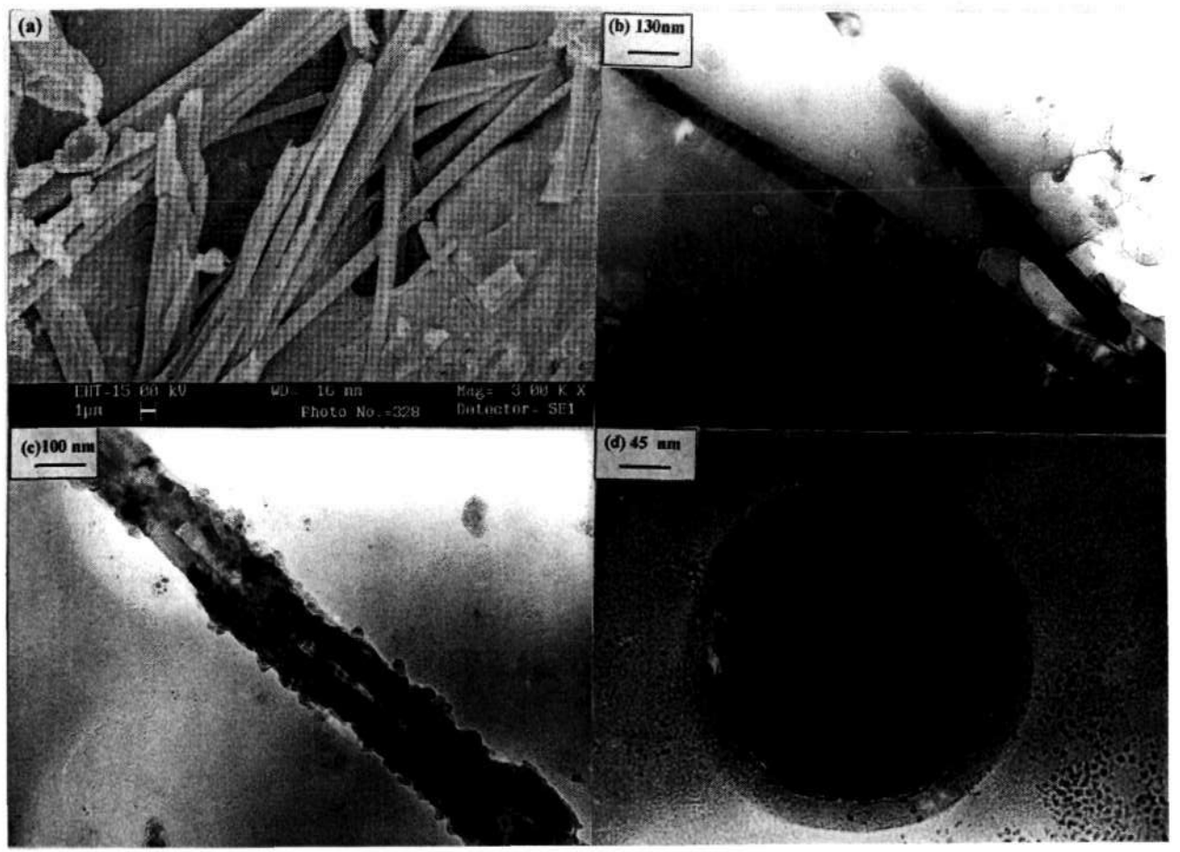

Figure 4.11: Nanostructures of BN obtained by the reaction of H_3BO_3 and catalytic Fe particles (dispersed over silica) with NH_3 by procedure (iii): (a) SEM image of plates and whiskers, (b) TEM image of nanowires, (c) TEM image of a nanotube and (d) TEM image of a BN coated Fe particle.

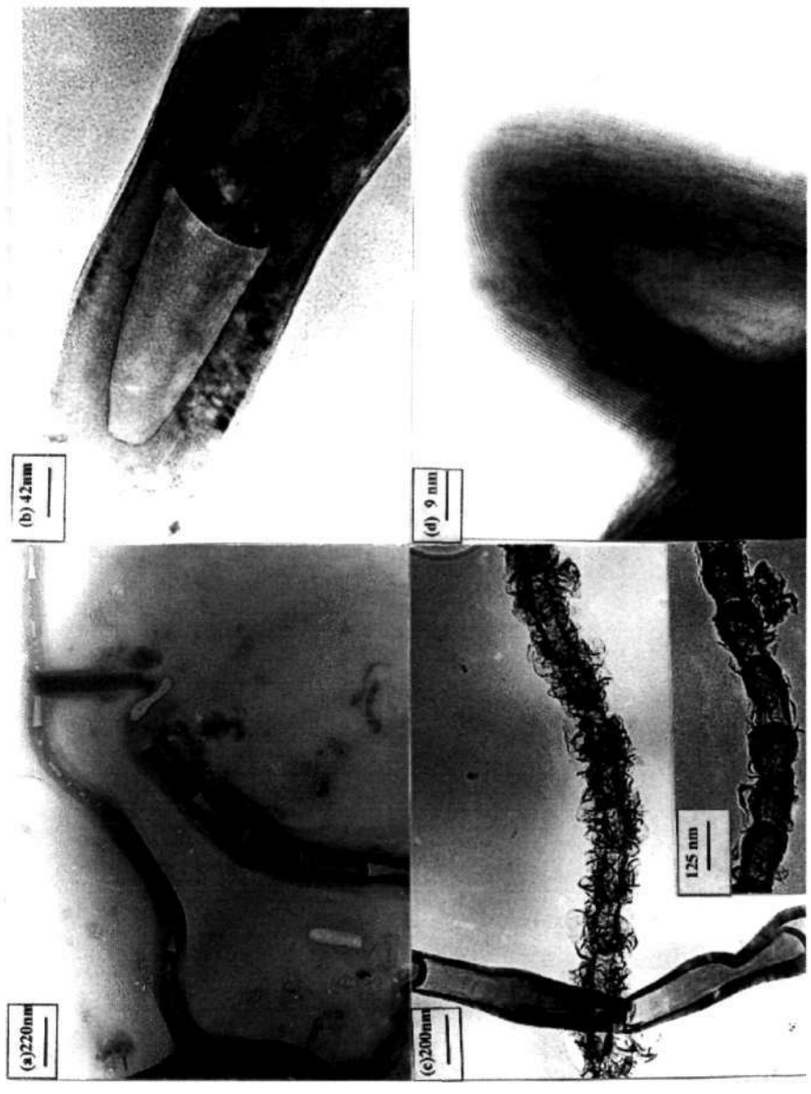

Figure 4.12: TEM images of nanotube structures of BN obtained by the reation of H_3BO_3 and activated carbon with NH_3 in the presence of catalytic Fe particles by procedure (iv): (a) TEM image of a BN nanotube with nested cones, (b) magnified TEM image of nested cones, (c) bamboo structure of BN with hair-like species attached to the outer surface, (d) HREM image of a nanotube with a spherical cap. Inset in (c) shows the magnified image of the hair-like bamboo structure

with ammonia at 1300°C in the presence of catalytic Fe particles by procedure (iv). This had the twin objective, one to achieve the reduction of boric acid by carbon and the second to provide catalytic particles for the growth of the BN nanostructures. This procedure yields various types of nanotubular structures, noteworthy among them being the nested cone and the bamboo structures. In Figure 4.12, we show the various types of nanotube structures obtained by this procedure. The TEM image in Figure 4.12 (a) reveals the presence of nested truncated cones along the axis of growth of the tube. This is clearly revealed by the magnified image Figure 4.12 (b). The growth of the nanotube here progresses outwards with an increase in the diameter as further layers are added during the formation [5]. A bamboo structure with tiny hair-like features attached to the outer surface is shown in Figure 4.12 (c). A BN nanotube with the conventional spherical tip is shown in the HREM image in Figure 4.12 (d). The layer spacing here is 0.34 nm and the concentric layers bend nicely at the tip. The B/N ratio of these nanotubes was also 1:1, with a very small carbon content (≤ 0.1).

The present study shows that clean BN nanotubes are obtained in high yields by heating boric acid with multiwalled carbon nanotubes in the 1000 - 1300 °C range. That the BN nanotubes are produced at a temperature as low as 1000 °C is noteworthy. Interestingly, aligned BN nanotubes are obtained by using aligned carbon nanotube bundles as the starting materials. The conversion of boric acid to BN in the presence of nanotubes is ~ 100%. Reaction of boric acid with activated carbon in the presence of catalytic Fe particles gives BN nanotubes exhibiting a variety of structures. In order to prepare BN nanowires, however, a mixture of boric acid with activated carbon appears to be the appropriate starting material.

4.4.2 GaN nanowires

The GaN nanowires obtained by the procedures described in the experimental section gave good XRD patterns characteristic of the wurtzite structure. We show typical XRD patterns in Figure 4.13. The lattice constants were (a = 3.18 Å and c = 5.18 Å) with minor differences. X-ray Photoelectron spectra gave characteristic *Ga(2p) and N(1s) signals.*

In Figure 4.14 (a) we show a SEM image of the GaN nanowires obtained by procedure (i), wherein MWNTs prepared by arc discharge were used as templates. The yield of the GaN nanowires by this procedure is excellent and the diameter of the majority of the nanowires is in the 35-50 nm range, but there were some in the 70-100 nm range. This variation occurs because of the non-uniformity in the nanotube diameter employed as templates. The length of the nanowires extends to a few microns. Most of the nanowires were straight as shown in the TEM image in Figure 4.14 (b), although some odd shapes of the type shown in Figure 4.14 (c) were encountered. The linear nanowires are generally single crystalline, showing a layer spacing of 0.276 nm corresponding to the [100] planes in the high resolution electron microscope (HREM) image as demonstrated in Figure 4.14 (d). The selected area electron diffraction (SAED) pattern of the linear nanowires, (see inset of Figure 4.14 (d)) shows the Bragg spots due to the (100) reflection of the wurtzite structure. The (100) planes are nearly perpendicular to the growth direction. The normal to the (100) planes actually forms an acute angle of 10° with respect to the growth direction as shown in Figure 4.14 (d). The quality and dimensions of the GaN nanowires were not significantly different when MWNTs prepared by pyrolysis were employed. Aligned nanotubes also gave similar results.

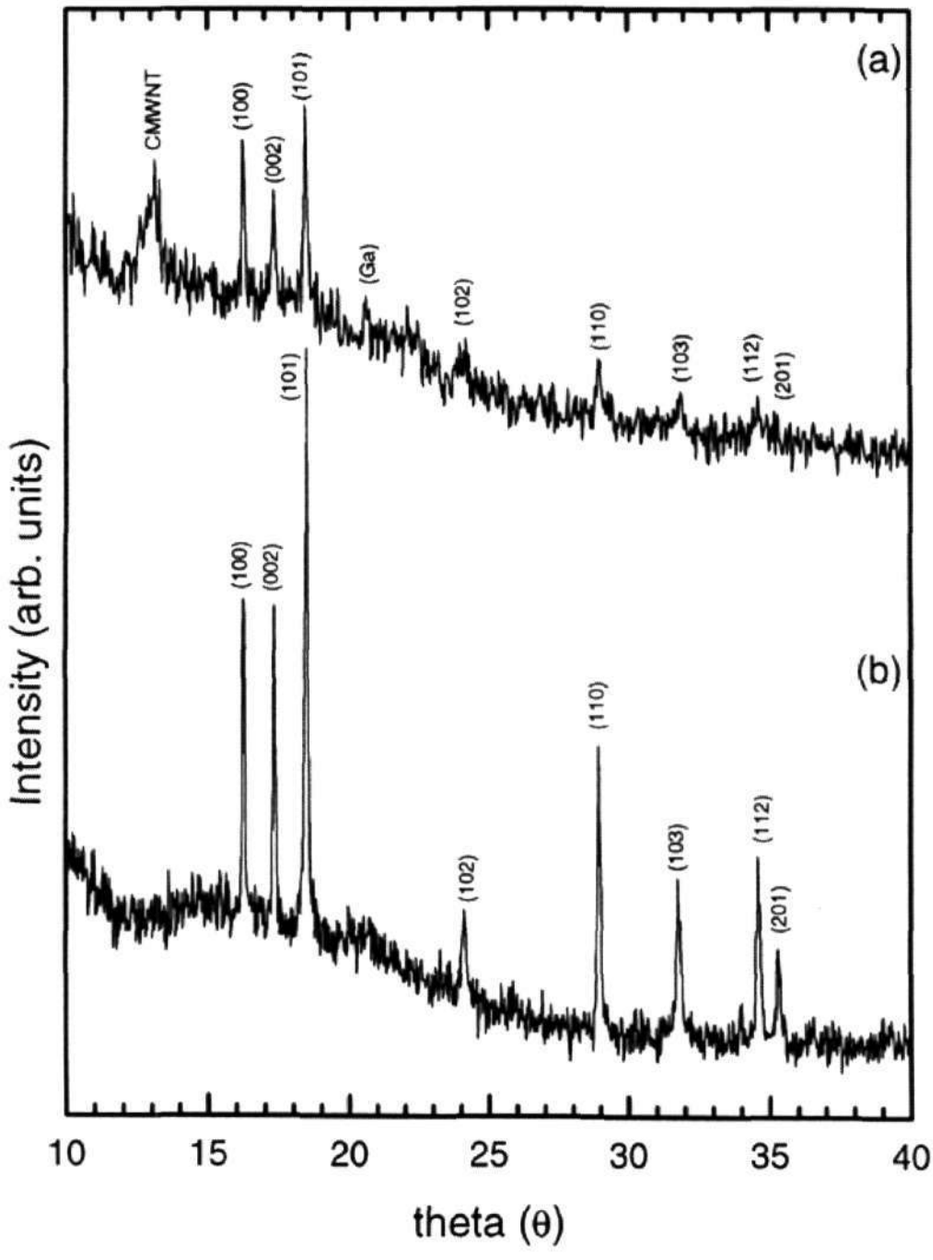

Figure 4.13: XRD patterns of the GaN nanowires prepared by (a) using MWNTs as templates as in procedure (i), (b) by using a Fe catalyst as in procedure (ii).

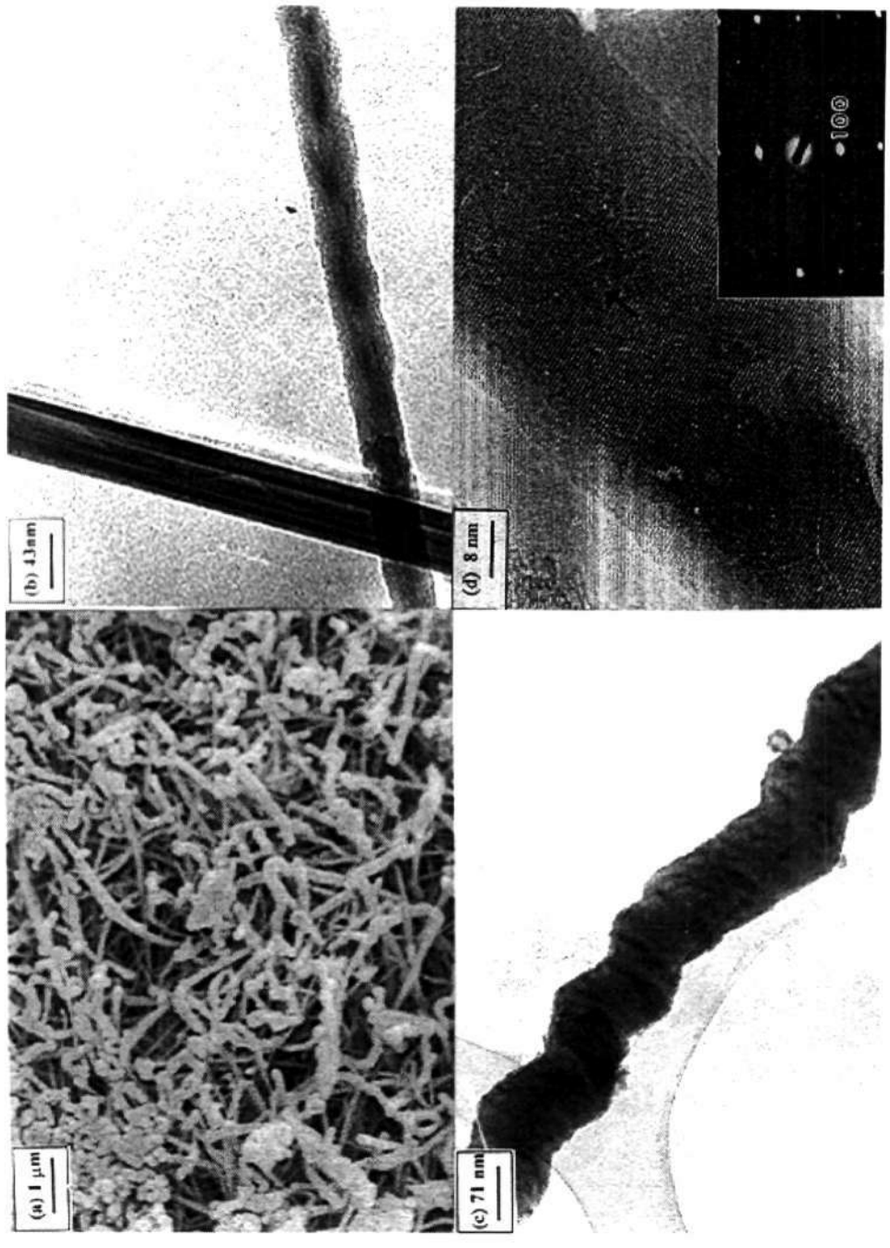

Figure 4.14: GaN nanowires obtained by procedure (i) wherein MWNTs are used as templates: SEM image; (b) and (c) TEM images. (d) HREM image. Inset in (d) shows the SAED pattern. The arrow in (d) is the growth direction, making an angle of ~ 10° with the normal to the (100) planes.

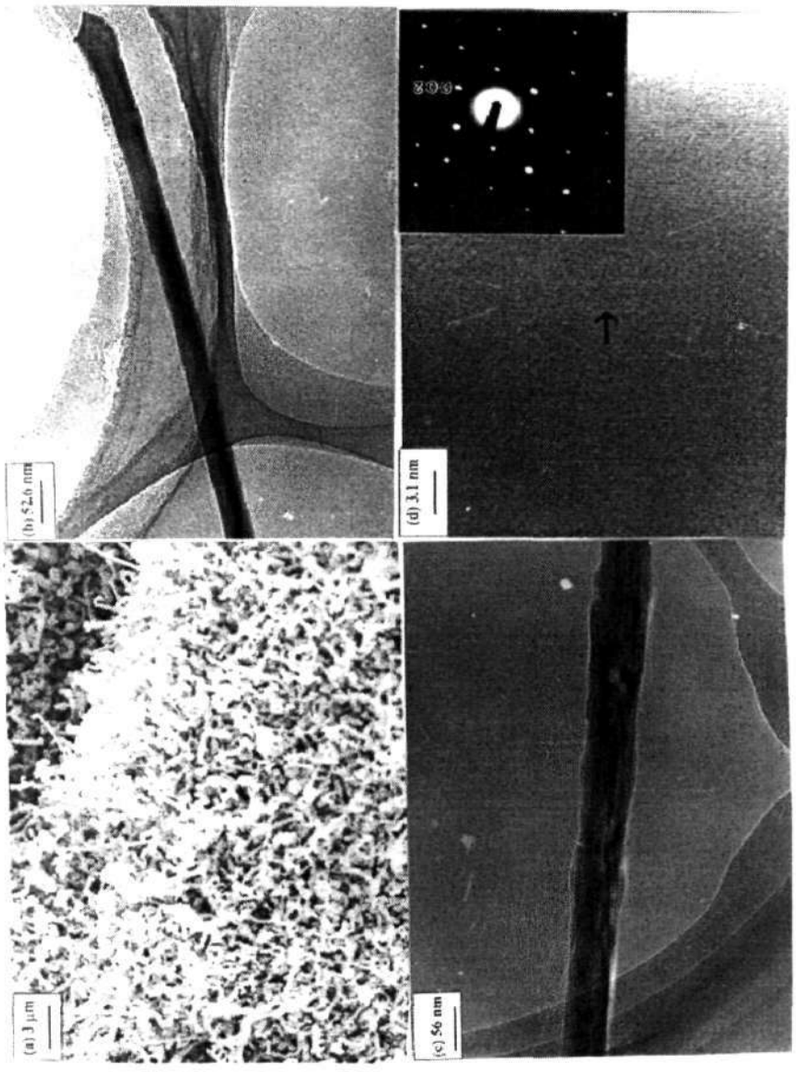

Figure 4.15: GaN nanowires obtained by procedure (ii) wherein catalytic nanoparticles are dispersed on silica. (a) SEM image, (b) and (c) TEM images. (d) HREM image. Inset in (d) shows the SAED pattern. The arrow in (d) is the growth direction.

In Figure 4.15 (a) we show a SEM image of the GaN nanowires obtained by procedure (ii) wherein the reaction of the GaO_x and NH_3 was carried out in the presence of catalytic Fe particles dispersed over silica. The yield of the nanowires is high by this procedure as well. The diameter of the nanowires is in the 30-50 nm range and the length goes up to several microns. This procedure yields good single-crystalline linear nanowires as shown in the TEM images in Figures 4.15 (b) and (c). A typical HREM image, shown in Figure 4.15 (d), reveals the characteristic 0.259 nm spacing between [002] planes. The SAED pattern given in the inset of Figure 4.15 (d) shows Bragg spots corresponding to the [002] reflections of the wurtzite structure. The growth direction of the nanowires obtained by this method was found to be perpendicular to the [002] planes. Use of the Ni catalyst instead of the Fe catalyst in procedure (ii) also gave satisfactory results as revealed in Figure 4.16. In Figures 4.16 (a) and (b), we show typical SEM and TEM images of GaN nanowires obtained by procedure (ii) wherein $Ni(acac)_2$ was used in place of $Fe(acac)_3$. The diameters of the nanowires by this method was around 40 nm or larger, with the length going up to several micrometers. Figure 4.16 (b) and (c), shows interesting nanotube-like structures. The nanostructure in Figure 4.16 (b) shows apparent narrowing on the left side where the nanotube becomes a nanowire. This is the first time that GaN nanotubes have been synthesized and observed microscopically.

The diameter of the nanowires obtained by both the procedures were around 50-100 nm or larger. In order to obtain thinner nanowires of GaN, we employed two strategies. In place of MWNTs, we employed single-walled carbon nanotubes (SWNTs) in procedure (i). The SWNTs were prepared following the literature procedure [39]. Another strategy involved the use of a smaller quantity of Fe catalyst

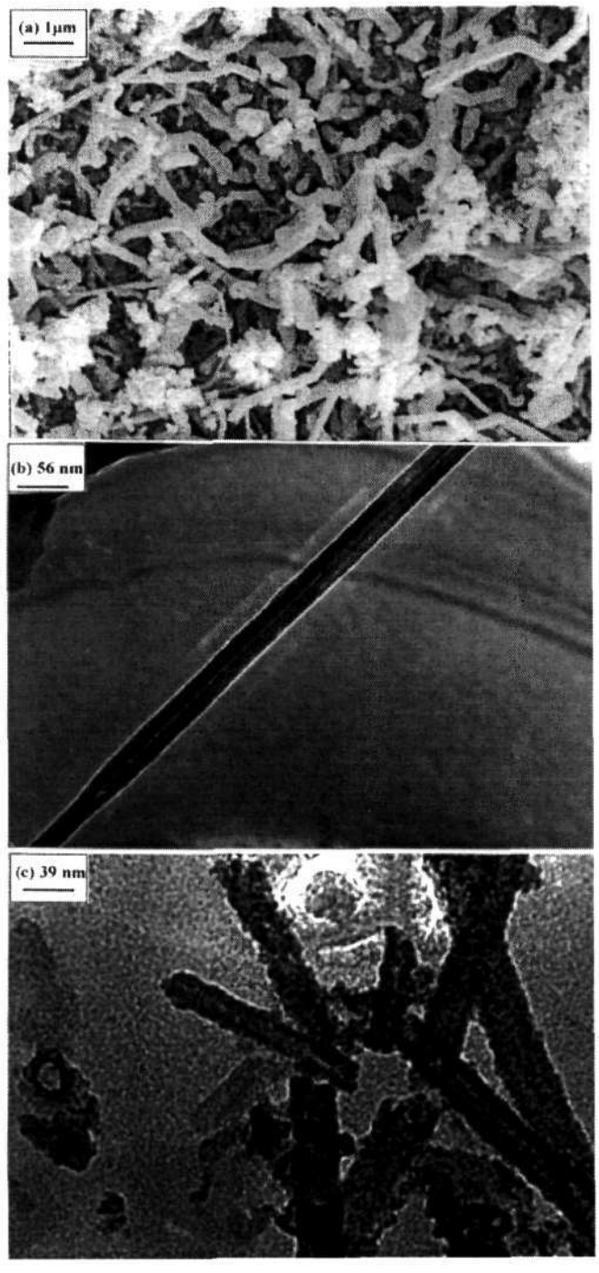

Figure 4.16: GaN nanowires obtained by using procedure (ii) with catalytic Ni particles. (a) SEM image, (b) TEM image of the nanowire and (c) TEM image of nanotube-like structures of GaN.

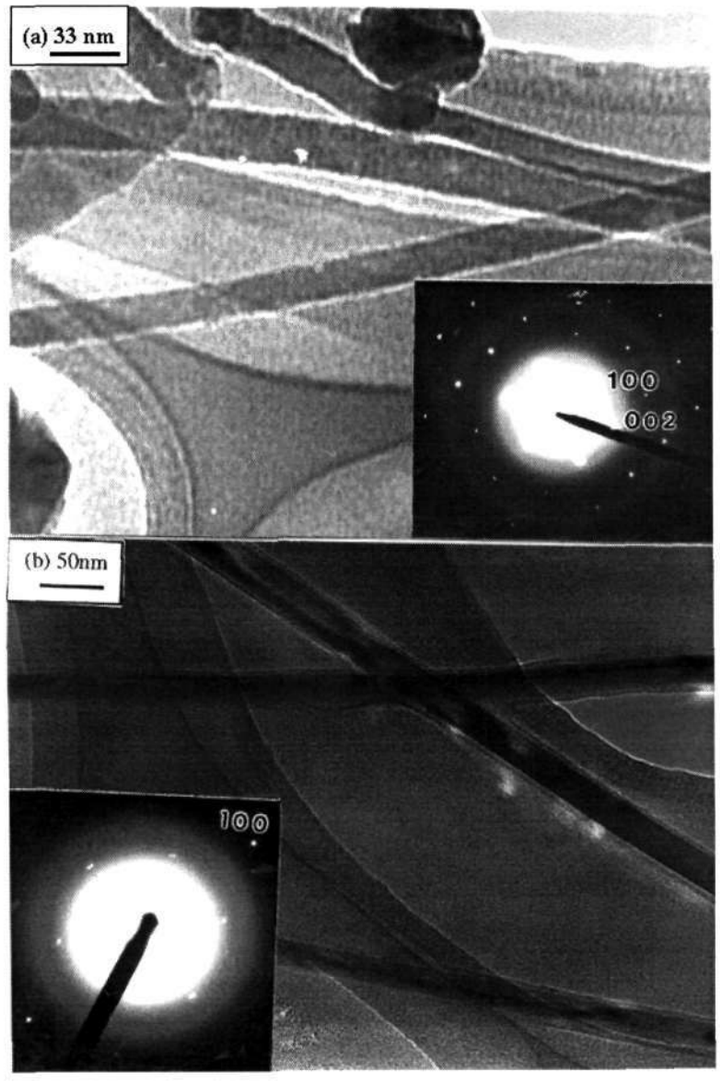

Figure 4.17: (a) TEM image of GaN nanowires obtained by procedure (i) using SWNTs and (b) TEM image of GaN nanowire obtained by procedure (ii) using a lower proportion of the Fe catalyst. Inset in (a) and (b) shows the corresponding SAED pattern.

in procedure (ii). In Figure 4.17, we show typical TEM images of the nanowires obtained by these two modified procedures. Figure 4.17 (a) shows the TEM image of the GaN nanowires prepared by using SWNTs (25 mg) and $Ga(acac)_3$ (100 mg). Figure 4.17 (b) shows the GaN nanowires prepared by using a lower proportion of Fe (0.018g $Fe(acac)_3$, 0.16g $Ga(acac)_3$ corresponding to 0.006 at% Fe and 0.06 at% Ga respectively) as catalyst. Nanowires obtained by these procedures were considerably thinner with diameters in the range of 15-20 nm. It is noteworthy that these procedures enable the tuning of the thickness of the nanowires. Inset in Figure 4.17 (a) shows the SAED pattern of the nanowires with the Bragg spots corresponding to [100] and [002] reflection of the wurtzite structure prepared by using SWNTs. The inset in Figure 4.17 (b) shows the SAED pattern of the nanowires with Bragg spots corresponding to [100] reflection of the wurtzite structure prepared by using a lower proportion of Fe.

In Figure 4.18, we show the photoluminescence (PL) spectra of the GaN nanowires prepared by two different procedures. The spectrum at an excitation wavelength (λ_{ex}) 220 nm shows a broad emission band with a well-defined peak around 380 nm. There is also a weak feature around 530 nm. The same spectra were obtained when λ_{ex} was 210 or 220 nm. The observed PL features are comparable to those of bulk GaN which is known to exhibit a strong blue PL peak around 360 nm and a weaker yellow peak around 540 nm.

A few observations on the nature of the reactions occurring in the different procedures are in the order. The basic reaction involves the nitridation of the gallium oxide species produced in-situ by the decomposition of $Ga(acac)_3$ in a reducing

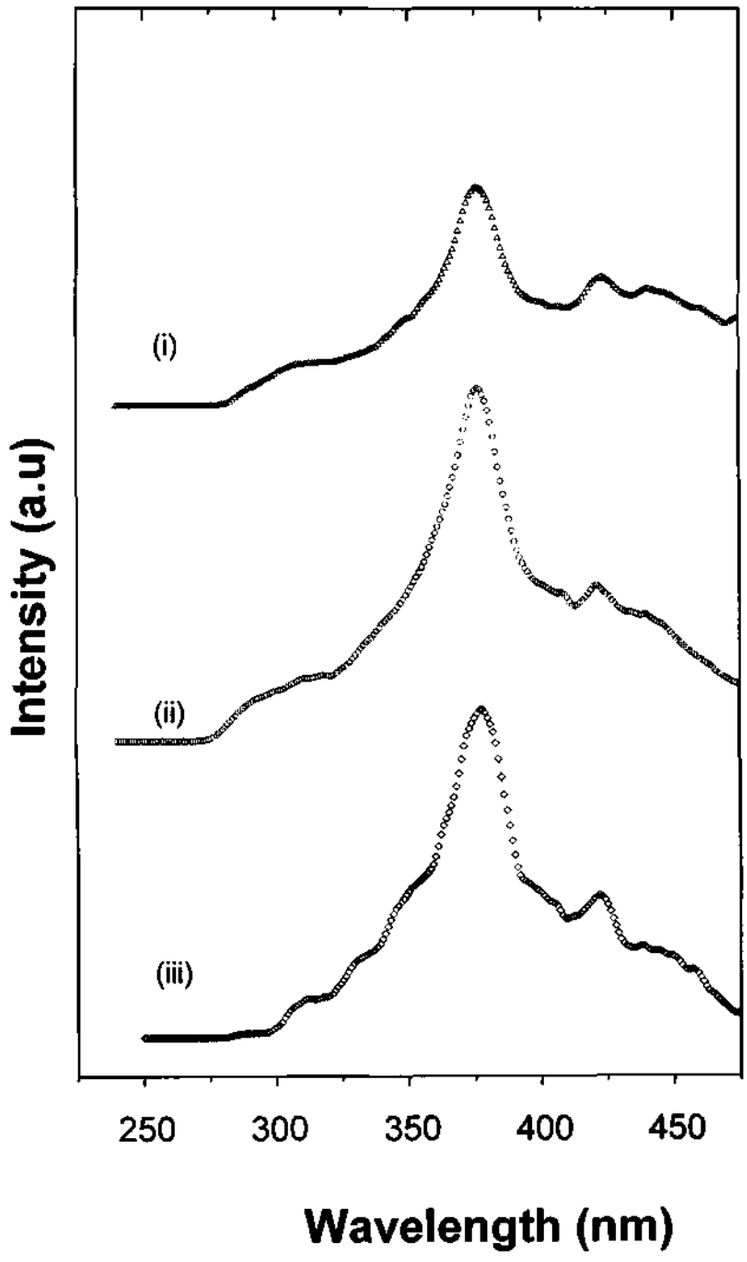

Figure 4.18: Photoluminescence spectra of GaN nanowires, prepared by procedures (i) and (ii). (iii) is the spectrum obtained with SWNTs, whereas (i) is with MWNTs.

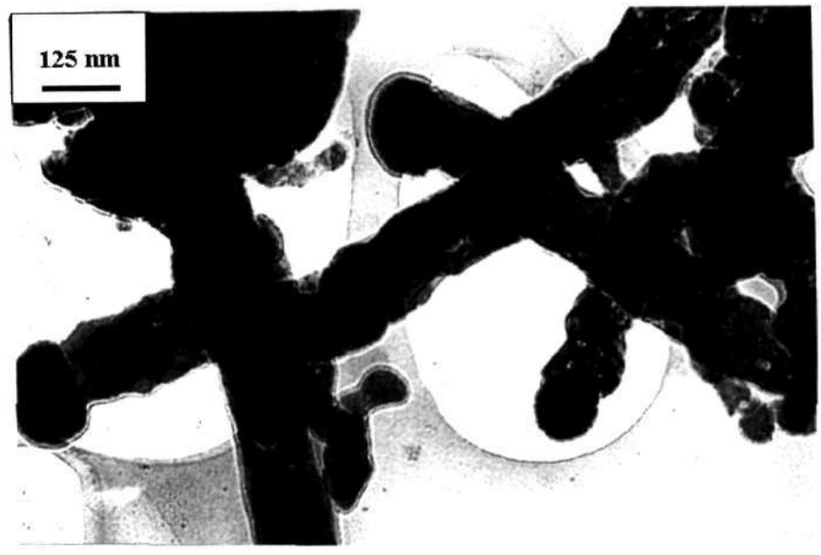

Figure 4.19: TEM images showing nucleation of GaN nanowires from metal-containing clusters obtained by procedure (ii) with the Fe catalyst.

atmosphere. We represent the gallium oxide species as GaO_x, although it is likely to be Ga_2O. The reaction may be written as,

$$GaO_x + NH_3 \rightarrow GaN + xH_2O + (3/2 - x)\, H_2$$

In procedure (i) the carbon nanotubes not only act as templates to confine the reaction and allow the growth of the GaN nanowire, but also take part in the reduction of the oxide. In procedures (ii), catalytic Fe or Ni particles are present. Chen *et al.* [15], employed NiO as one of the additives during the formation of nanowires. Under the reaction conditions employed by them, it is likely that they had metallic Ni particles. The metal particles probably control the diameter of the nanowire by a directed flow of the reactant gases. Furthermore, since the transition metal probably dissolves both Ga and N, it can provide an appropriate nucleation center for the

growth of the GaN nanowires, as suggested by Duan and Lieber [17]. We have also found some evidence for the formation of such clusters containing the metal from which the GaN nanowire emanates. In Figure 4.19, we show TEM images in order to demonstrate the nucleation of the nanowires from the Fe or Ni metal particles in the reactions carried out by procedure (ii). Interestingly, the diameter of the nanowires corresponds to that of the metal particles.

GaN nanowires have been synthesized by two different procedures of which the best results, both in terms of yield and the quality of the nanowires, are obtained by the procedure (i) involving the use carbon nanotubes as templates because it avoids the presence of the extraneous metal particles found in procedure (ii). The diameters of the wires are generally 50-100 nm or greater. The nanowires so produced possess the wurtzite structure and have high aspect ratios. The diameters of the nanowires could be reduced to ~ 20 nm by using single-walled nanotubes in procedure (i) or by using lower proportion of Fe catalyst in procedure (ii). They also exhibit good photoluminescence characteristics similar to those of bulk GaN. The growth direction of the nanowires from procedure (i) is nearly perpendicular to the [100] planes, while the nanowires obtained from procedure (ii) had a growth direction perpendicular to the [002] planes. Incidentally GaN nanotubes have been obtained for the first time.

4.4.3 Mn-doped GaN nanowires

Powder x-ray diffraction patterns of the Mn-doped GaN nanowires showed them to have the hexagonal structure, with the *c* - parameter increasing from 5.178 to 5.190 Å with the increase in Mn dopant concentration from 1 to 5% and the *a* - parameter remaining essentially constant around 3.190 Å [49,50]. This observation

showed that Mn was present substitutionally in GaN. Energy dispersive x-ray analysis (EDAX) carried out on several samples and on different regions of the nanowires, showed the Ga/Mn ratios to be close to those expected from the starting compositions [Figure 4.20]. SEM images of the GaN nanowires doped with 1%, 3% and 5% Mn prepared with MWNTs showed that the diameter of the nanowires to be generally in the 50-75 nm range, with the lengths going upto 1-2 microns. In Figure 4.21 (a) and (b), we show typical TEM images of Mn doped GaN nanowires prepared by the use of SWNTs as templates. It can be seen that the diameter of these nanowires are much smaller than those obtained previously by the use of MWNTs. The average diameter of the GaMnN nanowires obtained from SWNTs is in the 20-25 nm range. The inset in the figure shows an electron diffraction pattern (Figure 4.21 (b)) with the Bragg spots corresponding to the [100] reflection of the wurtzite structure of GaN. The electron diffraction patterns showed occasional streaks, but no extra spots due to other phases, and confirmed that the GaMnN samples had the same structure of GaN although with slightly different lattice constants [51]. In Figure 4.21 (c) we show a high resolution electron microscope image which not only reveals the single crystalline nature of the nanowire, but also that the growth direction is at an acute angle with respect to the (101) plane. No defects or other imperfections are apparent.

Magnetization measurements show that the nanowires prepared by using MWNTs with 1%, 3% and 5% Mn are all ferromagnetic with a T_c of around 325 K. The samples exhibit magnetic hysteresis at room temperature. We show typical hysteresis curves at 300 K and 50 K in Figure 4.22. The M vs H curves show a smooth S-shaped loop with a remnant magnetization (M_R) of 0.026 emu/g at 297 K

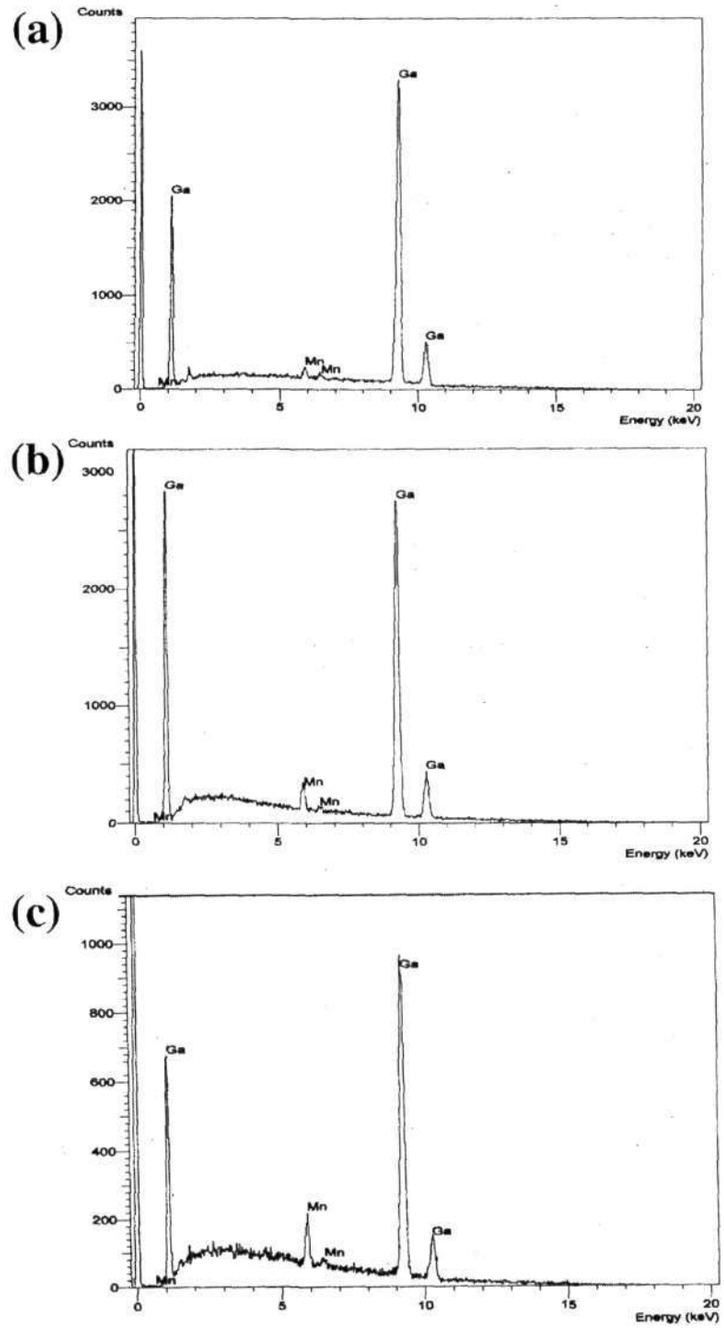

Figure 4.20: EDAX spectra of GaMnN nanowires: (a) 1% Mn, (b) 3% Mn (c) 5% Mn.

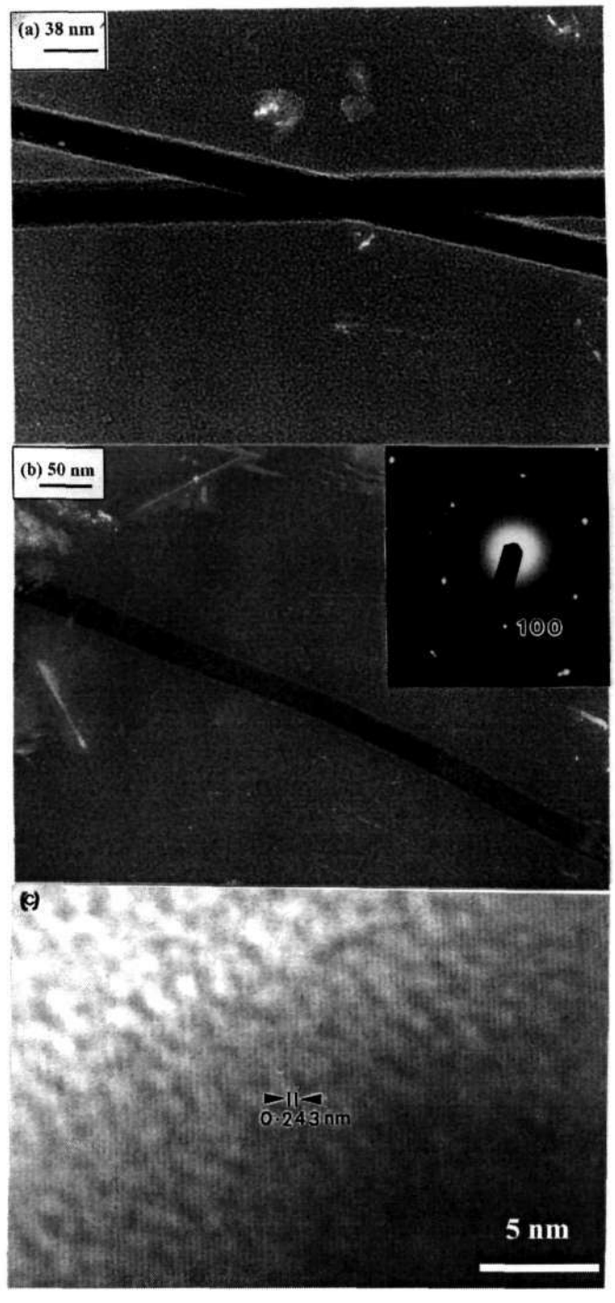

Figure 4.21: TEM images of the Mn doped GaN nanowires prepared with SWNTs: (a) 1% Mn, (b) 5% Mn, (c) HREM image of 5% Mn doped nanowire. Inset in (b) shows the electron diffraction pattern.

for the 1% Mn doped nanowires and 0.02 emu/g for the 5% Mn doped GaN nanowires. The coercivity (H_c) in the case of the 1% Mn doped GaN nanowires is 970 Oe and for the 5% doped nanowires 630 Oe. The value of remnant magnetization for the 5% doped sample at 50 K is 0.03 emu/g, whereas the coercivity is 620 Oe. The thinner diameter (25 nm) nanowires obtained from the use of SWNTs show a coercivity of 1400 Oe in the case of the 5% Mn doped samples. The 25 nm diameter nanowires also show a tendency for saturation at 50 K. The remnant magnetization of this sample is 0.06 emu/g at 50 K. The values of coercivity in the GaMnN nanowires found here are higher than those reported for thin films [52a]. The origin of ferromagnetism of Mn doped GaN nanowires is not entirely clear. We cannot rule out the formation of GaMn alloys which is known to be ferromagnetic [52b-d].

PL spectra of the GaMnN nanowires prepared with MWNTs are shown in Figure 4.23. At an excitation wavelength of 325 nm, the undoped nanowires show a broad emission band with a well-defined peak around 380 nm and a weak feature around 530 nm. These PL features are comparable to those of bulk GaN. The Mn doped samples show a PL band centered around 420 nm, the red shift arising from hole-doping [53]. We also see the characteristic Mn^{2+} emission around 610 nm, due to the $^4T_1 \rightarrow {}^6A_1$ internal Mn^{2+} ($3d^5$) transition [54]. The FWHM of the Mn^{2+} emission band decreases with increase in Mn concentration. We have also examined the PL spectra of the 25 nm GaMnN nanowires prepared with SWNTs. The spectra show interesting differences from the spectra of the nanowires prepared with MWNTs as evident. The PL spectrum of the 25 nm nanowires of GaN in Figure 4.24, shows the main feature at ~ 410 nm, slightly blue-shifted compared to that of the larger diameter nanowires (Figure 4.23). The Mn emission from the smaller nanowires is significantly

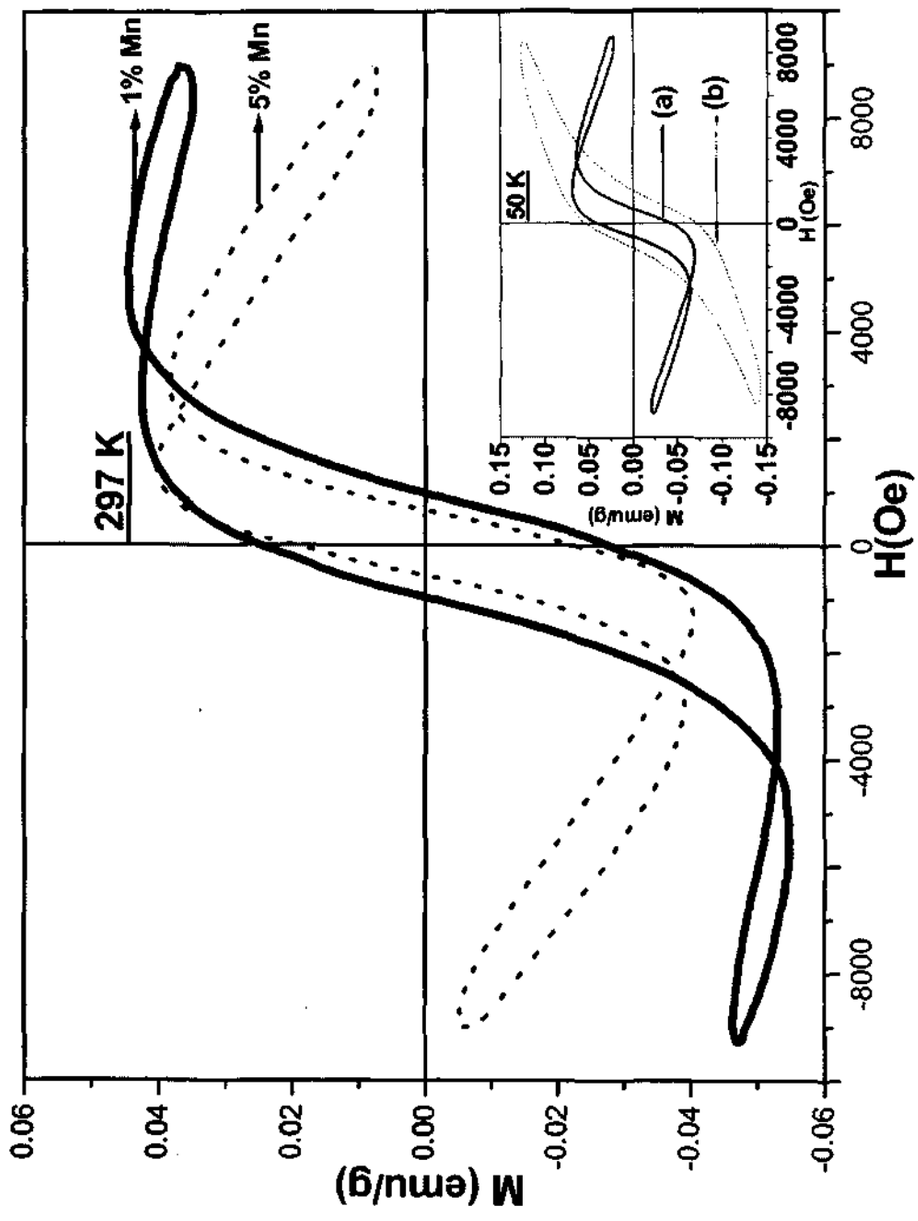

Figure 4.22: Typical magnetic hysteresis curves of GaMnN nanowires at 297 K. Inset shows the hysteresis curves at 50 K for the 5% Mn doped nanowires. (a) MWNTs, (b) SWNTs.

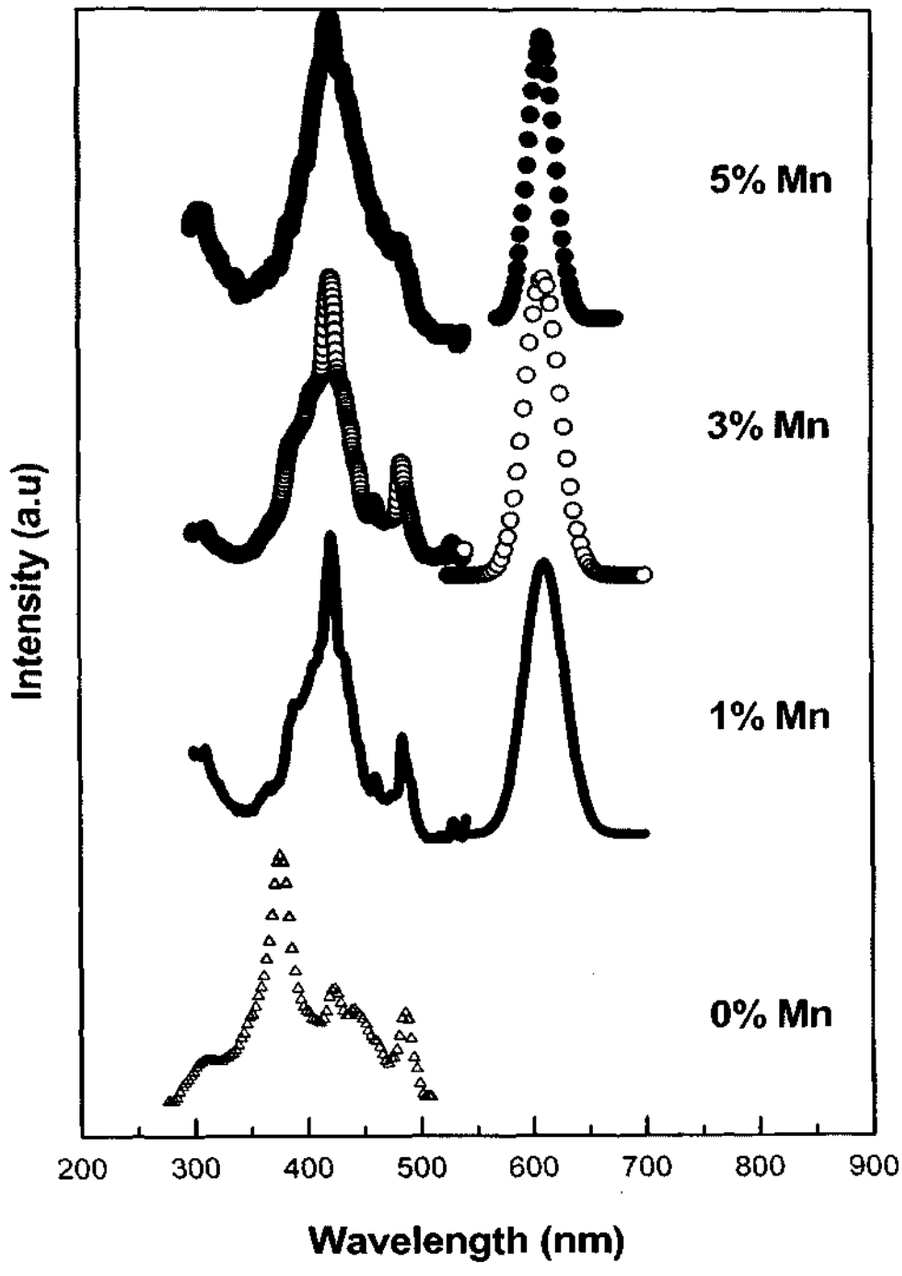

Figure 4.23: Photoluminescence spectra of the GaMnN nanowires prepared with MWNTs. The PL spectrum of the undoped nanowires is also shown. Mn^{2+} emission from the GaMnN nanowires is seen around 610 nm.

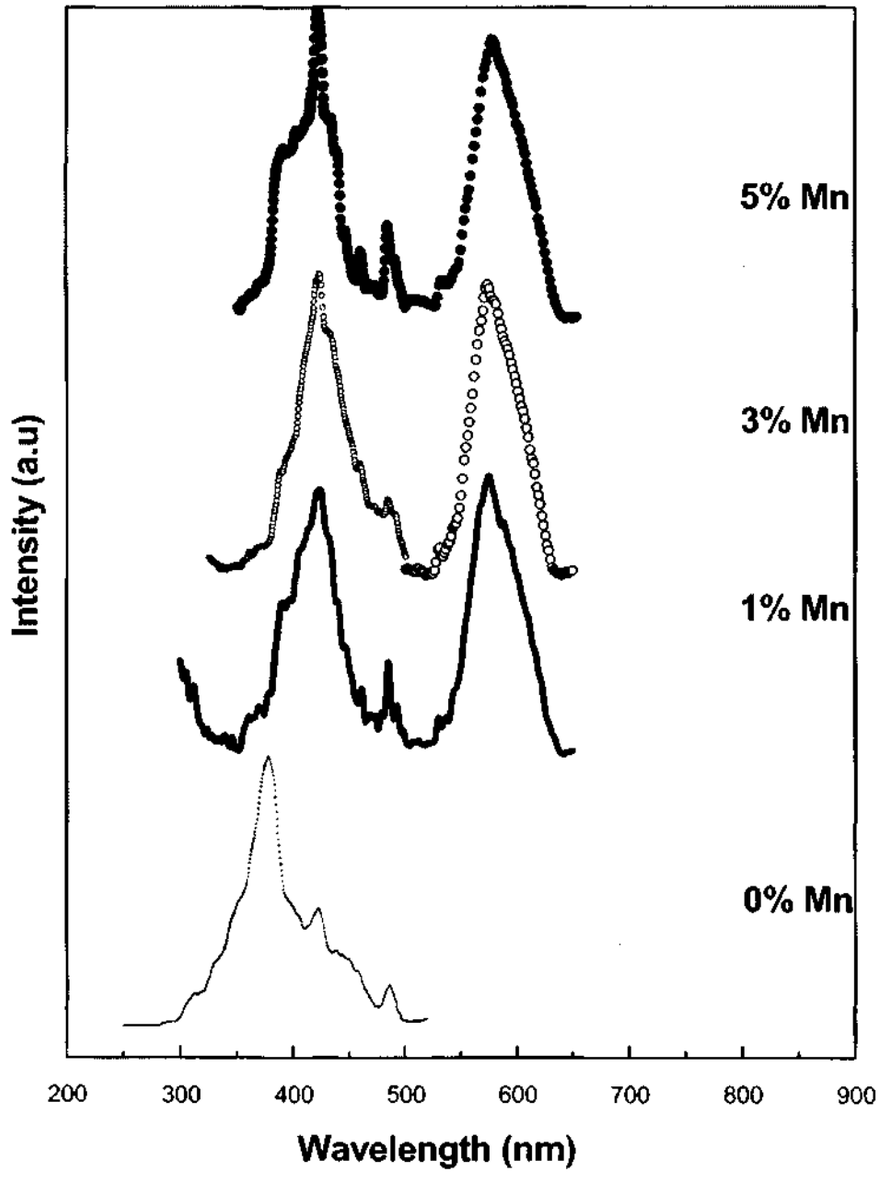

Figure 4.24: Photoluminescence spectra of the GaMnN nanowires prepared with SWNTs. The spectrum of the undoped nanowires is also shown. Mn^{2+} emission exhibits a blue-shift compared to the bands of the larger diameter nanowires in Figure 4.23.

different. The characteristic Mn^{2+} emission is strongly blue-shifted in the spectra of the smaller diameter nanowires as can be seen from Figure 4.24, compared to the spectra in Figure 4.23. Thus, the emission is shifted to around 574 nm. A similar blue-shift of the Mn^{2+} emission has been reported in doped ZnS nanoparticles, where the shift is essentially due to the decrease in the cluster size [55-57]. The intensity of the Mn emission also increases with the Mn content in the case of the 25 nm nanowires.

In conclusion, Mn-doped GaN nanowires have been prepared by heating appropriate mixtures of Ga and Mn acetylacetonates along with carbon nanotubes in the presence of NH_3 at 950 °C. The nanowires prepared with single-walled carbon nanotubes are much thinner (~ 25 nm) than those prepared with multi-walled carbon nanotubes (~ 70nm). This is the first time that doping has been carried out in the case of GaN nanowires. The nanowires are ferromagnetic at room temperature, a feature that may be of value in device technologies. The origin of magnetism is, however, not clear. Photoluminescence spectra show a significant blue-shift of the Mn^{2+} emission in the 25 nm nanowires.

4.4.4 Porous GaN

In Figure 4.25 (a), we show the TEM image of γ-Ga_2O_3. The image shows that the sample is nanostructured with evenly distributed worm-like pores. High magnification images were difficult to obtain due to the instability of the material under the electron beam. The average particle size estimated from the TEM images was around 5 (± 1) nm. The inset in Figure 4.25 (a) shows the electron diffraction (ED) pattern of the γ-Ga_2O_3, exhibiting diffuse rings. The d-spacings corresponding to the rings agree with those from x-ray diffraction. The x-ray diffraction pattern showed

the characteristic (220), (311) and (440) peaks of γ-Ga_2O_3 [JCPDS file: 20-0426]. This polymorph is known to be metastable and to have a spinel-type structure similar to that of γ-Al_2O_3. In Figure 4.25 (b), we show the N_2 adsorption isotherm of the sample obtained at 77K. The isotherm is a typical Type IV isotherm characteristic of a mesoporous material [58]. There is a slight hysteresis at higher p/p_0 values, as expected for mesoporous solids. The surface area calculated by the BET method was 187 m^2g^{-1}. The value is slightly higher than that reported in the literature [40,41]. The PL spectrum of the γ-Ga_2O_3 shown in Figure 4.25 (c), has a blue emission band centered at 440 nm. The emission probably occurs due to oxygen vacancies, which result during the synthesis [59].

In Figure 4.26 (a) and 4.27 (a), we show the SEM and TEM images respectively of GaN obtained by procedure (i). The images show an agglomeration of particles of uniform size and pore distribution. The particle size is in the 5-10 nm range. The x-ray diffraction pattern of the sample (Figure 4.28 (a)) showed it to be amorphous. The inset in Figure 4.26(a), shows the ED pattern of the nanoparticles obtained by this method, with rings corresponding to the (101), (102) and (110) Bragg reflections of hexagonal GaN [JCPDS file: 02-1078]. In Figure 4.29 (a), we show the PL spectrum of the GaN nanoparticles prepared by procedure (i). The spectrum shows the UV-blue emission band centered at 420 nm with a shoulder at 390 nm characteristic of near-band edge emission of wide band gap GaN. The N_2 adsorption of the sample showed a Type IV isotherm with a BET surface area of 53 m^2g^{-1} (Figure 4.30 (a)). It is noteworthy that the sample is reasonably porous, even after conversion to the corresponding nitride, though the surface area is greatly reduced. In comparison, the GaN obtained by procedures (ii) and (iii) gave BET surface areas of

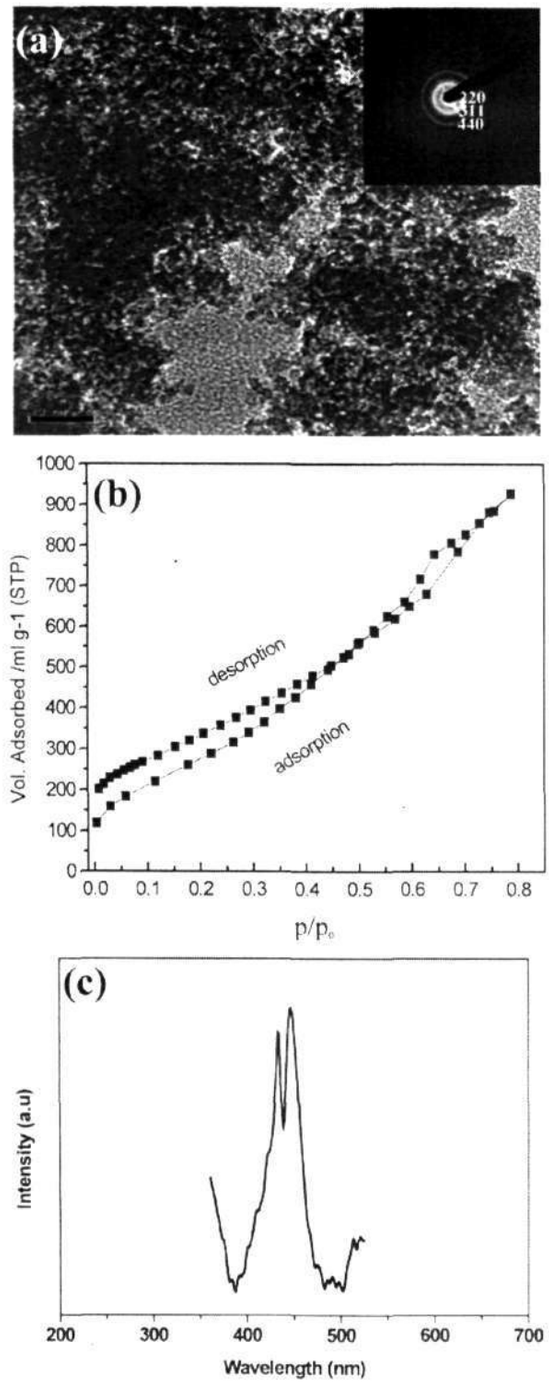

Figure 4.25: (a) TEM images of the γ-Ga_2O_3. (b) and (c) N_2 adsorption isotherm and PL spectrum of γ-Ga_2O_3.

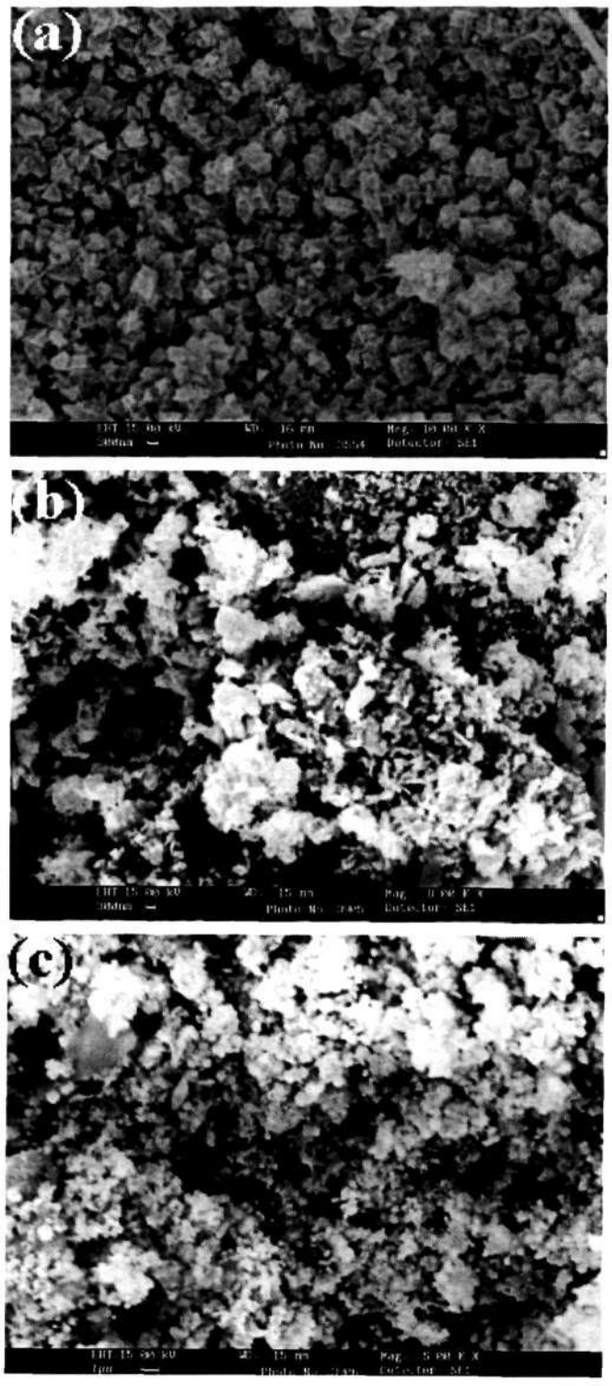

Figure 4.26: (a)-(c) SEM images of GaN obtained by procedure (i), (iv) and (v).

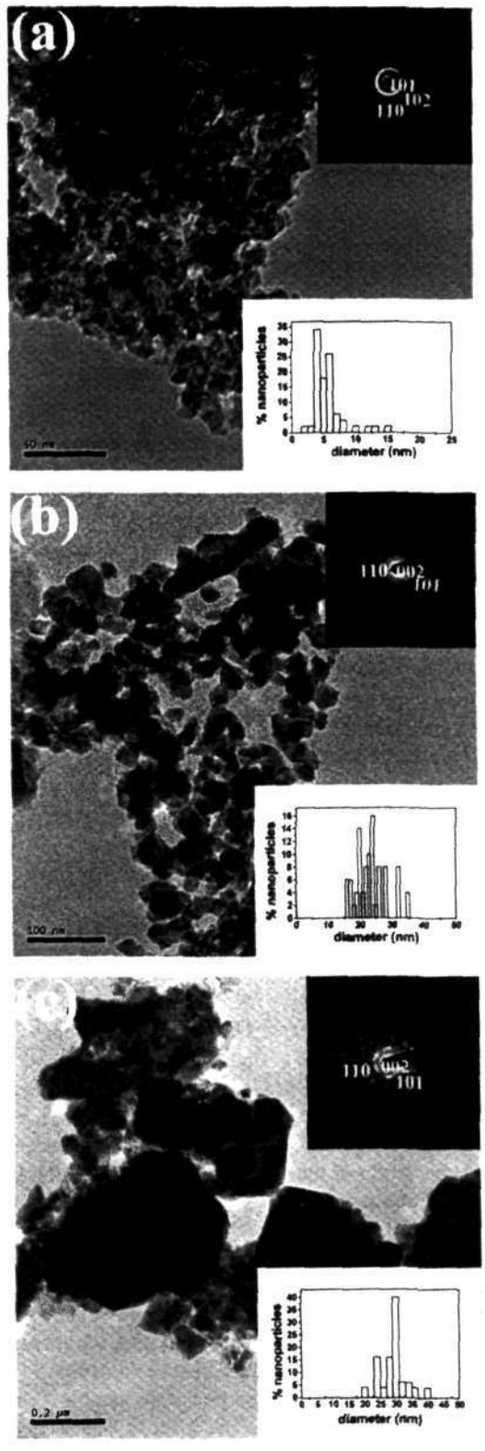

Figure 4.27: (a)-(c) TEM images of GaN obtained by procedure (i), (iv) and (v). Insets show the corresponding E.D. patterns.

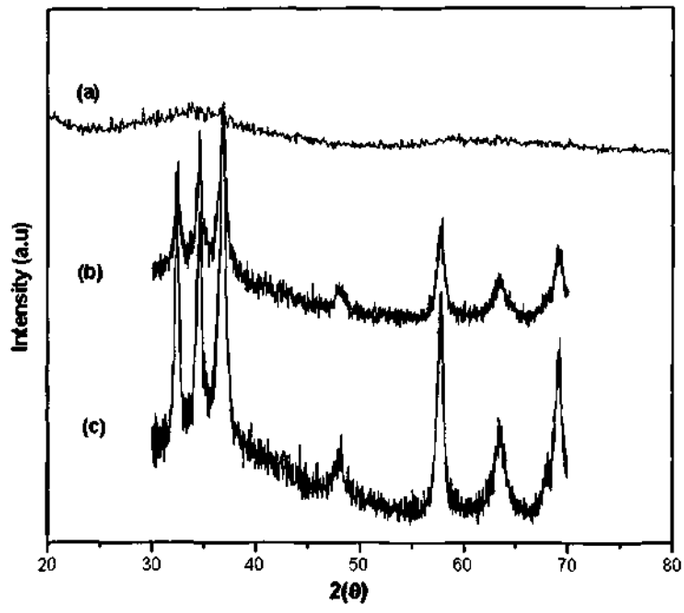

Figure 4.28: (a)-(c) XRD patterns of GaN obtained by procedure (i), (iv) and (v).

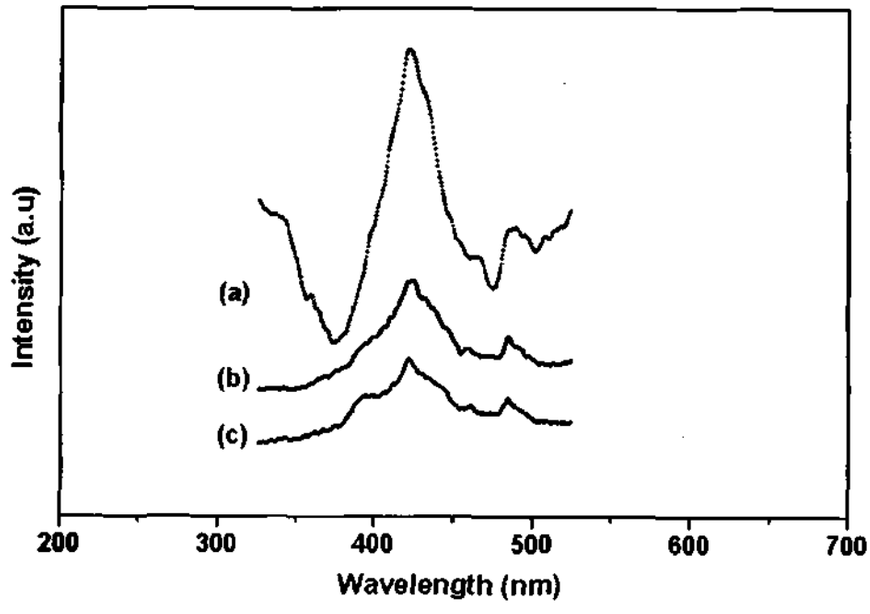

Figure 4.29: (a)-(c) PL spectra of GaN obtained by procedure (i), (iv) and (v).

36 m^2g^{-1} and 20 m^2g^{-1} respectively. GaN obtained by the reaction of NH_3 with Ga_2O_3 or $Ga(acac)_3$ mixed with carbon gave low surface areas of 20 m^2g^{-1} or less. We, therefore, employed a mixture of Ga_2O_3 and $Ga(acac)_3$ as the starting material based on a recent literature report [24]. We show the SEM and TEM images of the GaN particles obtained by procedure (iv) in Figures 4.26 (b) and 4.27 (b), respectively. The x-ray diffraction pattern of these GaN particles is shown in Figure 4.28 (b). The corresponding ED pattern shows rings with (002), (101) and (110) reflections (see the inset in Figure 4.28 (b)). The average size of the particles inferred from TEM images is around ~ 25 nm. The PL spectrum in Figure 4.29 (b) shows the characteristic emission of GaN. The BET surface area from the nitrogen adsorption isotherm is 45 m^2 g^{-1}. We show the SEM and TEM images of the GaN particles obtained by procedure (v) in Figure 4.26 (c) and 4.27 (c) respectively. The only difference in this procedure is that boric acid was present in the reaction mixture. The average size of the particles as inferred from the TEM images is ~ 30 nm. The ED pattern shows Bragg reflections (002), (101) and (110) (see the inset in Figure 4.27 (c)). The x-ray diffraction of the GaN particles obtained by this method is shown in Figure 4.28 (c). The PL spectrum in Figure 4.28 (c) shows the characteristic emission of GaN. In Figure 4.30 (b), we show the N_2 adsorption isotherm for the GaN, which appears to be of Type II unlike the previous cases. The BET surface area is 59 m^2g^{-1}. The GaN sample obtained by procedure (vi) gave a BET surface area of 10 m^2g^{-1}. However, the results from procedure (vii) were encouraging. The x-ray diffraction pattern of the GaN particles (Figure 4.31 (a)) by this procedure showed them to be amorphous. The surface area of the sample is 66 m^2g^{-1}, with a Type IV adsorption isotherm. The pore diameter is 43 Å. (see Figures 4.31 (b) and (c)). In some ways, the properties of the

GaN obtained by procedure (vii) are comparable to those obtained by procedure (i) starting from γ- Ga_2O_3.

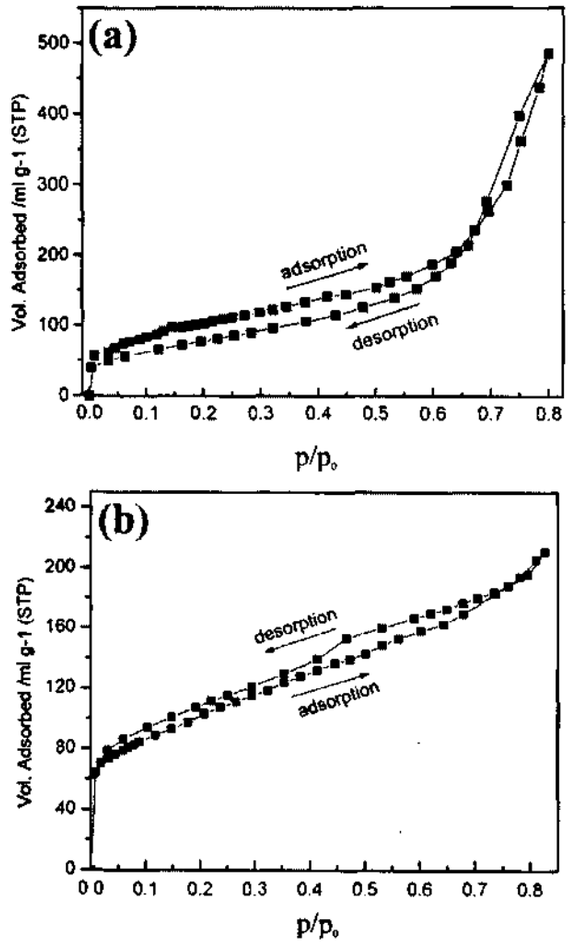

Figure 4.30: N_2 adsorption isotherms of GaN obtained by (a) procedure (i) and (b) procedure (v).

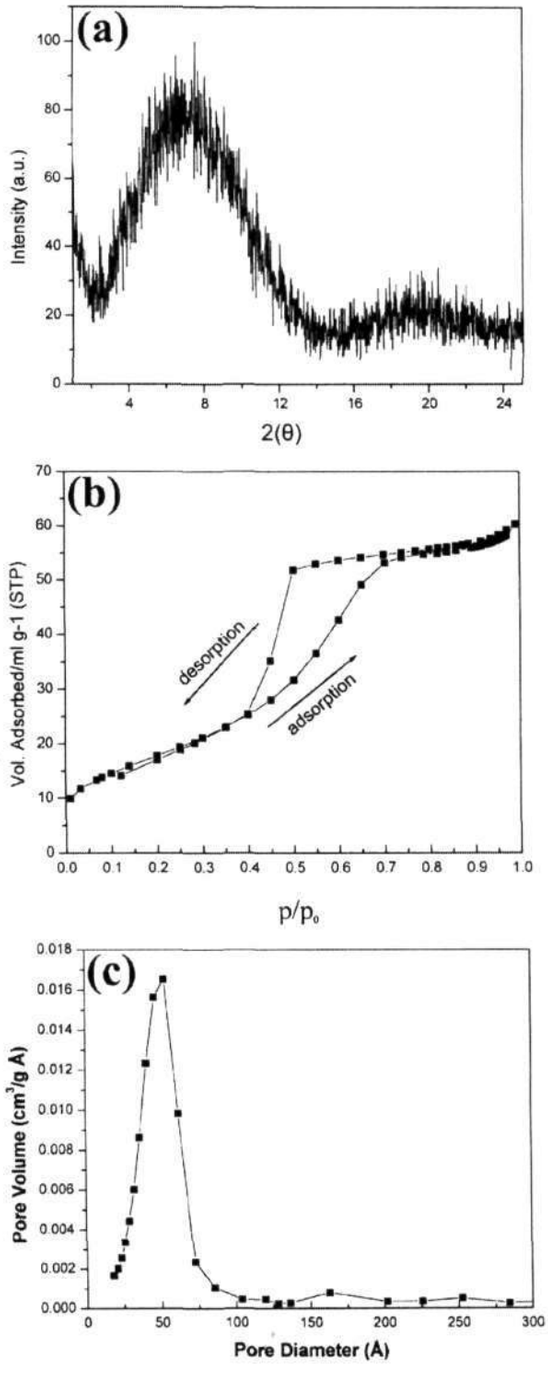

Figure 4.31: (a) XRD pattern of GaN obtained by procedure (vii). (b) N_2 adsorption isotherm and (c) pore diameter distribution of GaN obtained by procedure (vii).

Thus nanostructured GaN has been prepared by a variety of methods to investigate their properties, in particular the porous nature of the samples. Of all the methods employed for the preparation of nanoparticles, ammonolysis of γ-Ga_2O_3 as well as Ga_2O_3 prepared in the presence of a surfactant gave relatively good surface areas. GaN prepared by the ammonolysis of a mixture of Ga_2O_3 and H_3BO_3 also exhibits a high surface area (59 m^2g^{-1}). It is noteworthy that nanostructured GaN prepared starting from mesoporous Ga_2O_3 samples show type IV adsorption isotherms with surface areas of the order of 60 m^2g^{-1}.

4.4.5 InN nanowires and nanotubes

Reaction of indium acetate with HMDS in the absence of a solvent at 300 °C yielded interesting nanostructures consisting of both nanowires and nanotubes with yields of 40 and 60 %, repectively. The XRD pattern of these nanostructures was characteristic of wurtzite InN (Figure 4.32). The SEM image in Figure 4.33 (a) shows the presence of a large number of nanowires and nanotubes. The nanowires have diameters in the 50–100 nm range with lengths extending upto 1 μm, as seen in the low-resolution TEM images in Figure 4.33 (b). We have also found the presence of a few Y-junction nanowires (Figure 4.33 (c)). The nanowires are single-crystalline with Bragg spots corresponding to the (100), (101), and (002) planes in the selected-area electron diffraction (SAED) pattern (see inset of Figure 4.33 (c)). HREM images of the nanowires gave interplanar spacing of ~ 2.7 Å, which corresponds to the (101) plane of the wurtzite structure, with the growth direction of the nanowires being parallel to the (101) plane. Figure 4.33 (d) and (e) shows TEM images of the InN nanotubes. They show an interlayer spacing of 3.08 Å corresponding to the (100) planes as shown in the HREM image in Figure 4.33 (f). This spacing is distinctly

lower than the interlayer spacing of 3.4 Å in carbon nanotubes. The inset in Figure 4.33 (f) shows the SAED pattern of the InN nanotube with Bragg spots corresponding to the (100) planes.

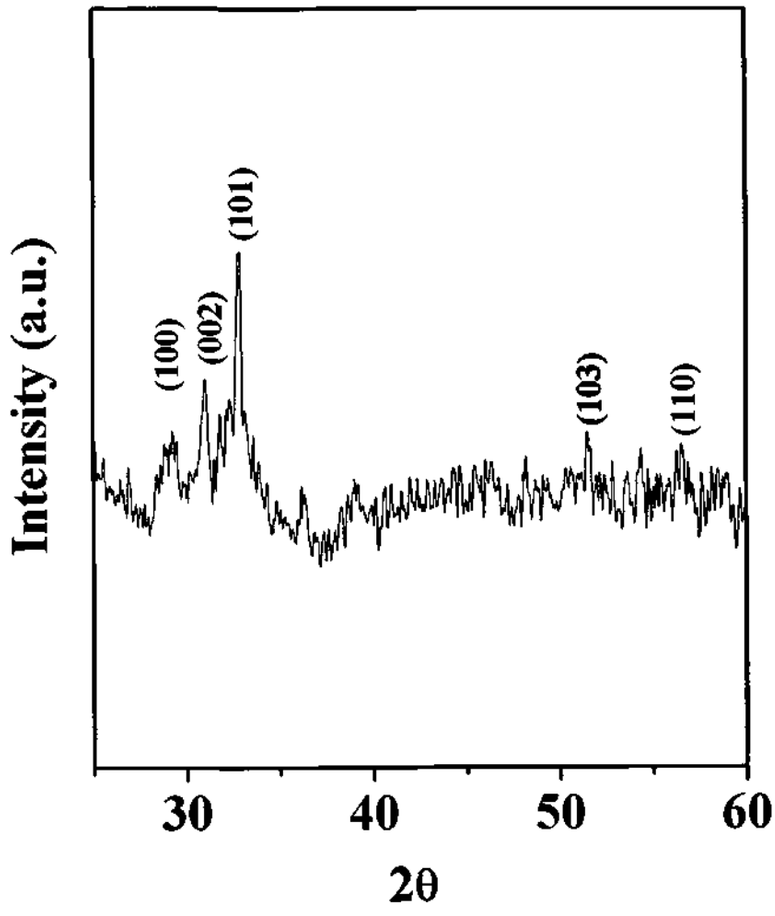

Figure 4.32: Powder XRD patterns of InN nanostructures.

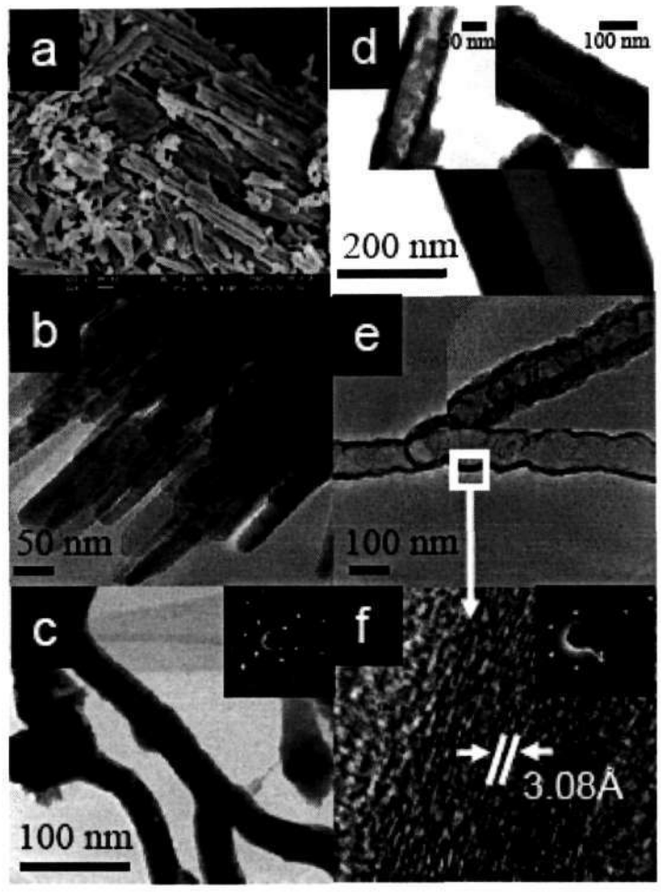

Figure 4.33: (a) SEM image of a mixture of InN nanowires and nanotubes, (b) and (c) TEM images of nanowires, (d) and (e) TEM images of nanotubes and (f) HREM image of a wall of the nanotube. Insets in (c) and (f) show electron diffraction patterns.

Optical absorption spectrum of the nanowires and nanotubes gave a sharp band around 1475 nm (~ 0.8 eV; Figure 4.34). Interestingly, no distinct absorption features were found in the 600–1000 nm region. This is significant since the nanostructures were prepared at a low temperature (300 °C), well below the decomposition temperature of InN (500 °C) [60]. We, therefore, propose that the 0.7 eV band is not due to an impurity, such as through the inclusion of metallic In [34]. Wu *et al.* [35 (a)] have pointed out that the intrinsic bandgap in the 0.7–0.8 eV range is characteristic of InN rather than the commonly reported 1.9 eV. The variation of the bandgap between 0.7 and 1.7 eV is reported to arise as a result of the dependence on the electron concentration [35 a–b] Theoretical calculations show that the intrinsic bandgap of InN is ~ 0.65 eV [36]. The 1.9 eV band has been considered to arise from oxygen incorporation [61] The absorption spectrum reported in the present study clearly show that the band in the 0.7–0.8 eV region is exhibited by the nanostructures of InN. Because of the absence of a clear band centered around 1.9 eV in the samples prepared by us at low temperatures, we have reason to believe that the 1.9 eV band may not be intrinsic, unlike the 0.7 eV band. Room-temperature PL emission spectrum of the InN nanostructures presented herein gave a band centered at around 675 nm (Figure 4.35), but we could not record the low-energy band in the near-infrared region. The 675 nm PL band arising from defects is known to be characteristic of InN [31,33]. The infrared spectra of the nanostructures showed a band around 450 cm^{-1} due to In-N stretching mode [27].

The present study has enabled the successful preparation of InN nanowires, and nanotubes by employing a new chemical route starting from indium acetate and HMDS. The nanostructures have been characterized by X-ray diffraction, electron

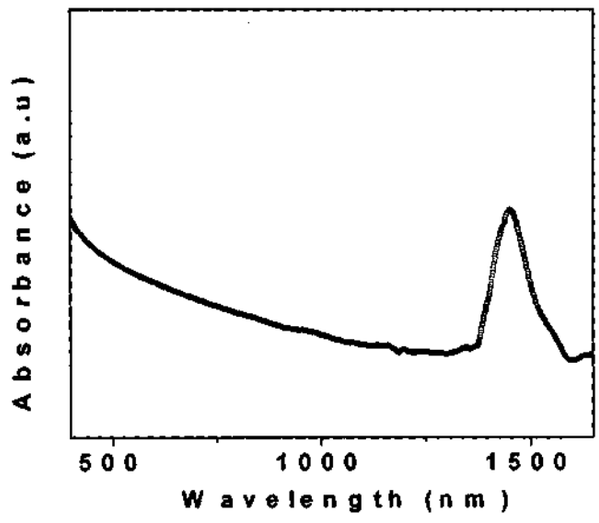

Figure 4.34: Electronic absorption spectrum of a mixture of nanowires and nanotubes (prepared by the reaction of indium acetate with HMDS).

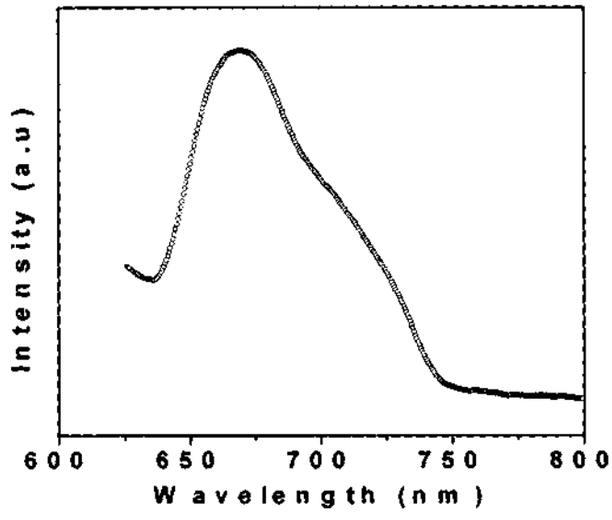

Figure 4.35: PL spectrum of a mixture of nanowires and nanotubes.

microscopy, and various spectroscopic methods. It has been shown that the near-infrared band around 0.7 eV is characteristic of these materials.

4.5 Conclusions

We have successfully synthesized a variety of nanostructures of group III-V nitrides by a combination of novel and simple chemical routes. In the case of BN and GaN this has been made possible by employing activated carbon, MWNTs and in some cases Fe (or Ni) catalyst. Interestingly we have observed GaN nanotubes for the first time. More importantly we have been able to successfully synthesize Mn-doped GaN nanowires (by a modified procedure similar to that of the synthesis of GaN nanowires) and study their optical and magnetic properties. This is the first effort towards doping of GaN nanowires.

A general scheme by which various nitride nanotubes (e.g., BN) and nanowires/nanorods (e.g., GaN) may be derived based on the use of carbon nanotubes as templates is given in Figure 4.36. It can be seen that the synthesis of BN nanotubes results from the substitution of carbon atoms in the graphite network. The synthesis of the other nitrides, on the other hand (e.g., GaN), is by a CNT confined reaction giving rise to nanowires/nanorods. The other reactions using activated carbon as a reactant involve a vapor-solid mechanism whereas those involving the catalyst proceed through the VLS mechanism resulting in nanowires. In the case of the synthesis of the various nitrides that is related to the use of carbon, the vapor phase reactions involved in the formation of nitrides need to be understood. In most of the cases involving the use of carbon the formation of a sub-oxide is inevitable as the first step which then

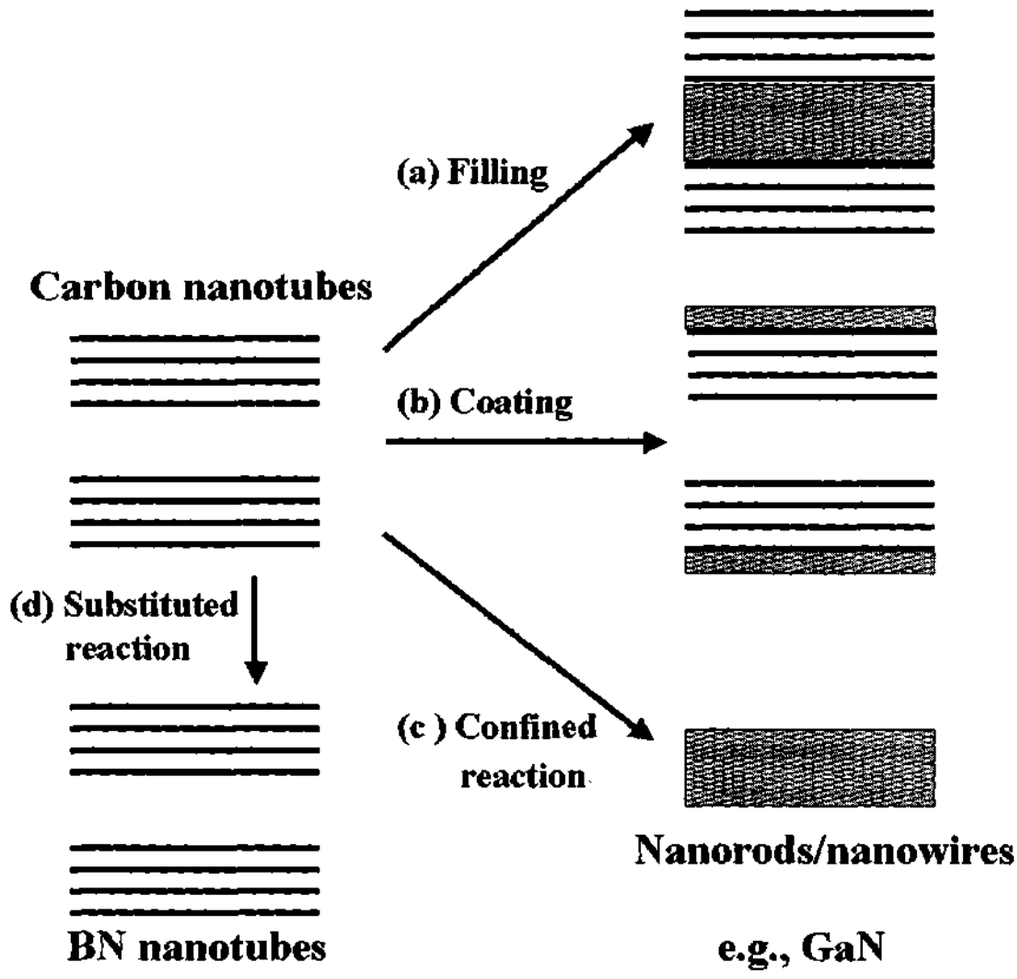

Figure 4.36: General scheme involved in the formation of the nitride nanostructures starting from CNTs as templates.

Table 4.1: Most abundant vapor species from laser ablation of oxides.

Metal oxides	N_2	NH_3	$C + N_2$
B_2O_3	BON	BON	BN
Al_2O_3	AlON, AlN	AlON	AlON, AlN
Ga_2O_3	GaN, GaON	$Ga_n(NH_3)_m$[(a)]	GaN
SiO_2	SiN	SiN	SiN
GeO_2	GeN	GeON[(b)]	GeN, GeON

(a) GaN species in presence of carbon

(b) GeON and GeN species in presence of carbon

goes onto form the nitride subsequently in the following step (e.g., BN and GaN). A mass-spectrometric study of the vapor species produced by means of a cluster apparatus through reactive laser ablation of metal oxides in different atmospheres has indeed shown that nitridic and oxynitridic are indeed formed in the vapor phase in the presence of nitrogen and ammonia [62] (Table 4.1). The nitridic species formed in the vapor phase appear to condense to form solid nanowires.

We have also been able to synthesize porous nanostructured GaN and have studied their adsorption properties. A novel chemical route has been identified in the case of the synthesis of InN nanostructures. Moreover, we have established the band gap of InN to be in the near-ir-region (~ 0.7 eV). Clearly, the simple and facile synthetic routes described here will enable the preparation of a variety of nitride nanostructures.

4.6 References

[1] B. Gil, *Group (III) Nitride Semiconductors: Physics and Applications*, Oxford University Press, 1998.

[2] S. Nakamura, S. Pearton, G. Fasol. *The Blue Laser Diode*, Springer Verlag, 1997.

[3] N. G. Chopra, R. J. Luyken, K. Cherrey, V. H. Crespi, M. L. Cohen, S. G. Louie, A. Zettl, *Science*, 1995, **269**, 966.

[4] Y. Saito, M. Maida, *J. Phys. Chem. A*, 1999, **103**, 1291.

[5] V. V. Pokropivny, V. V. Shorokod, G. S. Oleinik, A. V. Kurdyumov, T. S. Bartnitskaya, A. V. Pokropivny, A. G. Sisonyuk, D. M. Sheichenko, *J. Solid State Chem.*, 2000, **154**, 214.

[6] Y. Chen, J. F. Gerald, J. S. Williams, S. Bulcock, *Chem. Phys. Lett.*, 1999, **299**, 260.

[7] O. R. Lourie, C. R. Jones, B. M. Bartlett, P. C. Gibbons, R. S. Rouff, W. E. Buhro, *Chem. Mater.*, 2000, **12**, 1808.

[8] R. Ma, Y. Bando, T. Sato, *Chem. Phys. Lett.*, 2001, **337**, 61.

[9] D. Golberg, Y. Bando, K. Karashima, T. Sato, *Chem. Phys. Lett.*, 2000, **323**, 185 and references therein.

[10] C. C. Tang, M. L. de la Chapelle, P. Li, Y. M. Liu, H. Y. Dang, S. S. Fan, *Chem. Phys. Lett.*, 2001, **342**, 492.

[11] O. Ambacher, *J. Phys. D. Appl. Phys.*, 1999, **31**, 2653.

[12] (a) S. Nakamura, *J. Vac. Sci. Technol. A*, 1995, **13**, 307, (b) S. Nakamura, *Science*, 1998, **281**, 956, (c) T. Someya, R. Werner, A. Forchel, M. Catalano, R. Cingolani, Y. Arakawa, *Science*, 1999, **285**, 1905, (d) G. Fasol, *Science*,

1996, **272**, 1751, (e) F. A. Ponce; D. P. Bour, *Nature*, 1997, 386, 351, (f) H. Morkoc, S. N. Mohammad, *Science*, 1998, **281**, 956.

[13] W. Han, S. Fan, Q. Li, Y. Hu, *Science*, 1997, **277**, 1287.

[14] G. S. Cheng, L. D. Zhang, Y. Zhu, G. T. Fei, L. Li, C. M. Mo, Y. Q. Mao, *Appl. Phys. Lett.*, 1999, **75**, 2455.

[15] X. Chen, J. Li, Y. Cao, Y. Lan, H. Li, M. He, C. Wang, Z. Zhang, Z. Qiao, *Adv. Mater.*, 2000, **12**, 1432.

[16] C. –C. Chen, C. –C. Yeh, *Adv. Mater.*, 2000, **12**, 738.

[17] X. Duan, C. M. Lieber, *J. Am. Chem. Soc.*, 2000, **122**, 188.

[18] H. Y. Peng, . X. T. Zhou, N. Wang, Y. F. Zheng, L. S. Liao, W. S. Shi, C. S. Lee, S. T. Lee, *Chem. Phys. Lett.*, 2000, **327**, 263.

[19] M. Zajac, R. Doradzinski, J. Gosk, J. Szczytko, M. Lefeld-Sosnowska, M. Kaminska, A. Twardowski, M. Palczewska, E. Grzanka, W. Gebicki, *Appl. Phys. Lett.*, 2001, **78**, 1276.

[20] N. Theodoropoulou, A .F. Hebard, M. E. Overberg, C. R. Abernathy, S. J. Pearton, S. N. G. Chu, R. G. Wilson, *Appl. Phys. Lett.*, 2001, **78**, 3475.

[21] M. L. Reed, N. A. El-Masry, H. H. Stadelmaier, M. K. Ritums, M. J. Reed, C. A. Parker, J. C. Roberts, S. M. Bedair, *Appl. Phys. Lett.*, 2001, 79, 3473.

[22] G. Chaplais, K.Schlichte, O. Stark, R. A. Fischer, S. Kaskel, *Chem. Commun.*, 2003, 730.

[23] G. Chaplais, S. Kaskel, *J. Mater. Chem.*, 2004, **14**, 1017.

[24] S. Y. Bae, H. W. Seo, J. Park, H. Yang, B. Kim. *Chem. Phys. Lett.*, 2003, 376, 445.

[25] F. A. Ponce, D. P. Bour, *Nature*, 1997, **386**, 351.

[26] Y -J Bai, Z -G Liu, X -G Xu, D -L Cui, X -P Hao, X. Feng, Q -L Wang, *J. Cryst. Growth*, 2002, **241**, 189.

[27] J. Xiao, Y. Xie, R. Tang, W. Luo, *Inorg. Chem.* 2003, **42**, 107.

[28] N. Takahashi, A. Niwa, H. Sugiura, T. Nakamura, *Chem. Commun.*, 2003, 318.

[29] S. D. Dingman, N. P. Rath, P. D. Markowitz, P. C. Gibbons, W. E. Buhro, *Angew. Chem. Intl. Ed.*, 2000, **39**, 1470.

[30] H. Parala, A. Devi, F. Hipler, E. Maile, A. Birkner, H. W. Becker, R. A. Fischer, *J. Cryst. Growth*, 2001, **231**, 68.

[31] C. H. Liang, L. C. Chen, J. S. Hwang, K. H. Chen, Y. T. Hung, Y. F. Chen, *Appl. Phys. Lett.*, 2002, **81**, 22.

[32] J. Zhang, L. Zhang, X. Peng, X. Wang, *J. Mater. Chem.*, 2002, **12**, 802.

[33] T. Tang, S. Han, W. Jin, X. Liu, C. Li, D. Zhang, C. Zhou, B. Chen, J. Han, M. Meyyapan, *J. Mater. Res.*, 2004, **19**, 423.

[34] T. V. Shubina, S. V. Ivanov, V. N. Jmerik, D. D. Solnyshkov, V. A. Vekshin, P. S. Kopev, A. Vasson, J. Leymarie, A. Kavokin, H. Amano, K. Shimono, A. Kasic, B. Monemar, *Phys. Rev. Lett.*, 2004, **92**, 1174071.

[35] (a) J. Wu, W. Walukiewicz, K. M. Yu, J. W. Ager III, E. E. Haller, H. Lu, W. J. Schaff, Y. Saito, Y. Nanishi, *Appl. Phys. Lett.*, 2002, **80**, 3967. (b) J. Wu, W. Walukiewicz, S. X. Li, R. Armitage, J. C. Ho, E. R. Weber, E. E. Haller, H. Lu, W. J. Schaff, A. Barcz, R. Jakiela, *Appl. Phys. Lett.*, 2004, **84**, 2805.

[36] F. Bechstedt, J. Furthmüller, *J. Crystal Growth*, 2002, **246**, 315.

[37] X. C. Wu, W. H. Song, W. D. Huang, M. H. Pu, B. Zhao, Y. P. Sun, J. J. Du, *Mater. Res. Bull.*, 2001, **36**, 847.

[38] (a) C. N. R. Rao, R. Seshadri, A. Govindaraj, R. Sen, *Mat. Sci. Eng. R.* 1995,

15, 209, (b) C. N. R. Rao, R. Sen, B. C. Satishkumar, A. Govindaraj, *Chem. Commun.* 1998, 1525.

[39] C. Journet, W. K. Maser, P. Bernier, A. Loiseau, M. Lamy de la Chapelle, S. Lefrant, P. Denierd, R. Lee, J. E. Fischer, *Nature*, 1997, **388**, 756.

[40] M. R. Delgado, C. O. Arean, *Mater. Lett.*, 2003, **57**, 2292.

[41] C. O. Arean, A. L. Bellan, M. P. Mentruit, M. R. Delgado, G. T. Palomino, *Microporous Mesoporous Mater.*, 2000, **40**, 35.

[42] M. Yada, M. Ohya, M. Machida, T. Kijima, *Langmuir*, 2000, **16**, 4752.

[43] W. Han, Y. Bando, K. Kurashima, T. Sato, *Appl. Phys. Lett.*, 1998, **73**, 3085.

[44] D. Golberg, Y. Bando, L. Bourgeois, K. Kurashima, T. Sato, *Appl. Phys. Lett.*, 2000, **77**, 1979.

[45] K. B. Shelimov, M. Moskovits, *Chem. Mater.*, 2000, **12**, 250.

[46] V. Cholet, L.V. Vandenbulcke, J.P. Rouan, P. Baillif, H. Erre, *J. Mater. Sci.*, 1994, **29**, 1417.

[47] W. Han, J. Cumings, X. Huang, K. Bradley and A. Zettl, *Chem. Phys. Lett.*, 2001, **346**, 368.

[48] W. Han, Y. Bando, K. Kurashima, T. Sato, *Chem. Phys. Lett.*, 1999, **299**, 368.

[49] G. S. Sudhir, Y. Peyrot, J. Krüger, Y. Kim, R. Klockenbrink, C. Kisielowski, M. D. Rubin, E. R. Weber, W. Kriegseis, B. K. Meyer, *Mat. Res. Soc. Symp.*, 1998, **482**, 525.

[50] M. C. Park, K. S. Huh, J. M. Myoung, J. M. Lee, J. Y. Chang, K. I. Lee, S. H. Han, W. Y. Lee, *Solid. State. Comm.*, 2002, **124**, 11.

[51] N. Theodoropoulou, K. P. Lee, M. E. Overberg, S. N. G. Chu, A. F. Hebard, C. R. Abernathy, S. J. Pearton, R. G. Wilson, *J. Nanosci. Nanotech.* 2001, **1**, 101.

[52] (a) M. E. Overberg, C. R. Abernathy, S. J. Pearton, N. Theodoropoulou, K. T. McCarthy, A. F. Hebard, *Appl. Phys. Lett.*, 2001, **79**, 1312, (b) J. M. Baik, H. W. Jang, J. K. Kim, J –L. Lee, *Appl. Phys. Lett.*, 2003, **82**, 583, (c) J. M. Baik, H. S. Kim, C. G. Park, J –L. Lee, *Appl. Phys. Lett.*, 2003, **83**, 2632, (d) S. Dhar, O. Brandt, A. Trampert, L. Däweritz, K. J. Friedland, K. H. Ploog, *Appl. Phys. Lett.*, 2003, **82**, 2077.

[53] Y. Shon, Y. H. Kwon, Sh. U. Yuldashev, J. H. Leem, C. S. Park, D. J. Fu, H. J. Kim, T. W. Kang, X. J. Fan, *Appl. Phys. Lett.*, 2002, **81**, 1845.

[54] L. Chen, P. J. Klar, W. Heimbrodt, F. Brieler, M. Froba, *Appl. Phys. Lett.*, 2000, **76**, 3531.

[55] W. Chen, R. Sammynaiken, Y. Huang, J. –O. Malm, R. Wallenberg, J- O. Bovin, V. Zwiller, N. A. Kotov, *J. Appl. Phys.*, 2001, **11**, 1120.

[56] M. A. Malik, P. O. Brien, N. Revaprasadu, *J. Mater. Chem.*, 2001, **11**, 2382.

[57] G. Yi, B. Sun, F. Yang, D. Chen. *J. Mater. Chem.*, 2001, **11**, 2928.

[58] F. Rouquerol, J. Rouquerol, K. Sing, *Adsorption by Powders & Porous Solids*, Academic Press, San Diego, 1998.

[59] G. Gundiah, A. Govindaraj, C. N. R. Rao, *Chem. Phys. Lett.*, 2002, **351**, 189.

[60] Q. Guo, O. Kato, A. Yoshida, *J. Appl. Phys.*, 1993, **73**, 7969.

[61] A. G. Bhuiyan, A. Hashimoto, A. Yamamoto, *J.Appl. Phys.*, 2003, **94**, 2779.

[62] G. Raina, G. U. Kulkarni, C. N. R. Rao, *Mater. Res. Bull.*, 2004, **39**, 1271.

Chapter 5
Surfactant-assisted synthesis of metal chalcogenide nanostructures

Summary*

Semiconductor nanowires of metal chalcogenides have been synthesized by the use of surfactants such as Na-AOT (sodium bis(2-ethylhexyl sulfosuccinate)) and Triton X-100 ((t-octylphenoxypolyethoxyethanol). The nanowires of ZnS, ZnSe, CdS, CdSe, CuS and CuSe synthesized by such a surfactant-assisted method have high aspect ratios. Nanotubes of CdS and CdSe were obtained, for the first time, by using a high surfactant concentration. A lower surfactant concentration, on the other hand, favors the formation of nanowires. All the nanostructures have been characterized by X-ray diffraction, electron microscopy and optical spectroscopy. The chalcogenide nanostructures possess hexagonal structures, independent of the structures of the stable phases of these materials. The electronic absorption spectra and photoluminescence spectra of the nanostructures show blue-shifts in comparison to those of the bulk samples.

Raman studies have been carried out on the synthesized CdSe nanotubes and ZnSe nanowires obtained by the surfactant-assisted synthesis. The Raman spectrum of the CdSe nanotubes shows modes at 207.5 and 198 cm^{-1}; the former arises from the longitudinal optic phonon mode red-shifted with respect to the bulk mode because of

* Papers based on these studies have appeared in Appl. Phys. Lett. (2001), Israel J. Chem. (2001) and J. Nanosci and Nanotech. (June 2002), (Oct 2002) .

phonon confinement, and the latter is the $l = 1$ surface phonon. Analysis based on the phonon confinement model demonstrates that the size of the nanoparticle responsible for the red-shift is about 4 nm, close to the estimate from the blue-shift of the photoluminescence. The Raman spectrum of ZnSe nanowires shows modes at 257 and 213 cm^{-1}, assigned to longitudinal and transverse optic phonons, blue-shifted with respect to the bulk ZnSe modes because of compressive strain. The mode at 237 cm^{-1} is the surface phonon.

5.1 Introduction

Inorganic nanomaterials, in particular rods, wires, dots and related structures of II–VI semiconductors, are assuming great importance because of a variety of possible applications [1-3]. First, II-VI semiconductors present a broad range of band-gaps (from 0.15 eV in HgTe to 3.68 eV in ZnS). Second, most of them present direct energy gaps, which makes them particularly important for electro-luminescence devices such as light emitting diodes and lasers. They are efficient emitters in the blue to the ultraviolet spectral region and excitons in these compounds are much more stable than those in the conventional semiconductors that are widely used for optoelectronic applications [4-6]. Recent studies showed that the low-dimensional nanostructures of Zn-based II-VI wide band gap semiconductors exhibit exciton binding energies exceeding their optical phonon energies. As a consequence, the quantum yield of the II-VI-based devices is expected to be comparable to or greater than that of the other common semiconductor devices. This advantage makes the nanoscale II-VI materials distinct from the other semiconductor materials with respect to important applications for optoelectronics [7,8]. We have been interested in devising new routes for the synthesis of some of these nanomaterials, in particular the sulphides and selenides of Zn, Cd and Cu. In the present study, we have employed a surfactant- based approach for the synthesis of these materials. In what follows, we describe the scope of the investigations of these materials.

5.2 Scope of the present investigations

Of the II-VI semiconductor chalcogenides, zinc sulfide is a direct wide band gap transparent semiconductor (band gap ~ 3.68 eV) and one of the most important

materials used in photonics research [9-11]. It is also an important material for a variety of applications such as electroluminescent devices, solar cells, and other optoelectronic devices. One-dimensional nanostructures of ZnS are attractive because they are candidates for electronic and optoelectronic nanodevices [12,13]. ZnSe is also a direct band gap semiconductor, with a room temperature band gap energy and an emission at 2.8 eV. This suggests that ZnSe is potentially a good material for short-wavelength lasers and other photoelectronic devices. Therefore ZnSe is of great interest as a model material in a variety of forms such as thin films, quantum wells, and bulk crystals [4,5,14-17]. Thus ZnSe-based optoelectronic devices have been the subject of intensive research [18].

CdS is a wide band gap semiconductor (2.42 eV) and has extensive applications in nonlinear optical materials, light-emitting diodes, solar cells, electronic and optoelectronic devices. Routkevitch *et al.* [19], have obtained nanowires of CdS with the length upto 1 μm and diameter 9 nm by electrochemically depositing the semiconductor directly into the pores of AAO films from electrolyte in dimethyl sulfoxide. CdS single-crystal nanowires were prepared using electrochemically induced deposition in the pores of an AAO template from an acidic chemical bath containing cadmium chloride and thioacetamide [20]. Wurtzite-structured CdSe is an important II-VI semiconductor compound for optoelectronics [21]. CdSe quantum dots are the most extensively studied quantum nanostructure model system for investigating a wide range of nanoscale electronic, optical, optoelectronic, and chemical processes [22]. CdSe was also the first example of self-assembled semiconductor nanocrystal superlattices [23]. With a direct band gap of 1.8 eV, CdSe quantum dots have been used for laser diodes [24], nanosensing [25], and biomedical

imaging [26]. Although CdSe quantum dots have been the dominant material for studying the quantum confined effect, there are only a few reports on the synthesis of one-dimensional nanostructures of CdSe. Shape controlled synthesis of CdSe nanocrystals has been carried out by injection of precursor molecules into hot surfactants [27-29]. Nanorods of both CdS and CdSe have been prepared by the arrested precipitation of the respective ions in a micellar solution of CTAB [30]. CdS and CdSe nanowires have been prepared by injecting the reactants or by direct electrodeposition into AAO membranes [31,32].

CuS is interesting because besides being an excellent semiconductor it also exhibits properties of commercial importance as a pigment, catalyzer and a colored indicator of nigrosine [33]. Wang *et al.* [34], has grown nanowires of copper sulfide in a medium containing surfactant. In this method rough oxidized copper surface was treated with H_2S in the presence of Na–AOT to obtain nanowires of Cu_xS with diameter 10 –100 nm and length 0.3 –30 μm. Copper selenide on the other hand is widely used in solar cells as an optical filter and superionic material [35-37], as a sensor and as a laser material [38]. Various traditional methods have been utilized to synthesize copper selenides. The usual morphologies of copper selenides as prepared are microparticles [39], films [40], and plate-like nanocrystals [41].

From the discussion presented above it is evident that the synthesis of one-dimensional nanostructures of II-VI semiconductor chalcogenides is relatively unexplored. The successful synthesis of nanostructures of these chalcogenides by new chemical routes should offer a broad scope for a range of applications. In this connection, we have explored ways of preparing nanostructures of sulfides and selenides of Zn, Cd and Cu by soft chemical routes. For this purpose, we have

employed surfactant-assisted synthesis wherein Na-AOT (sodium bis(2-ethylhexyl) sulfosuccinate) and Triton X-100 (t-octyl- C_6H_4- $(OCH_2CH_2)_x$ OH (x=9,10)) are employed as surfactants. By this means, we have been able to obtain nanowires of sulfides and selenides of Zn, Cd and Cu with high aspect ratios. More importantly, we have been able to obtain nanotubes of some of these chalcogenides for the first time, typically those of CdS and CdSe. The nanowires and nanotubes of the various chalcogenides posses the hexagonal structure. We have investigated the optical absorption and emission spectra of the nanostructures of these materials since they have not been examined in detail earlier. In addition to the optical measurements, Raman spectroscopic studies were carried out on the CdSe nanotubes and ZnSe nanowires. The main motivation for the Raman study of these samples was to examine confinement effects of optical phonons, if any, in these nanotubes and nanowires.

5.3 Experimental

5.3.1 Synthesis

Surfactant-assisted synthesis was employed to prepare nanowires of sulfides as well as of selenides of Zn, Cd and Cu. A typical procedure for the synthesis of the sulfide nanostructures is as follows. The starting materials were the respective oxides of Zn, Cd and Cu. A suspension of the oxide (10 mmol) was prepared in the presence of the surfactant (AOT in 30 ml cyclohexane). An aqueous solution (40 ml) of thioacetamide (10 mmol) in an acidic or basic medium (HCl or NaOH was

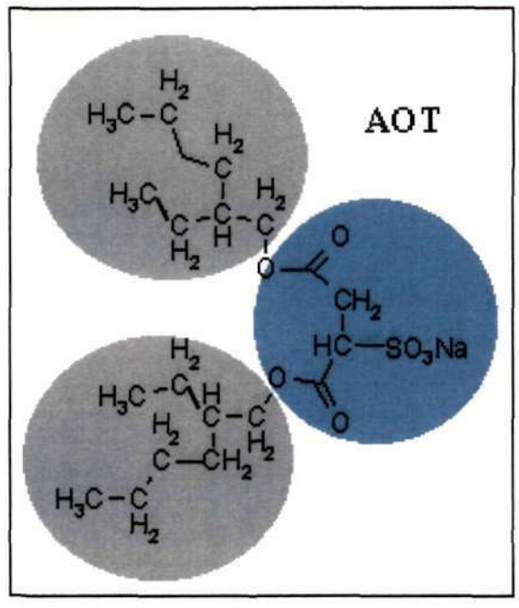

Structure of AOT, sodium bis(2-ethylhexyl sulfosuccinate)

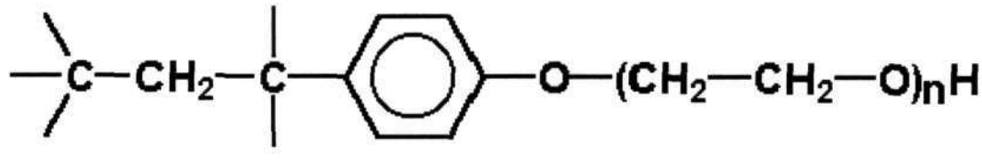

n = 9-10

Structure of Triton X-100 (t-octylphenoxypolyethoxyethanol)

used to liberate S^{2-}) was added drop-wise to the emulsion, under stirring. The reactant mixture was then refluxed in an inert atmosphere at ~ 40-60 °C for 16 hours and left overnight. The product obtained was washed thoroughly with ether and dried. Triton X-100 was used as the surfactant directly (without any cyclohexane) and the refluxing temperature was ~ 105 °C.

The selenide nanostructures were prepared by the following procedure: A suspension of the respective oxide (10 mmol) was prepared using AOT in 30 ml cyclohexane or Triton X-100. To this, a solution of NaHSe ($NaBH_4$/Se in 50 ml water) was added drop-wise under inert conditions, refluxed for 12 hours and left overnight. In both the sulfides and selenides, the starting material to chalcogenide ratios were 1:1. The product was washed with ether and dried. A Triton X-100 concentration of 8-16 mmol generally yielded nanowires of the metal chalcogenides. A higher surfactant concentration of 24–40 mmol predominantly yielded nanotubes in some cases. Similarly in the case of AOT, a lower concentration of 2.25 mmol gave nanowires while higher concentration of 4.5 mmol gave nanotubes. Bulk samples of these chalcogenides were prepared by standard procedures.

5.3.2 Characterization

The chalcogenide nanostructures obtained by the various procedures described above were characterized by a variety of techniques.

Powder X-ray diffraction (XRD) patterns of the products were recorded using CuKα radiation with a Rich-Seifert, XRD-3000-TT diffractometer. Samples were prepared by finely grinding the product and depositing on a glass slide.

Scanning electron microscope (SEM) images were obtained with a Leica S440 i scanning electron microscope. Energy dispersive analysis of X-rays (EDAX) was performed with a Oxford microanalysis group 5526 system attached to the SEM employing Links (ISIS) software and a Si(Li) detector. Samples for SEM and EDAX were prepared by spreading 10–20 mg of product onto a conducting carbon tape pasted on a aluminum stub, followed by sputter-coating with a gold film. EDAX

analysis was carried out in the spot profile mode with a beam diameter of 1 μm at several places on the sample.

Transmission Electron Microscopy (TEM) images were obtained with a JEOL (JEM 3010) operating with an accelerating voltage of 300 kV. Powder samples for TEM studies were prepared by dispersing the samples in CCl_4 and sonicating them using an ultrasonic bath. A drop of the suspension was put on a copper support grid covered with holey carbon film and allowed to evaporate slowly.

Electronic absorption spectra were recorded using a Perkin-Elmer Lambda 900 UV/VIS/NIR spectrophotometer. The samples were dispersed in absolute ethanol or toluene and recorded in the 2000-200 nm range.

Photoluminescence measurements were carried out at room temperature with a Perkin Elmer model LS50B luminescence spectrometer. The excitation wavelength used depended on the sample that was being studied.

Raman measurements were carried out at room temperature with a 5145-Å line from an argon ion laser and a micro-Raman setup in back-scattering geometry. The power on the sample was ~ 0.1 mW.

5.4 Results and discussion

5.4.1 Nanostructures of ZnS and ZnSe

The XRD pattern of the nanowires of ZnS (Figure 5.1) show them to have the hexagonal structure although the stable structure of bulk ZnS is cubic. The XRD pattern of ZnSe nanowires showed them to be predominantly hexagonal, with a small

proportion of the cubic phase (Figure 5.1). The stable phase of ZnSe is cubic. The XRD patterns of the nanowires were crystalline and some of the reflections are broad because of the small particle size, atleast in two dimensions. The hexagonal lattice parameters of ZnS and ZnSe nanostructures along with the bulk values are shown in Table 5.1. The uncertainities in the observed unit cell parameters are somewhat large because of the widths of the reflections. From the comparison of the lattice constants of the ZnSe nanowires with those of the bulk samples, it is clear that the lattice for ZnSe nanowires is stretched along the c-axis by ~ 0.37 Å and is compressed along the a-axis by ~ 0.15 Å. EDAX analysis of the ZnS and ZnSe nanowires showed the metal to chalcogen ratio to be 1:1.

In Figure 5.2 (a-c), we show TEM images of the ZnS nanowires obtained by using Triton X-100. The diameter is in the 10-50 nm range and the length in the range of 8-10 μm. The inset in Figure 5.2 (c) shows the electron diffraction pattern of ZnS nanowires corresponding to d(101) of 2.854 Å.

The electronic absorption spectrum of bulk ZnS shows a peak around 350 nm [42]. Nanowires of ZnS (10-30 nm dia) are reported to show an absorption peak at ~ 326 nm [42]. Nanoparticles of ZnS of 5 nm diameter are reported to show an absorption maximum around 270 nm, compared to 310 nm in the case of nanoparticles of 40 nm diameter [43]. We find that the ZnS nanowires with an average diameter in the 10-50 nm range prepared by us exhibit an absorption band between 325 and 365 nm with a peak around 340 nm (Figure 5.3 (a)). The PL spectrum of bulk ZnS is reported to show a band in the 450-500 nm regime [42]. The bulk sample prepared by us showed a PL band with features in the 450-550 nm region. ZnS nanowires of 10-30 nm diameter are reported to show a broad PL

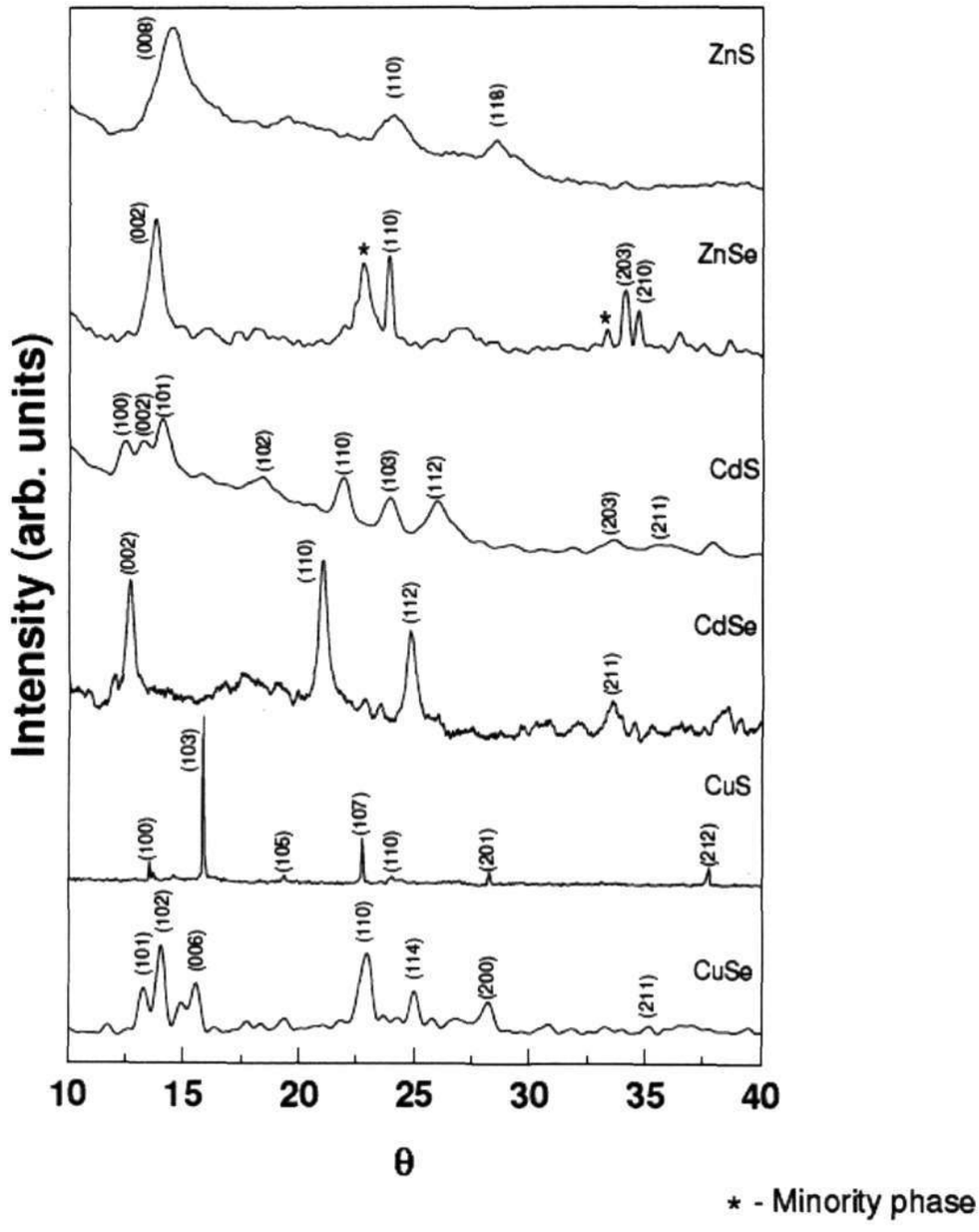

Figure 5.1: XRD patterns of the semiconductor chalcogenide nanostructures. Asterisk indicates a minority phase.

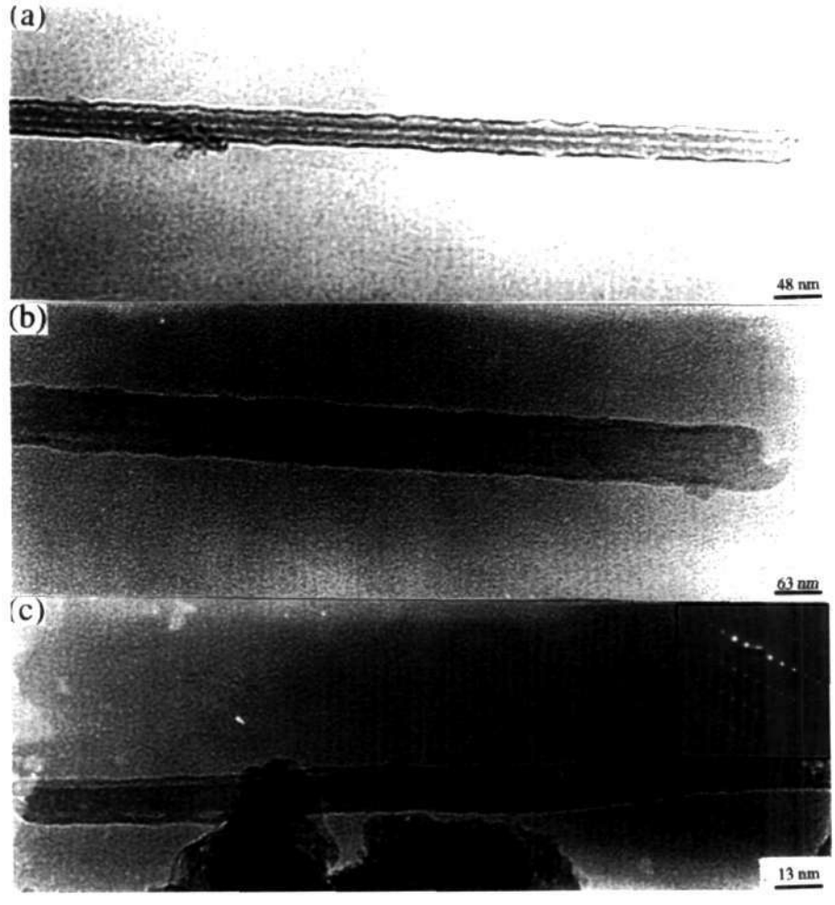

Figure 5.2: (a)-(c) TEM images of ZnS nanowires (10-50 nm dia) obtained by using Triton X-100 as the surfactant. Inset in (c) shows an electron diffraction pattern, suggesting the single crystalline nature of the nanowire.

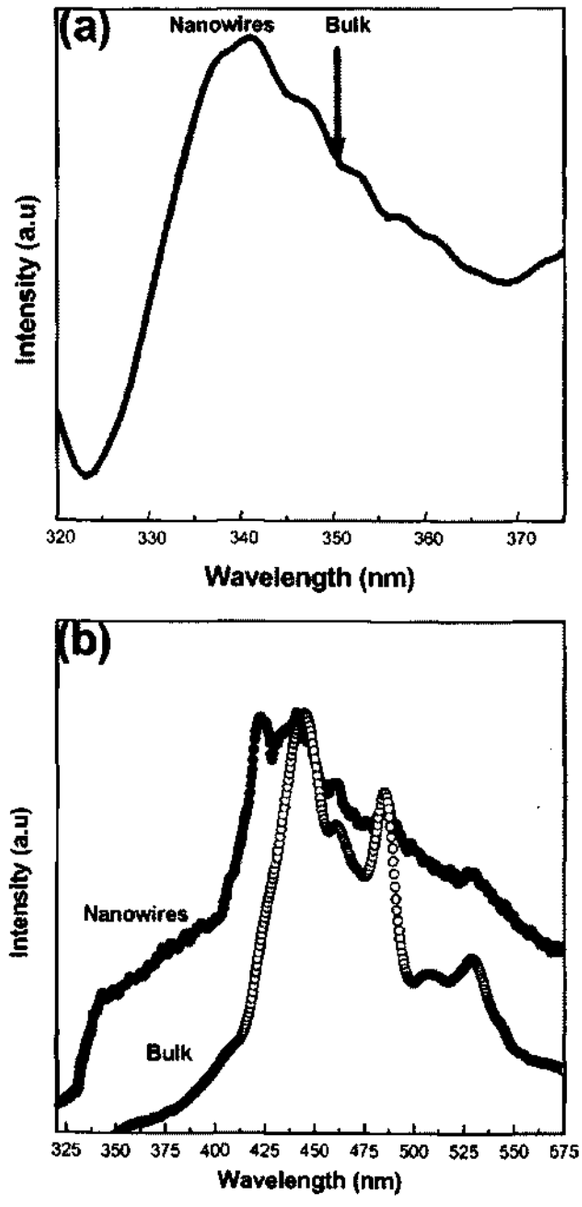

Figure 5.3: (a) Electronic absorption spectrum of ZnS nanowires. Position of the absorption maximum of the bulk sample is shown. (b) PL spectrum of ZnS nanowires relative to the bulk sample.

emission band centered at ~ 366 nm and a weak shoulder peak at ~ 330 nm [42]. The nanowires prepared by us show a broad band peaking around 430 nm and extending upto 550 nm (Figure 5.3 (b)). There is a definite blue-shift in the PL maximum of the nanowires (Table 5.2). It should be noted that ZnS nanoparticles of 2-5 nm diameter show a PL band at ~ 425 nm [43,44]. This band may be due to emission from the recombination of electron and holes in trapped surface states in the band gap region [45].

In Figure 5.4, we show the TEM images of the ZnSe nanowires obtained with Triton X-100. The diameter of the nanowires varies between 50 and 150 nm and the length is in the 5-15 μm range. The inset in Figure 5.4 (a) shows the electron diffraction pattern of ZnSe nanowires corresponding to d(110) of 1.97 Å. Shown in Figure 5.4 (c), is the TEM image of a ZnSe nanowire revealing that small spherical structures pack themselves together to form a wire-like structure. The average diameter of the nanowire in this case is ~ 100 nm.

The absorption spectrum of nanoparticles of ZnSe of 5 nm diameter shows a band around 420 nm, while nanoparticles of 3 nm diameter show the absorption maximum around 380 nm [46,47]. The ZnSe nanowires with 50-150 nm diameter prepared by us, on the other hand, show a broad band centered around 480 nm (Figure 5.5 (a)). The PL spectrum of bulk ZnSe has a band at 465 nm whereas in the case of the nanoparticles of 3 nm diameter it is reported at 400 nm [46,47]. The PL spectrum of ZnSe nanowires prepared by us shows a sharp peak at 425 nm and a weak shoulder at 435 nm (Figure 5.5 (b)). Here again there is a blue-shift of the PL band of the nanostructures (Table 5.2).

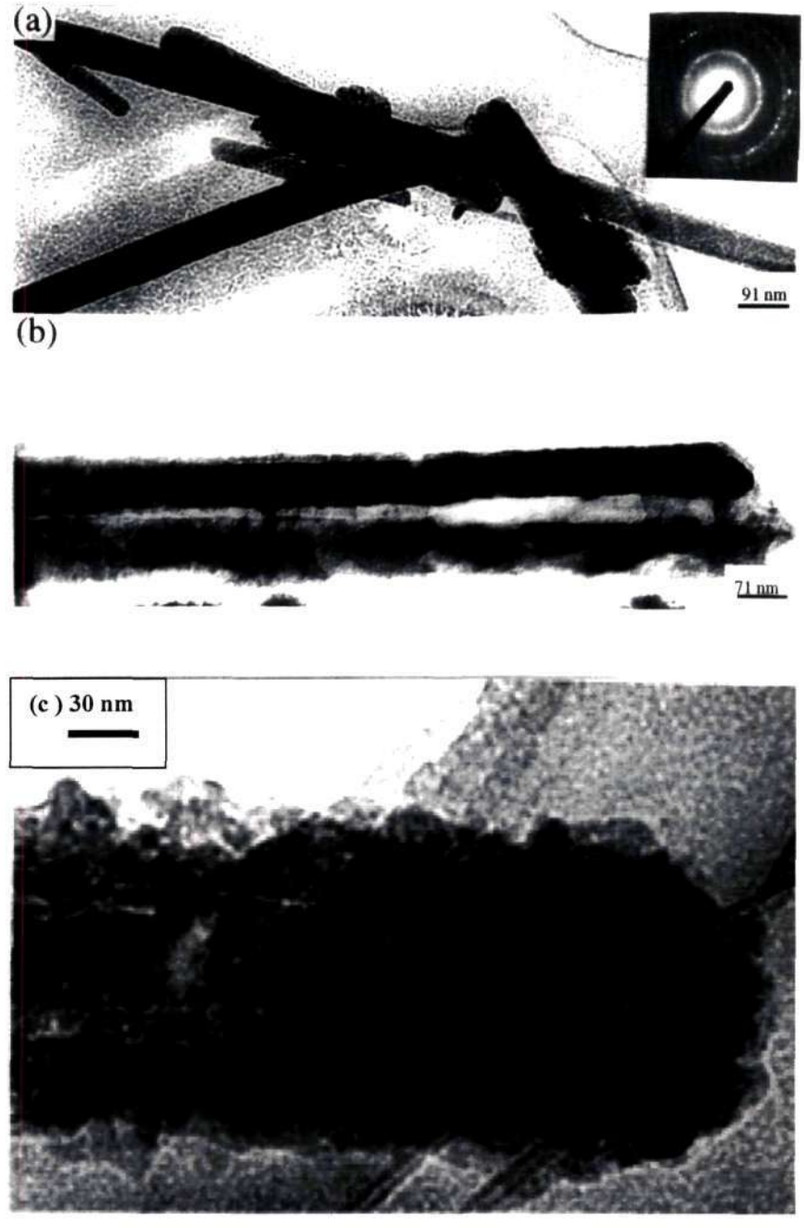

Figure 5.4: TEM images of ZnSe nanowires (50-150 nm dia) obtained by using Triton X-100 as the surfactant. Inset in (a) shows the electron diffraction pattern of the nanowire.

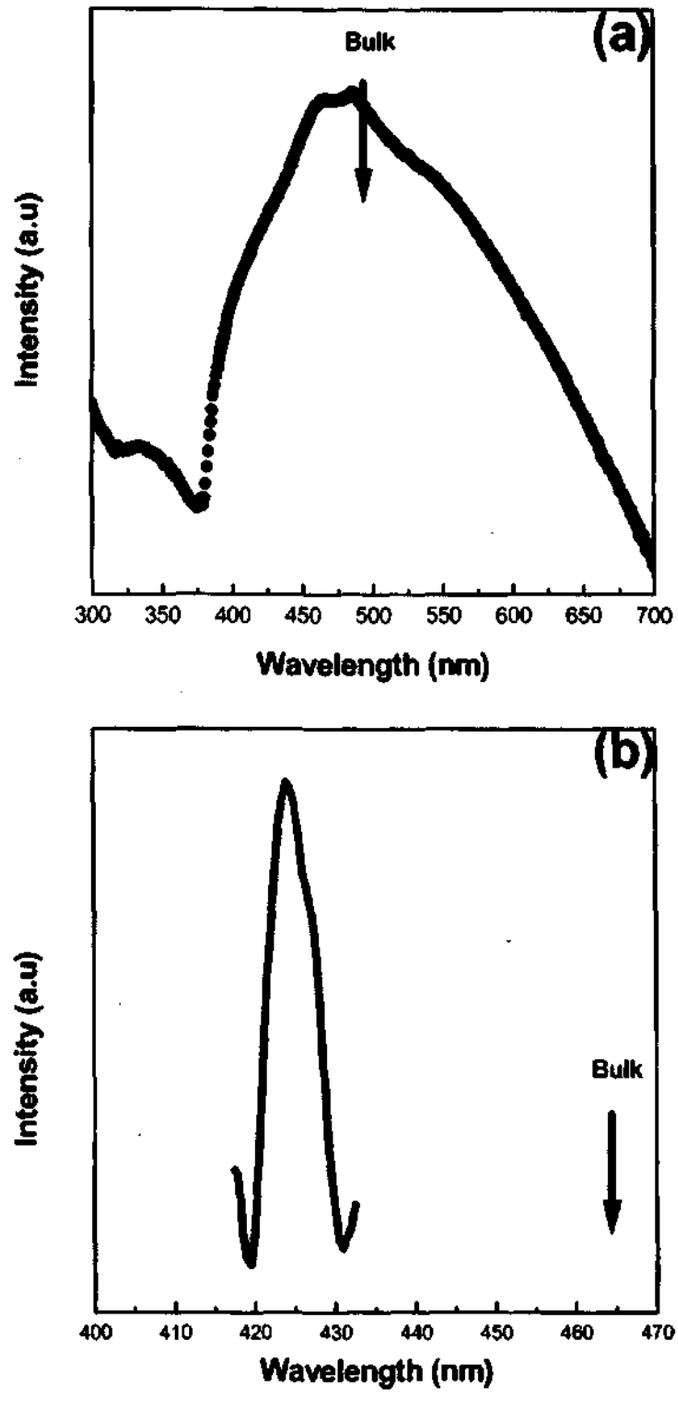

Figure 5.5: (a) Electronic absorption spectrum of ZnSe nanowires, (b) PL spectrum of ZnSe nanowires. Positions of the absorption/emission maxima of the bulk sample are shown

5.4.2 Nanostructures of CdS and CdSe

The CdS nanostructures obtained by us have the hexagonal structure as revealed by the XRD patterns (Figure 5.1), although the stable structure of CdS is ordinarily cubic. The lines were somewhat broad due to the small dimensions of the nanostructures. The observed hexagonal lattice parameters are close to those of the bulk phase (Table 5.1). It is noteworthy that CdS, which is ordinarily cubic, occurs in the hexagonal structure in the nanowires and nanotubes. EDAX analysis of the CdS nanostructures showed the metal to chalcogen ratio to be 1:1. In Figure 5.6 (a) we show a SEM image of the CdS nanowires obtained by using a lower concentration of Triton X-100 as the surfactant. TEM images of the CdS nanowires are shown in Figures 5.6 (b), (c) and (d). The diameter and the length of these nanowires are in the ranges 80-160 nm and 3-4 μm respectively. Most of the nanowires are polycrystalline as shown from the electron diffraction pattern given in the inset of Figure 5.6 (c). The value of d(100) in the diffraction pattern is of 3.66 Å as expected. The product obtained by using a higher surfactant concentration of Triton X-100 gave nanotubes. Figure 5.7 gives two TEM images of the nanotubes of CdS, with an external diameter in the 45-60 nm range and a central tubule diameter of ~ 15 nm. The central tubule appears to be surrounded by polycrystalline aggregates. The wall thickness is ~ 15 nm while the length of the nanotube varies between 2 and 5 μm. The inset in Figure 5.7 (b) shows a typical ED pattern of the CdS nanotube with diffuse rings. The innermost ring corresponds to d(100) = 3.66 Å. We have measured the electronic absorption spectrum of the nanotubes of CdS in comparison with that of the bulk samples in the powder form (Figure 5.8). We see that the high-intensity absorption maximum found in bulk CdS around 540 nm is blue shifted to considerably lower wavelengths in the

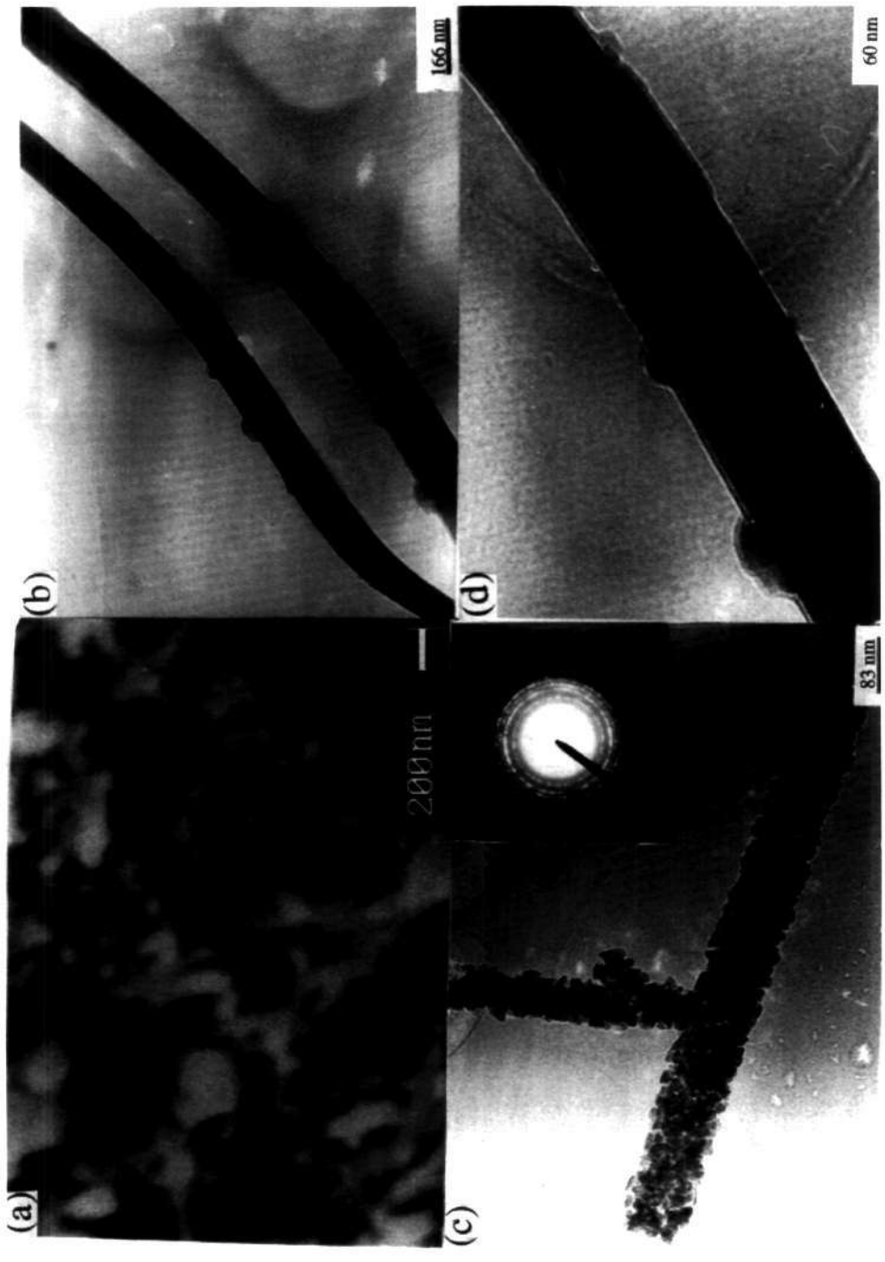

Figure 5.6: (a) SEM image of CdS nanowires (80-160 nm dia) obtained by using Triton X-100 as the surfactant. (b), (c) and (d) TEM images of CdS nanowires. Inset in (c) shows the electron diffraction pattern.

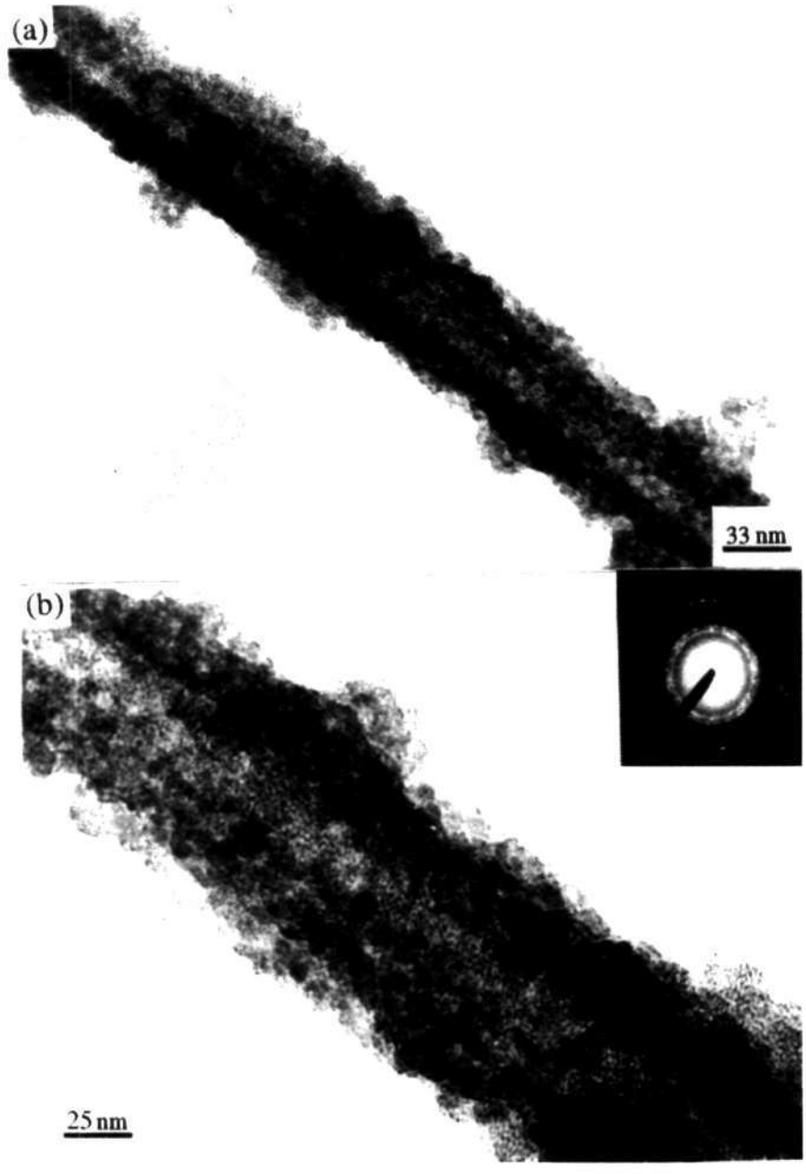

Figure 5.7: (a) and (b) TEM images of nanotubes of CdS (central tubule diameter ~ 15nm) obtained by using a higher concentration of Triton X-100. Inset in (b) shows the electron diffraction pattern.

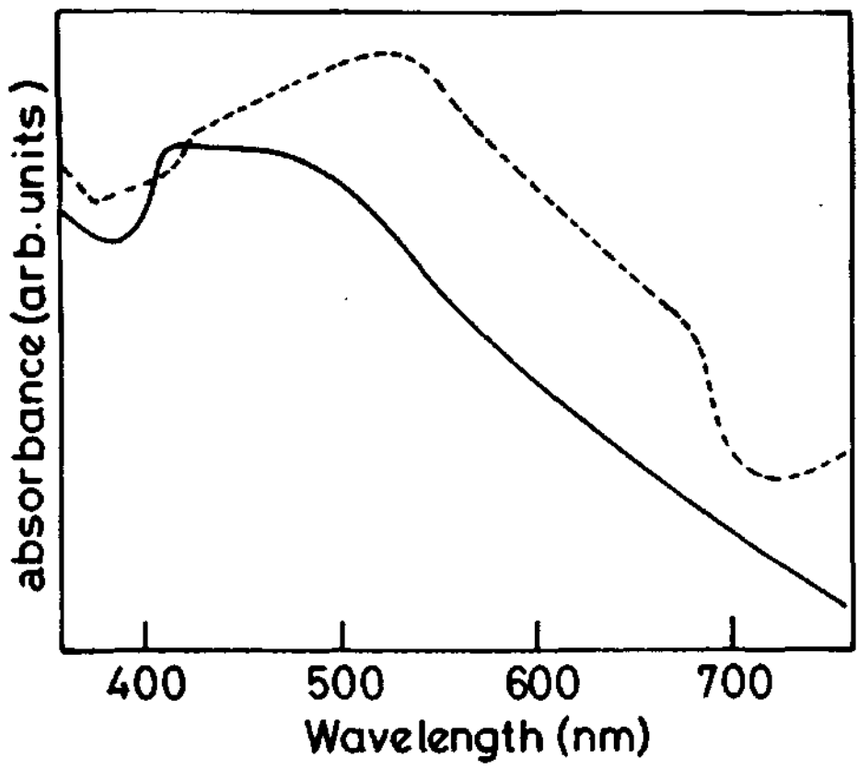

Figure 5.8: Electronic absorption spectra of CdS. Broken line curve represents the spectrum of the bulk and the solid curve represents that of the nanotubes.

nanotubes. This result is interesting in that the nanotubes are extended along one direction and have nanometric dimensions in only two directions. In spite of this limitation, there is the effect of quantum confinement.

The nanowires and nanotubes of CdSe possess the hexagonal structure just as the stable structure of this compound (Figure 5.1). The observed hexagonal lattice parameters are close to those of the bulk phase thus ruling out any kind of compressive or tensile strain in the sample (Table 5.1). The lines were somewhat broad due to the small dimensions of the nanostructures. EDAX analysis of the CdSe

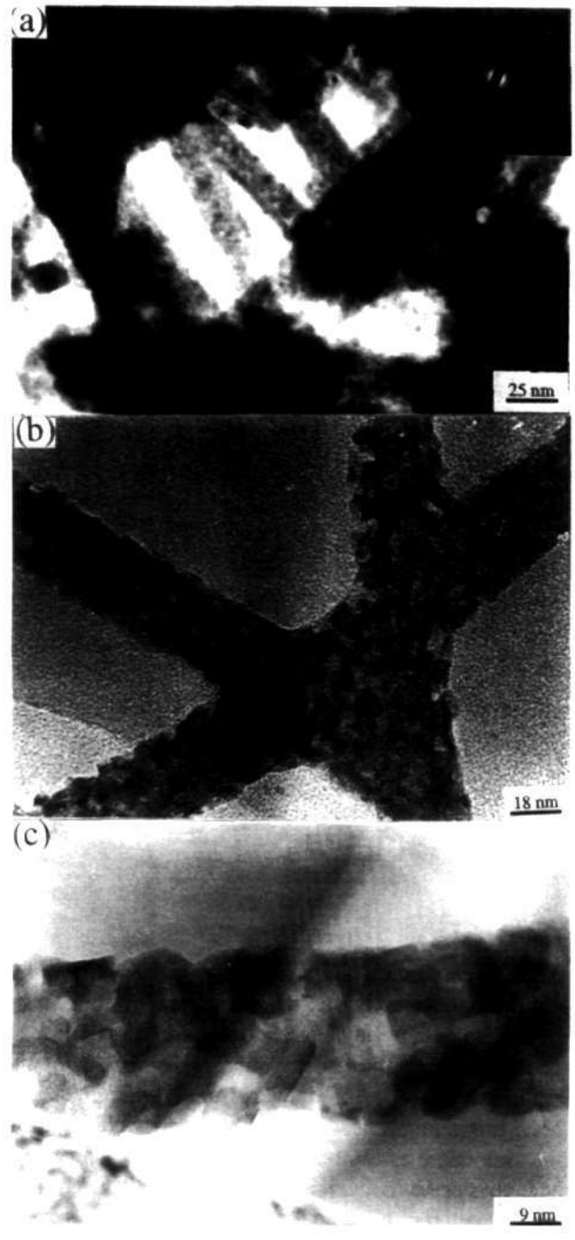

Figure 5.9: (a) and (b) TEM images of the nanowires of CdSe (15-20 nm dia) using Triton X-100 as the surfactant. (c) HREM image of a nanowire showing the polycrystalline nature. Inset in (a) shows the electron diffraction pattern of the nanowires.

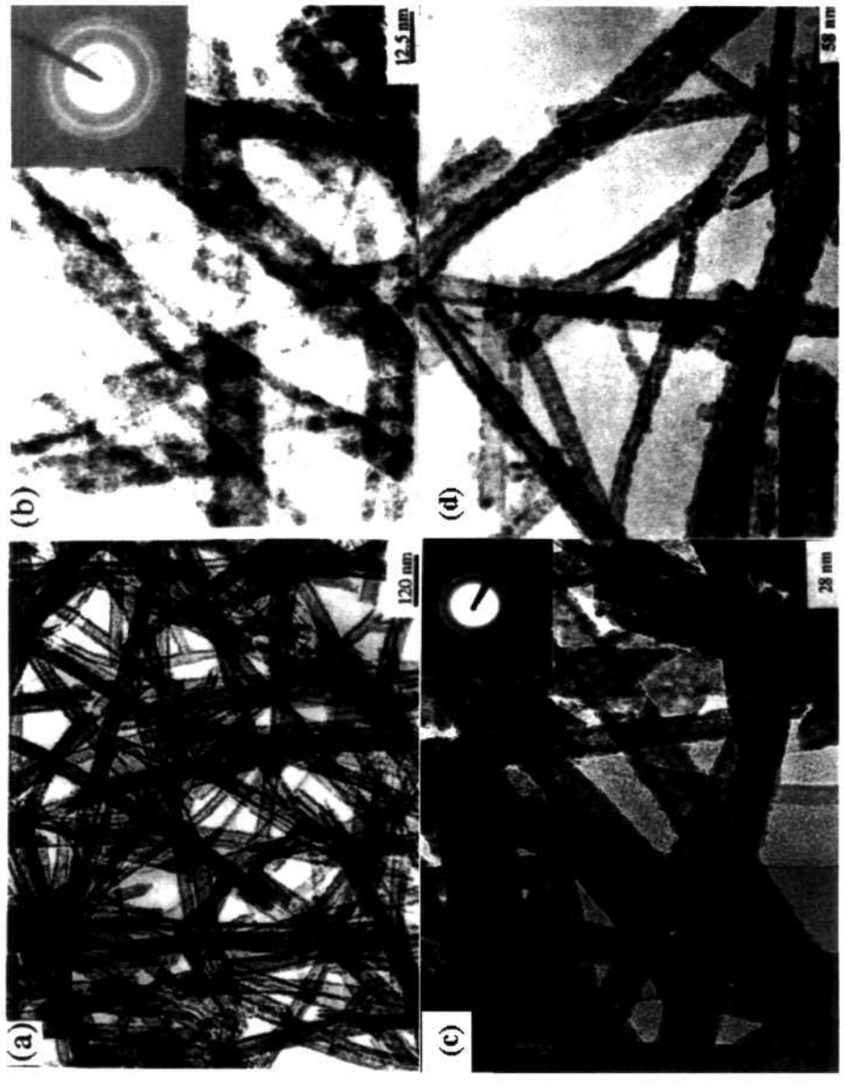

Figure 5.10: (a), (b) and (c) TEM image of the CdSe nanotubes obtained by using a higher concentration of Triton X-100 as the surfactant. The TEM image of the CdSe nanotubes obtained by using AOT as the surfactant is shown in (d). The inset in (b) and (c) shows the electron diffraction pattern of the nanotubes.

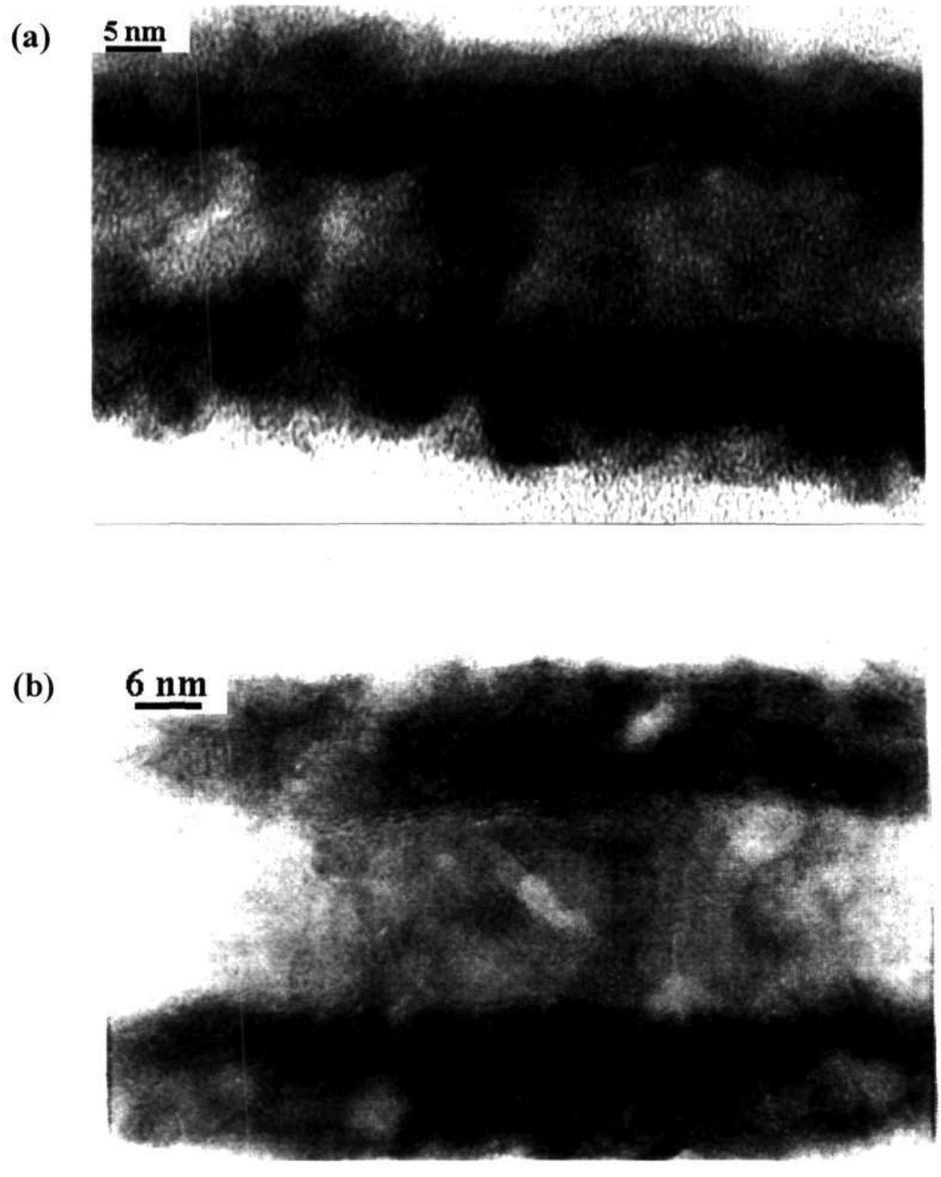

Figure 5.11: HREM image of CdSe nanotubes (a) as synthesized and (b) vacuum annealed at 300 – 400 °C.

nanostructures showed the Cd to Se ratio to be 1:1. CdSe nanowires and nanotubes are obtained depending on the concentration of Triton X-100. In Figure 5.9, we show the TEM images of the CdSe nanowires. The inset in Figure 5.9 (a) shows diffuse rings in the electron diffraction pattern of the nanowires, with a d(100) value of 3.69 Å. The TEM images in Figures 5.9 (b) and (c) also suggest the nanowires to be polycrystalline. The diameter of the nanowires is in the 15-20 nm range and the length in the 1-2 μm range. In Figure 5.10 we show TEM images of the CdSe nanotubes, to demonstrate their tubular nature. The nanotubes are generally long, with lengths going upto 5 μm. The outer diameter of the nanotubes is in the 15-20 nm range while the diameter of the central tubule is in the 10-15 nm range. The wall thickness is therefore around 5 nm. The nanotubes also appear to be polycrystalline as indicated by the electron diffraction pattern, given as an inset in Figure 5.10 (b) and (c). The ED pattern of the nanotubes, given as an inset in Figure 5.10 (b), shows diffuse rings indicating the polycrystalline nature of the material. The rings corresponding to d(101) = 3.25 Å and d(110) = 2.10 Å are clearly seen. The diffraction pattern given as an inset in Figure 5. 10 (c) gives a d(101) value of 3.24 Å. It must be noted that some nanowires are present even when nanotube structures predominate at high surfactant concentrations. The proportion of nanowires increases with the decrease in surfactant concentration. It appears that at the high concentrations employed, the surfactant molecules aggregate, providing a template for the growth of the nanotubes of the chalcogenides.

In Figure 5.11 we show the HREM images of (a) the as synthesized CdSe nanotube and (b) the nanotube after annealing the as-obtained material to 300-400 °C under high vacuum. The images clearly reveal the tubular space and the presence of

some ordered layers surrounding the central tubule. The interlayer spacing is 3.23 Å, just as in multiwalled carbon nanotubes. It appears that annealing the nanotubes removes the surfactant and also improves the crystallinity of the nanotubes. A closer look at the TEM images of the CdSe nanowires/nanotubes reveals that they are basically made up of spherical clusters which pack themselves to form the nanostructure. The electronic absorption spectrum of CdSe nanotubes show a broad band with the highest intensity maximum around 550 nm compared to the bulk polycrystalline sample, which has a maximum around 650 nm. It is interesting that the nanotubes show a blue-shift due to quantum confinement, even though they are extended along one dimension (Figure 5.12).

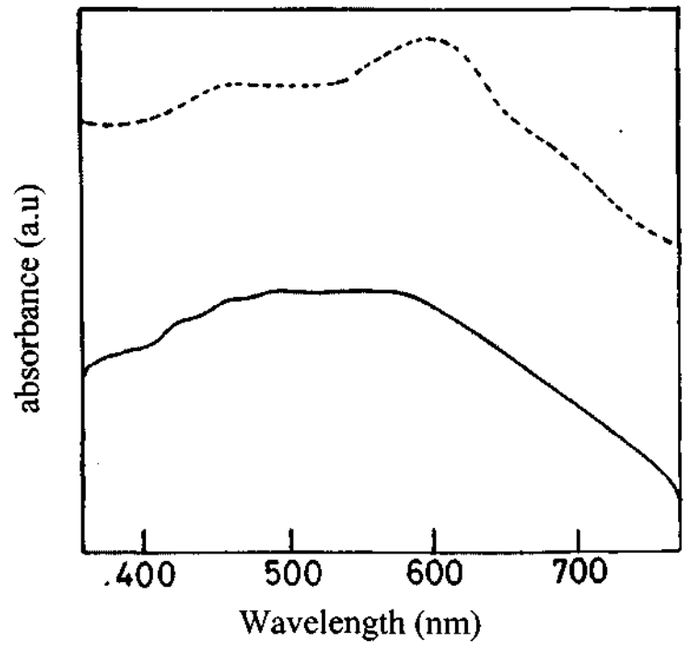

Figure 5.12: Electronic absorption spectra of CdSe. Broken curve represents the bulk and the solid curve represents nanotubes.

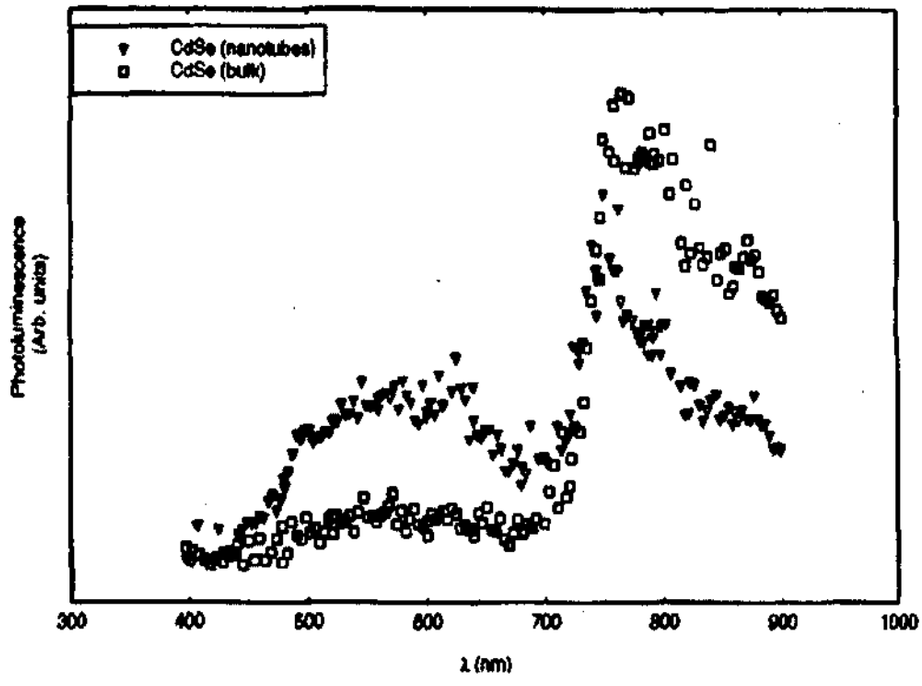

Figure 5.13: PL spectra of the nanotube and the bulk samples of CdSe.

Quantum confinement effects in the nanotube are also seen in the photoluminescence (PL) spectra. In Figure 5.13, we show the PL spectrum of the CdSe nanotubes. The spectrum of the nanotubes shows a broad maximum around 560 nm while the bulk sample does not show such a feature in this region. The band around 750 nm in the PL spectrum is blue-shifted in the case of the nanotubes.

5.4.3 Nanostructures of CuS and CuSe

In the case of copper sulfide, the product obtained corresponds to CuS with a hexagonal structure (Figure 5.1). The stable structure of CuS is also hexagonal (Table 5.1). EDAX analysis of the CuS nanowires showed the Cu to S ratio to be 1:1. In Figures 5.14 (a) and (b), we show the SEM and TEM images of CuS nanowires

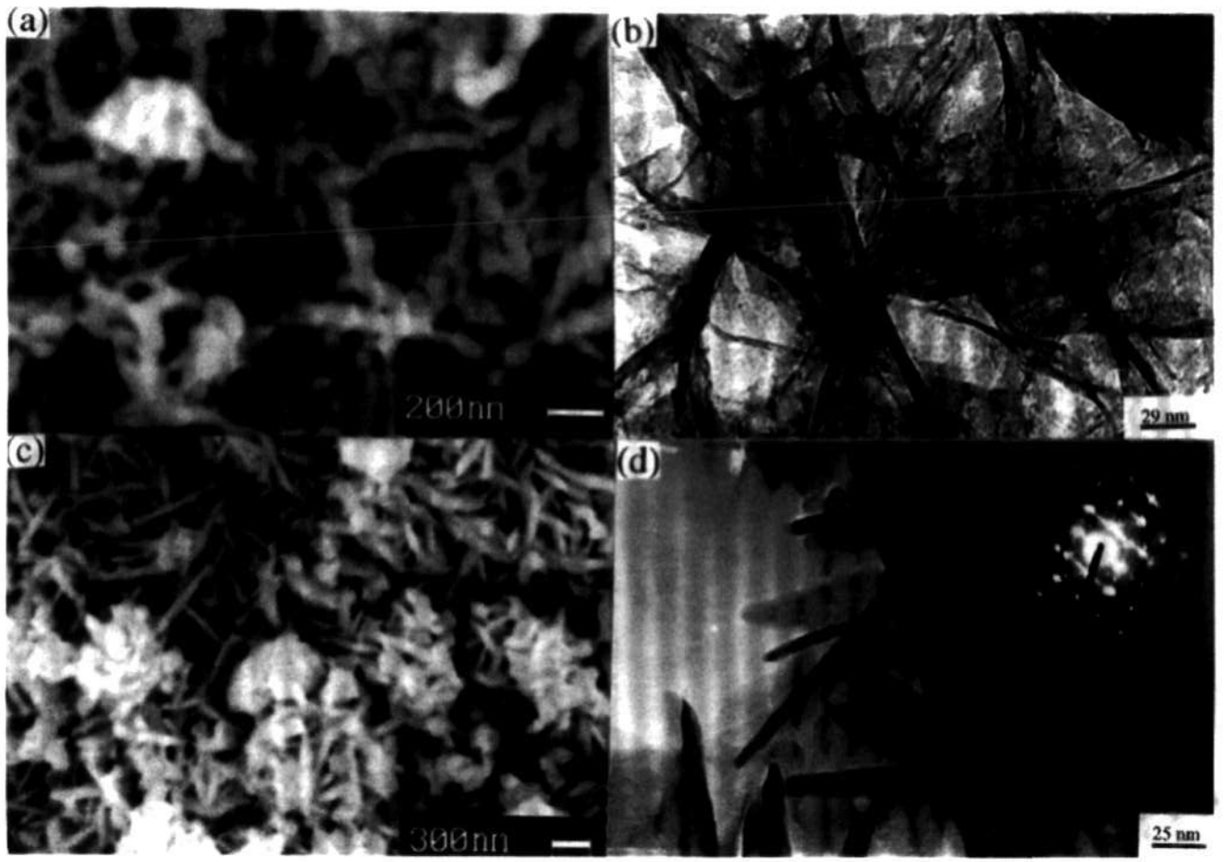

Figure 5.14: (a) SEM and (b) TEM images of CuS nanowires (5-20 nm dia) obtained by using AOT as the surfactant. (c) SEM and (d) TEM images of CuS nanowires (5-15 nm dia) obtained by using Triton X-100 as the surfactant. Inset in (d) shows the electron diffraction pattern.

obtained by using AOT as the surfactant. The average diameter of the wire-like structures varies between 5 and 20 nm, with the lengths extending upto 0.2 μm or longer. In Figures 5.14 (c) and (d), we show the SEM and TEM images of the CuS nanowires obtained by using Triton X-100 as the surfactant. The average diameter is in the 5-15 nm range and length varies between 150 and 900 nm. The inset in Figure 5.14 (d) shows the electron diffraction pattern of the CuS nanowires corresponding to d(103) of 2.8 Å. The CuS nanowires tend to be single-crystalline. Use of Triton X-100 yielded better CuS nanowires as can be seen from an examination of the Figure 5.14. Electronic absorption spectrum of the CuS nanowires of 5-20 nm diameter prepared by us exhibit a broad band between 300 and 600 nm with a distinct band around 400 nm and a long wavelength band peaking around 1000 nm (Figure 5.15 (a)). A 400 nm shoulder-like feature has been observed in CuS nanoparticles. The electronic absorption spectrum of Cu_2S nanowires is reported to have a broad feature extending between 350 nm and 750 nm with a maximum around 470 nm [48]. The band in the near infrared appears to be characteristic of CuS, arising from an electron acceptor state lying within the band gap [49]. The Photoluminescence (PL) spectrum of the CuS nanowires shows a broad band between 375 and 500 nm centered around 437 nm, with a shoulder-like features around 410 and 485 nm (Figure 5.15 (b)). A bulk sample of CuS prepared by us showed a broad band centered around 563 nm with a shoulder around 587 nm (Table 5.2).

The copper selenide nanowires obtained by us has the hexagonal structure (Figure 5.1), just as bulk CuSe under ordinary conditions (Table 5.1). In Figures 5.16 (a) and (b), we show the SEM and TEM images of the CuSe nanowires obtained with Triton X-100. Triton X-100 generally yields better nanowires than AOT. The inset in

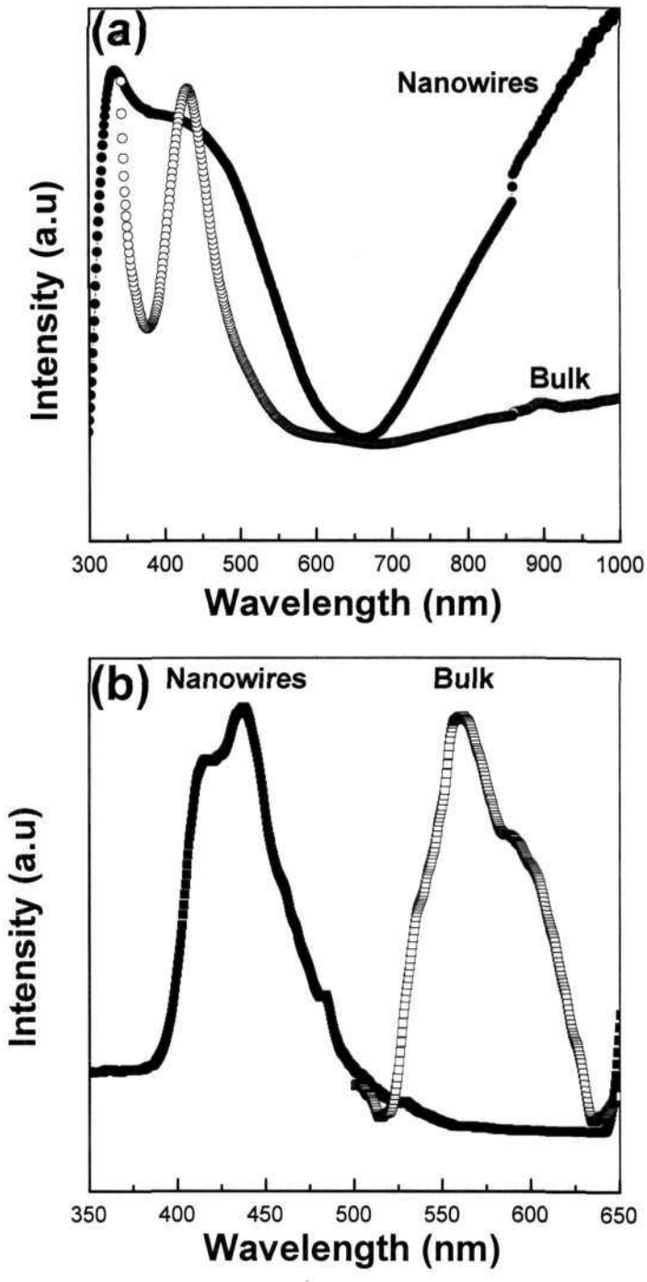

Figure 5.15: (a) Electronic absorption spectrum of CuS nanowires, (b) PL spectrum of CuS nanowires. Spectra of the bulk samples are also shown in the figures.

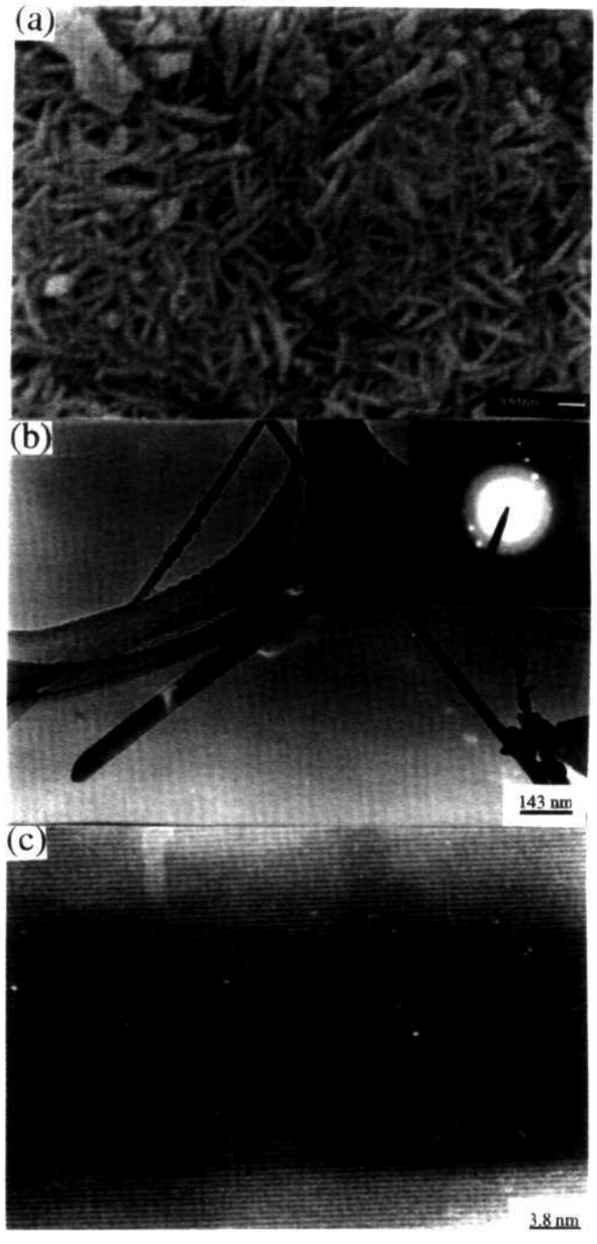

Figure 5.16: (a) SEM and (b) TEM images of CuSe nanowires (~ 70 nm dia) obtained by using Triton X-100 as the surfactant. (c) HREM image of a CuSe nanowire showing lattice resolution. Inset in figure (b) shows the electron diffraction pattern.

Figure 5.16 (b) shows the electron diffraction pattern of the CuSe nanowires with d(110) of 1.90 Å. The diameter of the nanowires is around 70 nm on the average, and the length is between 1 and 2 μm. A high resolution image (HREM) of a nanowire is shown in Figure 5.16 (c). The image clearly reveals an interplanar spacing of 0.33 nm corresponding to d (101). The electronic absorption spectrum of bulk Cu_xSe shows a feature in the 500 - 600 nm region and a broad maximum in the near IR region around 1200 nm [50]. The fundamental absorption edge is around 1.3 eV (950 nm) [51]. Our measurements on polycrystalline CuSe have shown a weak band centered around 570 nm and a strong band above 1000 nm. The CuSe nanowires with an average diameter of ~ 70 nm show a broad feature centered around 540 nm with some structure, along with an intense band above 1000 nm (Figure 5.17 (a)). The PL spectrum of the CuSe nanowires shows a broad band between 385 and 500 nm with a maximum centered around 435 nm (Figure 5.17 (b)). A bulk sample prepared by us shows a broad band centered around 600 nm (Table 5.2).

5.4.4 Raman studies of CdSe nanotubes and ZnSe nanowires

CdSe Nanotubes

Figure 5.18 shows the Raman spectrum of the CdSe nanotubes, displaying a strong peak at 207.5 cm^{-1} along with an asymmetry on the low frequency side. The spectrum shown by the thin solid line is fitted to a sum of two Lorentzians, shown individually by dotted lines. The thick line shows the resultant lineshape. The two modes are centered at 207.5 and 198 cm^{-1}. The observed peak at 207.5 cm^{-1} is assigned to the longitudinal optic (LO) mode of CdSe, red-shifted by 1.5 cm^{-1} with respect to the LO of bulk CdSe (209 cm^{-1}), [52] because of phonon confinement. To

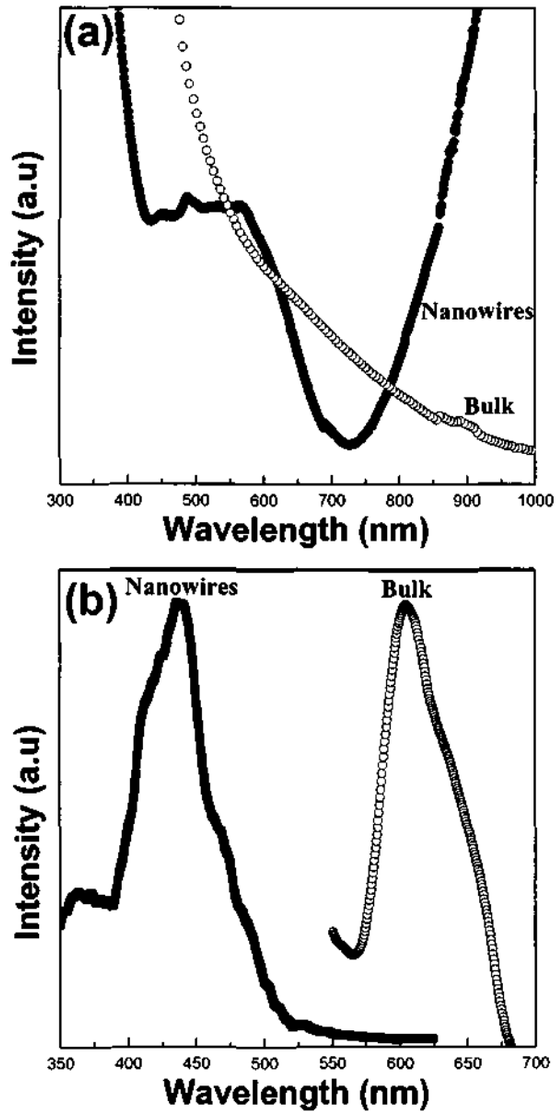

Figure 5.17: (a) Electronic absorption spectra and (b) PL spectra of CuSe nanowires.

estimate the size of the nanoparticles responsible for the observed red-shift of the LO mode, we use the phonon confinement model. The LO mode phonon dispersion curve in bulk CdSe along the ΓA direction is fitted to [52]

$$\omega (q)^2 = \omega^2_{LO} - \beta^2 q^2 \qquad (1)$$

where q is expressed in units of $(2\pi/c)$ and ω_{LO} is the bulk phonon frequency at $q = 0$. The corresponding value of β is 142.1 cm^{-1}. The inset in Figure 5.18 shows the experimental data (open circles) [52] and the fit to Eq. (1) (solid line). This dispersion relation is used to generate the Raman lineshape with the formula [53]

$$I(\omega) = \int_0^{q_{max}} \frac{d\vec{q}|C(0,\vec{q})|^2}{[\omega - \omega(q)]^2 + (\Gamma_0/2)^2} \qquad (2)$$

Guided by the results for nanocrystalline Si, where the Gaussian confinement function has a Fourier coefficient $(|C(0,\vec{q})|^2 = \exp(-q^2L^2/2\alpha)$ works well [54] when $\alpha =$ 9.67), we have taken the same function for $C(0,\vec{q})$ for CdSe. This analysis shows that the peak position of the Raman mode is at 207.5 cm^{-1} for L = 36 Å. This value of Γ_0 = 7 cm^{-1} was used because the linewidth of the LO Raman mode for bulk ZnS was of this order.

We have also estimated the size of the CdSe nanoparticles responsible for the red-shift of the Raman line by 1.5 cm^{-1}, using the quantization of the wavevector proposed by Trallero-Giner *et al.* [55]. In this model, for the phonon with angular momentum $l = 0$, q is quantized as $q_n = \mu_n/R$ (n = 1,2....), where μ_n is a solution of the transcendental equation tan $\mu_n = \mu_n$. This gives $\mu_1 = 4.492$. The frequency of the phonon and the size of the nanoparticles are related by

$$\omega^2 = \omega_{LO}^2 - \beta^2(\mu_n/R)^2 \qquad (3)$$

where β, is obtained by fitting the LO mode dispersion in bulk CdSe, as given by Eq. (1). Figure 5.19 shows the variation of the LO phonon frequency with radius R of the nanoparticles (in nm) for n = 1. The value of ω = 207.5 cm^{-1} corresponds to a diameter of 5.7 nm for the nanoparticle.

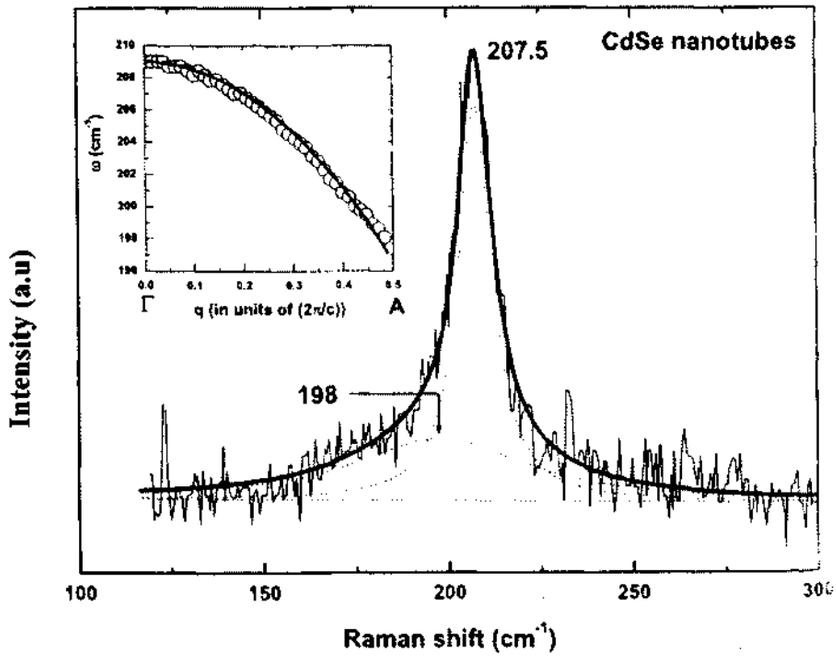

Figure 5.18: Raman spectra of CdSe nanotubes showing two peaks at 207.5 cm^{-1} and 198 cm^{-1}. The data (thin solid lines) are fitted to a sum of two Lorentzians (dotted lines). The resultant Lorentzian lineshape is shown by a thick solid line. The inset shows the phonon dispersion relation (open circles) for the LO branch of CdSe along the ΓA direction [52] fitted to Eq. (1), shown by solid line.

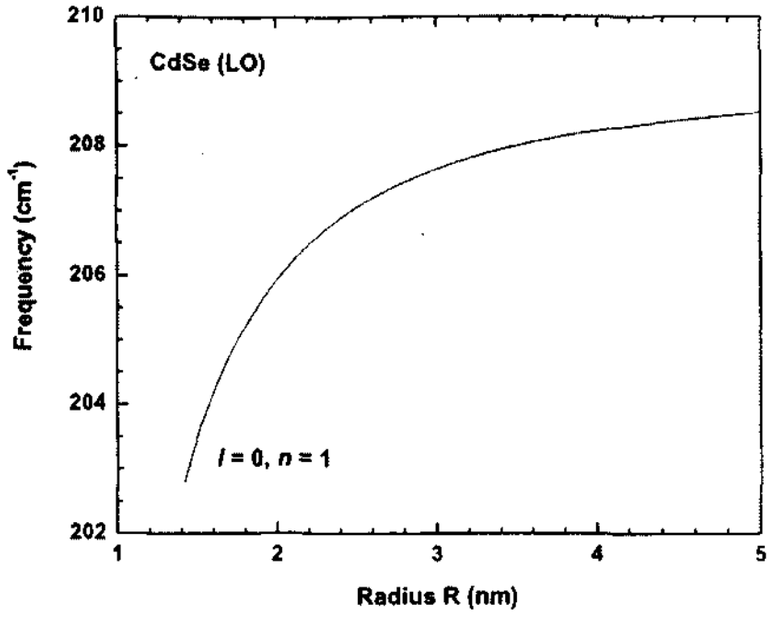

Figure 5.19: Variation of the LO phonon mode frequency with radius R of the CdSe nanoparticles according to Trallero-Giner's model [55], as shown by the solid line.

The photoluminescence (PL) spectrum of the same batch of CdSe nanotubes showed a broad maximum around 560 nm, whereas the bulk CdSe sample shows a photoluminescence band at ~ 750 nm (see Figure 5.13). This shift in the PL spectra corresponds to a blue-shift of the bandgap of 0.56 eV. We can estimate the size of the CdSe nanoparticles from this blue-shift by using the size dependence of the first interband transition energy in CdSe quantum dots calculated by Ramaniah and Nair [56], who have used the effective bond orbital model (EBOM) to calculate the blue-shift of the interband transition energy. The shift of 0.56 eV corresponds to a diameter of 3.5 nm for CdSe nanoparticles, agreeing very well with the diameter value obtained from the PCM model and observed in the TEM images. We now analyze the mode at

198 cm^{-1}. According to Eq. (1.40). The surface phonons satisfy the following equation [57]:

$$\epsilon(\omega) = -\frac{l+1}{l}\epsilon_m; \qquad l = 1, 2, \ldots \qquad (4)$$

where l is the phonon orbital angular momentum quantum number. Here $\epsilon(\omega)$ is the dielectric function of the bulk material, given by

$$\epsilon(\omega) = \epsilon_\infty + \frac{(\epsilon_0 - \epsilon_\infty)\omega_T^2}{\omega_T^2 - \omega^2 - i\gamma\omega} \qquad (5)$$

ϵ_m is the dielectric constant of the host medium (=1 in our case). From the Lyddane–Sachs–Teller (LST) relation, $\epsilon_0/\epsilon_\infty = (\omega_{LO}/\omega_{TO})^2$, the calculated surface phonon mode frequency for l = 1 is 199 cm^{-1}, for the parameters ω_{LO} = 209 cm^{-1}, ω_{TO} = 163 cm^{-1}, and ϵ_∞ = 6.2. We thus assign the observed mode at 198 cm^{-1} to the surface phonon mode of the CdSe nanoparticles. Adding all of these results together, we can thus say that the individual building blocks of CdSe nanotubes are nanoparticles of size ~ 36 Å to 50 Å, which show a confined LO phonon at 207.5 cm^{-1} along with a surface phonon mode at 198 cm^{-1} in the Raman spectra.

ZnSe Nanorods

The Raman spectrum of ZnSe nanorods is shown in Figure 5.20. The observed lineshape can be fitted to a sum of three Lorentzians centered at 257, 237, and 213 cm^{-1}. In bulk ZnSe, the LO and TO Raman modes are at 252 and 206 cm^{-1}, respectively [58]. The 257 cm^{-1} band is assigned to the LO mode showing a blue-shift of 5 cm^{-1} with respect to the LO mode of bulk ZnSe. Similarly, the mode at 213 cm^{-1} is the TO mode blue-shifted with respect to the bulk ZnSe TO mode by 7 cm^{-1}.

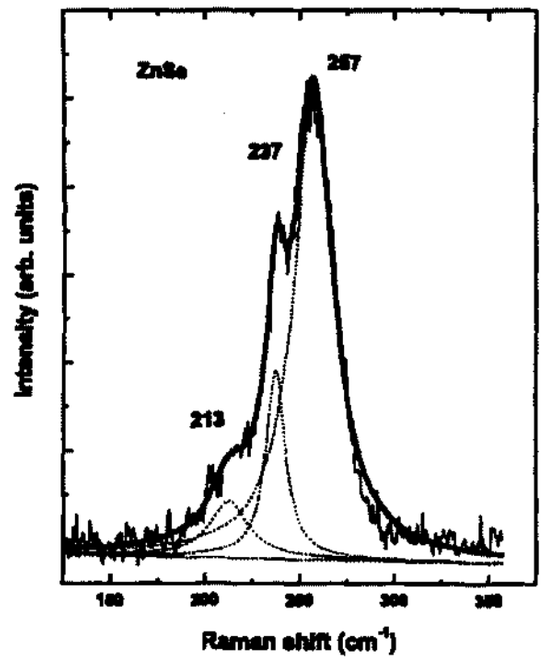

Figure 5.20: Raman spectra of ZnSe nanorods. The data (shown by thin solid lines) are fitted to a sum of three Lorentzian lineshapes, shown by the dotted line, and the total Lorentzian fit is shown by a thick solid line.

Phonon confinement effects should red-shift the LO phonon but blue-shift the TO phonon. The latter happens because the phonon dispersion of the TO phonon in bulk ZnSe is a convex function, that is, the frequency increases with q [59]. The observed blue-shift of the LO mode in ZnSe nanorods suggests that there is a compressive strain in the nanorods with respect to the bulk ZnSe. This is indeed the case, as seen in lattice constants given in Table 5.1. The changes in lattice constant in nanorods with respect to the bulk ZnSe are $\Delta a/a$ = - 0.038 (compressive) and $\Delta c/c$ = 0.56 (tensile). The volume strain will be $\Delta V/V = 2\,(\Delta a/a) + 2\,(\Delta c/c) = -0.0187$. Taking the experimentally observed value of the Grüneissen parameter [60] γ (LO) = 0.9 and

γ (TO) = 1.4 for ZnSe, the shift of the mode frequency will be $\Delta\omega$ (LO) = 4.2 cm^{-1} and $\Delta\omega$ (TO) = 5.4 cm^{-1} (recall that $\gamma = - \partial \ln \omega / \partial \ln V$). These shifts are close to the experimentally observed values in the ZnSe nanorods. We are therefore not able to assess phonon confinement effects in the observed Raman spectrum of ZnSe nanorods. We must point out, however, that the PL band of the nanorods (425 nm) was only slightly blue-shifted compared with the bulk sample (465 nm). The frequency for the l = 1 surface phonon mode for CdSe calculated with Eqs. (4) and (5), the LST relation, and ε_∞ = 6.1 is 233 cm^{-1}. We can thus assign the Raman peak at 237 cm^{-1} to the l = 1 surface phonon mode.

5.5 Conclusions

It has been possible to obtain nanowires and nanotubes of the sulfides and selenides of Zn, Cd and Cu by the surfactant-assisted synthesis. Triton X-100 appears to be an ideal surfactant for this purpose. The average diameter of the nanostructures is in the nanometric regime although the actual value varies from one material to another. The aspect ratio is large in all cases, the length going upto several micrometers. Interestingly CdS and CdSe nanotubes have been successfully prepared for the first time by this method. The semiconductor nanostructures prepared by us have hexagonal structures. The layered hexagonal structure probably favors the formation of the nanostructures. A low concentration of the surfactant yields nanowires. At intermediate concentrations both nanowires and nanotubes are formed. It appears that at high surfactant concentrations employed, the surfactant molecules aggregate, providing a template for the growth of the nanotubes of the chalcogenides (Scheme 5.1).

TABLE: 5.1 Unit Cell Parameters and dimensions of the chalcogenides.

Chalcogenides.	Stable structure and unit cell parameters. [a] (Å)	Observed structural cell parameters. (Å)
ZnS	Cubic a = 5.406 (Hexagonal a = 3.82 , c = 24.96)	Hexagonal a = 3.767 , c = 24.848
ZnSe	Cubic a = 5.668 (Hexagonal a = 3.99 , c = 6.55)	Hexagonal [b] a = 3.84, c = 6.92
CdS	Cubic a = 5.818 (Hexagonal a = 4.13, c = 6.713)	Hexagonal a = 4.14, c = 6.695
CdSe	Hexagonal a = 4.299, c = 7.010 (Cubic a = 6.077)	Hexagonal a = 4.3070, c = 7.046
CuS	Hexagonal a = 3.792 , c =16.344	Hexagonal a = 3.868, c = 16.977
CuSe	Hexagonal a = 3.939 , c =17.2 (Orthorhombic a = 3.948, b = 6.958, c = 17.239)	Hexagonal a = 3.896, c =16.060

(a) The structure of the less stable form is shown in parenthesis.

(b) Minority cubic phase (a = 5.6247 Å) is present.

TABLE: 5.2 Optical spectra of nanowires of Cu and Zn chalcogenides.

Nanowires	Absorption maximum (nm)	Photoluminescence maximum (nm)
ZnS (30) [a]	326 (350) [b]	430 (500)
ZnSe (100)	475 (485)	425 (465)
CuS (5 - 20)	400 (470)	437 (563)
CuSe (70)	540 (570)	435 (600)

(a) average diameter in nm

(b) Values in parenthesis correspond to the bulk samples

The electronic absorption spectra and photoluminescence spectra of the nanostructures of these metal chalcogenides have been studied in detail (see Table 5.2). Raman spectroscopy of the CdSe nanotubes reveals a confined LO phonon mode at 207.5 cm^{-1} along with a surface phonon mode at 198 cm^{-1}. We believe that the red-shift of the LO mode by 1.5 cm^{-1} is due to the presence of nanosized particles acting as building blocks of CdSe nanotubes. The phonon confinement model and the blue-shift of the PL band are used to estimate the size of these building blocks at about 35 Å. In the Raman spectra of the ZnSe nanowires, the $l = 1$ surface phonon mode is seen at 237 cm^{-1}. Since the compressive strain in the sample overcompensates for the quantum confinement effects for the LO mode, it is difficult to estimate the confinement effect.

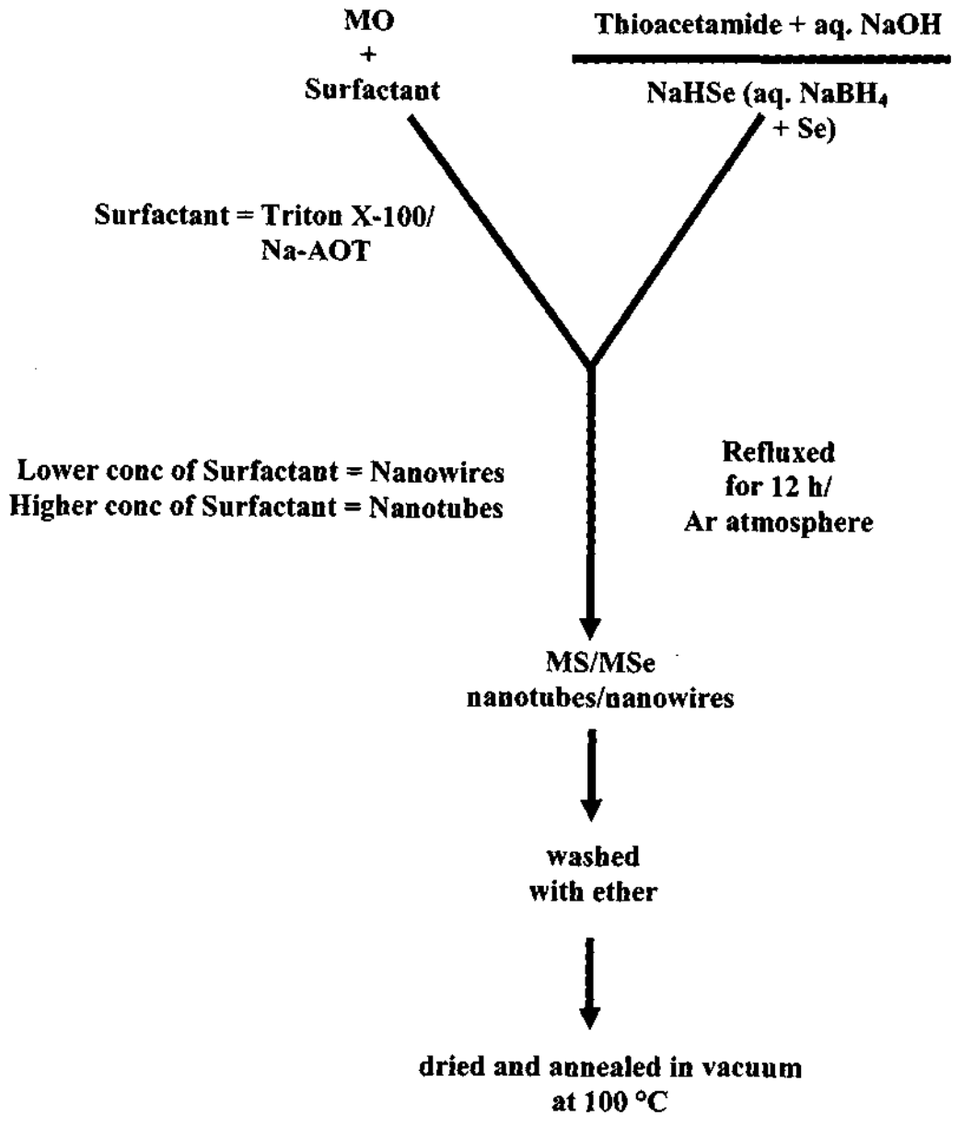

Scheme 5.1: General outline of the synthesis of the various chalcogenide nanostructures

5.6 References

[1] C. R. Martin, *Science*, 1994, **266**, 1961.

[2] J. M. Heath (ed.), " Nanoscale materials special issue,"*Acc. Chem. Res.*, 1999, **32**.

[3] A. P. Alivisatos, " Semiconductors clusters, nanocrystals and quantum dots, *Science*, 1996, **271**, 933.

[4] J. Gutowski, P. Michler, H. I. Ruckmann, H. G. Breunig, M. Rowe, K. Sebald, T. Voss, *Phys. Status. Solidi B*, 2002, **234**, 70.

[5] J. A. Garcia, A. Remon, A. Zubiaga, V. Munoz-Sanjose, C. Martinez-Tomas, *Physics. Status. Solidi A*, 2002, **194**, 338.

[6] I. Enculescu, M. Sima, V. Ghiordanescu, M. Secu, *Chalcogenide Letters*, 2005, **2**, 9.

[7] M. F. Pereira, K. Henneberger, *Phys. Rev. B.*, 1998, **58**, 2055.

[8] K. Lischka, *Phys. Status. Solidi B*, 1997, **202**, 673.

[9] S. Kishimoto, A. Kato, A. Naito, Y. Sakamoto, S. Iida, *Phys. Stat. Sol.*, 2002, **1**, 391.

[10] L. Sun, C. Liu, C. Liao, C. Yan, *J. Mater. Chem.*, 1999, **9**, 1655.

[11] X. Jiang, Y. Xie, J. Lu, L. Zhu, W. He, Y. Qian, *Chem. Mater.*, 2001, **13**, 1213.

[12] S. Gupta, J. C. McClure, V. P. Singh, *Thin Solid Films*, 1999, **299**, 22.

[13] W. Park, J. S. King, C. W. Neff, C. Liddell, C. J. Summers, *Phys. Stat. Sol.*, 2002, **2**, 949.

[14] L. I. Burov, G. I. Ryabtsev, A. S. Smal, I. N. Waraxe, *Appl. Phys. B.*, 2002, **75**, 63.

[15] C. –H. Su, M. A. George, W. Palosz, S. Feth, S. L. Lehoczky, *J. Cryst. Growth*, 2000, **213**, 267.

[16] H. Kato, H. Udono, I. Kikuma, *J. Cryst. Growth*, 2001, **229**, 79.

[17] E. Tournie, C. Morhain, G. Neu, J. P. Faurie, R. Triboulet, J. O. Ndap, *Appl. Phys. Lett.*, 1996, **68**, 1356.

[18] K. Lischka, *Phys. Status. Solidi B*, 1997, **202**, 673.

[19] D. Routkevitch, T. Bigioni, M. Moskovits and J. M. Xu , *J. Phys. Chem.*, 1996, **100**, 14037.

[20] D. Xu, Y. Xu, D. Chen, G. Guo, L. Gui and Y. Tang, *Adv. Mater.*, 2000, **12**, 520.

[21] (a) G. Hodes, A. Albu-Yaron, F. Decker, P. Motisuke, *Phys. Rev. B.*, 1987, **36**, 4215, (b) M. Ichimura, N. Sato, A. Nakamura, K. Takeuchi, E. Arai, *Phys. Status. Solidi*, 2002, **193**, 132.

[22] (a) S. H. Tolbert, A. P. Alivisatos, *Science*, 1994, **265**, 373, (b) M. G. Bawendi, A. R. Kortan, M. L. Steigerwald, L. E. Brus, *J. Chem. Phys.*, 1989, **91**, 7282.

[23] C. B. Murray, C. R. Kagan, M. G. Bawendi, *Science*, 1995, **270**, 1335.

[24] V. L. Colvin, M. C. Schlamp, A. P. Alivisatos, *Nature*, 1994, **370**, 354.

[25] P. T. Tran, E. R. Goldman, G. P. Anderson, J. M. Mauro, H. Mattoussi, *Phys. Status Solidi*, 2002, **229**, 427.

[26] (a) W. C. Chan, S. M. Nie, *Science*, 1998, **281**, 2016, (b) M. Bruchez, M. Moronne, P. Gin, S. Weiss, A. P. Alivisatos, *Science*, 1998, **281**, 2013.

[27] X. Peng, L. Manna, W. Yang, J. Wickham, E. Scher, A. Kadavanich, A.P. Alivisatos, *Nature*, 2000, **404**, 59.

[28] X. G. Peng, J. Wickham, A. P. Alivisatos, *J. Am. Chem. Soc.*, 1998, **120**, 5343.

[29] C. G. Murray, D. J. Norris, M.G. Bawandi, *J. Am. Chem. Soc.*, 1993, **115**, 8706.

[30] C. -C. Chen, C. -Y. Chao, Z. -H. Lang, *Chem. Mater.*, 2000, **12**, 1516.

[31] Y. Li, D. Xu, Q. Zhang, D. Chen, F. Huang, Y. Xu, G. Guo, Z. Gu, *Chem. Mater.*, 1999, **11**, 3433.

[32] D. Xu, X. Shi, G. Guo, L. Gui, Y. Tang, *J. Phys. Chem. B*, 2000, **104**, 5061.

[33] L. Gao, E. Wang, S. Lian, Z. Kang, Y. Lan, D. Wu, *Solid. State. Commun.*, 2004, **130**, 309.

[34] S. Wang, S. Yang, *Chem. Phys. Lett.*, 2000, **322**, 567.

[35] S. T. Lakshmikumar, *Sol. Energy. Mater. Sol. Cells.*, 1994, **32**, 7.

[36] H. Toyoji, Y. Hirosh, *Japan Kokai Tokkyo koho*, 2002, **173**, 622.

[37] A. A. Korzhuev, *Fiz. Khim. Obrab. Mater.*, 1991, **3**, 131.

[38] C. Heske, *Appl. Phys. Lett.*, 1997, **70**, 1022.

[39] (a) G. Henshaw, I. P. Parkin, G. Shaw, *J. Chem. Soc. Dalton Trans.*, 1997, 231, (b) G. Henshaw, I. P. Parkin, G. Shaw, *Chem. Commun.*, 1996, 1095.

[40] M. Kemell, M. Ritala, H. Saloniemi, M. Leskela, T. Saljavaara, E. Rauhula, *J. Electrochem. Soc.*, 2000, **147**, 1080.

[41] (a) W. Wang, Y. Geng, P. Yan, F. Liu, Y. Xie, Y. Qian, *J. Am. Chem. Soc.*, 1999, **121**, 4062, (b) W. Wang, P. Yan, F. Liu, Y. Xie, Y. Gen, Y. Qian, *J. Mater. Chem.*, 1998, **8**, 2321, (c) W. Zhang, X. Zhang, L. Zhang, J. Wu, Z. Hui, Y. Cheng, J. Liu, Y. Xie, Y. Qian, *Inorg. Chem.* 2000, **39**, 1838.

[42] X. Jiang, Y. Xie, J. Lu, L. Zhu, W. He, Y. Qian, *Chem. Mater.*, 2001, **13**, 1213.

[43] P. H. Bose, N. Deshmukh, R. F. Shinde, S. K. Date, S. K. Kulkarni, *J. Mater. Sci.*, 1999, **34**, 6087.

[44] N. Arul Dhas, A. Zaban, A. Gedanken, *Chem. Mater.*, 1999, **11**, 806.

[45] J. Cizeron, M. P. Pileni, *J. Phys. Chem. B*, 1997, **101**, 8887.

[46] J. Zhu, Y. Koltypin, A. Gedanken, *Chem. Mater.*, 2000, **12**, 73.

[47] D. J. Norris, N. Yao, F. T. Charnock, T. A. Kennedy, *Nano Lett.*, 2001, **1**, 3.

[48] S. Wang, Sh. Wang, *Mat. Sci. Eng. C*, 2001, **16**, 37.

[49] M. C. Brelle, C. L. Torres-Martinez, J. C. McNulty, R. K. Mehra, J. Z. Zhang, *Pure. Appl. Chem.*, 2000, **72**, 101.

[50] V. S. Gurin, V. B. Prokopenko, A. A. Alexeenko, Sh. Wang, K. V. Yumashev, P. V. Prokoshin, *Intl. J. Inorg. Mater.*, 2001, **3**, 493.

[51] V. S. Gurin , V. B. Prokopenko, A. A. Alexeenko, Sh. Wang, P. V. Prokoshin, *Mat. Sci. Eng. C*, 2001, **15**, 93.

[52] F. Widulle, S. Kramp, N. M. Pyka, A. Göbel, T. Ruf, A. Debernardi, R. Lauck, and M. Cardona, *Physica B*, 1999, **263**, 448.

[53] P. Fauchet and I. H. Campbell, *Crit. Rev. Solid State Mater. Sci.*, 1988, **14**, S79.

[54] J. Zi, K. Zhang, and X. Xie, *Phys. Rev. B: Solid State*, 1997, **55**, 9263.

[55] C. Trallero-Giner, A. Debernardi, M. Cardona, E. Menendez- Proupin, and A. I. Ekimov, *Phys. Rev. B: Solid State*, 1998, **57**, 4664.

[56] L. M. Ramaniah and S. V. Nair, *Phys. Rev. B: Solid State*, 1993, **47**, 7132.

[57] S. Hayashi, *Jpn. J. Appl. Phys.*, 1984, **23**, 665.

[58] S. S. Mitra, O. Brafman, W. B. Daniels, and R. K. Craeford, *Phys. Rev.* 1969, **186**, 942.

[59] H. Bilz and W. Kress, editors, *Phonon Dispersion in Solids*, Springer-Verlag,

Berlin (1979).

[60] B. Weinstein and R. Zallen, in *Light Scattering in Solids IV*, edited by M. Cardona and G. Güntherodt, Springer-Verlag, Berlin (1984).

Chapter 6

Mn- and Co-doped ZnO

Summary*

Following the theoretical predictions of ferromagnetism in Mn- and Co-doped ZnO, several workers reported ferromagnetism in thin films as well as in bulk samples of these materials. While some observe room-temperature ferromagnetism, others find magnetization at low temperatures. Some of the reports, however, cast considerable doubt on the magnetism of Mn- and Co-doped ZnO. In order to conclusively establish the properties of Mn- and Co-doped ZnO, samples with 6 % and 2 % dopant concentrations have been prepared by the low-temperature decomposition of acetate solid solutions. The samples have been characterized by X-ray diffraction, EDAX and spectroscopic methods to ensure that the dopants are substitutional. All the Mn- and Co-doped ZnO samples (prepared at 400 °C and 500 °C) fail to show ferromagnetism. Instead, their magnetic properties are best described by a Curie–Weiss type behavior. It appears unlikely that these materials would be useful for spintronics, unless additional carriers are introduced by some means.

* A paper based on this study has appeared in J. Mater. Chem., (2005).

6.1 Introduction

Materials for spintronics are receiving increasing attention in the last few years. A variety of materials, specially diluted magnetic semiconductors, have been investigated in this connection [1,2]. One of the materials that has been of interest in this area is ZnO. ZnO is a wide band gap semiconductor (band gap ~ 3.34 eV) having the wurtzite structure (Figure 6.1). ZnO is therefore a candidate for optoelectronic applications in the short wavelength range (green, blue, UV). In fact, the high exciton binding energy in ZnO (about 60 meV) would allow for excitonic transitions even at room temperature, which could mean higher radiative recombination efficiency for spontaneous emission as well as a lower threshold voltage for laser emission. It is more radiation hard and is multifunctional (piezoelectric and ferroelectric).

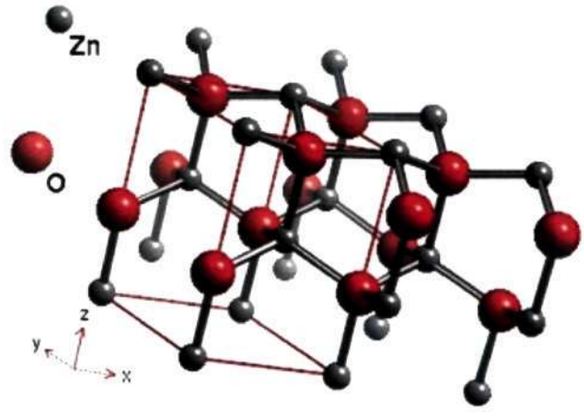

Figure 6.1: Structure of ZnO.

6.2 Scope of the present investigations

In the year 2000, Dietl *et al.* [3] made the theoretical prediction that Mn-doped ZnO and GaN would be ferromagnetic at room temperature and would therefore be suitable for applications in spintronics. A report of ferromagnetism in Co-doped TiO_2 [4] gave the hope that Co- and Mn-doped oxides may indeed be useful for spintronics. The theoretical calculations of Sato and Katayama-Yoshida [5] showed that ZnO doped with several 3d transition metal ions such as V, Cr, Fe, Co and Ni may exhibit ferromagnetic ordering. A number of workers have, therefore, investigated ZnO doped with transition metal ions in the last few years, in particular thin films of Co- and Mn-doped ZnO. Results of these studies have been reviewed by Chambers and Farrow [6] and Prellier *et al.* [7]. The latter authors conclude that the Co-doped ZnO films generally exhibit ferromagnetism above room temperature, and that a definitive T_C is not always found in Mn-doped ZnO thin films. Results from the recent literature, however, reveal many contradictions. Thus, thin films of $Zn_{1-x}Mn_xO$ (x = 0.1 and 0.3) grown on Al_2O_3 substrates by laser MBE are reported to show a T_C in the 30-45 K range by Jung *et al.* [8] but Fukumura *et al.* [9] find a spin-glass behavior with strong antiferromagnetic exchange coupling in similar films. A first principles study of $Zn_{1-x}Mn_xO$ thin films predicts the coupling between the Mn ions to be antiferromagnetic [10]. Studies have been reported on bulk samples of Mn-doped ZnO as well. Han *et al.* [11] report a ferrimagnetic phase transition in the case of $Zn_{0.95}Mn_{0.05}O$ processed at 1170 K, which they attribute to the $(Mn,Zn)Mn_2O_4$ spinel impurity. Such a transition was not found in samples prepared at 1370 K. Polycrystalline and single crystalline $Zn_{1-x}Mn_xO$ samples have not been found to be ferromagnetic [12]. Mn-doped ZnO nanowires prepared at high temperatures by carbon-assisted synthesis in

this laboratory were only paramagnetic. The recent report of room-temperature ferromagnetism in both bulk and thin films of $Zn_{1-x}Mn_xO$ (x = 0.01, 0.02 and 0.1) by Sharma *et al.* [13] has aroused much interest. These workers prepared their samples at relatively low temperatures and observed weak ferromagnetism (T_C > 420 °C) with an average magnetic moment of 0.16 μB per ion. The samples prepared at higher temperatures (> 700 °C) did not exhibit ferromagnetism. Sharma *et al.* prepared their samples by mixing ZnO and MnO_2 powders and calcining the mixture at 400 °C or above. The state of Mn in such preparations seems rather uncertain. Clearly, the present situation with regard to the magnetic properties of Mn-doped ZnO is far from being clear.

The experimental situation of Co-doped ZnO is similar to that of Mn-doped ZnO. Although earlier work on Co-doped ZnO films showed them to be ferromagnetic with a T_C > 280 K [14], recent results are not altogether conclusive. $Zn_{1-x}Co_xO$ films obtained by the sol-gel method were found to be ferromagnetic with a T_C > 300 K by Lee *et al.* [15] although the presence of a secondary phase was noted in the samples $x \geq 0.25$. Films of Co-doped ZnO prepared by pulsed laser deposition are reported to be ferromagnetic at room temperature [16], but Norton *et al.* [17] suggest that Co nanocrystallites present in the sample could be responsible for the ferromagnetism. Room-temperature ferromagnetism and negative magnetoresistance were reported recently by Yan *et al.* [18] on thin films synthesized on the subnanometer scale by sputtering. Polycrystalline monophasic samples do not appear to exhibit ferromagnetism [12a]. Risbud *et al.* [19] show that well-characterized stoichiometric bulk samples of $Zn_{1-x}Co_xO$ are not ferromagnetic and indicate dominant nearest-neighbour antiferromagnetic interaction. These samples were

prepared by heating a solid solution of zinc and cobalt oxalates at a temperature of 1173 K for 15 min. Deka *et al.* [20] have reported ferromagnetism upto 750 K in polycrystalline $Zn_{1-x}Co_xO$ prepared by combustion synthesis. The reaction temperature in such a combustion synthesis will be rather high. Colloidal Co^{2+} doped ZnO nanocrystals prepared by the isocrystalline core-shell method are reported to be ferromagnetic [21]. Interestingly, $Zn_{1-x}Mn_xO$ (x = 0.05 - 0.1) nanocrystals prepared under solvothermal conditions by the decomposition of the cupferron precursor was only paramagnetic [22]. A first principles study has, however, shown that Co-doped ZnO prefers to be in a spin-glass state due to antiferromagnetic superexchange interactions [23].

The above discussion demonstrates how the occurrence of ferromagnetism in bulk as well as in thin films of Mn- and Co-doped ZnO is by no means established. A careful examination of the previous results indicates that where ferromagnetism has been found, the samples were heated to relatively high temperatures, which could give rise to spinel impurity phases. Risbud *et al.* [19] however, report the absence of ferromagnetism in samples prepared at high temperatures. Even where the temperature of synthesis is relatively low, some of the synthetic procedures are not convincing as to whether the dopant has substituted the Zn site. While it is possible that Co clusters may be present in some of the Co-ZnO samples due to the reduction of Co^{2+} (that can occur in solution phase even at low temperatures), the presence of the magnetic spinel phases cannot be entirely eliminated in some of the preparations. Furthermore, the magnetization values reported by many workers is very low and can arise from the presence of magnetic impurities, which cannot be detected by x-ray diffraction.

Considering the situation described above, it seemed desirable to investigate the magnetic properties of Mn- and Co-doped ZnO prepared at low temperatures, ensuring that the dopant ions are present in substitutional sites. This has been accomplished by preparing the doped ZnO samples by the thermal decomposition (330 °C) of the solid solutions of $Zn(acetate)_2$ with $Mn(acetate)_2$ and $Co(acetate)_2$ and subjecting to them all possible means of characterization. We have carried out careful studies on samples with 6 % Mn and 6 % Co, as well as 2 % Mn and 2 % Co. The latter was necessary since the proponents of ferromagnetism state that the dopant concentration has to be low ($\leq$4 %) for observing ferromagnetism [13, 24]. Samples prepared at 400 °C and 500 °C have been studied to avoid any doubtful conclusions that may arise because of the temperature employed for the sample preparation. Interestingly, we find that both the 2 % and 6 % Mn- and Co-doped ZnO samples fail to exhibit ferromagnetism.

6.3 Experimental

Zinc acetate, $(CH_3COO)_2$ $Zn.2H_2O$, and manganese acetate, $(CH_3COO)_2$ $Mn.4H_2O$, supplied by Aldrich, were taken in the required molar ratios (6 mole % or 2 mole % Mn) and dissolved in 15 ml double distilled water. It was made sure that the solution did not have precipitates before drying at 100 °C overnight (~ 10 h). The powder obtained after drying was heated in air at 400 °C for 5 h. This sample is referred to as I. Another sample was prepared by heating the product of decomposition of the acetate solid solutions at 500 °C for 5 h. This sample is referred to as II. Heating and cooling rates in both the cases were 1 °C/min. The product obtained was light brown in colour in both I and II.

Zinc acetate and cobalt (II) acetate, $(CH_3COO)_2$ $Co.4H_2O$, supplied by Aldrich were taken in the required molar ratios (6 mole % and 2 mole %) and dissolved in 15 ml double distilled water. It was made sure that the solution did not have any precipitate before drying at 100 °C overnight (~ 10 h). The powder obtained after drying was heated in air at 400 °C for 5 h (sample I). Another sample was prepared by heating the product of decomposition of the acetate solid solutions at 500 °C for 5 h (sample II). Heating and cooling rates in both the cases were 1 °C/min. The product obtained was dark green in colour in both these cases.

Thermogravimetric analysis (TGA) of the Zn-Mn and Zn-Co acetate solid solutions was carried out on a Mettler-Toledo-TG-850 instrument. X-ray diffraction (XRD) patterns were recorded using a Seifert (XRD, XDL, TT, and Cu target) instrument. The chemical composition was determined with an Oxford EDX analyzer attached with a Leica S-440i SEM instrument. Transmission electron microscopy was carried out with a JEOL JEM 3010 instrument operating at an accelerating voltage of 300 kV. X-ray photoelectron spectra of the samples were recorded with an ESCALAB MKIV spectrometer employing AlKα radiation (1486.6 eV). Electronic absorption spectra were recorded in the 2000-200 nm range using a Perkin-Elmer Lambda 900 UV/VIS/NIR spectrophotometer. Photoluminescence (PL) measurements were carried out with a Perkin-Elmer LS50B luminescence spectrophotometer with an excitation wavelength of 325 nm. Electron paramagnetic resonance (EPR) spectra were recorded with a ER 200 D X-Band Bruker instrument. Magnetic properties of the various powder samples were measured using a SQUID magnetometer (Quantum Design MPMS) which has a base temperature of 2 K and a maximum magnetic field of 5 T.

6.4 Results and discussion

Thermogravimetric analysis curves of the Zn-Mn and Zn-Co acetate solid solutions showed that they decompose sharply around 330 °C, giving doped ZnO as the product (Figure 6.2).

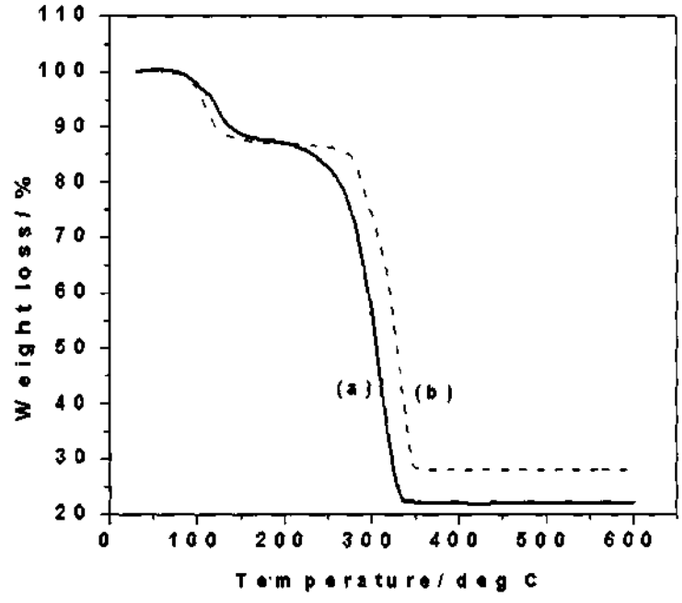

Figure 6.2: TGA plots of (a) Mn-Zn and (b) Co-Zn acetate solid solutions.

We have characterized the Mn- and Co-doped ZnO samples prepared by the decomposition of the acetate solid solutions at 400 °C (I) and 500 °C (II) by employing various techniques. X-ray diffraction patterns of the products of decomposition of the acetate solid solutions (Figure 6.3) showed the hexagonal structure, the Mn-doped samples exhibiting a slightly larger c-parameter (6 % Mn-doped, a = 3.250 Å, c = 5.224 Å; 6 % Co-doped, a = 3.249 Å, c = 5.207 Å and 2 % Mn-doped, a = 3.250 Å, c = 5.220 Å; 2 % Co-doped, a = 3.249 Å, c = 5.206 Å) in

comparison to that of the undoped sample (a = 3.249 Å, c = 5.206 Å). The increase in the c-parameter results from the substitution of Mn^{2+} ions because of the larger radius of Mn^{2+} (0.66 Å) compared to Zn^{2+} (0.60 Å) [8]. On the other hand, the radius of Co^{2+} (0.58 Å) is close to that of Zn^{2+} and as a result the cell parameters do not vary significantly [19]. The absence of impurity peaks arising from secondary phases or precipitates implies that the percentage doping employed is within the solubility limits of Mn or Co in ZnO. That the solubility limit of Mn^{2+} and Co^{2+} is far greater than the percentages employed by us is well documented [11,15].

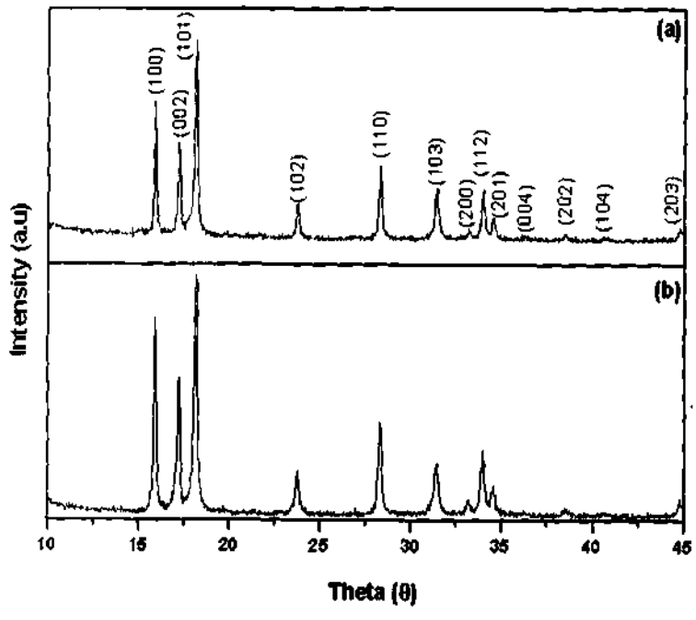

Figure 6.3: XRD patterns of (a) 6 % Mn-doped and (b) 6 % Co-doped ZnO.

Energy dispersive X-ray (EDAX) analysis (see typical data in Figure 6.4) was carried out by comparing the peak areas. The analysis confirms the concentrations of Mn and Co to be close to those in the stated compositions.

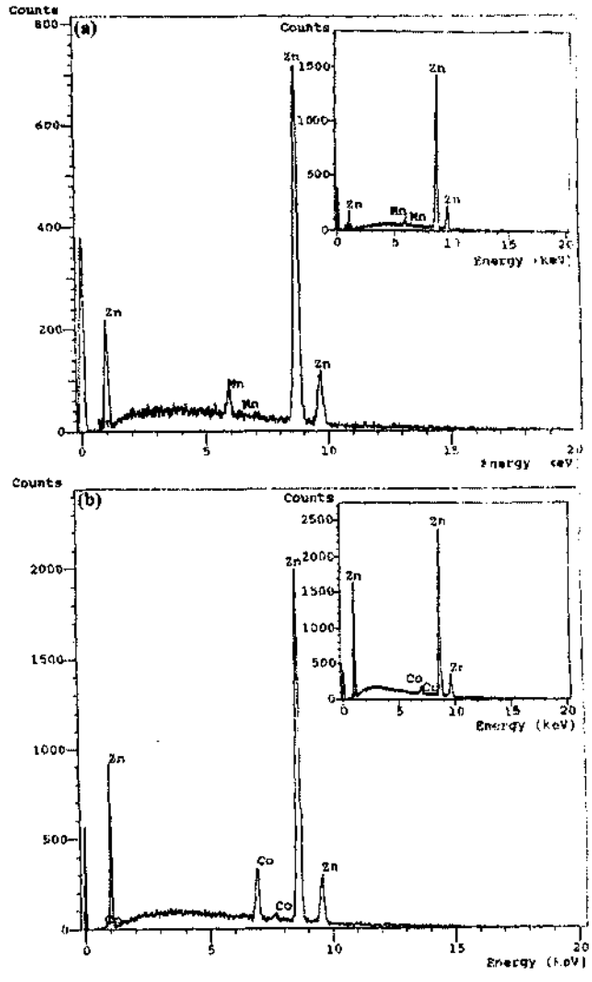

Figure 6.4: EDAX spectra of (a) 6 % Mn-doped and (b) 6 % Co-doped ZnO. Insets show the corresponding EDAX spectra for the 2 % Mn and Co-doped ZnO.

Transmission electron microscope examination showed the doped samples to consist of particles of 30-50 nm diameter. X-ray photoelectron spectroscopy revealed that the Mn and Co ions were in the +2 oxidation state. Thus, the Mn (2p) and Co (2p) signals were found at 641.45 eV and 778.93 eV respectively [15].

The Mn-doped ZnO samples gave a broad absorption band in the 400-450 nm region due to $^6A_1$ (S) → $^4T_1$ (G) transition (Figure 6.5).

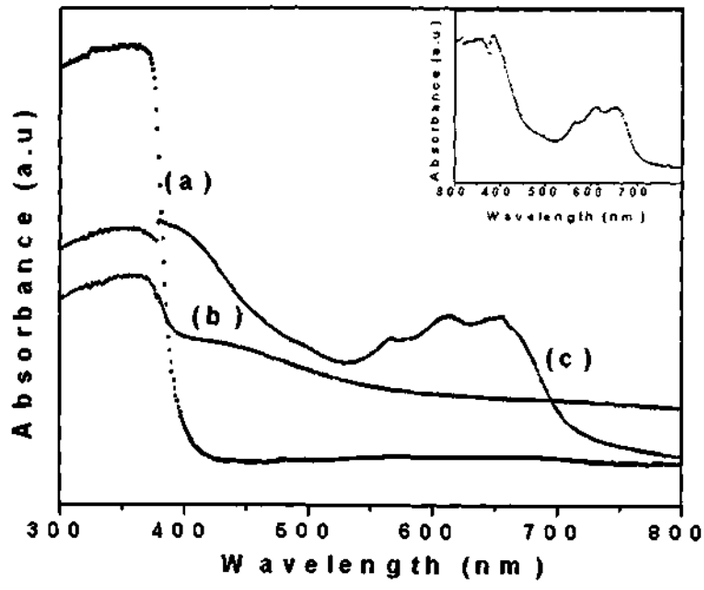

Figure 6.5: Absorption spectra of (a) ZnO, (b) 6 % Mn-doped and (c) 6 % Co-doped ZnO. Inset shows the spectrum of 2 % Co-doped ZnO.

The Mn-doped sample also gave the characteristic EPR spectrum of Mn^{2+} (Figure 6.6) with a g value of 2.003, consistent with that reported in single crystals of Mn-doped bulk ZnO [12b]. The Co-doped ZnO samples (Figure 6.5) gave three bands

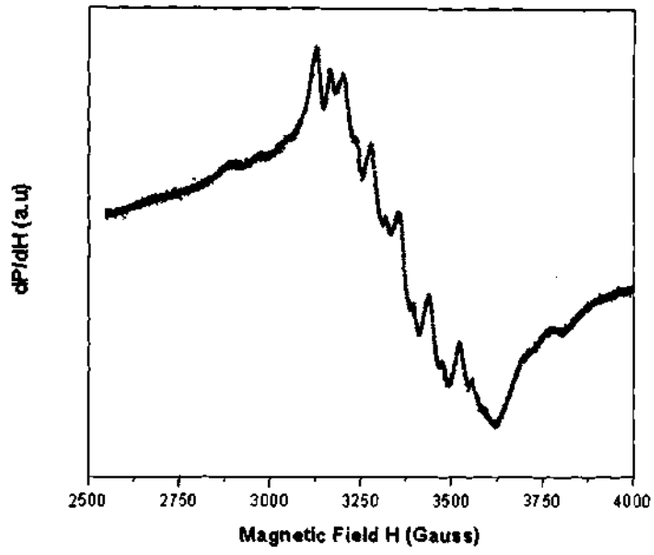

Figure 6.6: EPR spectrum of the 6 % Mn-doped ZnO.

in the 550-700 nm region due to the $^4A_2$ (F) → ^2E (G) (659 nm), $^4A_2$ (F) → $^4T_1$ (P) (615 nm) and $^4A_2$ (F) → $^2A_1$ (G) (568 nm) transitions characteristic of the tetrahedral Co^{2+} ions [25]. The optical energy gaps of the doped ZnO samples were considerably smaller, showing thereby that the band gap of ZnO can be tuned by such doping [8]. Both the doped samples gave UV as well as blue-green emissions, somewhat weaker than in undoped ZnO [26,27]. With the various characterization data mentioned above, we conclude that both Mn^{2+} and Co^{2+} ions are present substitutionally in the Zn^{2+} sites of ZnO, in the samples prepared by us.

Detailed magnetic measurements were carried out on the 6 % and 2 % Mn (Co)-doped ZnO samples. We show the temperature variation of the inverse susceptibility χ_M^{-1} of the Mn-doped samples in Figure 6.7 and the Co-doped samples

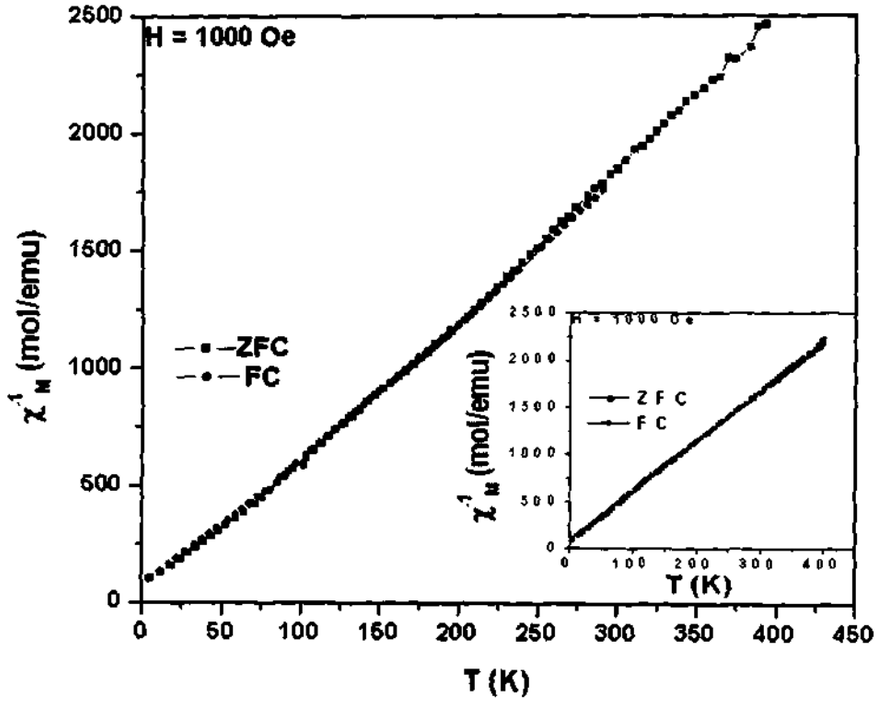

Figure 6.7: Temperature variation of inverse magnetic susceptibility of 6 % Mn-doped ZnO heated to 400 °C (I). Inset shows the data for sample II heated to 500 °C.

in Figure 6.8. The zero-field cooled (ZFC) and field cooled (FC, 1000 Oe) data are comparable indicating that the material does not possess the characteristics of a spin glass. Extrapolation of the inverse susceptibility data in the high temperature region gave negative Curie temperatures of – 5 and – 15 K for Mn-doped samples I and II respectively; the values were – 65 and – 15 K for Co-doped I and II samples.

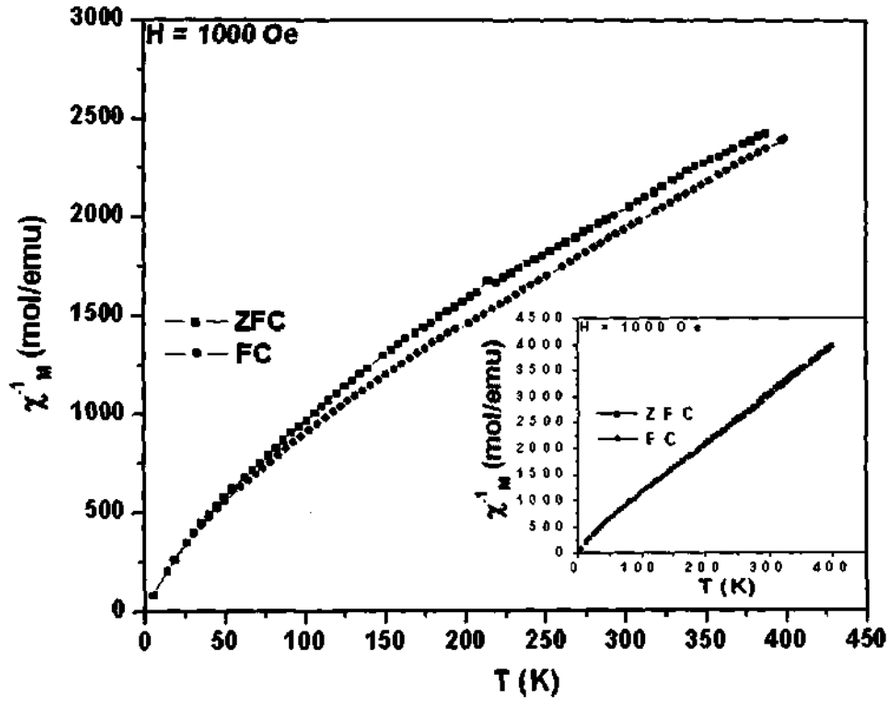

Figure 6.8: Temperature variation of inverse magnetic susceptibility of 6 % Co-doped ZnO heated to 400 °C (I). Inset shows the data for sample II heated to 500 °C.

The data can be understood in terms of the model of Spalek *et al.* [28] employing a modified Curie-Weiss law, or the model of Lawes *et al.* [29] wherein magnetization is treated as a sum of a Curie-Weiss term and a Curie term with a large Weiss temperature. Furthermore, we do not observe magnetic hysteresis or any other evidence for ferromagnetic ordering down to 2 K. The results show that the 6 % Mn- and 6 % Co-doped ZnO prepared by us exhibit only antiferromagnetic superexchange interactions but no ferromagnetism.

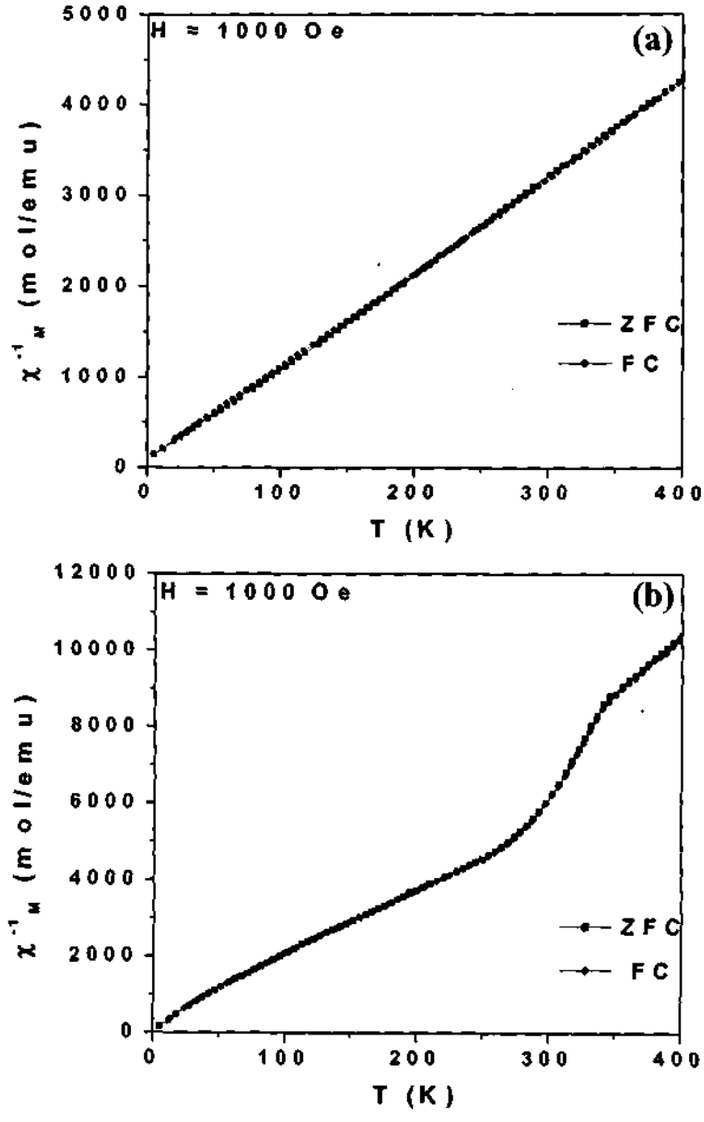

Figure 6.9: Temperature variation of inverse magnetic susceptibility of (a) 2 % Mn doped and (b) 2 % Co-doped ZnO.

Some workers claimed that it was necessary to have lower percentage of dopants (< 4 %) to observe ferromagnetism [13,24]. We, have therefore, carried out investigations of 2 % Mn- and Co-doped ZnO samples. (see insets of Figures 6.4 and 6.5). In Figure 6.9 (a) and (b), we show the temperature variation of the inverse susceptibility χ_M^{-1} of the 2 % Mn- and Co-doped ZnO samples (I). The ZFC and FC data show little difference. The data in the high-temperature region give paramagnetic Curie temperatures of 5 K and 50 K for the Mn- and Co- doped samples, but the M vs H curves show no hysteresis (Figure 6.10).

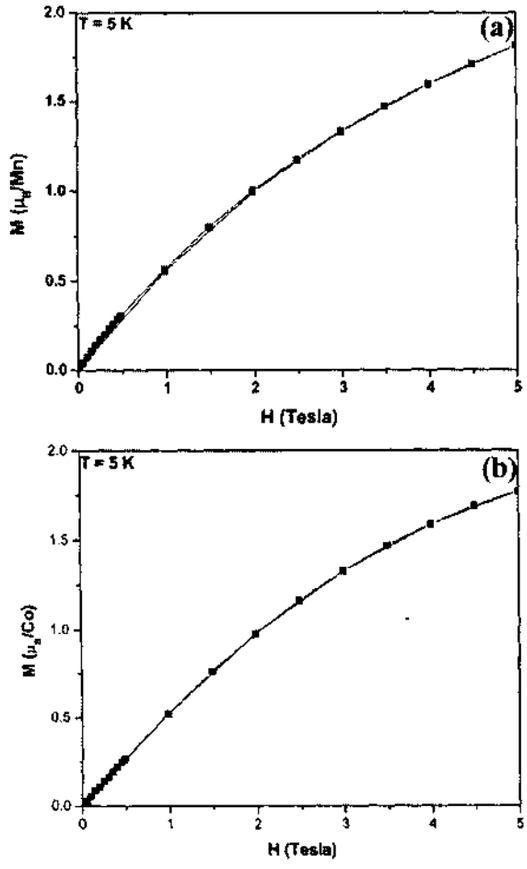

Figure 6.10: M vs H plots of (a) 2 % Mn-doped and (b) 2 % Co-doped ZnO obtained at an external field of T = 5 K.

6.5 Conclusions

The present investigations on Mn- and Co-doped ZnO establish them not to be ferromagnetic and throw considerable doubt about the ferromagnetic nature of these materials reported in the literature. It seems unlikely that these materials would be candidates for spintronics. This conclusion finds support from the recent work of Spaldin [30] who finds that robust ferromagnetism cannot occur in Mn- and Co-doped ZnO. If at all, it may occur if additional charge carriers are present, as indeed pointed out by Dietl *et al.* [3] as well. In order to obtain robust ferromagnetism, it may be worthwhile to investigate the effect of codoping of Mn- or Co-doped ZnO samples with other cations to induce additional charge carriers, or samples with defect-induced carriers.

6.6 References

[1] S. A. Chambers, Y. K. Yoo, *MRS Bulletin*, 2003, **28**, 706.

[2] M. Ziese, M. F. Thornton, eds., *Spin Electronics* (Springer, Berlin, 2001).

[3] T. Dietl, H. Ohno, F. Matsukura, J. Gilbert, D. Ferrand, *Science*, 2000, **287**, 1019.

[4] Y. Matsumoto, M. Murakami, T. Shono, T. Hasegawa, T. Fukumura, M. Kawasaki, P. Ahmet, T. Chikyow, S.-Y. Koshihara, H. Koinuma, *Science*, 2001, **291**, 854.

[5] K. Sato, H. Katayama-Yoshida, *Japan. J. Appl.* Phys., 2000, **39**, L555.

[6] S. A. Chambers, R. F. C. Farrow, *MRS Bulletin*, 2003, **28**, 729.

[7] W. Prellier, A. Fouchet, B. Mercey, *J. Phys. Condens. Matter*, 2003, **15**, R1583.

[8] S. W. Jung, S. -J. An, G –C. Yi, C. U. Jung, S. Lee, S. Cho, *Appl. Phys. Lett.*, 2002, **80**, 4561.

[9] T. Fukumura, Z. Jin, M. Kawasaki, T. Shono, T. Hasegawa, S. Koshihara, H. Koinuma, *Appl. Phys. Lett.*, 2001, **78**, 958.

[10] Q. Wang, P. Jena, *Appl. Phys. Lett.*, 2004, **84**, 4170.

[11] S -J. Han, T. - H. Jang, Y. B. Kim, B. –G. Park, J. –H. Park, Y. H. Jeong, *Appl. Phys. Lett.*, 2003, **83**, 920.

[12] (a) S. Kolesnik, B. Dabrowski, J. Mais, *Phys. Stat. Sol.*, 2004, **1**, 900; (b) V. Yu. Ivanov, M. Godlewski, S. Yatsunenko, A. Khachapuridze, Z. Golacki, M. Sawicki, A. Omelchuk, M. Bulany, A. Gorban, *Phys. Stat. Sol.*, 2004, **1**, 250.

[13] P. Sharma, A. Gupta, K. V. Rao, F. J. Owens, R. Sharma, R. Ahuja, J. M. Osorio Guillen, B. Johansson, G. A. Gehring, *Nature Mater.*, 2003, **2**, 673.

[14] K. Ueda, H. Tabata, T. Kawai, *Appl. Phys. Lett.*, 2001, **79**, 988.

[15] H -J. Lee, S -Y. Jeong, C. R. Cho, C. H. Park, *Appl. Phys. Lett.*, 2002, **81**, 4020.

[16] (a) K. Rode, A. Anane, R. Mattana, J. –P. Contour, O. Durand, R. LeBourgeois, *Appl. Phys. Lett.*, 2003, **93**, 7676; (b) S. Ramachandran, A. Tiwari, J. Narayan, *Appl. Phys. Lett.*, 2004, **84**, 5255.

[17] D. P. Norton, M. E. Overberg, S. J. Pearton, K. Pruessner, J. D. Budai, L. A. Boatner, M. F. Chisholm, J. S. Lee, Z. G. Khim, Y. D. Park, R. G. Wilson, *Appl. Phys. Lett.*, 2003, **83**, 5488.

[18] S-s. Yan, C. Ren, X. Wang, Y. Xin, Z. X. Zhou, L. M. Mei, M. J. Ren, Y. X. Chen, Y. H. Liu, H. Garmestani, *Appl. Phys. Lett.*, 2003, **84**, 2376.

[19] A. S. Risbud, N. A. Spaldin, Z. Q. Chen, S. Stemmer, R. Seshadri, *Phys. Rev. B.*, 2003, **68**, 205202-1.

[20] S. Deka, R. Pasricha, P. A. Joy, *Chem. Mater.*, 2004, **16**, 1168.

[21] D. A. Schwartz, N. S. Norberg, Q. P. Nguyen, J. M. Parker, D. R. Gamelin, *J. Am. Chem. Soc.*, 2003, **125**, 13205.

[22] M. Ghosh, R. Seshadri, C. N. R. Rao, *J. Nanosci. Nanotech*, 2004, **4**, 136.

[23] E –C. Lee, K. J. Chang, *Phys. Rev. B.*, 2004, **69**, 085205-1.

[24] H. J. Blythe, R. M. Ibrahim, G. A. Gehring, unpublished results.

[25] F. A. Cotton, D. M. L. Goodgame, M. Goodgame, *J. Am. Chem. Soc.*, 1961, **83**, 4690.

[26] M. Liu, A. H. Kitai, P. Mascher, *Jl. of Luminescence*, 1992, **54**, 35.

[27] X. T. Zhang, Y. C. Liu, J. Y. Zhang, Y. M. Lu, D. Z. Shen, X. W. Fan, X. G. Kong, *J. Crystal Growth*, 2003, **254**, 80.

[28] J. Spalek, A. Lewicki, Z. Tarnawski, J. K. Furdyna, R. Galazka, Z. Obuszko, *Phys. Rev. B.*, 1986, **33**, 3407.

[29] G. Lawes, A. P. Ramirez, A. S. Risbud, Ram Seshadri, Phys. Rev. B., 2005, **71**, 045201-1.

[30] N. A. Spaldin, *Phys. Rev. B.*, 2004, **69**, 125201-1.